Mechanics of Flow and Sediment Transport
Over Nonuniform Erodible Beds

by

Jonathan Mark Nelson

A dissertation submitted in partial fulfillment
of the requirements for the degree of

Doctor of Philosophy

University of Washington

1988

Approved by _____
(Chairperson of Supervisory Committee)

Program Authorized
to Offer Degree _____ Geophysics Program _____

Date _____ January 27, 1988 _____

Doctoral Dissertation

Signature _____

Date _____ January 29, 1988 _____

University of Washington

Abstract

**Mechanics of Flow and Sediment Transport
Over Nonuniform Erodible Beds**

by Jonathan Mark Nelson

Chairperson of the Supervisory Committee: Professor J. Dungan Smith

Geophysics Program

The morphology of erodible channels is intimately related to nonlinear interactions between the flow field, the bed topography, and the transport of sediment. This dissertation is directed toward understanding these interactions in terms of basic physical processes, and toward the development of predictive techniques which characterize these interactions in an appropriate manner. The approach taken herein divides the wide spectrum of possible bed morphologies into two distinct categories: those whose genesis and finite amplitude characteristics are explicitly dependent on spatial variations in the vertical structure of the flow (bedforms), and those which depend primarily on horizontal nonuniformity in the flow field (bars).

The development of bars in riverine channels is addressed by coupling a flow algorithm, a bedload transport equation, and an expression enforcing conservation of sediment mass. The flow model is based on an expansion about a lowest-order solution which employs a similarity vertical structure for the streamwise velocity, thereby eliminating bed deformations that are caused by changes in the vertical flow structure. Coupling of the flow and sediment transport calculations allows prediction of the temporal evolution of a channel bed with a prescribed sediment size and flow discharge. The evolution model is shown to predict the growth and stability of a point bar in an initially curved channel, as well as the development of alternate bars in an initially straight channel.

To investigate flow and sediment transport over bedforms, a predictive model for velocity and boundary shear stress fields over finite amplitude two-dimensional bedforms is presented. This flow model treats the production of wakes caused by separation of the flow over the bedform crests, as well as the effect of near-bed spatial accelerations induced both topographically and as a result of the diffusion of momentum into the wake deficit. Results of the model are in excellent agreement with laboratory measurements taken over immobile

bedforms using a laser-Doppler velocimeter. The finite amplitude model yields accurate predictions of the fluid dynamical effects ultimately responsible for the height, wavelength, and shape of well-developed bedforms.

TABLE OF CONTENTS

Chapter 4: Mechanics of Flow Over Ripples and Dunes

Chapter 5: Summary and Future Research Directions

LIST OF FIGURES

v

ACKNOWLEDGMENTS

DEDICATION

To my parents,

Byron and Evelyn

and my brothers and sisters,

James, Benjamin, Bethel, Barbara, Kathleen, and Phillip

Chapter 1: Introduction

The morphology of erodible beds is a direct result of a complicated nonlinear coupling that exists between the fluid flow field, the topography of the bed, and the transport of sediment. The goal of the work presented in this dissertation is to develop techniques whereby this coupling may be investigated quantitatively and, by doing so, to generate an understanding of the basic physical processes responsible for the production and equilibrium morphology of bars and bedforms in natural channels with erodible bottoms.

In the past, a great deal of the research on the morphology of natural beds has been focussed on the classification of various types of bars and bedforms, and on the empirical determination of the flow regimes in which these bed irregularities may be expected to occur. For the case of bedforms, this approach has led to the development of so-called bed phase diagrams, wherein flume and field observations are employed to relate integral parameters of the flow and sediment (e.g., depth, average velocity, average sediment size) to the observed bed geometry. Similarly, a substantial portion of the work on channel morphology has been directed toward the development of empirical "hydraulic geometry" relationships, in which observations are used as the basis for constructing empirical formulae relating various parameters of the flow and channel geometry. While there is no question that these approaches are both important and useful, they are ultimately unsatisfying in a scientific sense, because they do not provide a physical understanding of the processes which act to produce the observed morphology. Attempts to use these empirical results to generate some integral understanding of fluvial systems has inevitably led to descriptions of channel and bed dynamics which rely more on anthropomorphism than on physical principles. For example, stream meandering is often attributed to the stream "wanting" to lower its gradient. The fundamental tenet of this dissertation is that the deformation of an erodible

bed is governed by the well-known conservation laws of physics, and that any attempt to understand the processes by which bed evolution and stability occur must be based on the application of these principles.

1.1. Approach to the Problem

In the work presented herein, the wide spectrum of topographic nonuniformities observed on shear-erodible beds is separated into two basic categories. The first of these consists of forms which are generated primarily by variation in the horizontal structure of the flow field, while the second is made up of features which are generated by variation in the vertical structure of the streamwise velocity field. Henceforth, these will be referred to as bars and bedforms, respectively. Obviously, this classification is incomplete, since there are features for which both vertical structure changes and horizontal nonuniformity are important, as in the case of three-dimensional dunes. However, this distinction allows the overall problem of erodible bed morphology to be divided into two separate problems that are soluble at a reasonable level of complexity; this clearly is the first step toward a more general theory. Separate treatments of each of these problems are provided in this dissertation, with the idea firmly in mind that only keen physical insight into the various elements of the bed-flow-sediment coupling can ever lead to a comprehensive understanding of the problem.

One alternative to the bipartite approach described above would be to obtain numerical solutions of the full governing equations for turbulent flow and sediment transport over an erodible boundary. Indeed, some investigators have attempted to do this; however, the complexity of the interactions between the bed and the flow almost certainly precludes the possibility of retaining any physical grasp of the salient processes if this approach is used. Furthermore, it is not clear that a turbulent closure scheme currently exists which is capable

of handling the multiplicity of length scales present in the full problem. At any rate, the goal here is the scientific task of discovering the physical effects that govern this problem, not the engineering task of constructing models which simulate natural phenomenon. One of the by-products of the attempt to understand the various facets of the problem addressed herein is a set of numerical algorithms which reproduce important natural phenomena reasonably well; however, it must be stressed that the goal of this work is not the development of models, rather, it is the development of understanding through the use of concise, physically-based models.

The methods used in investigating each of the two problems briefly delineated above are essentially the same. In either the bar or bedform case, the first step in examination of the interactions between the flow and the bed topography is the construction of a fluid dynamical model that accurately predicts the flow and boundary shear stress fields over a bed of known geometry. As a result, one of the elements of this dissertation research has been the construction and verification of two flow models: one for the case of turbulent flow in channels with nonuniform bed and bank geometry, and another for the case of flow over well-developed two-dimensional ripples and dunes. These fluid dynamical components of the investigation allow the examination of the response of the flow to given bed topography. This is only half of the erodible bed problem; the other half involves characterization of the response of the bed to a given flow field. This latter part of the problem is addressed by using the results of the flow calculations in sediment transport relationships. By exploiting the separation of the temporal scales associated with the flow and the evolution of the bed topography, it is possible to isolate the fluid dynamical effects from the response of the bed, a powerful and robust approximation that allows segregation of the various physical processes active in the flow-bed coupling.

Because the investigation presented herein is directed at the processes responsible for

the morphology of well-developed forms, rather than just the genesis (initial instability) of bed features, the flow models employed must incorporate finite amplitude effects. As discussed in Chapters 3 and 4, a great deal of the previous work on erodible bed deformation has employed the technique of linear stability analysis. This method is based on the assumption that the nonlinearity caused by topographic nonuniformity in the flow is relatively weak, and that the governing equations can be linearized using a regular perturbation expansion about a uniform zero-order flow. While this technique is unquestionably useful for the identification of instability mechanisms and often yields accurate predictions of the initial wavelength of bed disturbances, it generates very little information about the well-developed features typically observed in nature, a point that will be addressed in more detail in Chapter 3. Even casual observation of typical river channels in which bars have formed clearly shows that the flow field does not consist of weak perturbations about a spatially uniform flow. Convective accelerations are typically important contributors to the overall momentum balance, as verified by the measurements of Yen and Yen [1971] and Dietrich and Smith [1983]. Similarly, flow over well-developed bedforms is typically affected strongly by the highly nonlinear effects of flow separation and wake formation. To investigate the equilibrium geometry of bars and bedforms, and how these features interact with the flow field, finite amplitude effects must be considered. As a result, a substantial part of the work presented in this dissertation has been directed toward the careful construction and verification of fluid dynamical models which encompass the salient finite amplitude effects for the cases of bars and bedforms.

1.2. The Bar Problem

The investigation of the development and stability of bars presented herein can be divided into three separate parts. The first element is the construction and experimental

verification of a fluid dynamical model for flow in curved channels. The second part of the investigation consists of utilizing the insight and techniques obtained in the development and use of the meander flow model to construct a more general channel flow model. This general model is capable of accurately predicting flow and bottom stress fields in a wide variety of natural nonuniform channels. Finally, this general model is coupled to a comprehensive sediment transport algorithm and then used to examine the salient interactions between the flow and the bed that produce channel-scale topographic features. In the next few pages, these three elements of this research are briefly described.

In Chapter 2, a method for calculating surface elevations, velocity fields, boundary shear stresses, and bedload sediment fluxes in typical natural meander bends is presented. This model is made up of two parts: (1) a numerical algorithm for predicting flow and total shear stress in a channel with spatially varying bank curvature and bed topography, and (2) a form drag partitioning algorithm that permits parameterization of form drag in terms of local roughness lengths and provides a method whereby the total boundary shear stress predicted by the flow algorithm may be reduced to the value of bottom stress responsible for sediment transport. This second part of the model is of crucial importance in calculating sediment fluxes accurately, and allows the bedform problem to be linked to the bar problem parameterically, rather than dynamically. The meander flow model is a modified and extended version of the theory presented by Smith and Mclean [1984]. The governing equations employed are shown to proceed from a consistent scaling of the full equations describing nonuniform turbulent flow. In accord with the discussion above, these equations retain the convective accelerations associated with bed and bank variations at lowest order. These terms are intimately associated with flow around point bars of finite amplitude in meandering channels. Specifically, the streamwise convection of downstream momentum is associated with the prediction of outward flow (toward the concave bank) over the point

bar [Dietrich and Smith, 1983], a phenomenon that is often neglected in discussions of point bar stability. The vertical profile of the streamwise velocity is assumed to have a similarity structure, the specific characteristics of which depend upon the functional form chosen for the eddy viscosity. By employing a similarity profile, this model specifically excludes changes in streamwise vertical structure associated with spatial accelerations.

To test both the meander flow model and the form drag partitioning arguments, calculations are performed for a bend in Muddy Creek, a well-studied natural meandering stream near Pinedale, Wyoming. The field observations include high density measurements of velocity, boundary shear stress, and sediment transport, as described by Dietrich [1982], and thus provide an excellent opportunity to test the model. Comparison of measured and computed values demonstrates that the theoretical approach is sufficiently accurate to predict sediment fluxes in channels for which topographic and curvature-induced convective accelerations are important.

The meander flow model can be used along with a specific sediment transport model to predict the initial instability, growth, and equilibrium morphology of a point bar in a channel with a typical meandering planform [Nelson and Smith, 1985]. However, since this investigation is focussed on bar forms in general, rather than just the specific case of point bars in curved channels, it is desirable to extend the techniques tested in the meander flow model to a more general model capable of making accurate predictions of flow in a wide variety of natural channels. With this in mind, the first part of Chapter 3 describes the construction of a more powerful algorithm for calculating flow fields and shear stresses in channels with arbitrary bed and bank geometry. This general model evolved from the original meander flow model described and verified in Chapter 2 and, although new physics are incorporated, the approach relies heavily on insights and techniques developed in the simpler algorithm. In fact, the general model essentially reduces to the meander flow

model for the case where the curvature of the primary flow streamlines is well-approximated by the curvature of the banks, but it is also valid for the case of straight channels containing alternate bars or braids. The general channel flow model is coupled with sediment transport calculations in order to produce an algorithm capable of predicting the instability, temporal evolution, and fully-developed morphology of a wide variety of bar forms, including point bars and alternate bars. This is accomplished by noting that the time scales associated with bed deformation are typically much longer than the time scales of the flow. This means that the flow model can be employed in a quasi-steady sense to predict the growth and stability of bars, as discussed in depth in Chapter 3.

In order to use the flow and sediment transport models to develop channel bathymetry, one assumes some initial bed geometry (typically flat), and employs the flow model to predict the boundary shear stress on that initial bed. This bottom stress distribution is then used along with a bed slope correction to calculate the streamwise and cross-stream sediment fluxes, which in turn are used to calculate the rate of erosion and deposition on the initial bed. This last step is accomplished using an expression that enforces the conservation of sediment volume. With these rates of erosion and deposition, it is possible to predict what the bed topography will be some small time increment later. The flow model can then be run using the modified bed topography, and the whole process is repeated iteratively until a stable bed morphology is attained. This method of applying the flow and sediment transport models, referred to subsequently as the bar evolution model, is described schematically in Figure 1.1. Since this model, like the meander model, is based on the assumption of a similarity vertical structure for the streamwise velocity field, the evolution model is specifically limited to bar type instabilities; bedform instabilities are suppressed. This approximation allows the bar and bedform problems to be decoupled, thereby permitting the isolation and inspection of the salient physical processes for the two different

T=0

```
┌─────────────────────────┐
│   CHANNEL PLANFORM      │
│  DISCHARGE, GRAINSIZE AND│
│   INITIAL BATHYMETRY    │
└─────────────────────────┘
            │
            ▼
┌─────────────────────────┐
│    NUMERICAL MODEL      │◄──────────────┐
│     FOR FLOW IN         │               │
│   NATURAL CHANNELS      │               │
└─────────────────────────┘               │
            │ τ TOTAL                      │
            ▼                              │
┌─────────────────────────┐               │
│   FORM DRAG CORRECTION  │               │
└─────────────────────────┘               │
  τ SKINFRICTION │                         │
            ▼                              │
┌─────────────────────────┐               │
│   SEDIMENT TRANSPORT    │               │
│  CALCULATION INCLUDING  │               │
│  GRAVITATIONAL CORRECTION│              │
└─────────────────────────┘               │
            │                              │
            ▼                          NO │
┌─────────────────────────┐               │
│  EROSION AND DEPOSITIONAL│              │
│   PATTERNS ON THE BED   │               │
└─────────────────────────┘               │
            │ T= T+ΔT                      │
            ▼                   ╱─────────────╲
┌─────────────────────────┐   ╱   IS CHANNEL AT ╲
│   NEW BATHYMETRY        │──►  QUASI-EQUILIBRIUM  │
│  AFTER SOME SMALL       │   ╲                 ╱
│ INCREMENT OF TIME PASSES│    ╲───────────────╱
└─────────────────────────┘           │ YES
                                      ▼
                              ┌─────────────┐
                              │     END     │
                              └─────────────┘
```

Figure 1.1. Flow chart depicting the iterative technique used in predicting equilibrium bed morphology in channels. Quasi-stability refers to the condition in which any bars present are not changing in height, wavelength, or shape; in some cases, these well-developed features migrate in a streamwise direction.

cases.

In Chapter 3, the bar evolution model is shown to make accurate predictions of the growth and equilibrium characteristics of various riverine bar forms. First, the approach described above is shown to predict the formation and growth of point bars in a variety of channels with initially flat beds and meandering planforms. Following the observations of Langbein and Leopold [1966], the channel path for these cases is described by a sine-generated curve, although results for some other planforms are also easily obtained. As expected, the initial growth of a point bar in these channels is a result of near-bed flow (and hence, bottom stress) directed obliquely toward the inner (convex) bank. This well-known effect is a result of the production of helical flow in the bend, as discussed in more detail in Chapter 3. The inward component of the bottom stress drives a sediment flux that produces deposition near the inner bank and erosion near the outer one, resulting in the growth of a point bar and pool. This simple idea is modified slightly due to the presence of streamwise curvature variations, which induce streamwise convergences and divergences of sediment transport, as discussed in more detail in Chapter 3. The eventual stability of point bar and pool bathymetry is related to gravitational corrections to the sediment fluxes due to bed slopes, as well as to the production of streamwise convective accelerations at the upstream end of the point bar. The convective accelerations and the accompanying adjustments in the pressure field produce outward flow over the point bar, in a process referred to hereafter as "topographic steering". This latter effect is ignored in models of point bar stability which are based on well-developed bend flow. In the well-developed flow approximation, both the stream geometry and the flow field are assumed to be independent of streamwise position. This is a poor approximation in the majority of natural meandering channels, and models which employ this assumption are clearly only of limited value in developing an understanding of natural channel and bed morphology.

Comparison of the evolution model results with the experiments of Hooke (1975) and Whiting (1987) demonstrate that both the growth rates and equilibrium morphology of point bars are accurately predicted by the approach taken herein. Furthermore, by running the evolution model for sine-generated curves of various amplitudes, it is possible to examine the connection between the planform of the channel and the spatial position and shape of well-developed point bars. This process also links the problem of point bar evolution to the case of alternate bar growth and migration. If the sinuousity is very low, the bar instability forced by the presence of curvature is overwhelmed by another instability which produces migrating alternate bars.

The alternate bar instability is distinct from the point bar evolution process in that no planform forcing is needed to produce alternate bars. These features arise spontaneously from any small perturbation to a steady, uniform flow in a straight channel. In order to investigate the physics governing the initiation of alternate bars, a linear stability analysis of the full equations used in the finite amplitude model is presented in Chapter 3. There are two advantages to the preliminary use of this approach. First, the results of the linear analysis allow the precise identification of the physical process causing the bed instability. Second, comparison of the linear results with the results of the bar evolution model clarifies the importance of the finite amplitude effects and demonstrates the failings of the linear theory. As expected, the linear theory provides physical insight into the governing process, as well as good predictions of the initial wavelength of alternate bars. As discussed in Chapter 3, the growth of alternate bars from an initial perturbation is intimately tied to the same topographic steering response important in the stability of point bars. The prediction of this instability is tied to the inclusion of streamwise convective accelerations in the flow model, as shown using the linear theory.

While the linear theory provides an understanding of the basic instability and

identifies a fastest-growing wavelength, the quantitative results of this approach are incorrect for fully-developed alternate bars. For example, finite amplitude effects produce an alteration in the wavelength as alternate bars grow to their equilibrium heights, a phenomenon that has been carefully observed and quantified by Fujita and Muramoto [1985]. Furthermore, the linear analysis yields no information about the height or shape of fully-developed bar forms; this information can only be obtained using the full non-linear modelling approach.

The results of the bar evolution model are shown to predict quite accurately the initiation, growth, and equilibrium morphology of alternate bars in straight and weakly sinuous channels. This is done in section 3.4, where model predictions are compared to measured values for flume experiments performed by Whiting [1987] and Fujita and Muramoto [1985]. The agreement between measured and predicted bathymetries clearly demonstrates the validity of the techniques employed in the bar evolution algorithm. As in the point bar problem, stability is found to be related both to the gravitational correction to sediment fluxes and to spatial accelerations in the flow field induced by the bed topography. The finite amplitude evolution model is also a viable way of examining the physical processes which act to produce bar forms of a complex nature. Thus, this method is a powerful predictive technique for examining bar forms in general.

1.3. The Bedform Problem

The technique used in the bar evolution model explicitly excludes the production of bedform instabilities. As shown in the linear stability analysis presented by Smith [1970], the instability mechanism that produces bedforms is associated with spatial changes in vertical structure. These variations are produced by the interaction of a shear flow with topographically-induced convective accelerations. Thus, by employing similarity vertical

structure for the streamwise flow in the bar model, bedform instabilities are eliminated. Similarly, it is advantageous to construct a fluid dynamical model for bedforms that is decoupled from bar-type responses. This is accomplished by restricting the investigation to the case of two-dimensional bedforms. This prohibits responses which depend on fluxes of mass and momentum in the cross-stream direction, and thereby eliminates the bar instabilities discussed above.

The algorithm used herein for the calculation of velocity and boundary shear stress fields over well-developed two-dimensional bedforms is based on techniques originally presented by McLean and Smith [1986]. They developed a theoretical approach that explicitly treats the production of a wake due to separation of the flow over bedforms. Flow separation occurs near the crest of most natural bedforms and is an important factor in the determination of bottom stress patterns on the surfaces of bedforms. In the theoretical development presented by McLean and Smith [1986], the interaction of the wake region with the near-bed flow was treated using a nonuniform internal boundary layer theory. This boundary layer model includes the effects of spatial accelerations induced both topographically and as a result of the wake forcing. In the original McLean-Smith model, the wake and boundary layer regions of the flow were coupled to the flow interior using a potential flow solution in conjunction with a semi-empirical form drag closure. This latter part of the model allows the parameterization of changes in vertical structure in the interior due to the coalescing of wake regions generated by bedforms upstream.

In the bedform flow model presented in this dissertation, three improvements have been made to the original McLean-Smith model. First, the need for a form drag closure has been eliminated through the development of a theory that specifically treats the role of wakes from upstream bedforms coalescing in the interior. Second, nonhydrostatic effects associated with the inviscid response of the flow to the bedform are included both in the

interior and in the wake region near the bed. This improvement permits more accurate calculations to be made for short wavelength features, and is an important factor in the prediction of the cessation of dune growth at some fraction of the flow depth. Finally, the boundary layer formulation developed by McLean and Smith has been extended to the region between the dune crest and the point of reattachment. This allows spatially complete predictions of flow and bottom stress, as are necessary for sediment transport calculations.

As in the case of the channel flow model, verification of the flow model for dunes using carefully measured data is desirable. However, while previous work by other investigators provided an excellent data set to test the channel flow model, available measurements of flow over two-dimensional dunes were not comprehensive enough to serve as a model test. Therefore, a simple flume experiment was carried out to obtain the necessary data. This experiment involved making extremely dense measurements of the velocity field over immobile two-dimensional dunes using laser-Doppler velocimetry. These measurements include accurate velocity determinations a fraction of a centimeter from bed, as required for studying the structure of the developing internal boundary layer on the stoss side of a bedform.

Comparisons of measured and predicted velocities indicate that the theory presented herein provides accurate predictions of the flow field over bedforms. These predictions include the flow in the recirculation region in the lee of the bedform crest, and they explicitly include the effects of flow separation and wake formation. Boundary shear stress patterns predicted by the model are also compared to values measured downstream of a backward step by Jones [1978]. This demonstrates the accuracy of the technique employed for coupling the wake region to the internal boundary layer. The comparison with experimental results shows that the flow model is capable of making predictions that are accurate enough to be used in sediment transport calculations.

Using sediment transport considerations, but avoiding a specific sediment transport model, the flow predictions are employed to explore the coupling between the fluid and the bed. First, in conjunction with sediment transport arguments, the flow model is shown to predict the initial growth of bedforms. Second, this method reproduces the fluid dynamical effects responsible for the determination of the wavelengths of bedforms of finite amplitude. This is related to the coupling between the wake and the internal boundary layer downstream of the reattachment point, as discussed in more detail in Chapter 4. The interaction between the flow and the bedform that causes the cessation of bedform growth at some fraction of the flow depth is also predicted by the fluid dynamical theory. The accuracy of this prediction is dependent on the inclusion of non-hydrostatic effects. Finally, the shape and migration rates of bedforms can be predicted using the theoretical results by applying well-known techniques for relating local topographic elevation of the bedform surface to sediment flux rates (e.g., Fredsoe, 1982).

Preliminary results from coupling of the model for flow over bedforms with calculations of bedload and suspended load transport have been used to predict the wash-out of dunes [Nelson and Smith, 1986a] and the dependence of lee-side slip faces of dunes on weak suspended load transport [Nelson and Smith, 1986b]. However, a comprehensive treatment of sediment transport over bedforms requires the inclusion of the effects of sediment inertia [Smith, 1970] and bed slopes on the sediment flux field. The bed slope correction employed in the bar evolution algorithm is, strictly speaking, only valid for relatively small slopes, especially when the bed gradient is in the direction of the sediment transport, rather than transverse to it. This approach is inadequate for the case of bedforms. Currently, the effects of bed slope on bedload transport are being addressed using the saltation model of Wiberg and Smith [1985]. However, as of this writing, these techniques have not been incorporated into the work presented here.

In synopsis, this dissertation consists of the development and verification of two fluid dynamical theories, each of which is designed to address a specific piece of the erodible bed instability problem. In developing these models, emphasis is placed on the careful treatment of the physical processes that play a role in coupling the flow to the sediment transport field, since the ultimate goal is to understand and make accurate predictions of the deformation and stability of natural beds. Although the text deals primarily with the theoretical development, verification, and results of these models, this research clearly has important implications in the fields of hydrology, sedimentology, and geomorphology. Continued development and application of well-grounded theoretical formulations, such as those developed herein, will lead to a comprehensive understanding of a broad spectrum of erodible bed phenomena in terms of basic physical processes.

Accurate specification of the spatial distribution of bottom stress in fluvial and estuarine systems is of crucial importance in calculations of patterns of erosion and deposition, primarily because erosion and deposition depend on the divergence of the sediment flux and bedload equations are rather sensitive functions of boundary shear stress. Unfortunately, direct measurement of boundary stress in these systems is often very difficult and quite inaccurate. This is especially true in reaches where large convective accelerations are produced by the presence of curvature and irregular bed topography. The amount of time and data required to resolve the structure of the stress field in systems of this nature usually is prohibitively large. Because most streams and rivers are curved and have irregular beds, many important sediment transport problems are incompletely characterized as a result of insufficient or inaccurate knowledge of the stress field.

The difficulty encountered in measuring boundary shear stresses in nonuniform flows indicates the desirability of a physically-based model which accurately predicts these values. Several investigators [e.g., Engelund, 1974; De Vriend, 1977; Ascanio and Kennedy, 1983] have attempted to characterize the flow and bottom stress fields in curved channels. In order to simplify the governing equations, their models either consider the convective accelerations due to downstream-varying depth and curvature to be perturbations about a lowest-order solution that neglects these effects, or they ignore these terms entirely. Models of this nature will only be accurate when momentum fluxes associated with bed topography and changes in radius of curvature are much smaller than the pressure gradient and bottom stress terms in the vertically-averaged downstream momentum equation. However, it has been clearly demonstrated, first by Yen and Yen [1971] in a

laboratory flume and later by Dietrich and Smith [1983] in a natural meandering stream, that the vertically-integrated convective accelerations described above are of the same order of magnitude as the pressure gradient and shear stress forces in meandering channels with typical bar-pool topography. It is clear from these field and laboratory observations that a valid model of flow in curved channels with naturally-occurring bed topography must include these terms in the lowest-order equations.

Recently, Smith and McLean [1984] developed a model for flow in meandering streams based on a regular perturbation expansion about a zero-order flow that included the convective acceleration terms described above. In order to demonstrate the validity of the model, Smith and McLean compared predicted bottom shear stress and water surface topography to values measured by Hooke [1975] in a curved laboratory channel. The good agreement between the predictions of the model and Hooke's data indicate that the salient features of the flow are well described by the model. This is encouraging, especially because Hooke's flume had bottom topography and curvature characteristics similar to those of a natural stream. The centerline of Hooke's flume was described by a sine-generated curve, which Langbein and Leopold [1966] identified as a trace that closely defines the centerline of many naturally-occurring meanders. Furthermore, the bed of the flume was in equilibrium with the flow and displayed the bar-pool structure typical of natural sediment-transporting streams. However, while Hooke's flume was similar to natural meanders in these two respects, it also had features that were definitely not representative of natural situations. For example, the flume had vertical sidewalls and was of constant width, unlike natural meandering channels. In addition, the experimental run Smith and McLean attempted to reproduce with their model was one in which the bed was stabilized, so there was no sediment transport and there were no bedforms on the channel bottom. Thus, while the favorable comparison of the model results and measurements for

this laboratory case is an important and encouraging first step, it is clear that a more comprehensive verification must be completed if the model is to be employed in natural streams, which are, after all, the ultimate domain of interest.

In this chapter, a consistent scaling of an appropriate set of momentum equations is shown to produce a model similar to that of Smith and McLean [1984], and then this model is extended to the case in which width varies slowly in the downstream direction and depth smoothly approaches zero at the banks of the stream. The technique presented also allows for the presence of bedforms and sediment transport, thus providing a model that should be applicable to the majority of natural streams and rivers. In order to verify this expanded version of the Smith-McLean model, we apply it to a bend (the so-called IMR bend) in Muddy Creek, a sand-bedded meandering stream in Wyoming. This site was studied extensively by Dietrich [1982], and the data from this location permits calculated boundary shear stresses and other flow variables to be compared to values measured in a system possessing the dominant characteristics of natural meandering channels. The calculations and subsequent comparision with data from the study site clearly indicate both the importance of including appropriate convective accelerations at lowest order and the overall veracity of the model.

2.1. Mathematical Formulation

2.1.1. Fundamental Equations

Since bottom slopes in streams and rivers are usually gentle and the time scale of discharge variations is large compared to the time required for a parcel of water to traverse a typical meander, it is reasonable to assume that the pressure distribution is hydrostatic and the flow is quasi-steady. using these approximations, Smith and McLean [1984] obtained equations expressing conservation of mass and momentum in a "channel-fitted"

orthogonal curvilinear coordinate system. Defining s, n, and z as the coordinates in the downstream, cross-stream, and vertical directions, respectively, and defining R as the centerline radius of curvature, these equations are as follows:

$$\frac{1}{1-N}\frac{\partial u}{\partial s} - \frac{v}{(1-N)R} + \frac{\partial v}{\partial n} + \frac{\partial w}{\partial z} = 0 \tag{2.1}$$

$$\frac{u}{1-N}\frac{\partial u}{\partial s} + v\frac{\partial u}{\partial n} + w\frac{\partial u}{\partial z} - \frac{uv}{(1-N)R} = \tag{2.2}$$

$$\frac{-g}{1-N}\frac{\partial E}{\partial s} + \frac{1}{\rho}\left[\frac{1}{1-N}\frac{\partial \tau_{ss}}{\partial s} + \frac{\partial \tau_{ns}}{\partial n} + \frac{\partial \tau_{zs}}{\partial z} - 2\frac{\tau_{ns}}{(1-N)R}\right]$$

$$\frac{u}{1-N}\frac{\partial v}{\partial s} + v\frac{\partial v}{\partial n} + w\frac{\partial v}{\partial z} + \frac{u^2}{(1-N)R} = \tag{2.3}$$

$$-g\frac{\partial E}{\partial n} + \frac{1}{\rho}\left[\frac{1}{1-N}\frac{\partial \tau_{ns}}{\partial s} + \frac{\partial \tau_{nn}}{\partial n} + \frac{\partial \tau_{zn}}{\partial n} + \frac{\tau_{ss} - \tau_{nn}}{(1-N)R}\right]$$

$$0 = -\frac{1}{\rho}\frac{\partial p}{\partial z} - g \tag{2.4}$$

where u, v, and w are the velocities in the downstream, cross-stream, and vertical directions, respectively, and where E and B are the elevations of the surface and bottom. The quantity 1-N=(1-n/R) is simply the downstream metric associated with the channel coordinate system, which was described formally by Smith and McLean [1984] and used extensively by Dietrich [1982] and Dietrich and Smith [1983].

In the above equations, τ_{ss}, τ_{ns}, τ_{zs}, τ_{nn}, τ_{zn}, and τ_{zz} are the independent components of the deviatoric stress tensor. Since rivers and streams are fully developed turbulent boundary layers, viscous stresses are negligible in comparison with Reynold's stresses and can be ignored. If the existence of a scalar kinematic eddy viscosity is assumed, the Reynold's stresses may be expressed in terms of the rate of strain tensor. In the given coordinate system, this relationship results in the following equations for the stress components:

$$\tau_{ss} = 2\rho K \left[\frac{1}{1-N} \frac{\partial u}{\partial s} - \frac{v}{(1-N)R} \right] \tag{2.5a}$$

$$\tau_{nn} = 2\rho K \left[\frac{\partial v}{\partial n} \right] \tag{2.5b}$$

$$\tau_{zz} = 2\rho K \left[\frac{\partial w}{\partial z} \right] \tag{2.5c}$$

$$\tau_{zs} = \rho K \left[\frac{1}{1-N} \frac{\partial w}{\partial s} + \frac{\partial u}{\partial z} \right] \tag{2.5d}$$

$$\tau_{zn} = \rho K \left[\frac{\partial w}{\partial n} + \frac{\partial v}{\partial z} \right] \tag{2.5e}$$

$$\tau_{ns} = \rho K \left[\frac{1}{1-N} \frac{\partial v}{\partial s} + \frac{u}{(1-N)R} + \frac{\partial u}{\partial n} \right] \qquad (2.5f)$$

In order to calculate the boundary shear stress, it is necessary to average the continuity and momentum equations vertically by integrating them from the channel bottom, z = B(s,n), to the water surface, z = E(s,n). Integral conservation of mass yields

$$\frac{1}{1-N} \frac{\partial}{\partial s} (<u>h) - \frac{<v>h}{(1-N)R} + \frac{\partial}{\partial n} (<v>h) = 0 \qquad (2.6)$$

where $< >$ has been used to indicate vertically-averaged variables. Treating this equation as an ordinary differential equation for $<v>h$ and noting that this quantity must equal zero at the banks of the stream, one finds the solution

$$<v>h = \frac{-1}{1-N} \int_{\frac{-W}{2}}^{n} \frac{\partial}{\partial s} (<u>h) dn \qquad (2.7)$$

where W denotes the stream width.

Vertical integration of the horizontal momentum equations yields the following equations:

$$\frac{1}{1-N} \frac{\partial}{\partial s} (<u^2>h) + \frac{\partial}{\partial n} (<uv>h) - \frac{2<uv>h}{(1-N)R} =$$

$$\frac{-gh}{1-N}\frac{\partial E}{\partial s} + \frac{1}{\rho}\left[\frac{1}{1-N}\frac{\partial}{\partial s}(<\tau_{ss}>h) + \frac{\partial}{\partial n}(<\tau_{ns}>h)\right. \tag{2.8}$$

$$\left.-2\frac{<\tau_{ns}>h}{(1-N)R} + \frac{1}{1-N}(\tau_{ss})_B\frac{\partial B}{\partial s} + (\tau_{ns})_B\frac{\partial B}{\partial n} - (\tau_{zs})_B\right]$$

and

$$\frac{1}{1-N}\frac{\partial}{\partial s}(<uv>h) + \frac{\partial}{\partial n}(<v^2>h) + \frac{(<u^2> - <v^2>)h}{(1-N)R} =$$

$$-gh\frac{\partial E}{\partial n} + \frac{1}{\rho}\left[\frac{1}{1-N}\frac{\partial}{\partial s}(<\tau_{ns}>h) + \frac{\partial}{\partial n}(<\tau_{nn}>h)\right. \tag{2.9}$$

$$\left.+ \frac{<\tau_{ss} - \tau_{nn}>h}{(1-N)R} + \frac{1}{1-N}(\tau_{ns})_B\frac{\partial B}{\partial s} + (\tau_{nn})_B\frac{\partial B}{\partial n} - (\tau_{zn})_B\right]$$

Equations (2.1) through (2.9) form the mathematical basis of the meander flow model developed here. The complete formulation of the model can be divided into two distinct parts and, for the sake of clarity, this approach will be taken here. The two parts of the model are as follows:

(a) Using assumptions based on physical reasoning and observations, Smith and McLean [1984] transformed equations (2.7), (2.8), and (2.9) into a single integro-differential equation for $(\tau_{zs})_B$, the downstream bottom shear stress, which may easily be solved numerically. The work presented here demonstrates that this equation may be arrived at directly from a consistent scaling of the

full vertically-averaged momentum equations, and describes a simple and efficient numerical algorithm for its solution. This solution to the vertically-averaged equations will include effects due to downstream-varying radius of curvature and bottom topography.

(b) A regular perturbation expansion is constructed based on the correct ordering of the terms in the full horizontal momentum equations, (2.2) and (2.3). The lowest order of this expansion corresponds to the solution of the vertically-averaged equations found in (a), i.e., only the vertically-averaged convective acceleration terms are retained at lowest order in the downstream momentum equation. Using this expansion, we are able to calculate approximate solutions for the complete stress distribution, surface elevation, and the velocity field. These solutions include convective accelerations associated with bed and bank variations and can be expected to be good approximations to the flow found in natural meanders.

2.1.2. Scaling and Numerical Solution of the Vertically-averaged Equations

In order to scale the equations it is convenient to introduce scaled nondimensional variables. We define m_0 , W_0 , h_0 , and R_0 as length scales typical of meander length, width, depth, and minimum radius of curvature, respectively. Furthermore, U_0 is used to represent a typical streamwise velocity scale, l_0 is used to scale surface elevations, and τ_0 is a typical bottom stress value. Using these scales, the equations may be nondimensionalized using the following definitions:

$$u = U_0 \hat{u} \qquad v = \frac{h_0}{W_0} U_0 \hat{v} \qquad w = \frac{h_0}{m_0} U_0 \hat{w}$$

$$s = m_0 \hat{s} \qquad n = W_0 \hat{n} \qquad z = h_0 \hat{z}$$

$$R = R_0 \hat{R} \qquad E = l_0 \hat{E} \qquad h = h_0 \hat{h}$$

$$B = h_0 \hat{B} \qquad \tau_{ij} = \tau_o \hat{\tau}_{ij} \qquad Fr = \frac{U_0}{\left[g h_0 \right]^{\frac{1}{2}}}$$

(2.10)

Inserting these variables into the vertically-averaged equations and dropping the carets for convenience yields

$$\left[\frac{h_0}{m_0} \right] \left[\frac{1}{1-N} \frac{\partial}{\partial s} (<u^2>h) \right] + \left[\frac{h_0}{W_0} \right]^2 \left[\frac{\partial}{\partial n} (<uv>h) \right] - \left[\frac{h_0}{W_0} \right] \left[\frac{h_0}{R_0} \right] \left[2\frac{<uv>h}{(1-N)R} \right] =$$

$$Fr^{-2} \left[\frac{l_0}{m_0} \right] \left[\frac{gh}{1-N} \frac{\partial E}{\partial s} \right] + \left[\frac{\tau_0}{\rho U_0^2} \right] \left[\left[\frac{h_0}{m_0} \right] \left[\frac{1}{1-N} \frac{\partial}{\partial s} (<\tau_{ss}>h) \right] \right.$$

(2.11)

$$+ \frac{h_0}{W_0} \left[\frac{\partial}{\partial n} (<\tau_{ns}>h) \right] - \frac{h_0}{R_0} \left[\frac{2<\tau_{ns}>h}{(1-N)R} \right]$$

$$\left. + \frac{h_0}{m_0} \left[\frac{1}{1-N} (\tau_{ssB}) \frac{\partial B}{\partial s} \right] + \frac{h_0}{W_0} \left[(\tau_{ns})_B \frac{\partial B}{\partial n} - (\tau_{zs})_B \right] \right]$$

$$\left[\frac{h_0}{W_0}\right]\left[\frac{h_0}{m_0}\right]\left[\frac{1}{1-N}\frac{\partial}{\partial s}(<uv>h)\right] + \left[\frac{h_0}{W_0}\right]^3\left[\frac{\partial}{\partial n}(<v^2>h)\right] + \left[\frac{h_0}{R_0}\right]\left[\frac{<u^2>h}{(1-N)R}\right]$$

$$-\left[\frac{h_0}{R_0}\right]\left[\frac{h_0}{W_0}\right]^2\left[\frac{<v^2>h}{(1-N)R}\right] = -Fr^{-2}\left[\frac{l_0}{W_0}\right]\left[h\frac{\partial E}{\partial n}\right] + \qquad (2.12)$$

$$\left[\frac{\tau_0}{\rho U_0^2}\right]\left[\frac{h_0}{m_0}\left[\frac{\partial}{\partial s}(<\tau_{ns}>h)\right] + \frac{h_0}{W_0}\left[\frac{\partial}{\partial n}(<\tau_{nn}>h)\right] + \frac{h_0}{R_0}\left[\frac{<\tau_{ss}-\tau_{nn}>h}{(1-N)R}\right]\right.$$

$$\left.+ \frac{h_0}{m_0}\left[\frac{1}{1-N}(\tau_{ns})_B\frac{\partial B}{\partial s}\right] + \frac{h_0}{W_0}\left[(\tau_{nn})_B\frac{\partial B}{\partial n} - (\tau_{zn})_B\right]\right]$$

The nondimensional numbers appearing in the equations must be ordered with respect to each other so that it is possible to determine the important terms in the equations. The first of these numbers is the depth-to-width aspect ratio defined by h_0/W_0 . In natural streams this ratio is typically a minimum of $0(10^{-1})$, which will be denoted as $0(\varepsilon)$. The ratio of average depth to minimum radius of curvature, h_0/R_0, is also $0(\varepsilon)$ because R_0 is of the same order as the width in well-developed meanders. However, the ratio of h_0 to m_0, the meander length, will be $0(\varepsilon^2)$, since the lengths of meanders are typically an order of magnitude greater than their widths. These three non-dimensional numbers describe the geometry of the meander only. The dynamical balance present is described by the Froude number, the ratio of the crossing-to-crossing drop in surface elevation to the meander length, and the drag coefficient defined by $\tau_0/\rho U_0^2$. Since the drag coefficient in geophysical flows of this nature is generally of $0(10^{-2})$, this last number will be $0(\varepsilon^2)$. The combination Fr^{-2} (l_0/m_0) must be of lowest order in the downstream equation since gravity is the ultimate driving force for the flow. Similarly, Fr^{-2} (l_0/W_0) must be of lowest order in the

cross-stream equation in order for the cross-stream pressure gradient to balance the centrifugal force term. As a consequence of these scaling arguments, the lowest-order balances in the dimensional vertically-averaged equations are given by

$$\frac{1}{1-N}\frac{\partial}{\partial s}(<u^2>h) + \frac{\partial}{\partial n}(<uv>h) - 2\frac{<uv>h}{(1-N)R} =$$

$$\frac{-gh}{1-N}\frac{\partial E}{\partial s} - \frac{1}{\rho}(\tau_{zs})_B$$

(2.13)

and

$$\frac{<u^2>h}{(1-N)R} = -gh\frac{\partial E}{\partial n}$$

(2.14)

This scaling supports the observation that topographically-induced convective accelerations must be retained at lowest order in the downstream momentum equation in order to describe flow in natural streams. Smith and McLean [1984] include these acceleration terms in the lowest order because observations of flow in meanders indicated that these terms were of primary importance, but they did not present scaling arguments supporting this result. However, the scaling presented here clearly demonstrates that their conclusion was correct.

Using the observation that $<uv> \approx <u><v>$ and the simple closure assumption $\rho<u^2> \approx \rho<u>^2 = \alpha(\tau_{zs})_B$, where α is the reciprocal of the drag coefficient, Smith and McLean [1984] transformed equations (2.7), (2.13), and (2.14) into a single integro-differential equation for $(\tau_{zs})_B$:

$$\left[\frac{1-N}{h}\right](\tau_{zs})_B = -\rho g\frac{\partial E_c}{\partial s} - \alpha(\tau_{zs})_B\frac{\partial}{\partial s}(\ln(1-N))$$

$$- \frac{1}{2}\frac{\partial}{\partial s}(\alpha(\tau_{zs})_B) + \int_0^N\frac{1}{1-N}\frac{\partial}{\partial s}(\alpha(\tau_{zs})_B)dN + \tag{2.15}$$

$$\left[\frac{1}{h}\frac{\partial}{\partial n}(\alpha(\tau_{zs})_B)^{\frac{1}{2}} - \frac{(\alpha(\tau_{zs})_B)^{\frac{1}{2}}}{(1-N)Rh}\right]\int_{\frac{-W}{2}}^n\frac{\partial}{\partial s}(\alpha(\tau_{zs})_Bh^2)^{\frac{1}{2}}dn$$

where E_c is the surface elevation at the stream centerline.

The solution of equation (2.15) is subject to the constraint that downstream discharge must be held constant. In order to apply this constraint, it is necessary to define a complete velocity field as follows.

$$u = \left[\frac{(\tau_{zs})_B}{\rho}\right]^{\frac{1}{2}}f_1(\zeta,\zeta_0) = u_*f_1(\zeta,\zeta_0) \tag{2.16}$$

where $\zeta = (z-B)/h$ and $\zeta_0 = z_0/h$, where z_0 is the overall bottom roughness parameter. The z_0 used in this equation must be representative of all the drag effects present in the meander, including sediment transport and form drag due to channel geometry and bed-forms. This parameterization is based on the fact that these effects all occur near the bed, so that the associated wake regions extract momentum from the flow in a manner analogous to skin friction effects. A suitable manner for calculating the overall z_0 is given below. In conjunction with the closure assumption, the equation above yields

$$\alpha = \left[\int_{\zeta_0}^{1} f_1\left[\zeta,\zeta_0\right] d\zeta \right]^2 \tag{2.17}$$

Using the assumed velocity profile the downstream flux constraint has the form

$$Q = \int_{\frac{-W}{2}}^{\frac{W}{2}} h \int_{\zeta_0}^{1} u \, d\zeta \, dn = \int_{\frac{-W}{2}}^{\frac{W}{2}} u_* \alpha^{\frac{1}{2}} h \, dn \tag{2.18}$$

Equation (2.15) is solved by treating the integral terms as quantities which may be brought in iteratively as inhomogeneous terms in a simple first-order linear differential equation. In other words, we initially solve equation (2.15) assuming the integral terms are zero (thus reducing it to a simple differential equation), then use the solution obtained thereby to calculate the value of the integrals involving $(\tau_{zs})_B$ on the right hand side. These values are then inserted into the equation as inhomogeneous terms and the equation is again solved, yielding an improved estimate for the bottom stress field. Obviously, this procedure may be repeated until the solution for $(\tau_{zs})_B$ converges, usually about three or four times. Thus, the complicated integro-differential equation is exchanged for a series of first-order inhomogeneous ordinary differential equations of the form

$$\partial \frac{(\alpha|\tau_{zs}|_B)}{\partial s} + 2\gamma_1(s,n)(\alpha|\tau_{zs}|_B) = 2\gamma_2(s,n) \tag{2.19}$$

where

$$\gamma_1 = \frac{1-N}{\alpha h} + \frac{\partial}{\partial s}(\ln(1-N))$$

$$\gamma_2 = -\rho g \frac{\partial E_c}{\partial s} + \int_0^N \frac{1}{1-N} \frac{\partial(\alpha|\tau_{zs}|_B)}{\partial s} dN$$

$$+ \left[\frac{1}{h}\frac{\partial}{\partial n}(\alpha|\tau_{zs}|_B)^{\frac{1}{2}} - \frac{(\alpha|\tau_{zs}|_B)^{\frac{1}{2}}}{(1-N)Rh} \right] \int_{\frac{-W}{2}}^{n} \frac{\partial}{\partial s}(\alpha|\tau_{zs}|_B)^{\frac{1}{2}} dn$$

Although the solution of these equations can be written down immediately in terms of integrals which may be evaluated numerically, it is simpler and more efficient computationally to solve these equations directly using a finite difference approximation.

Assuming that values for the downstream bottom stress are known at the entrance to the bend, the finite difference form of equation (2.19) will yield the values of the bottom stress at the gridpoints immediately downstream, provided that some value for the centerline surface slope is prescribed. Of course, these values will not satisfy the flux integral above, unless the initial guess for the centerline slope is an extremely fortunate one. However, one may use the calculated discharge and the desired discharge values to improve the value of the centerline surface slope using a simple shooting method. In other words, the finite difference equation coupled with the flux integral yields discharge as a function of centerline surface slope at each cross-section (s = constant). Therefore, as long as the true river discharge is known, the solution is completely specified. The simple shooting method employed here generally converges on the correct slope in less than five iterations. Once this procedure is followed at each section, the differential equation is solved, so one may calculate the integral terms from the solution, reformulate the differential equation with improved values for the inhomogeneous terms and repeat the procedure. This continues

until the entire field of $(\tau_{zs})_B$ values has converged.

The procedure described above requires that the values of the boundary shear stress be known at the upstream section of the numerical grid. Unfortunately, due to the difficulty involved in measuring bottom stress, this upstream boundary condition is usually unknown or only very roughly determined. However, the equations are not at all sensitive to the upstream boundary condition, and the solution is essentially independent of the initial prescribed values about one meander length downstream, provided that the initial values are even remotely reasonable and yield the correct value for the discharge. Therefore, in order to find the solution in a given bend, it is only necessary to know the geometry and topography of the given bend and the bend immediately upstream. Then, even if the initial upstream values of $(\tau_{zs})_B$ are inaccurate, the stress values calculated in the bend of interest (or any subsequent bend) will be correct. If the geometric data for the upstream bend is more or less similar in geometry to the bend of interest, it is sufficient to perform the calculation through a few identical bends, each of which is the known bend or its reflection about a line through the crossings.

This numerical procedure is well-posed for the case of constant width, in which the banks of the stream correspond to lines of constant n. However, if the width varies, as it does in most natural streams, the method by which the solution is marched downstream along lines of constant n will no longer determine the solution in the entire domain of interest. As long as the variations in the width are not abrupt, this problem can be avoided by linearly straining the numerical grid used so that lines of constant n correspond to the banks of the stream. The calculation is then performed exactly as described above, except that the discharge integral is calculated across widths which vary downstream. This procedure is only valid if width variations are such that convective accelerations due to them are small and can be neglected, which is the same as saying that taking $\partial/\partial s$ outside the

integral in the numerical evaluation of the integral in equation (2.7) will cause an error of the same order of magnitude as terms already dropped from the equation due to scaling arguments. Since the limits of integration in this integral will be a slowly varying function of s in the strained coordinate system, Liebnitz' rule may be used to show that the error incurred by this procedure is of higher order than the rest of the terms in the downstream equation providing that width variations over the length of the meander are an order of magnitude smaller than the average width. If this condition is not met, width-induced convective accelerations must be included at lowest order, and a more complicated numerical procedure must be used. It is important to note that the basic equations of the model are valid even for the case of abrupt width changes; there is a large class of problems, however, for which width is nearly constant and these are addressed here, chiefly for the sake of numerical simplicity.

2.1.3. The Non-averaged Equations

The solution of the vertically-averaged equations above yields the downstream boundary shear stress field, the downstream transport field, and the centerline and cross-stream surface slopes, all based on the assumption of a vertical structure function for the downstream velocity. In order to calculate the cross-stream bottom stress and velocity, as well as the error associated with the assumption of a vertically similar downstream velocity profile at each point in the stream (i.e., that u= u_* f(ζ, ζ_0)), one must return to the non-averaged horizontal momentum equations, (2.2) and (2.3). To scale these equations correctly, it is necessary to examine the nature of vertical profiles of horizontal velocity in typical streams and rivers.

Observations of velocities in channels with a wide variety of geometries indicate that, except in a small region near the bottom, the deviation of the downstream velocity from its

vertical average is small compared to that average. For example, in a logarithmic velocity profile it is easy to show that the deviations from the vertical average are of order 10^{-1} times the vertical average above a height d, where d is of order 10^{-1} times the the flow depth. This is the same as assuming $u_*/<u> \approx 0(10^{-1})$ or, equivalently, that the square root of the drag coefficient is $0(10^{-1})$, which is generally true in most boundary layer flows.

In scaling and expanding the full momentum equations, the assumption that $u = <u> + \varepsilon u'(z)$ is employed, which is equivalent to assuming that deviations from the vertical average are small, as described above. Using this reasoning and the definitions for the geometric parameters as given above, it is appropriate to to define the following set of non-dimensional variables:

$$u = U_0 \hat{u} \qquad v = U_0 \hat{v} \qquad\qquad w = U_0 \hat{w}$$

$$E = l_0 \hat{E} \qquad s = m_0 \hat{s} \qquad\qquad n = W_0 \hat{n}$$

$$z = h_0 \hat{z} \qquad\qquad\qquad\qquad R = R_0 \hat{R}$$

$$K = k u_* z \kappa(z) = \varepsilon u_0 h_0 \hat{K} \qquad \frac{\partial u}{\partial z} = \frac{\partial}{\partial z}\left[<u> + \varepsilon u'(z)\right] = \frac{\varepsilon u_0}{h_0}\frac{\partial \hat{u}}{\partial \hat{z}}$$

(2.20)

Using these nondimensional quantities along with the scaling for the various aspect ratios yields the following equations:

$$\frac{1}{1-N}\frac{\partial \hat{u}^2}{\partial \hat{s}} + \frac{1}{\varepsilon}\frac{\partial \hat{u}\hat{v}}{\partial \hat{n}} + \frac{1}{\varepsilon^2}\frac{\partial \hat{u}\hat{w}}{\partial \hat{z}} - \frac{1}{\varepsilon}\frac{2\hat{u}\hat{v}}{(1-N)\hat{R}} = \frac{-1}{1-N}\frac{Fr^{-2}}{\varepsilon^2}\frac{l_0}{m_0}\frac{\partial \hat{E}}{\partial \hat{s}}$$

$$+ \frac{\partial}{\partial \hat{z}}\left[\hat{K}\frac{\partial \hat{u}}{\partial \hat{z}}\right] + \varepsilon\left[\frac{\partial}{\partial \hat{n}}\hat{K}\frac{\partial \hat{v}}{\partial \hat{s}} + \frac{\partial}{\partial \hat{n}}\left(\frac{\hat{K}\hat{u}}{(1-N)\hat{R}}\right) + \frac{\partial}{\partial \hat{n}}\hat{K}\frac{\partial \hat{u}}{\partial \hat{n}} + \frac{\partial}{\partial \hat{z}}\hat{K}\frac{\partial \hat{w}}{\partial \hat{s}}\right. \tag{2.21}$$

$$\left. - \frac{2}{(1-N)\hat{R}}\left[\hat{K}\frac{\partial \hat{v}}{\partial \hat{s}} + \frac{\hat{K}\hat{u}}{(1-N)\hat{R}} + \hat{K}\frac{\partial \hat{u}}{\partial \hat{n}}\right]\right] + 0(\varepsilon^2)$$

$$\varepsilon\frac{\hat{u}}{1-N}\frac{\partial \hat{v}}{\partial \hat{s}} + \hat{v}\frac{\partial \hat{v}}{\partial \hat{n}} + \frac{1}{\varepsilon}\hat{w}\frac{\partial \hat{v}}{\partial \hat{z}} + \frac{\hat{u}^2}{(1-N)\hat{R}} = -Fr^{-2}\frac{l_0}{\varepsilon w_0}\frac{\partial \hat{E}}{\partial \hat{n}} \tag{2.22}$$

$$+ \frac{\partial}{\partial \hat{z}}\hat{K}\frac{\partial \hat{v}}{\partial \hat{z}} + \varepsilon\frac{\partial}{\partial \hat{z}}\hat{K}\frac{\partial \hat{w}}{\partial \hat{n}} + 0(\varepsilon^2)$$

The quantities Fr^{-2} $(l_0/\varepsilon^2 m_0)$ and Fr^{-2} $(l_0/\varepsilon w_0)$ will be $0(1)$ in natural streams since the pressure gradient terms provide the ultimate driving force for the flow. Substitution of typical values also shows that these terms are $0(1)$, thus demonstrating the validity of the scaling used. The terms which are multiplied by $1/\varepsilon$ and $1/\varepsilon^2$ will not produce terms of lower order than the pressure gradient and stress terms because the cross-stream and vertical velocities are smaller (higher order) than the downstream velocity, consistent with the aspect ratio scaling used in the vertically-averaged equations. Before introducing the perturbation expansion, the fact that deviations from the vertical average are small may be used to separate the convective accelerations appearing at lowest order in the above equations into a vertically-averaged part and a remainder which will be of higher order. For example, the first convective acceleration term in the downstream momentum equation may be written as follows:

$$\frac{\partial \hat{u}^2}{\partial s} = \frac{\partial <\hat{u}>^2}{\partial s} + \left[\frac{\partial}{\partial \hat{s}}(\hat{u}^2 - <\hat{u}>^2)\right] \tag{2.23}$$

Using the scaling for the vertical profile of downstream velocity described above, it is easy to show that the quantity in brackets on the right-hand side of the equation above is small compared to the first term on the right-hand side or, in other words, that convective accelerations not associated with topographic steering enter the equations at one order higher than those which are. This same scaling justifies the approximations $<u^2> \approx <u>^2$ and $<uv> \approx <u><v>$ used by Smith and McLean [1984] in the solution of the vertically averaged equations. Using similar reasoning on the other lowest order convective acceleration terms in the equation yields

$$\frac{1}{\hat{h}(1-N)}\frac{\partial <\hat{u}>^2 h}{\partial \hat{s}} + \frac{1}{\varepsilon\hat{h}}\frac{\partial <\hat{u}><\hat{v}>h}{\partial \hat{n}} - \frac{1}{\varepsilon}\frac{2<\hat{u}><\hat{v}>}{(1-N)\hat{R}} +$$

$$\varepsilon\left[\frac{1}{1-N}\frac{\partial}{\partial \hat{s}}(\hat{u}^2 - <\hat{u}>^2) + \frac{1}{\varepsilon}\frac{\partial}{\partial \hat{n}}(\hat{u}\hat{v} - <\hat{u}><\hat{v}>) + \frac{1}{\varepsilon^2}\frac{\partial}{\partial \hat{z}}(\hat{u}\hat{w})\right.$$

$$-\frac{1}{\hat{h}}\left[\frac{<\hat{u}>^2}{1-N}\frac{\partial \hat{h}}{\partial \hat{s}} + \frac{1}{\varepsilon}<\hat{u}><\hat{v}>\frac{\partial \hat{h}}{\partial \hat{n}}\right] - \frac{2}{\varepsilon}\frac{(\hat{u}\hat{v} - <\hat{u}><\hat{v}>)}{(1-N)\hat{R}}\right] = \tag{2.24}$$

$$-\frac{1}{1-N}\frac{\partial \hat{E}}{\partial \hat{s}} + \frac{\partial}{\partial \hat{z}}\hat{K}\frac{\partial \hat{u}}{\partial \hat{z}} + \varepsilon\left[\frac{\partial}{\partial \hat{n}}\hat{K}\frac{\partial \hat{v}}{\partial \hat{s}} + \frac{\partial}{\partial \hat{n}}\left(\frac{\hat{K}\hat{u}}{(1-N)\hat{R}}\right)\right.$$

$$+\frac{\partial}{\partial \hat{n}}\hat{K}\frac{\partial \hat{u}}{\partial \hat{n}} + \frac{\partial}{\partial \hat{z}}\hat{K}\frac{\partial \hat{w}}{\partial \hat{s}} - \frac{2}{(1-N)\hat{R}}\left[\hat{K}\frac{\partial \hat{v}}{\partial \hat{s}} + \frac{\hat{K}\hat{u}}{(1-N)\hat{R}} + \hat{K}\frac{\partial \hat{u}}{\partial \hat{n}}\right]\right] + O(\varepsilon^2)$$

and

$$\frac{\varepsilon \hat{u}}{1-N}\frac{\partial \hat{v}}{\partial s} + \hat{v}\frac{\partial \hat{v}}{\partial \hat{n}} + \frac{1}{\varepsilon}\hat{w}\frac{\partial \hat{v}}{\partial \hat{z}} + \frac{<\hat{u}>^2}{(1-N)\hat{R}} + \frac{\varepsilon(\hat{u}^2 - <\hat{u}>^2)}{(1-N)\hat{R}} = \qquad (2.25)$$

$$-\frac{\partial \hat{E}}{\partial \hat{n}} + \frac{\partial}{\partial \hat{z}}\hat{K}\frac{\partial \hat{v}}{\partial \hat{z}} + \varepsilon\frac{\partial}{\partial \hat{z}}\hat{K}\frac{\partial \hat{w}}{\partial \hat{n}} + 0(\varepsilon^2)$$

A regular perturbation expansion employing ε as a small parameter is applied at this point. The flow variables are expanded as follows:

$$\hat{u} = u_0 + \varepsilon u_1 + \varepsilon^2 u_2 \cdots$$

$$\hat{v} = v_0 + \varepsilon v_1 + \varepsilon^2 v_2 \cdots$$

$$\hat{w} = w_0 + \varepsilon w_1 + \varepsilon^2 w_2 \cdots \qquad (2.26)$$

$$\hat{E} = E_0 + \varepsilon E_1 + \varepsilon^2 E_2 \cdots$$

$$\hat{K} = K_0 + \varepsilon K_1 + \varepsilon^2 K_2 \cdots$$

where $v_0 = w_0 = w_1 = 0$ from the simple aspect ratio scaling. The lowest-order equations in dimensional form will be

$$\frac{1}{h(1-N)}\frac{\partial <u_0>^2 h}{\partial s} + \frac{1}{h}\frac{\partial <u_0><v_1>h}{\partial n} - \frac{2<u_0><v_1>}{(1-N)R} = \qquad (2.27)$$

$$\frac{-g}{1-N}\frac{\partial E_0}{\partial s} + \frac{\partial}{\partial z}K_0\frac{\partial u_0}{\partial z}$$

and

$$\frac{<u_0>^2}{(1-N)R} = -g\frac{\partial E_0}{\partial n}$$

(2.28)

Consistency between equation (2.13) and (2.26) requires that

$$\tau_{zs} = (\tau_{zs})_B(1 - z/h) = \rho u_*^2(1 - \zeta) = \rho_0 K_0\frac{\partial u_0}{\partial z}$$

(2.29)

where $(\tau_{zs})_B$ is the solution to the vertically-averaged equations found above. This allows the velocity profile assumed to be related to the lowest-order eddy viscosity. Using $K_0 = u_* h\kappa(\zeta)$ in the above equation, where $\kappa(\zeta)$ is the non-dimensional eddy viscosity, yields the following relationship between the lowest-order vertical velocity profile and the eddy viscosity:

$$\frac{1-\zeta}{\kappa} = \frac{\partial f_1}{\partial \zeta} \quad or \quad f_1(\zeta,\zeta_0) = \int_{\zeta_0}^{\zeta}\frac{1-\zeta}{\kappa}d\zeta$$

(2.30)

Thus, by assuming a vertical velocity profile (or alternatively, a nondimensional eddy viscosity) solutions are found for the lowest-order downstream boundary shear stress, velocity, and centerline and cross-stream surface slope, as detailed above in the solution of the vertically-averaged equations. The non-dimensional eddy viscosity used in the calculations performed to obtain the results presented here is given by

$$\kappa(\zeta) = k\zeta(1 - \zeta)^{\frac{1}{2}} \tag{2.31}$$

This eddy coefficient yields slightly greater vertical momentum transfer than an eddy coefficient corresponding to a logarithmic velocity profile, which is given by

$$\kappa(\zeta) = k\zeta(1 - \zeta) \tag{2.32}$$

The eddy coefficient given by equation (2.31) is used because the enhanced near-surface momentum transport it predicts is thought to represent the effect of boils. Smith and McLean [1984] tried several eddy coefficients in their model of meandering streams, and concluded that this choice was the most appropriate one.

It is important to note that although equations (2.27) and (2.28) were arrived at using scaling that is only valid in the upper 90% of the flow depth or so, they yield the appropriate value of the boundary shear stress if they are assumed to hold all the way to the bottom. If the full horizontal momentum equations are scaled in the lower part of the flow, where it is not reasonable to assume that deviations from the vertical average are small, the lowest-order equation simply yields a constant stress profile (i.e. the variations in the stress are $0(\varepsilon)$ compared to the bottom stress, because $z/h \ll 1$). Thus, by extending the domain of the equations found to be valid in the outer layer all the way to the boundary, some (but not necessarily all) higher order terms are included in the solution near the boundary. The alternative to this approach is to solve the appropriate equations in each domain and match them at some intermediate level. Rather than use this more complicated approach, equations (2.27) and (2.28) are applied throughout the flow depth, which is essentially equivalent. Of course, the details of the flow in the lowest layer will never be totally

correct due to the presence of sediment transport, ripples, and dunes, the effects of which are included here only parametrically, through the specification of z_0.

In order to calculate the lowest order cross-stream velocity and bottom stress, it is necessary to resort to the $0(\varepsilon)$ equations, which are given by

$$\frac{2}{h(1-N)}\frac{\partial}{\partial s}(<u_0><u_1>h) + \frac{1}{h}\frac{\partial}{\partial n}(<u_1><v_1> + <u_0><v_2>h)$$

$$-2\frac{<u_1><v_1> + <u_0><v_2>}{(1-N)R} + \frac{1}{1-N}\frac{\partial}{\partial s}(u_0^2 - <u_0>^2) + \frac{\partial}{\partial n}(u_0v_1 - <u_0><v_1>) +$$

$$\frac{\partial}{\partial z}(u_0w_2) - \frac{1}{h}\left[\frac{<u_0>^2}{1-N}\frac{\partial h}{\partial s} + <u_0><v_1>\frac{\partial h}{\partial n}\right] - \frac{(u_0v_1 - <u_0><v_1>)}{(1-N)R} = \qquad (2.33)$$

$$-\frac{g}{1-N}\frac{\partial E_1}{\partial s} + \frac{\partial}{\partial z}K_1\frac{\partial u_0}{\partial z} + \frac{\partial}{\partial z}K_0\frac{\partial u_1}{\partial z} + \frac{\partial}{\partial n}\left[\frac{K_0u_0}{(1-N)R} + K_0\frac{\partial u_0}{\partial n}\right]$$

$$-\frac{2K_0u_0}{(1-N)^2R^2} - \frac{2}{(1-N)R}K_0\frac{\partial u_0}{\partial n}$$

and

$$\frac{2<u_0><u_1>}{(1-N)R} + \frac{(u_0^2 - <u_0>^2)}{(1-N)R} = -g\frac{\partial E_1}{\partial n} + \frac{\partial}{\partial z}K_0\frac{\partial v_1}{\partial z} \qquad (2.34)$$

The cross-stream equation may immediately be integrated twice with respect to z, since $u_0(z)$ is known. Using the boundary conditions that the surface is unstressed and v=0 at the bottom and $K_0 = u_*h\kappa(\zeta)$, this procedure yields

$$v_1 = \frac{1}{u_*}\left[\frac{-u_*^2 h}{(1-N)R}f_2(\zeta) - \left\{gh\frac{\partial(E_1 + E_0)}{\partial n} + \frac{2h<u_0><u_1>}{(1-N)R}\right\}f_1(\zeta)\right] \qquad (2.34)$$

where

$$f_2(\zeta) = \int_{\zeta_0}^{\zeta}\frac{1}{\kappa}\int_{\zeta'}^{1}f_1^2(\zeta)\ d\zeta d\zeta'$$

Since the value of $<v_1>$ is known from equation (2.7), equation (2.35) may be integrated to set the value of the terms multiplying f_1 in equation (2.35). This yields

$$-g\frac{\partial(E_0 + E_1)}{\partial n} - \frac{2<u_0><u_1>}{(1-N)R} = \frac{u_*^2}{(1-N)R}\frac{F_2}{\alpha^{\frac{1}{2}}} - \qquad (2.36)$$

$$\frac{u_*}{(1-N)h^2\alpha^{\frac{1}{2}}}\int_{\frac{-w}{2}}^{n}\frac{\partial}{\partial s}(u_* h\alpha^{\frac{1}{2}})dn$$

where we have defined

$$F_2 = \int_{\zeta_0}^{1}f_2\ d\zeta$$

Substituting the above solution back into (2.35) yields the solutions for the cross-stream velocity and stress, given by

$$v_1 = \frac{u_* h}{(1-N)R} \left[\frac{F_2}{\alpha^{\frac{1}{2}}} f_1 - f_2 \right] - \left[\frac{1}{(1-N)h\alpha^{\frac{1}{2}}} \int_{\frac{-w}{2}}^{n} \frac{\partial}{\partial s}(u_* h \alpha^{\frac{1}{2}})dn \right] f_1 \qquad (2.37)$$

and

$$\left[\tau_{zn} \right]_1 = \frac{\rho u_*^2 h}{(1-N)R} \left[\frac{F_2}{\alpha^{\frac{1}{2}}}(1-\zeta) - \int_{\zeta}^{1} f_1^2 d\zeta \right] - \frac{\rho u_*(1-\zeta)}{(1-N)h\alpha^{\frac{1}{2}}} \int_{\frac{w}{2}}^{n} \frac{\partial}{\partial s}(u_* h\alpha^{\frac{1}{2}})dn \qquad (2.37)$$

Thus, without resorting to the $0(\varepsilon)$ downstream momentum equation, it is possible to calculate lowest-order solutions for all flow variables. The $0(\varepsilon)$ downstream equation will yield corrections to these lowest-order solutions. Although this equation may be solved in a relatively straightforward manner, it is worth examining the veracity of the lowest-order solution before adding this complication. The higher-order corrections brought in through the solution of equation (2.33) are principally associated with the redistribution of downstream momentum by the helical part of the cross-stream velocity, the changes in vertical structure associated with local accelerations in the flow, and the effects of lateral friction.

2.2. Specification of the Roughness Parameter and Form Drag Partitioning

In order to specify $f(\zeta, \zeta_0)$, the non-dimensional velocity profile, it is necessary to determine a value for z_0, the roughness parameter. In simple flows where the effective roughness of the bottom is only due to the actual geometric roughness, z_0 may be determined easily using the experimental results of Nikuradse as presented, for example, by Schlicting [1979, p. 620]. However, this technique is rarely suitable for natural streams, due to the presence of channel nonuniformity, bedforms, and sediment transport. Each of

these tends to increase the effective roughness of the bottom acting on the flow outside the region where they have a direct dynamic influence on the flow. Thus, a method is required whereby the total effective roughness of the channel can be accounted for in terms of an overall z_0. The boundary shear stress resulting from the calculations using these values for the roughness will include the actual skin friction shear stress as well as the momentum losses due to pressure distributions on bed and bank irregularities (e.g., ripples, dunes, bars, slump blocks, channel constrictions, and organic debris). Sediment transport depends upon the skin friction shear stress, and since one of the principle goals of this work is to make accurate predictions of sediment fluxes, clearly a general method for reducing the overall boundary shear stress to the skin friction value is necessary.

To treat both the determination of roughness lengths and the form drag partitioning, a generalized version of the technique presented by Smith and McLean [1977] is employed. Following their formulation, the total boundary shear stress as a sum of skin friction and form drag components:

$$\tau_B = \tau_{SF} + \tau_D + \tau_{CH} \qquad (2.39)$$

where τ_B is the magnitude of the total boundary shear stress vector, τ_{SF} is the skin friction bottom stress (the stress acting to move sediment on the bed), τ_D is the boundary shear stress equivalent to the dune or ripple form drag, and τ_{CH} represents the form drag associated with any other channel nonuniformities. The general relationship between form drag and an equivalent bottom stress may be written as follows:

$$\tau = \tfrac{1}{2}\rho C_D U_r^2 \frac{A_X}{A_B} \qquad (2.40)$$

In this expression, ρ is the fluid density, C_D is a drag coefficient which must be set empirically, U_r is an appropriate reference velocity, A_X is the cross-sectional area of the obstacle perpendicular to the principal flow direction, and A_B is the area of the bed covered by the obstacle. The reference velocity is usually defined as the average over A_X of the velocity field that would exist if the obstacle were not present in the flow (the unperturbed velocity). For the case of obstructions on a channel bed, vertical shears and pressure forces generated normal to the boundary by vertical accelerations are expected to be much larger than those associated with lateral responses. In keeping with this, the reference velocity for a given obstacle is defined here to be the vertical average of the unperturbed velocity over a two-dimensional obstruction with cross-sectional area equivalent to the original obstacle. For the case of a two-dimensional dune, this definition of the reference velocity reduces to the average of the unperturbed velocity over the cross-section of the dune, as expected. In contrast, for the case of a three-dimensional obstruction, the reference velocity is taken to be the vertical average of the unperturbed velocity over an equivalent two-dimensional obstruction. For example, in the case of a channel constriction, the reference velocity is taken to be the vertical average of the unperturbed velocity over a two-dimensional bump across the channel bottom. This height of this bump is chosen such that the cross-sectional area of the bump is equivalent to that of the original constriction. This approach, which is entirely consistent with the inclusion of the form drag effects through a total boundary shear stress and roughness length, permits the use of empirically determined drag coefficients for two-dimensional obstacles to be employed in all cases.

Using data measured over two-dimensional sand waves in the Columbia River, Smith and McLean [1977] found $C_D = .21$ for the case of separated flow over dunes, and $C_D = .84$ for unseparated flow. Although these values were originally computed from data using a slightly different formulation for the reference velocity, subsequent work has shown

that the approach described herein is essentially equivalent, and their values for the two-dimensional drag coefficients are appropriate. Clearly, more experimental verification of these values is in order, especially for the unseparated case, but these values are employed in the calculations presented here.

For the case of two-dimensional bedforms in a turbulent flow, the unperturbed velocity is simply a logarithmic profile characterized by the skin friction shear stress and roughness. This follows from the fact that, if the bedform were not present in the flow, the near-bed velocity profile would be given by

$$u = \frac{\left[\frac{\tau_{SF}}{\rho}\right]^{1/2}}{k} \ln\left[\frac{z}{(z_0)_{SF}}\right] \tag{2.41}$$

where $(z_0)_{SF}$ is the actual grain roughness if the sediment is immobile, and is a roughness length proportional to the height of the saltation layer if bedload transport is occurring. A theoretical method for calculating the thickness of the bedload layer and an experimental determination of the relation between that thickness and the effective roughness length has been provided by Dietrich [1982]. Averaging equation (2.41) over the dune height in order to obtain the reference velocity and noting that $A_X = H_D b$ and $A_B = \lambda b$, where H_D, λ, and b are the height, wavelength, and cross-stream width of the bedform, from equation (2.40) the following expression is found for the form drag associated with bedforms:

$$\tau_D = \tau_{SF} \frac{C_D}{2k^2} \frac{H_D}{\lambda} \left[\ln\left[\frac{H_D}{(z_0)_{SF}}\right] - 1\right]^2 \tag{2.42}$$

Above the region in which the dunes have a substantial effect on the spatial structure of the flow, the velocity profile will be quasi-logarithmic. This outer profile will be

characterized by a shear stress equal to the sum of the skin friction value and the dune form drag, along with a roughness length which describes the extraction of momentum from the flow by both skin friction and form drag. This roughness length is determined by matching the velocity profile given by equation (2.41) with the outer velocity profile at the height of the obstacle. Thus, one obtains

$$\frac{\left[\dfrac{\tau_{SF}}{\rho}\right]^{\frac{1}{2}}}{k}\ln\left[\frac{H_D}{(z_0)_{SF}}\right] = \frac{\left[\dfrac{\tau_{SF}+\tau_D}{\rho}\right]^{\frac{1}{2}}}{k}\ln\left[\frac{H_D}{(z_0)_D}\right] \tag{2.43}$$

which leads to the following expression for $(z_0)_D$:

$$(z_0)_D = H_D\left[\frac{H_D}{(z_0)_{SF}}\right]^{-\frac{1}{\gamma_D}} \tag{2.44}$$

where

$$\gamma_D = \left[\frac{\tau_{SF}+\tau_D}{\tau_{SF}}\right]^{\frac{1}{2}} = \left\{1 + \frac{C_D}{2k^2}\frac{H_D}{\lambda}\left[\ln(\frac{H_D}{(z_0)_{SF}}) - 1\right]^2\right\}^{\frac{1}{2}} \tag{2.45}$$

Equations (2.42) and (2.44) provide the relationships necessary to reduce the total boundary shear stress to the skin friction shear stress and to compute the total effective roughness of a channel, respectively, provided that bedforms are the only source of nonuniformity. This is rarely the case in natural channels, where form drag associated with bars and bank variations typically is a significant proportion of the total channel drag. To account for this effect, the form drag on each channel-scale non-uniformity must be calculated using equation (2.40). The drag coefficient must either be chosen as that of an

equivalent two-dimensional obstruction, as described above, or it must be found by analogy with laboratory results obtained for certain special geometries. For example, in the case of a log obstructing the flow, well-known classical results for the drag coefficient of a circular cylinder at various angles of attack may be employed. It is important to note that, by extracting the form drag of channel-scale irregularities in this manner, this technique explicitly concentrates on accounting for the total drag of the channel in a spatially-averaged sense; no attempt is made to distribute the drag force over the obstacle, which requires a much more complicated approach.

In the case of a meandering stream with smooth banks and a nearly constant cross-sectional area, the channel form drag is essentially that associated with the point bar. The reference velocity for the channel-scale features producing form drag is the outer velocity profile over the bedforms, as described above, averaged vertically over the cross-section of a two-dimensional bump with the cross-sectional area of the point bar. If H_b and λ_b are the height and wavelength of the point bar and the cross-sectional shape of the point bar is approximated as a triangular wedge, the bottom stress equivalent to the form drag of the point bar is given by

$$\tau_{CH} = \left[\tau_{SF} + \tau_D\right]\frac{C_D}{2k^2}\frac{H_B}{2\lambda_B}\left[\ln\left(\frac{H_B}{(z_0)_D}\right) - 1\right]^2 \tag{2.46}$$

Because the flow typically does not separate over point bars, $C_D = .84$ is employed. This expression allows the channel form drag to be related to the skin friction form drag. To calculate the field of overall roughness lengths in the channel, the process used in obtaining equation (2.44) is used, with one minor difference. Rather than matching at the height of the point bar or the height of the equivalent two-dimensional obstruction, the matching is enforced at the water surface. This is to avoid matching at points above the water surface,

which would typically occur over much of the meander bend if the height of the point bar was used. Physically, this matching enforces the fact that the free surface inhibits the growth of wakes associated with large scale obstructions. The matching yields

$$z_0 = h \left[\frac{h}{(z_0)_D} \right]^{-\frac{1}{\gamma_{CH}}} \tag{2.47}$$

where

$$\gamma_{CH} = \left[\frac{\tau_{CH} + \tau_D + \tau_{SF}}{\tau_{SF} + \tau_D} \right]^{\frac{1}{2}} = \left\{ \frac{C_D}{2k^2} \frac{H_B}{2\lambda_B} \left[\ln \left(\frac{H_B}{(z_0)_D} \right) - 1 \right]^2 \right\}^{\frac{1}{2}} \tag{2.48}$$

Equation (2.47) predicts values of the total roughness length at various locations in a meander bend. This effective roughness includes the form drag of both the dunes or ripples and the point bar. In cases where other types of nonuniformities are important, expressions similar to equation (2.46) must be developed using geometrical arguments. The resulting expressions for the various types of channel form drag are summed, and equations (2.47) and (2.48) are employed to calculate the field of roughness lengths in the channel.

An important by-product of the determination of the overall roughness is an expression relating the overall boundary shear stress to the skin friction value. From equations (2.45) and (2.48), we find

$$\frac{\tau_B}{\tau_{SF}} = \gamma_D^2 \gamma_{CH}^2 \tag{2.49}$$

This equation allows the boundary shear stress values predicted by the numerical model

described above to be reduced to the value of boundary shear stress responsible for the sediment transport on the bed. This value may be used in any of various bedload equations to predict sediment fluxes. Although the procedure described here may seem complicated, the mathematical structure of equations (2.44) through (2.48) is such that many simple approximations may be made allowing computations of the overall roughness and form drag partitioning even in cases where the dune and point bar geometry are only very roughly known. The quantities in brackets in each of these equations tend to vary only weakly in typical natural streams. Thus, equation (2.47) is nearly equivalent to holding ζ_0 constant, a result that has often been used without theoretical support. Other simplifications are addressed below in the context of a specific meander bend, but the full approach described here is of general validity, and is applicable to a wide range of bed and bank geometries.

2.3. The Study Site

Muddy Creek is a sand-bedded stream in western Wyoming characterized by the strongly meandering structure typical of many natural streams, as shown in Figure 2.1. Between 1976 and 1982, a comprehensive field investigation was undertaken in one of the meander bends of this stream, the so-called IMR bend. Some of the results of this study have been presented by Dietrich [1982], and by Dietrich and Smith [1983,1984]. As a consequence of this work, a comprehensive set of data exists for this site, consisting of careful measurement of the stream geometry, as well as detailed measurements of velocity, surface elevation and sediment transport rates; this makes the Muddy Creek site a perfect test case for the model described above.

The values of the mean depth, width, and meander length in the bend of interest are about .40, 5.0, and 25 meters, respectively. These values yield a depth-to-width aspect
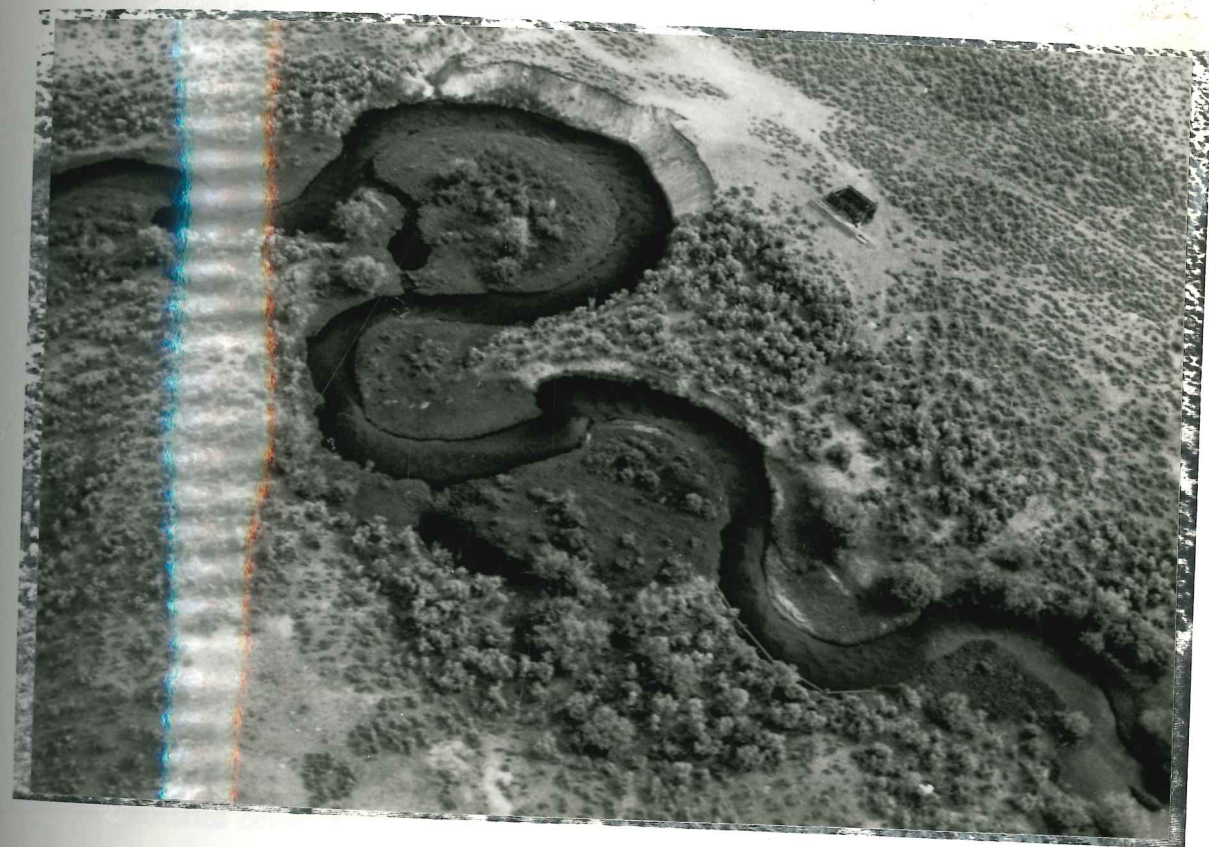
Figure 2.1. Aerial photograph of the Muddy Creek study site taken in 1979. The bend with the railing along the outer bank is the IMR study bend.

ratio of 0.08, which is $0(10^{-1})$, and a depth-to-meander length ratio of 0.016, which is $0(10^{-2})$. A typical value for the discharge is 1.0 m^3/s, so the value of the Froude number Q/W $(gh^3)^{1/2}$ will be 0.25. The crossing-to-crossing drop in the surface elevation in the bend in Muddy Creek was about 4.0 cm., so the non-dimensional number Fr^{-2} (l_0/m_0) is $0(10^{-2})$. These observations clearly demonstrate that the scaling employed is valid in this typical natural meander.

The topography of the IMR bend is characteristic of stream meanders, with fairly flat areas near the crossings (where R approaches infinity) and well-developed bar-pool structure in the region of the minimum radius of curvature. A contour map of the IMR bend is shown in Figure 2.2. The topography was measured by making many cross-stream transects and averaging them together to remove the effect of bedforms migrating through the section of interest, as described by Dietrich [1982]. This procedure was repeated at enough downstream positions to ensure that the bathymetric structure was well resolved.

The radius of curvature of the centerline was calculated from the channel centerline digitized from maps constructed from surveys of the channel banks. The resulting radius of curvature as a function of downstream position, shown in Figure 2.3, is quite close to a sine-generated curve, identified by Langbein and Leopold [1966] as the curve most accurately describing typical natural meanders.

Unfortunately, the topography and radius of curvature of the meanders upstream of the bend were not measured, so the upstream conditions were not well specified. However, the bend immediately upstream of the IMR bend is quite similar to it in form and so this bend has been replaced with an image of the study bend reflected about a line through the crossings. The justifications for this approach are described above in the discussion of the numerical solution. This approximation is also justified by the fact that the cross-sectional depth profile of the upstream crossing is nearly identical to that of the downstream crossing
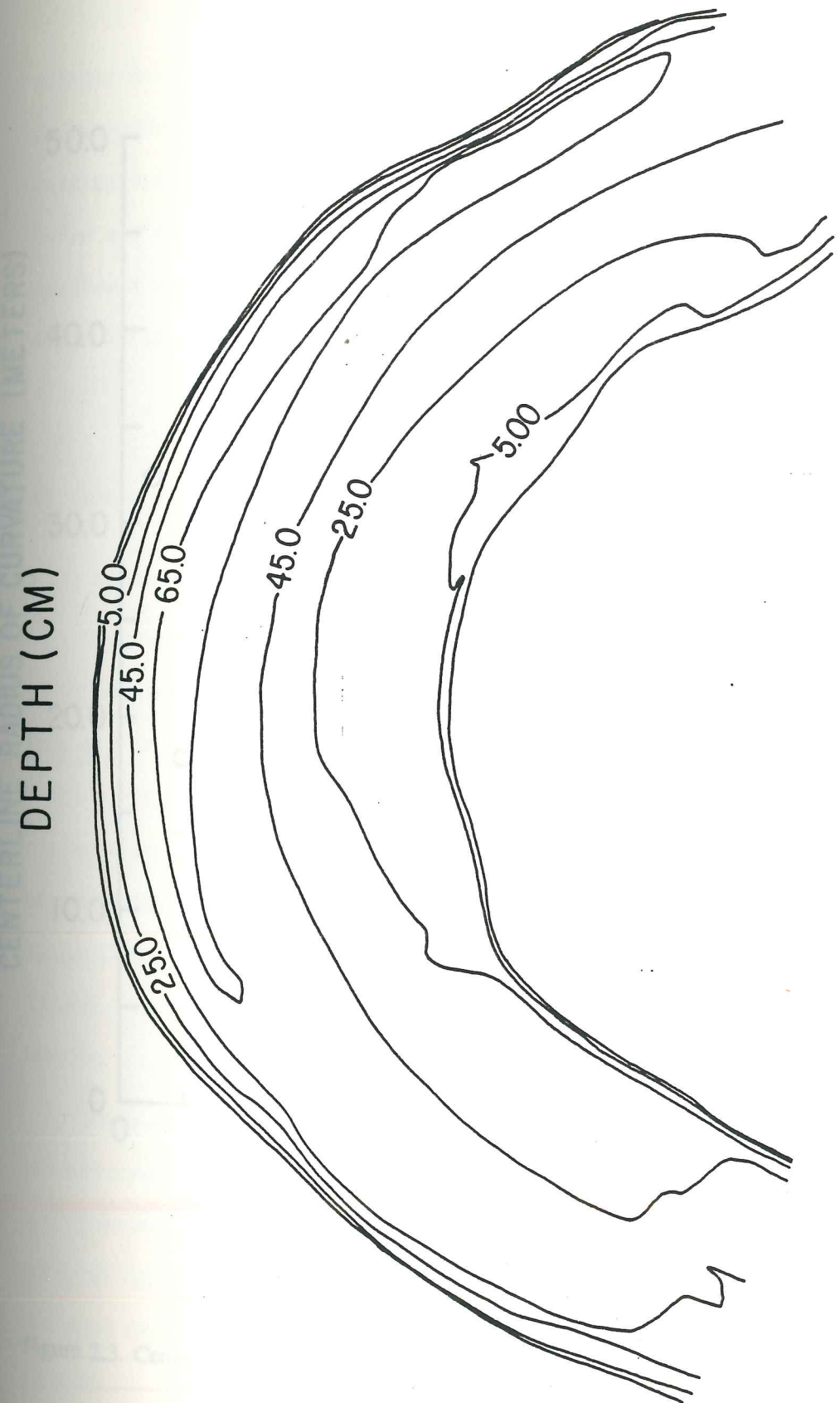
Figure 2.2. Depth contours in the IMR meander bend in Muddy Creek after the removal of mobile bedforms by time averaging. Depth contours are shown at 20 centimeter intervals.
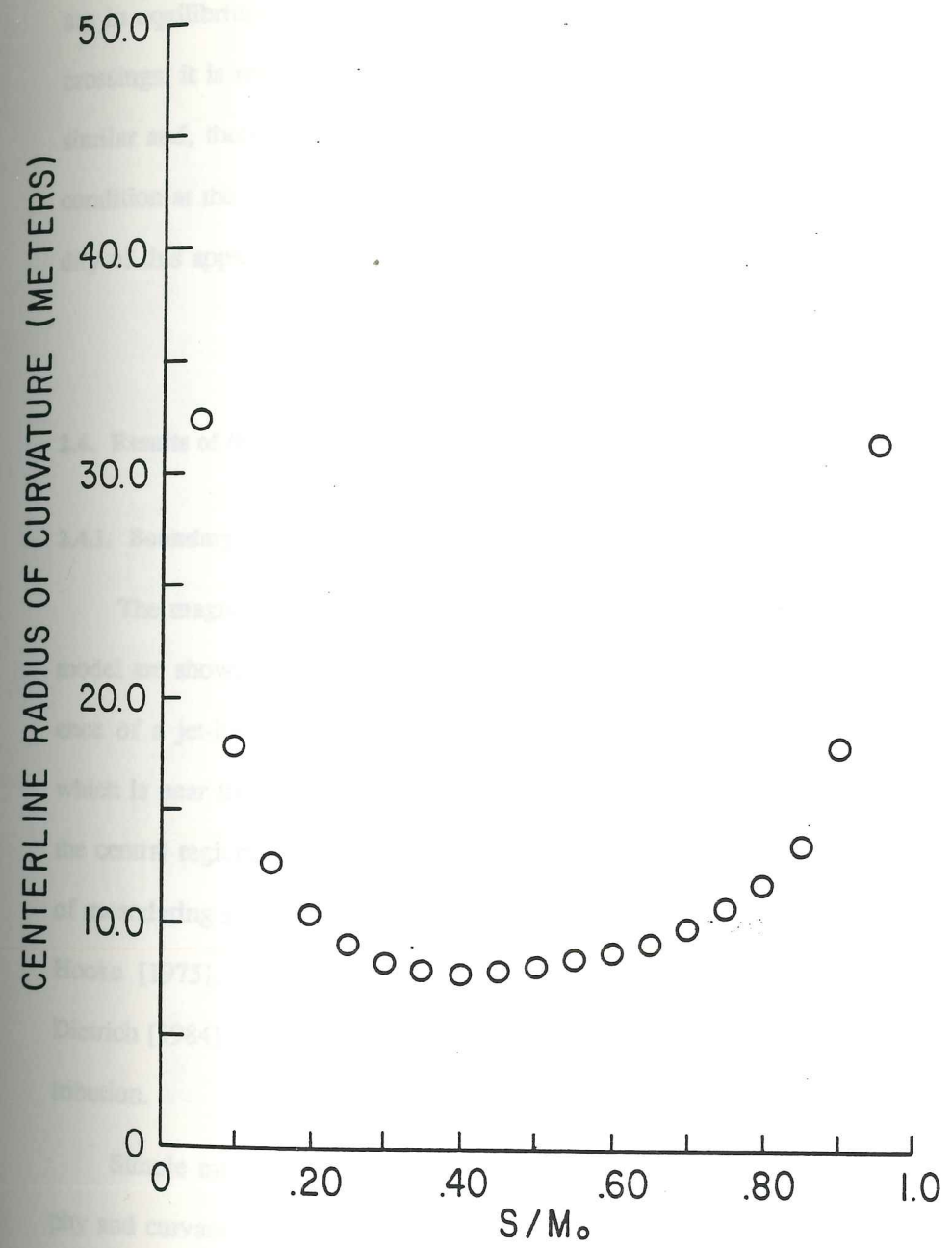
Figure 2.3. Centerline radius of curvature for the study bend in Muddy Creek.

reflected about the centerline, as shown in Figure 2.4. Since the topography and the flow are in equilibrium, and the topography and stream geometry are nearly identical at the two crossings, it is reasonable to assume that the boundary stress fields at the two crossings are similar and, therefore, that the solution at the downstream crossing provides a good initial condition at the upstream one. Furthermore, the results of the calculations support the validity of this approximation.

2.4. Results of the Model

2.4.1. Boundary Shear Stress and Sediment Transport

The magnitude and direction of the overall boundary shear stress calculated using the model are shown in Figure 2.5. The highly nonuniform structure is dominated by the presence of a jet-like region of bottom stress which traverses the meander, following a path which is near the bar-side bank in the upstream part of the meander, crosses the stream in the central region, and exits the meander along the pool-side bank. This structure is typical of meandering streams, and is clearly present in the data presented by Yen and Yen [1971], Hooke [1975], and Dietrich [1984]. Measurements of sediment transport published by Dietrich [1984] are also indicative of this type of structure in the boundary shear stress distribution.

Simple models of meandering streams that neglect streamwise variations in topography and curvature predict cross-stream boundary shear stresses that are everywhere directed toward the inner or bar-side bank. This conclusion has been used extensively in theories of point bar stability, in which inward shear stresses are often balanced against an outward (i.e. down the face of the point bar) gravitational force. However, as is clear from our calculations and from the observations of Dietrich [1982], Yen [1967], and Onishi [1972], the
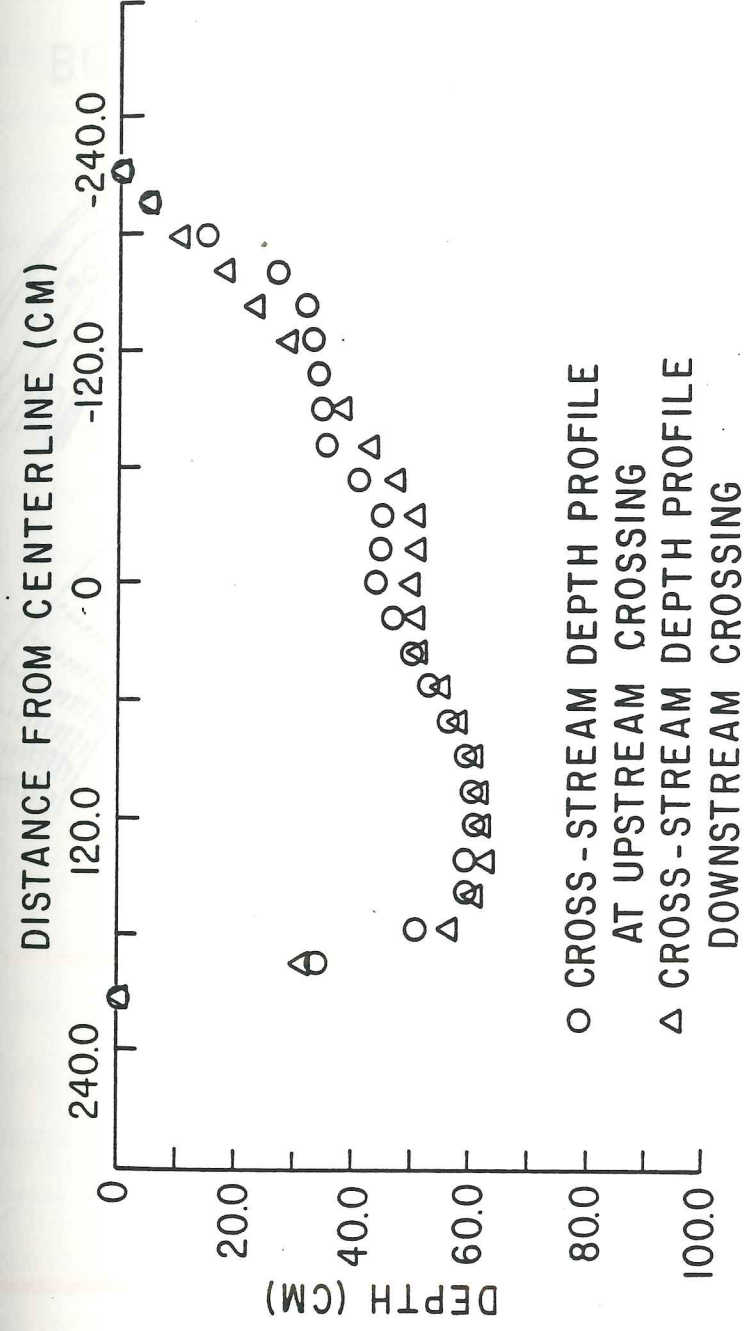
Figure 2.4. Cross-stream depth profiles at the upstream and downstream crossings of the study bend in Muddy Creek. Note that one profile has been rotated about a vertical axis through the channel centerline to facilitate comparison.

BOUNDARY SHEAR STRESS (DY/CM²)
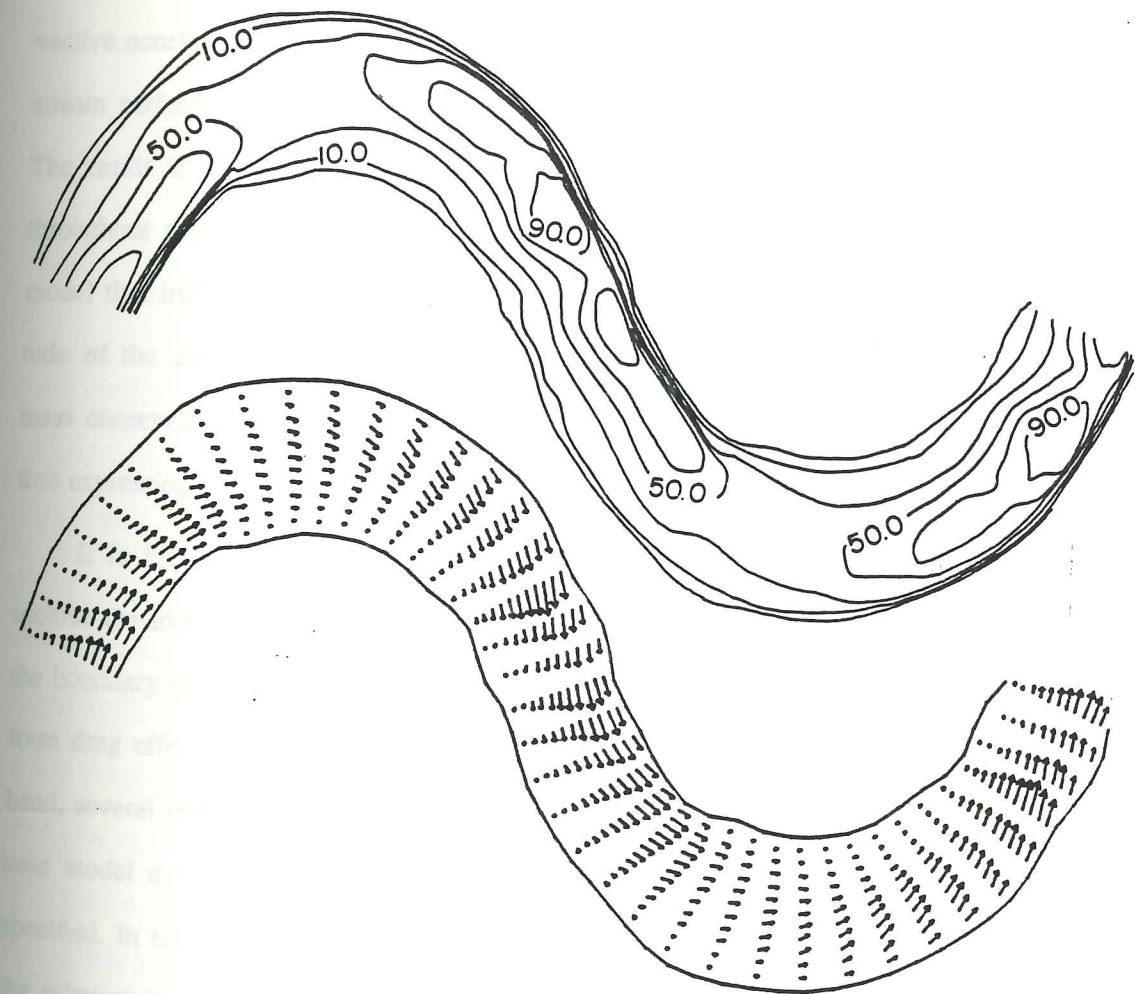
Figure 2.5. Magnitude and direction of the overall boundary shear stress in the study bend in Muddy Creek is shown. Note the presence of slightly poolward shear stresses over the point bar. The maximum amplitude of about 90 dynes/*cm*² agrees quite well with the maximum of 85 dynes/*cm*² measured by Dietrich [1982] near the same location.

boundary shear stress over the point bar is actually directed downstream or even slightly outward. This is easily explained by the presence of topographic steering, as discussed in detail by Dietrich and Smith [1983]. As the flow approaches the point bar, shoaling of the bottom and deceleration of the fluid both act to produce a large negative downstream convective acceleration. As can be seen from equation (2.13), this tends to reduce the downstream surface slope, which in turn causes a relaxation of the cross-stream surface slope. The result is an excess of centrifugal force over the bar that forces the flow outward throughout the entire water depth. This clearly demonstrates the importance of using a model that includes topographic steering terms in the lowest-order equations. The magnitude of the downstream nonuniformity also requires that the full equation for sediment mass conservation be employed in calculations of point bar stability, rather than an equation expressing some cross-stream balance.

It is important to note that the boundary shear stress values shown in Figure 2.5 include the form drag effects of bedforms and meander geometry. To determine values of the boundary shear stress responsible for sediment transport, it is necessary to remove these form drag effects using the model discussed above. In applying this technique to the IMR bend, several simplifications were made. In order to apply the form drag and overall roughness model described above, a value for the skin friction roughness ($(z_0)_{SF}$) must be specified. In Muddy Creek, the value of this parameter is primarily related to the height of the saltation layer, since most of the momentum extraction very near the bed is associated with grain saltation. A theoretical model for the height of this layer has been presented by Dietrich [1982], but the calculation of the thickness of the bedload transport layer requires that the skin friction stress be known. However, the value of δ_B, the thickness of the saltation layer, is usually between one and three grain diameters, depending on the ratio of the skin friction shear stress to the critical shear stress. Postulating a linear relationship

between δ_B and $(z_0)_{SF}$ based on dimensional arguments, Dietrich empirically found a coefficient of proportionality of 0.08. Subsequent theoretical work by Wiberg [1987] and further measurements by Dietrich [personal communication] indicate that this value is about 0.10. Since equations (2.42) and (2.44) depend only weakly on the value of $(z_0)_{SF}$, and the ratio between the saltation layer height and the grain diameter only varies slowly in the IMR study bend, the following approximation is employed:

$$(z_0)_{SF} = .1\delta_B \approx .2D \qquad (2.50)$$

This approximation removes the necessity of iteration of the form drag model, and is valid if active bedload transport (i.e., $\tau_B \gg \tau_c$) occurs over most of the bed, as is the case in the IMR bend. If transport only occurs in isolated parts of a channel, then the form drag calculation requires iteration. In practice, one begins by guessing reasonable values for the skin friction roughnesses (e.g., the Nikuradse values), and then calculates the ratio given by equation (2.49) using (2.42) through (2.48). This ratio allows the skin friction boundary shear stresses to be calculated and inserted in the expression for the bedload layer height provided by Dietrich [1982]. Thus, an improved value of $(z_0)_{SF}$ is obtained and the process is repeated. This iteration is well-posed and converges rapidly. However, as discussed above, this process is not always necessary, and nearly identical results are obtained in the case of the IMR study bend using equation (2.50), which does not require knowledge of the skin friction stress in calculating the skin friction roughness.

To apply equations (2.42) through (2.49), the heights and wavelengths of the dunes or ripples present on the bed must be known. However, these quantities are rarely measured in detail, so a simple closure for these values is desirable. For the case of fully-developed quasi-two-dimensional dunes, the heights of the dunes may be approximated as a constant

proportion of the water depth. Both experimental [Yalin, 1977; Jones, 1978] and theoretical work (see Chapter 4) show that dunes tend to grow to a height of about one sixth to one fifth of the flow depth. Although the dunes in the IMR bend are often oriented somewhat obliquely to the streamwise flow direction [Dietrich, 1982], they are quasi-two-dimensional in the sense that the near-bed flow tends to go over them, rather than being steered around them as in the case of true three-dimensional dunes. Thus, in applying the form drag model to the IMR bend, it is reasonable to use

$$H_D \approx \frac{h}{5.5} \tag{2.51}$$

The wavelength of the dunes may be approximated either of two ways: the ripple index may be assumed to be roughly constant, or the average dune wavelength in the meander may be employed. In the IMR bend, observations of the dune geometry indicates that the second of these assumptions may be more valid. This is a result of the fact that the dunes often have a cross-stream extent reaching from the deepest part of the pool to well up the flank of the point bar. Thus, the flow depth changes by a factor of two or three, but the wavelength is nearly constant. The dune heights decrease as one moves up the flank of the point bar in response to the shoaling of the flow; however, since the wavelength varies only slightly, the ripple indices (H_D/λ) change substantially. In fact, all the form drag calculations were performed using both of the assumptions described above for the wavelength of the dunes, and only very minor differences in the skin friction bottom stress values were noted. All results shown herein use the bend-averaged value of the dune wavelength, which was 147 cm.

Dietrich's measurements of the boundary shear stress responsible for sediment transport were made at six sections in the bed, as shown in Figure 2.6. The numbering system
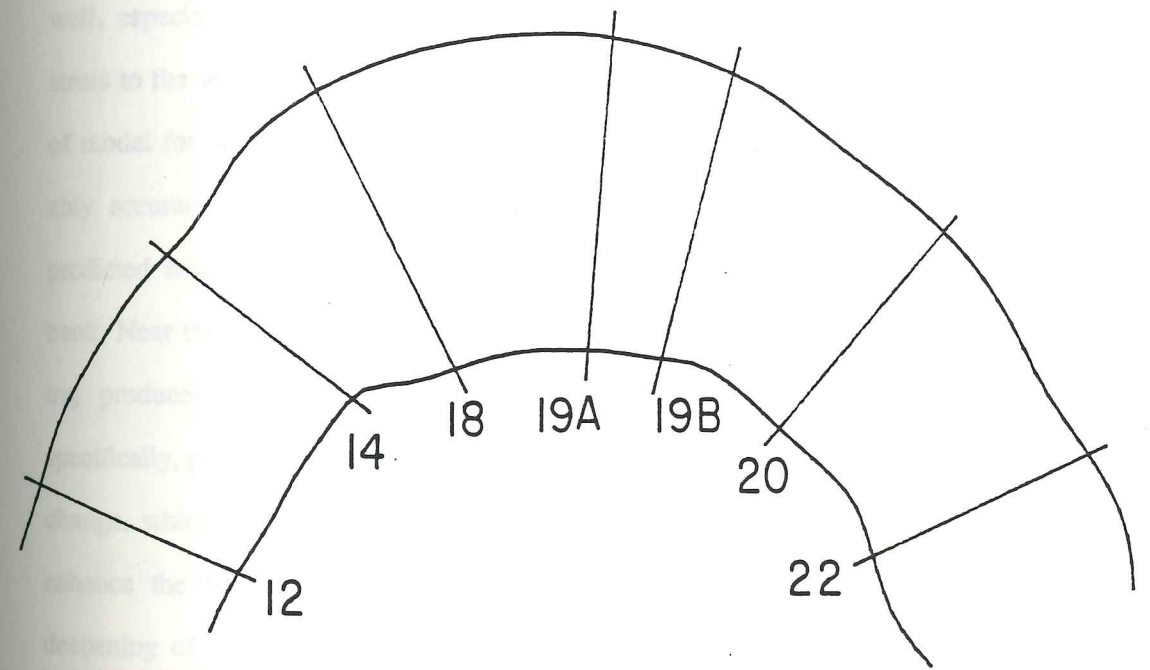
Figure 2.6. Numbering system and location of sections at which measurements were made.

of the sections is the scheme used by Dietrich, and is employed here to allow easy comparison of the model results to Muddy Creek observations published in other papers. The methods used to measure the boundary shear stress, flow velocities, and surface elevations are described in detail by Dietrich [1982]. The measured values of sediment transport boundary shear stress are shown with the model results in Figure 2.7. It is clear from this figure that the model predicts the structure of the sediment transport boundary stress fairly well, especially considering the rough assumptions used in the reduction of the overall stress to the sediment transport value. This, of course, indicates the desirability of this type of model for calculations of bedload transport. However, while the predictions are reasonably accurate, there are some systematic discrepancies. For example, at section 18, the predicted skin friction bottom stress is low near the inner bank and high near the outer bank. Near the inner bank, there is substantial streamwise shoaling of the flow. This shoaling produces a change in the streamwise vertical structure of the flow and, more specifically, produces enhanced shear near the boundary. The effect of this vertical structure change, which appears in the model at the next order in the perturbation expansion, is to enhance the bottom stress. Near the outer bank, there is relatively rapid streamwise deepening of the flow, which results in less shear near the boundary, and a diminished boundary stress. Thus, some of the differences between the measured and predicted bottom stresses are associated with the assumption of a spatially invariant similarity structure for the streamwise velocity. However, these errors may be accounted for by solving the perturbation equations to one higher order and, by doing so, treating the effects of spatial accelerations on the vertical structure of the streamwise velocity and shear stress.

In order to calculate the downstream sediment flux fields from the sediment transport boundary shear stresses discussed above, it is necessary to employ a bedload equation. The results presented here are from the equation presented by Yalin [1963], which is given by
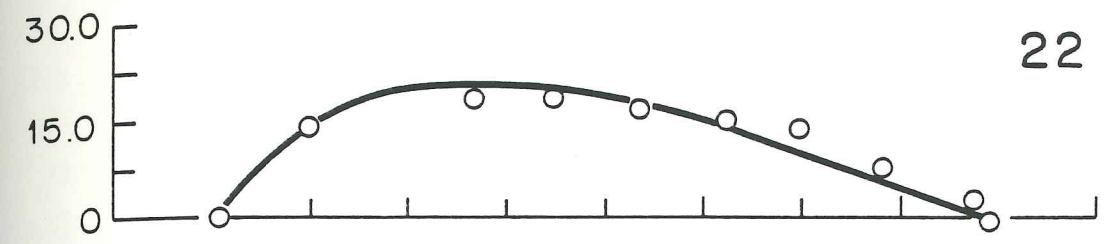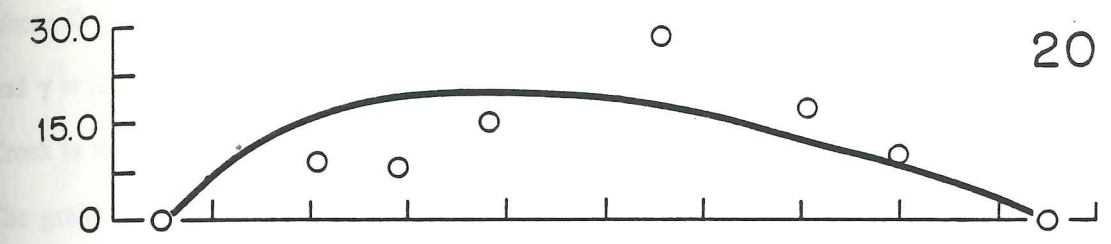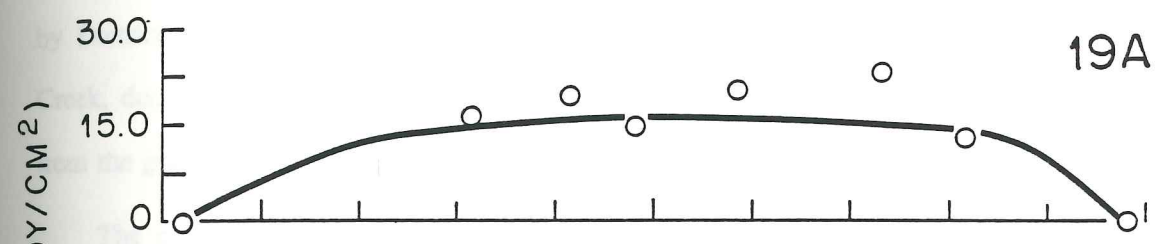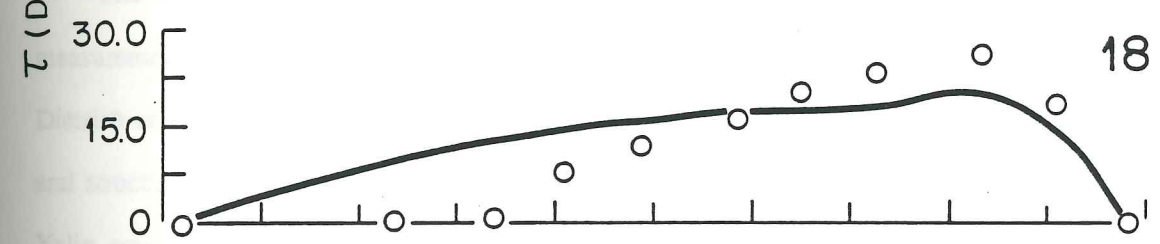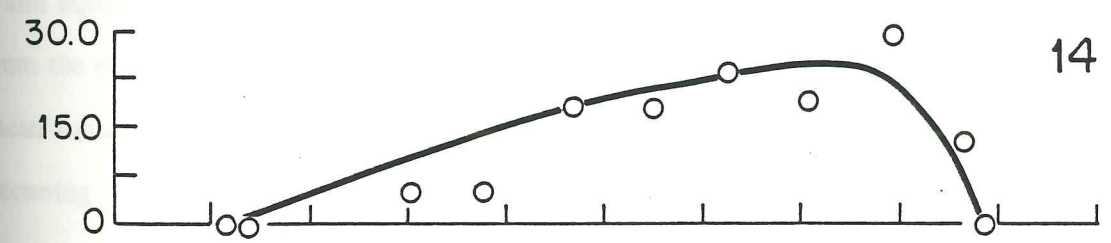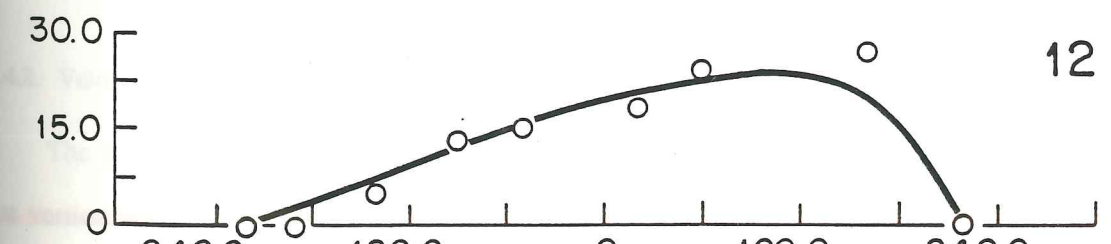
Figure 2.7. Comparison between measured and calculated values of the boundary shear stress responsible for sediment transport at six sections in Muddy Creek, Wyoming.

$$Q_s = 0.635 u_* DS \left[1 - \frac{1}{\gamma S} \ln(1 + \gamma S) \right] \tag{2.52}$$

where D is the particle diameter, S is the local excess shear stress defined by $(\tau_{SF} - \tau_c)/\tau_c$, and $\gamma = 2.45 \, (\rho_s/\rho)^{-.4} \, (\tau_c/(\rho_s - \rho)gD)^{0.5}$. Since by far the majority of the sediment in Muddy Creek is make up of quartz sand grains, the sediment density ρ_s is given by 2.65 gm/cm^3. The grain diameters used in the calculations are the median sizes measured and presented by Dietrich and Smith [1984], which vary from about .03 to .20 centimeters in Muddy Creek, depending upon location in the stream. The critical shear stresses τ_c were found from the grain size data using Shields' diagram as presented by Smith [1977].

The calculated downstream sediment flux field is shown in Figure 2.8, along with measurements of bedload transport taken in Muddy Creek using a bedload sampler (from Dietrich and Smith, 1984). Although there are some discrepancies, it is clear that the general structure of the bedload transport field is reproduced well by the model results and the Yalin equation. The total downstream discharges of sediment at each section calculated from the model results were fairly close to constant, with about a 10% variation about the mean value. This is consistent with the observation that no net erosion or deposition was occurring in Muddy Creek during the period when measurements were taken.

2.4.2. Velocities and Surface Elevations

The Muddy Creek observations presented by Dietrich [1982] also include values for the vertically-averaged downstream velocity. This data is shown with the model results in Figure 2.9. This comparison clearly demonstrates that the lowest-order vertically-averaged equations employed in the model represent the salient physics well. The only noteworthy discrepancy between the measured and calculated vertically-averaged velocities is found
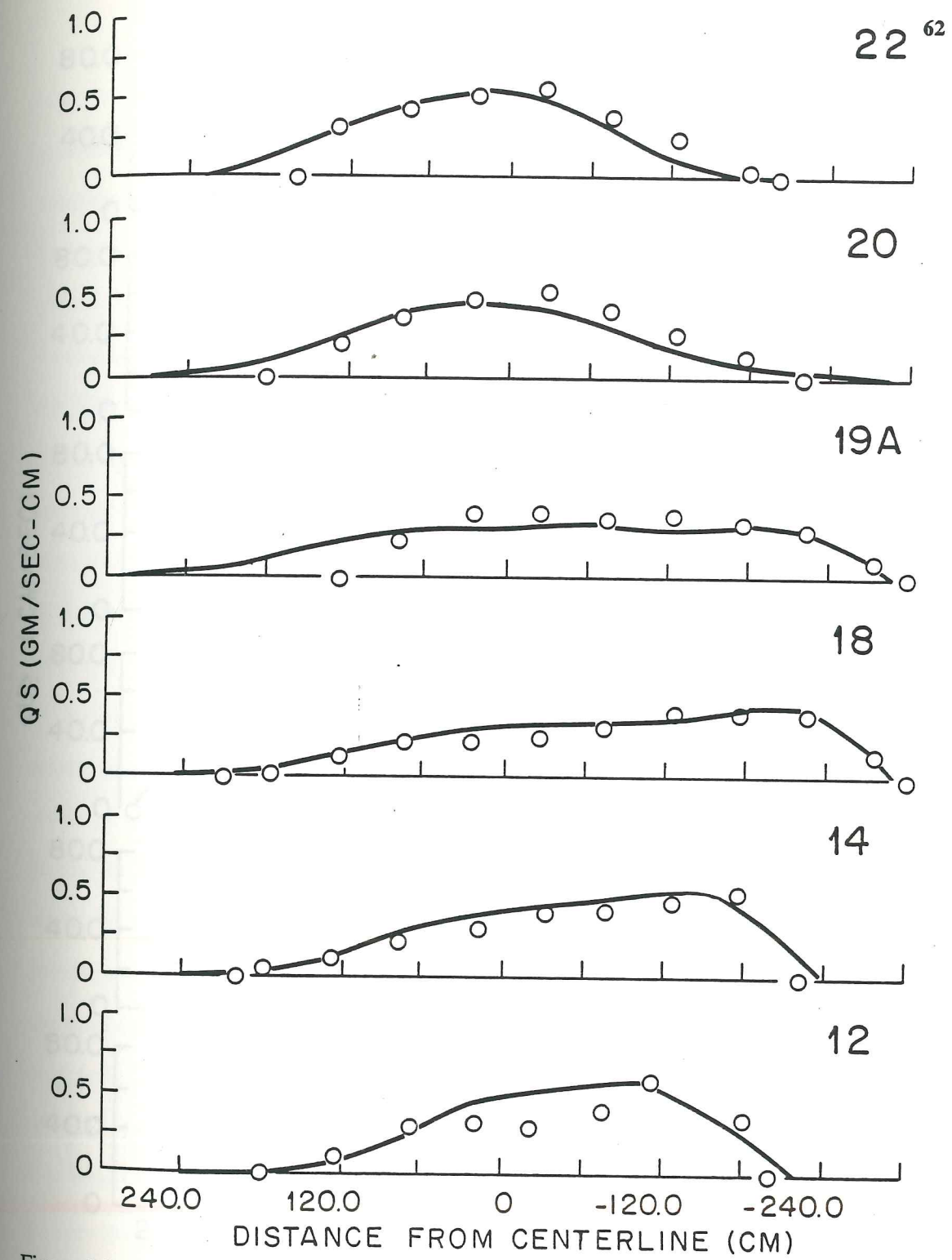
Figure 2.8. Values of downstream sediment flux at six sections in Muddy Creek. The data points are those given by Dietrich and Smith [1984], while the solid line is the value calculated using the skin friction bottom stress from the model in the Yalin bedload equation.
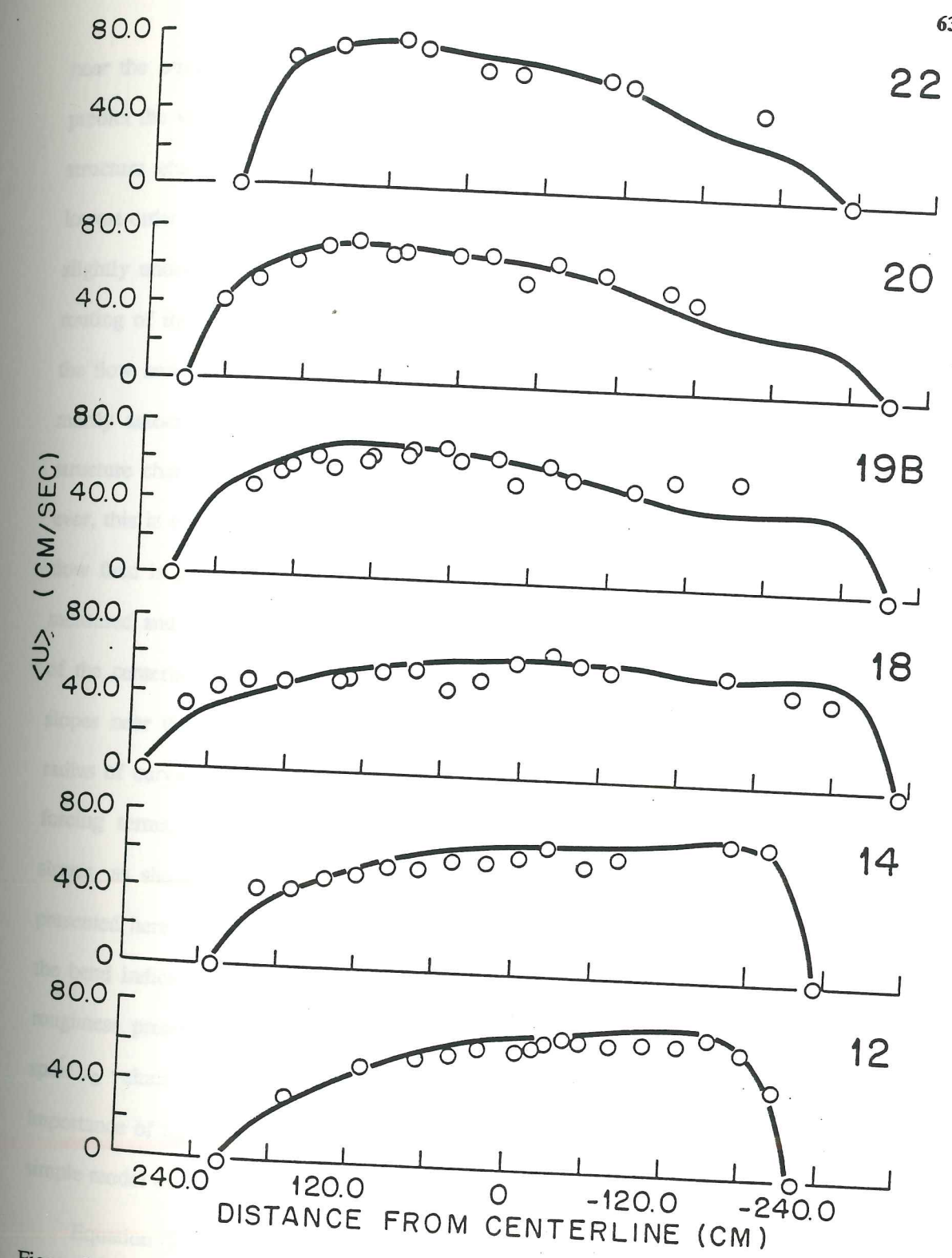
Figure 2.9. Comparison of values of vertically-averaged velocity measured in the IMR bend with those calculated from the model.

near the inner bank from sections 19B to 22. In this region, the model tends to under-predict the velocities. This minor error is almost certainly due to the exclusion of vertical structure changes over the point bar. By holding the vertical structure constant in the lowest-order equations, but including the effect of topographic steering, the model tends to slightly underpredict the volume flux over a three-dimensional obstruction. In reality, the routing of the flow over an obstruction consists of a component of steering, which routes the flow around the obstacle, and a component of vertical structure variation, which is pri-marily associated with the flow going directly over the obstacle. By neglecting vertical structure changes, the model underpredicts the flux of water up over the point bar. How-ever, this is only a minor error, as is consistent with the model scaling and, in general, the flow field is predicted accurately. This conclusion is also supported by comparison of the measured and calculated centerline surface elevations, shown in Figure 2.10. The structure of the centerline elevation is typical of natural meandering streams, with relatively small slopes near the crossings joined by a region of much steeper slope near the minimum radius of curvature. This structure is clearly produced by the presence of the topographic forcing terms, since flat-bedded channels have essentially constant centerline surface slopes, as shown experimentally by Yen and Yen [1971] and verified using the model presented here. The match between the measured and predicted overall head loss through the bend indicates that the form drag is well-predicted by the model for the total channel roughness presented above. Using the Nikuradse roughness values or the sediment tran-sport z_0 values yields much lower total head loss through the bend, which indicates the importance of including the form drag effects associated with bars and bedforms using the simple model described above.

Equation (2.14) yields the cross-stream surface slope which may then be used to con-struct the overall surface elevation, which is shown in Figure 2.11. Both the measurements
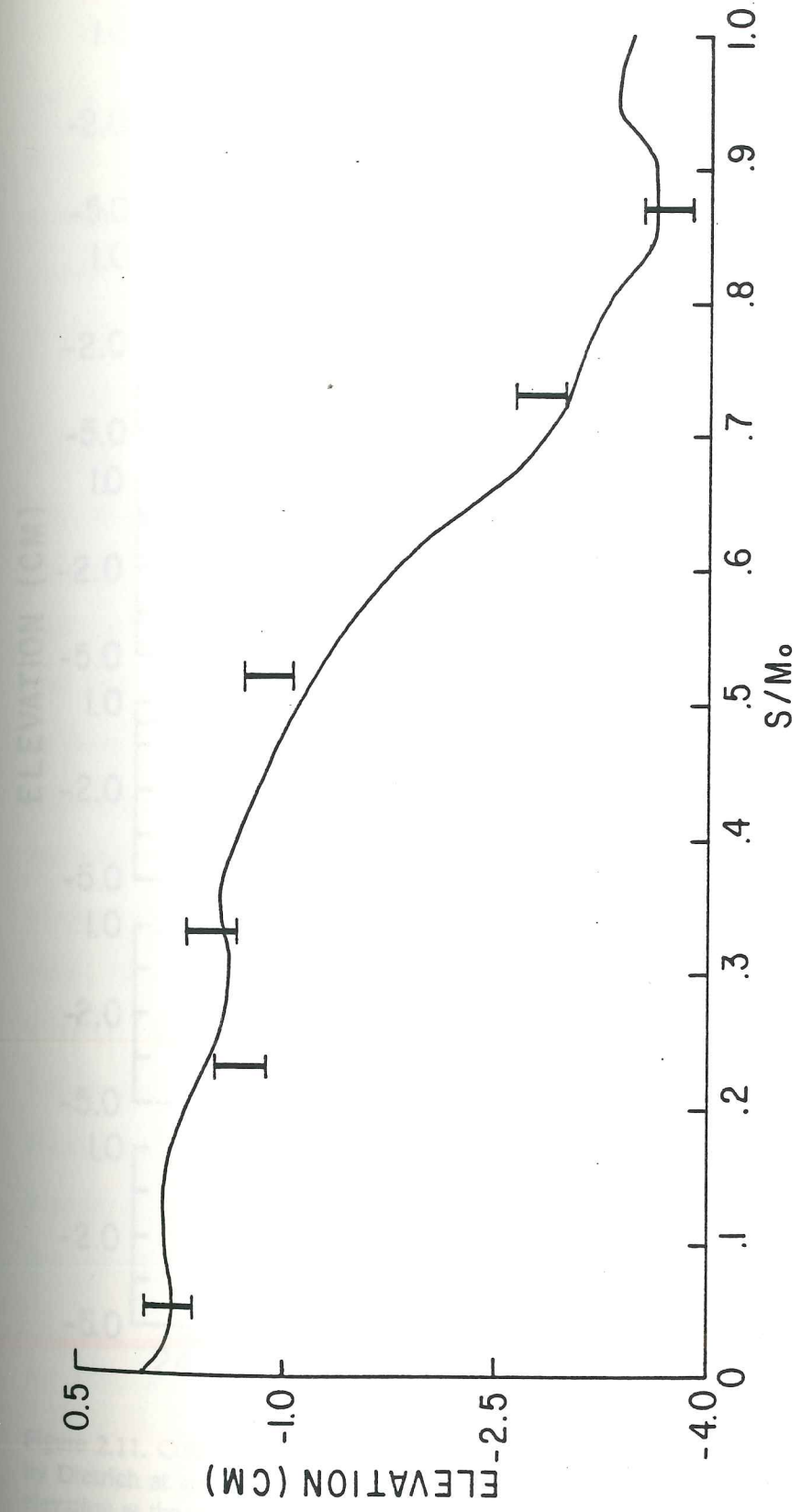
Figure 2.10. Centerline surface elevation in the IMR bend at Muddy Creek. The solid line is the elevation predicted by the model and the data points are from measurements made by Dietrich [1982]. The measurements are accurate to within about .2 cm, as shown by the error bars.
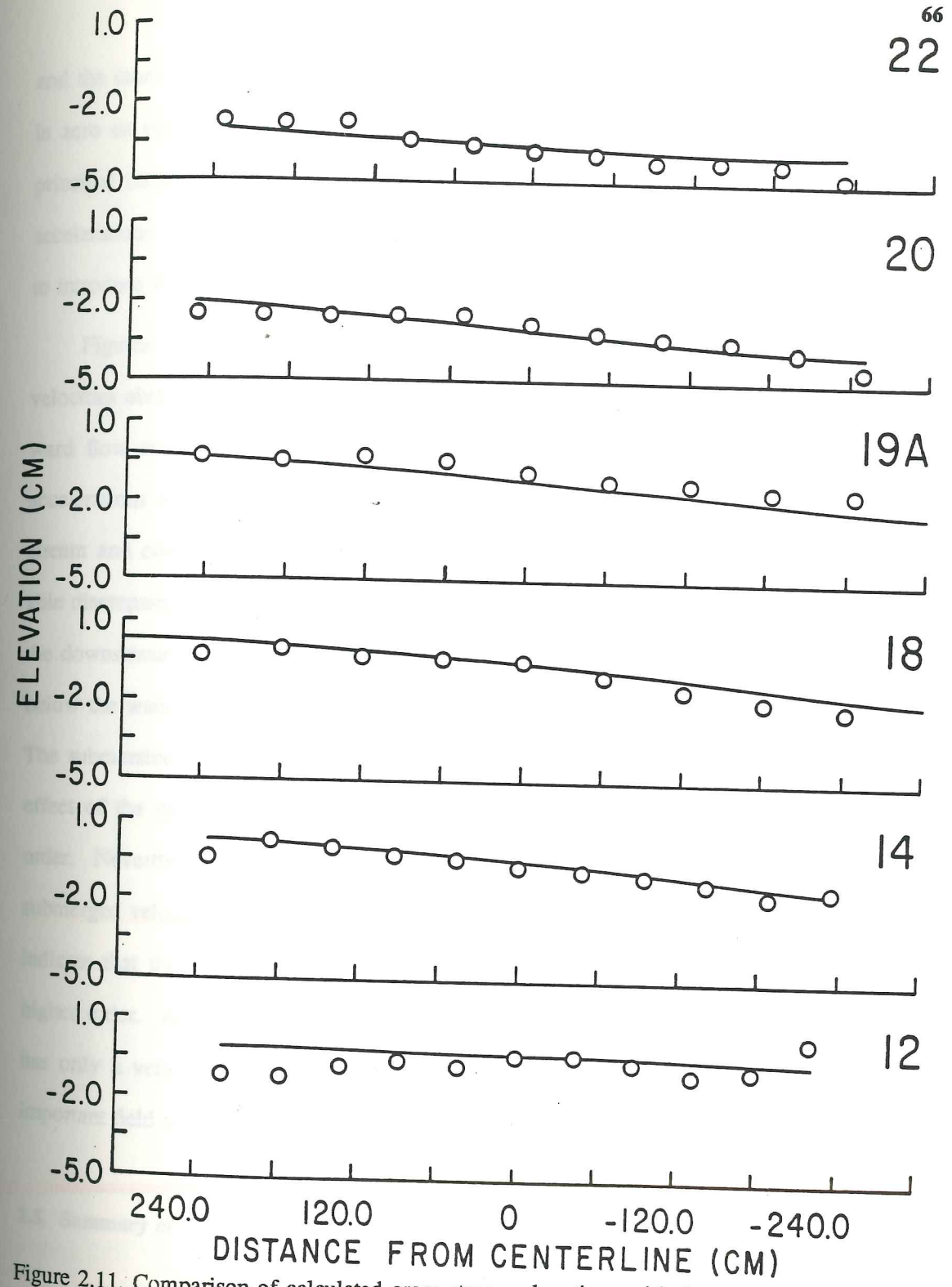
Figure 2.11. Comparison of calculated cross-stream elevations with the measurements made by Dietrich at six sections in the IMR study bend. Elevations are relative to the centerline elevation at the upstream crossing.

and the model show a region upstream of the pool where the downstream pressure gradient is zero or even slightly positive but the boundary shear stress is still downstream. The principal balance in this area is clearly between the pressure gradient and the convective accelerations included in equation (2.13), which again demonstrates that it is inappropriate to introduce these terms as perturbation quantities.

Figures 2.12 and 2.13 show sectional contours of the downstream and cross-stream velocities obtained from the model and measurements, respectively. The production of outward flow throughout the water depth over the bar due to the presence of large fluid accelerations is clear in both cases. Furthermore, the lateral position and value of downstream and cross-stream velocity maxima are in quite good agreement. The most noticeable discrepancy between the model results and the data is found in the vertical position of the downstream velocity maxima. The observations indicate that the peak velocity is often below the water surface, while the model can only predict velocity maxima at the surface. The submersion of the velocity jet is almost certainly due to the momentum redistribution effect of the cross-stream circulation terms, which only appear in the model at the next order. Nevertheless, the overall agreement and the fact that the surface velocities above submerged velocity maxima are only about 10-20% lower in magnitude than the maximum indicate that the circulation-induced convective acceleration terms are correctly placed at higher order. At any rate, this error is a minor one, especially in light of the fact that it has only a very small effect on the sediment transport, which is the most sensitive and important field one hopes to predict.

2.5. Summary of the Meander Flow Model

In summary, it has been demonstrated that the simple model for flow in curved channels with typical topography presented in this chapter does an admirable job of reproducing
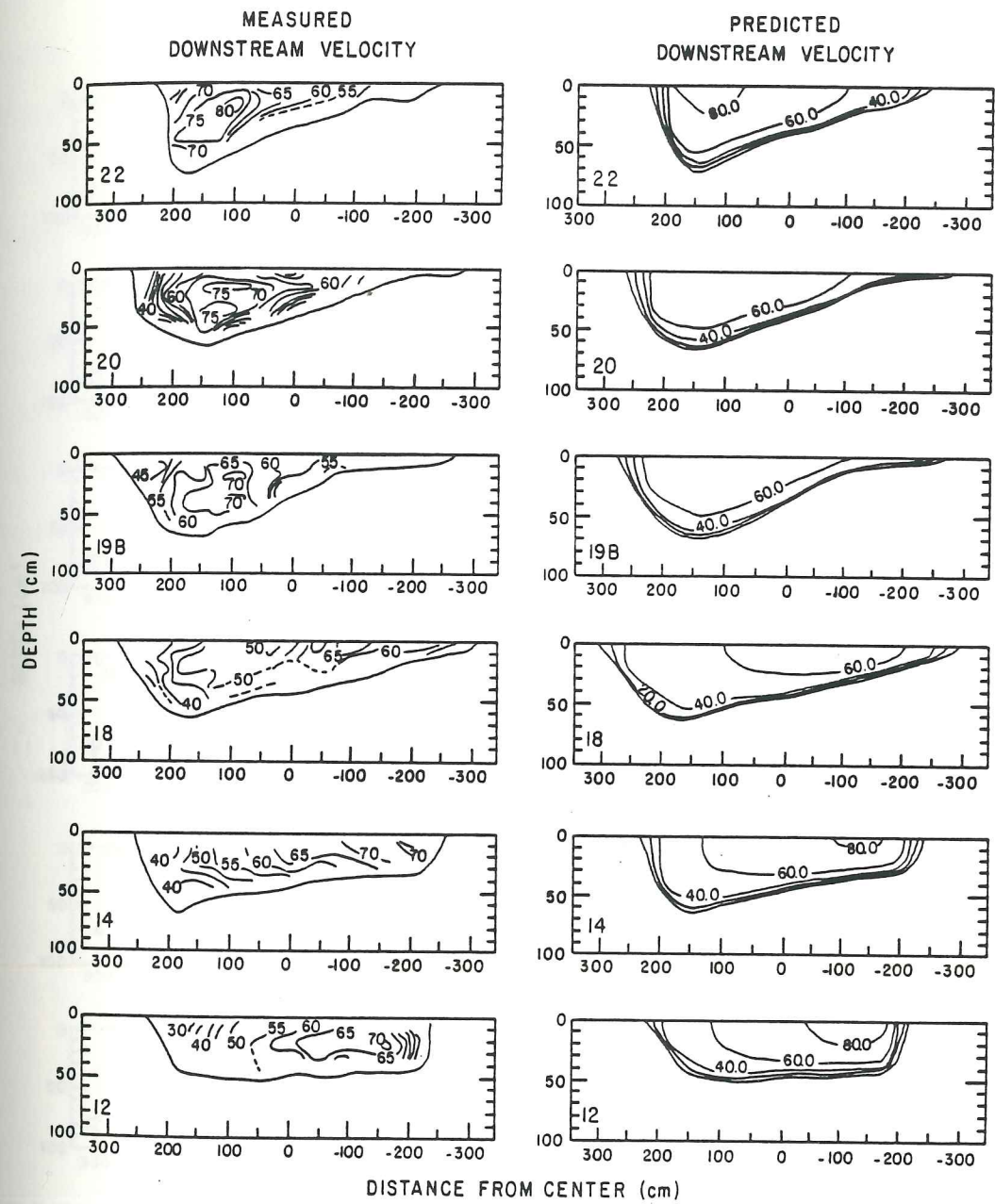
Figure 2.12. Measured and predicted contours of downstream velocity at six sections in the Muddy Creek bend. The contour interval is 20 cm/sec for the predicted velocities (on the right), and 5 cm/sec for the measured velocities. The left-hand column is reproduced with permission from Dietrich [1982].
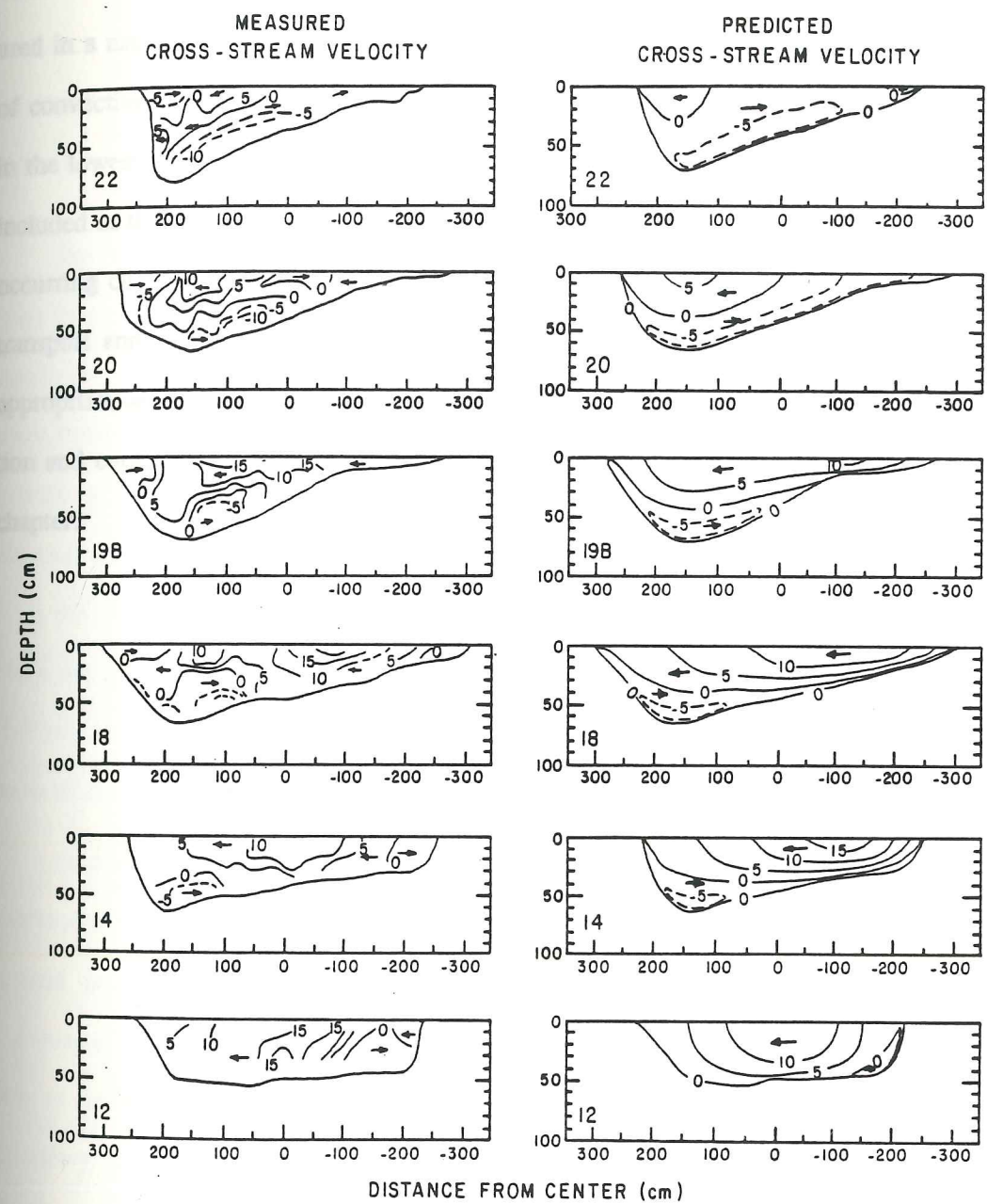
Figure 2.13. Measured and predicted contours of cross-stream velocity in Muddy Creek in 1978. Contours are every 5 cm/sec. Incomplete contours on the sections in the left-hand column are the result of missing data. The left-hand column is reproduced with permission from Dietrich [1982].

velocities, surface elevations, boundary shear stresses, and sediment transport fields measured in a natural meandering stream. The primary reason for this accuracy is the inclusion of convective accelerations due to downstream-varying topography and radius of curvature in the lowest-order equations. The scaling presented here indicates that these terms must be included at the lowest order in order to construct a model which is applicable to naturally-occurring curved channels. This result has important implications in the areas of sediment transport and meander stability, and it is certain that the coupling of this model with an appropriate sediment transport algorithm will provide interesting information on the formation and evolution of meandering streams and rivers, as will be described in the following chapter.
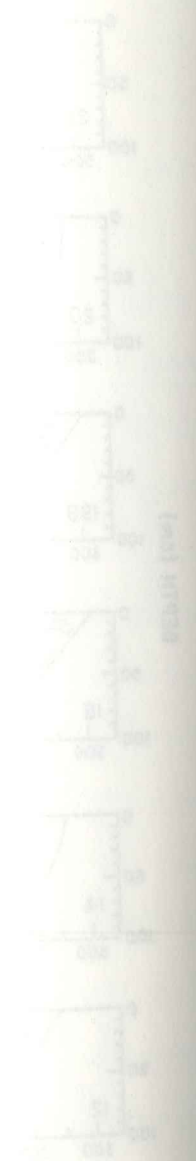
3.1. Overview

By definition, a stable channel morphology is attained when no net deposition or erosion is occurring on the channel bed for a prescribed flow and sediment discharge. This condition is reached when the amount of sediment arriving in a given length of time at each location on the bed is precisely equal to that departing from that point or, in other words, when the divergence of the sediment flux is zero everywhere on the bed. If the channel geometry or flow is modified in a manner such that the flow is not in equilibrium with the channel, erosion and deposition will occur on the bed until stability is reinstated. Both the mechanism by which the channel adjusts to a perturbation from equilibrium and the time scale over which adjustment occurs is of fundamental importance in several problems of concern to hydrologists and geomorphologists.

In order to investigate the evolution and stability of natural channels, the interactions between the flow field, the channel bathymetry, and the sediment transport must be characterized in a realistic manner. These interactions may be loosely divided into three categories. First of all, there is a strong coupling between the flow and channel geometry due to topographic forcing of the flow field. The spatial distributions of velocities and boundary shear stresses are strongly affected by bathymetry through the production of convective accelerations associated with channel nonuniformity. These effects are perhaps the most often neglected in previous work on stable channels configurations, and yet, as is made clear below, they are of primary importance in many, if not most, natural channels. The second type of interaction considered herein is that between sediment transport over the bed and the slope of the bed. Clearly, both cross- and downstream slopes modify

sediment fluxes over the bed through the gravitational forces that act on the sediment particles as they move. These forces are important in the determination of stable bar and bank slopes. Lastly, and perhaps obviously, there is a strong coupling between the flow over the bed and the transport of sediment. For the case of bedload transport, only the boundary shear stress pattern is important, while in the case of mixed or suspended load transport, the bottom stress, velocities, and turbulent diffusivities all are important for predicting patterns of erosion and deposition. Any attempt to understand the basic processes by which a channel adjusts to its equilibrium form must include a physically-based sediment transport model which includes the effect of bed slopes, as well as a fluid dynamical model that accurately treats the response of the flow to topographic nonuniformities.

In this chapter, a method whereby predictions of the evolution and stability of natural channels may be made is presented. The basic idea behind the approach presented here is shown in the form of a flow chart in Figure 1.1. To predict the temporal development of channel morphology, one begins by assuming that the flow discharge and the initial geometry of the stream are known. Using these values, a numerical flow model is employed to obtain the distributions of velocity and bottom shear stress in the flow through the initial channel. Since the time scales associated with the flow are much shorter than the time scales associated with the slow evolution of the bed topography, the fluid dynamical model can be constructed using the assumption that the flow is steady. However, in order to treat topographic steering of the flow by channel nonuniformities, appropriate convective accelerations must be retained in the model equations. This is discussed in more detail below in the context of specific flow calculations.

The boundary shear stresses and velocities obtained from the flow model can be used along with the particle size distributions in order to predict the flux of suspended load and bedload. As mentioned above, the effect of the bed slopes on the bedload sediment fluxes

must be included. As shown in the Figure 1.1, these sediment fluxes can be used along with an expression enforcing the conservation of sediment mass in order to predict erosion and deposition on the bed. This pattern of scour and fill can then be employed to predict how the bed will change in form in a specified time interval. Thus, the calculated rates of erosion and deposition are employed to predict what the bed will look like at some small increment of time later. The flow over this new bed geometry is calculated using the fluid dynamical model, and the entire procedure is repeated. The procedure is continued until the flow variables calculated over the evolved topography yield sediment fluxes for which no erosion or deposition occurs, or until all the erosion and deposition goes into migration of the bar forms on the bed. When this condition is met, the topography has evolved to the equilibrium condition.

As of this writing, there have been two attempts to construct fully nonlinear flow and bed deformation models similar to the one presented here. The first of these is presented by Shimizu and Itakura [1985], while the second is very briefly discussed by Struiksma et al, [1985]. Each of these two formulations considers only the solution of the vertically-averaged equations, while the model presented herein treats the vertically-averaged equations as well as the vertical structure of the flow. As a result of this, these other models must employ theoretical expressions for fully-developed bend flow to calculate the helical part of the cross-stream velocity distribution. Thus, the near-bed veering of the shear stress vector is treated in the models presented by these other workers using results obtained for well-developed bend flow. This is inappropriate and, although it may perform adequately in meander bend calculations, clearly it does not account for the production of helical circulation in straight channels, as discussed below. Furthermore, these models do not provide any information about the vertical structure of the flow, so they cannot be employed without modification to examine any phenomena related to the variations of velocity and

stress in the vertical (e.g., suspended load transport). Nevertheless, they clearly represent substantial improvements over the use of linear theories for predicting bed topography and, as such, are a step in the right direction.

The work described herein begins with a discussion of the fluid dynamical and sediment transport models that are to be utilized. After building this framework, the general scheme for predicting bed evolution and equilibrium topography described above is applied in two fundamental and relatively well-understood cases in order to strengthen confidence in the technique. First, the method is used to predict the evolution and stability of a point bar and pool in a curved channel with an initially flat cross-sectional shape. Second, this technique is shown to predict the formation and eventual stability of alternate bars downstream of a perturbation in an initially straight, uniform channel. In conjunction with the finite amplitude alternate bar evolution, a linear stability analysis of the governing equations is presented, both in order to clarify the physical processes responsible for alternate bar formation, and to demonstrate the failings of the linear theory.

3.2. The Fluid Dynamical Model

The numerical flow model used in the bed evolution calculations is a generalization of the meander flow model described and tested in the previous chapter. In the meander model, the technique of solution is centered upon a perturbation expansion about a simplified set of vertically-averaged equations. Simplification of the vertically-averaged equations arises from careful scaling arguments specifically valid for typical natural meander bends. In order to construct a model of general validity, the scaling constraints employed in Chapter 2 are relaxed. However, most of the physical assumptions employed in the meander model are also used in the more general flow model developed in this

chapter. These are restated briefly here:

(1) Streamwise velocities are assumed to be much larger than cross-stream velocities, which are, in turn, much greater than vertical velocities. This assumption is valid in natural streams, except perhaps near very abrupt obstructions and vertical banks.

(2) The pressure field is assumed to be hydrostatic or, in other words, vertical accelerations are assumed to be negligible in the vertical momentum equation. As in the case of assumption (1), this is valid except perhaps near abrupt obstructions in the flow or in the vicinity of steep banks.

(3) The flow is considered to be fully turbulent and the exchange of momentum associated with the turbulent fluctuations is described using a physically-appropriate scalar kinematic eddy viscosity. This eddy diffusivity depends only on the local shear velocity and the distance from the boundary; thus, production and dissipation are assumed to be in balance locally and any advective influences on the turbulence field are neglected. This assumption specifically excludes the local effects of wakes in the model solutions.

(4) The total roughness of the channel is assumed to be representable in terms of a field of values for z_0, the roughness length. These values represent momentum extraction associated with grain roughness, as well as that due to sediment transport and form drag on channel nonuniformities (e.g., bedforms and bars), as discussed in Chapter 2.

(5) The lowest-order structure of the velocity field is assumed to be character-ized by strong shear near the boundary and relatively weak shear (nearly con-stant velocity) in the region away from the boundary. Thus, the downstream velocity is assumed to be nearly equal to the vertically-averaged velocity over most of the flow depth. This leads to an assumption that the vertically-averaged convective accelerations in the downstream momentum equation are reasonable approximations to the full convective acceleration terms (see Chapter 2). In conjunction with (2) and (3) above, this assumption yields the result that, to lowest order, the velocity profile measured along the direction of a vertically-averaged streamline is well-described by a similarity velocity profile.

(6) The effects of lateral friction are neglected in the model formulation. These terms clearly have an influence on the flow very near the banks, but since most rivers and streams are wide relative to their depth, this effect is not of zero-order importance in determining the overall flow field. Furthermore, these terms are not related to the genesis and growth of bars, although they may have some weak effect on finite amplitude bar morphology.

These assumptions form the foundation of the flow model employed herein and will be adhered to henceforth.

3.2.1. Solution of the Routing Problem

As in the meander model, the first step in this theoretical model is the solution of the vertically-averaged equations. Employing the channel-fitted coordinate system presented by

Smith and McLean (1984) in conjunction with assumptions (1) and (5), the full vertically-averaged equations expressing conservation of mass and momentum (equations 2.6, 2.8, and 2.9) are reduced to the following balances:

$$\frac{1}{1-N}\frac{\partial}{\partial s}(<u>h) - \frac{<v>h}{(1-N)R} + \frac{\partial}{\partial n}(<v>h) = 0 \tag{3.1}$$

$$\frac{1}{1-N}\frac{\partial}{\partial s}(<u^2>h) + \frac{\partial}{\partial n}(<uv>h) - \frac{2<uv>h}{(1-N)R} = \frac{-gh}{1-N}\frac{\partial E}{\partial s} - \frac{1}{\rho}(\tau_{zs})_B \tag{3.2}$$

$$\frac{1}{1-N}\frac{\partial}{\partial s}(<uv>h) + \frac{\partial}{\partial n}(<v^2>h) + \frac{(<u^2>-<v^2>)h}{(1-N)R} = -gh\frac{\partial E}{\partial n} - \frac{1}{\rho}(\tau_{zn})_B \tag{3.3}$$

Following the conventions employed in Chapter 2, s and n are the streamwise and cross-stream coordinates, respectively, R is the radius of curvature of the channel centerline, and $1-N$ is the downstream metric of the coordinate system. Furthermore, u and v are the streamwise and cross-stream velocity components, respectively, E is the surface elevation above some arbitrary datum, and $(\tau_{zs})_B$ and $(\tau_{zn})_B$ are the streamwise and cross-stream components of the bottom stress. Surface stresses are assumed to be zero and < > is used to represent vertically-averaged quantities.

In order to solve these equations, it is necessary to specify a closure between the velocity and the components of the bottom stress. Extending the approach taken in the streamwise equation of the meander model, the following closures are utilized:

$$\rho <u>^2 = \alpha(\tau_{zs})_B \qquad \rho <u><v> = \alpha(\tau_{zn})_B \tag{3.4}$$

where the assumption that the cross-stream velocities are small compared to the streamwise velocities has been employed to simplify the full drag closure.

The specification of α proceeds in a manner analogous to that used in the meander flow model. In that model, the fact that vertically-averaged convective accelerations are good approximations to the full convective accelerations over most of the flow depth was employed in obtaining a linear stress profile at lowest order. The linear stress profile along with the definition of the eddy viscosity was used to arrive at a similarity structure for the lowest-order streamwise velocity field. This similarity profile was shown to depend only on the functional form chosen for the eddy viscosity and the roughness of the bed. In the more general model developed here, the same physical ideas are used to argue that a linear stress profile is a good lowest-order approximation to the stress profile measured along the direction of the vertically-averaged streamlines of the flow. In other words, the vertical structure of the velocity field along the direction of the vector defined by these two components of averaged velocity is well-described by a similarity profile. This reasoning along with the definition of the eddy viscosity immediately leads to the following equations:

$$u_0 = \left[\frac{(\tau_{zs})_B}{\rho}\right]^{\frac{1}{2}} f_1(\zeta,\zeta_0) = u_* f_1(\zeta,\zeta_0) \tag{3.5}$$

and

$$v_s = \left[\frac{(\tau_{zn})_B}{\rho u_*}\right] f_1(\zeta,\zeta_0) = v_* f_1(\zeta,\zeta_0) \tag{3.6}$$

In these equations, the subscript 0 on the streamwise velocity shows that, following the

conventions used in Chapter 2, this is the lowest-order streamwise velocity. The subscript s on the cross-stream velocity component indicates that this quantity is the similarity part of v_1, the first-order cross-stream velocity. This point will be made clearer below. Nondimensionalization of the lowest-order eddy viscosity using $K_0 = u_* h \kappa(\zeta)$ yields

$$f_1(\zeta, \zeta_0) = \int_{\zeta_0}^{\zeta} \frac{1 - \zeta}{\kappa} d\zeta \qquad (3.7)$$

Thus, as in the meander model, specification of a non-dimensional eddy viscosity and the bed roughness provides the lowest-order vertical structure for the velocity field. Unless otherwise noted, the eddy viscosity used in the calculations presented here is given by equation 2.30, and the drag partitioning algorithm described in the previous chapter is employed to calculate local roughness lengths. Using equations (3.4), (3.5), and (3.6), it is easy to show that

$$\alpha = \left[\int_{\zeta_0}^{1} f_1 \left[\zeta, \zeta_0 \right] d\zeta \right]^2 \qquad (3.8)$$

and that

$$u_* = \frac{<u>}{\alpha^{1/2}} \qquad v_* = \frac{<v>}{\alpha^{1/2}} \qquad (3.9)$$

Equation (3.4) above allows the components of the boundary shear stress in equations (3.2) and (3.3) to be expressed in terms of the components of the vertically-averaged velocity and α. The value of α proceeds directly from the specification of a lowest-order eddy

viscosity or, equivalently, the choice of a similarity vertical profile for the velocity. However, in order to solve the vertically-averaged equations, the quantities $<u^2>$, $<uv>$, and $<v^2>$ must be expressed in terms of the vertically-averaged velocities, $<u>$ and $<v>$. This is accomplished by expanding the horizontal velocities in terms of their vertical average and the deviation from that average, and then inserting these expansions in the various vertical averages appearing in equations (3.2) and (3.3). Using primes to denoted deviations from the vertical average, the following results are obtained:

$$<u^2> = <u><u> + <u'^2> \quad <uv> = <u><v> + <u'v'> \quad <v^2> = <v><v> + <v'^2> \quad (3.10)$$

In the meander model, the last terms on the right-hand sides of the above equations (the vertical correlation terms) were assumed to be small, and were neglected in the vertically-averaged solution. As a result of neglecting these effects, correction terms appeared in the perturbation equations for the vertical structure (the last four terms on the left-hand side of equation (2.33)). This approach was justified by the measurements taken by Dietrich (1982), which demonstrated that this approximation was reasonable in typical meander bends. Here, this same approximation is used in the solution of the vertically-averaged equations, but a technique whereby higher order corrections to this closure may be made is also described. It is worth noting here that, if the similarity structure were exactly correct, setting the vertical correlation terms equal to zero would be a very good approximation. For the case of a logarithmic vertical profile and typical values for ζ_0, the value of these terms is typically a maximum of 5% of the value of the uncorrelated part of the vertical averages. However, the deviations from similarity weaken this assumption somewhat, making a technique allowing for the inclusion of these effects of some value.

As detailed below, dropping the vertical correlation terms allows the vertically-averaged equations to be solved in a straightforward manner. These solutions along with

the similarity vertical structure are then inserted as forcing terms in the full (non-averaged) momentum equations in order to calculate the deviations about the linear stress profile and the similarity velocity profile. As developed more fully below, the variations about the similarity assumption can be used to reformulate the vertically-averaged equations incorporating the vertical correlation terms as forcing terms. In contrast to the original meander flow model, this procedure effectively moves the entire flow routing problem to the vertically-averaged equations, and does not require corrections to the local streamwise or cross-stream discharge in the non-averaged equations.

Inserting the drag closure and separating the correlated and uncorrelated parts of the vertical averages in the equations (3.2) and (3.3) produces the following results:

$$\frac{1}{1-N}\frac{\partial}{\partial s}(<u>^2 h) + \frac{\partial}{\partial n}(<u><v>h) - \frac{2<u><v>h}{(1-N)R} + F' = \frac{-gh}{1-N}\frac{\partial E}{\partial s} - \frac{<u>^2}{\alpha h} \quad (3.11)$$

$$\frac{1}{1-N}\frac{\partial}{\partial s}(<u><v>h) + \frac{\partial}{\partial n}(<v>^2 h) + \frac{(<u>^2 - <v>^2)h}{(1-N)R} + G' = -gh\frac{\partial E}{\partial n} - \frac{<u><v>}{\alpha h} \quad (3.12)$$

where

$$F' = \frac{1}{1-N}\frac{\partial}{\partial s}(<u'^2>h) + \frac{\partial}{\partial n}(<u'v'>h) - \frac{2<u'v'>h}{(1-N)R}$$

$$G' = \frac{1}{1-N}\frac{\partial}{\partial s}(<u'v'>h) + \frac{\partial}{\partial n}(<v'^2>h) + \frac{(<u'^2> - <v'^2>)h}{(1-N)R}$$

In obtaining solutions of these equations, the vertical correlation forcing terms F' and G' are initially set to zero but may be brought in iteratively. In order to solve these equations, one also needs the integral form of the equation expressing conservation of mass given by

$$<v>h = \frac{-1}{1-N} \int_{\frac{-w}{2}}^{n} \frac{\partial}{\partial s}(<u>h)dn \qquad (3.13)$$

The three equation immediately above are easily solved numerically using any of a variety of techniques. Primarily for historical reasons, the solutions shown here are found using the same method described in detail in Chapter 2 for the meander flow model. In short, equation (3.12) is used to rewrite the pressure gradient in (3.11) in terms of the centerline surface slope and various integral terms. Equation (3.13) is then employed to eliminate the vertically-averaged cross-stream velocity. Using the drag closure, the final result of these manipulations is an integro-differential equation for $(\tau_{zs})_B$. This equation, along with an integral constraint on the streamwise discharge, is easily solved using a simple finite difference approximation in conjunction with an iterative scheme for determining the integral terms (see Chapter 2 for a complete description of this approach). This technique offers some advantage over more standard numerical techniques in that, because the iterative scheme exploits the fact that the vertically-averaged streamwise velocity is typically substantially greater than cross-stream velocity, it tends to be much more cost effective than a full finite difference or finite element solution. However, this advantage is gained at the expense of some generality in a geometric sense. For instance, the technique is inappropriate for the case of very rapid width variations in the streamwise direction. It is important to point out, however, that equations (3.11) to (3.13) are valid in general, and that specific solution techniques can easily be constructed for even the most complicated geometries. The only inputs required to obtain a solution to this set of equations are the stream geometry, the discharge, and the distribution of roughness lengths on the bed.

Solution of the vertically-averaged equations yields values for $< u >$, $< v >$, $(\tau_{zs})_B$, $(\tau_{zn})_B$, and the surface elevation, E. Using the similarity velocity structure and the linear

stress profile predicts values for both velocity and stress throughout the flow. In some sense, this lowest-order model corresponds to pure topographic steering; the solution predicts the routing of flow over a complex nonuniform bed, but it does not yield predictions of variations in the vertical structure associated with spatial accelerations. In order to calculate the deviations about the similarity structure, it is necessary to resort to the full momentum equations.

3.2.2. Deviations From Similarity

Although deviations about the similarity profile may be relatively small, these effects are often of primary importance in determining depositional patterns. For instance, the helical flow typically observed in parts of meander bends clearly plays a critical role in the initial growth of point bars. By definition, helical circulation is flow with no net cross-stream discharge, so this important physical effect is not predicted by the solution for $< u >$ and $< v >$ described in the previous section. In the meander flow model, this problem was rectified by using a perturbation expansion about the vertically-averaged equations. The helical component of velocity and the associated cross-stream stress term were found from a balance of the cross-stream stress divergence, first-order pressure gradient, the first-order averaged centrifugal force term, and the deviation from the vertical average of the zero-order centrifugal force term, as shown in equation (2.34). Using the more complete solution to the vertically-averaged equations described above essentially moves the entire flow routing problem to zero order, so the vertical average of the streamwise perturbation velocity is zero. In this case, equation (2.34) reduces to the following balance:

$$\frac{(u_0^2 - <u_0>^2)}{(1 - N)R} = -g\frac{\partial E_1}{\partial n} + \frac{\partial}{\partial z}K_0\frac{\partial v_1}{\partial z} \tag{3.14}$$

Adding the zero-order balance given by equation (2.28) to the above equation yields the result that, to first order, the cross-stream momentum equation is given by

$$\frac{u_0^2}{(1-N)R} = -g\frac{\partial E}{\partial n} + \frac{\partial}{\partial z}K_0\frac{\partial v_1}{\partial z} \tag{3.15}$$

Using the similarity solution for u_0 and $<v_1>$ in conjunction with the boundary conditions that the free surface is unstressed and the velocity goes to zero at the bed, this equation is easily solved for the cross-stream velocity and stress (see Chapter 2). The expression for the cross-stream velocity is of the form

$$v_1 = \frac{u_*h}{(1-N)R}g_1(\zeta,\zeta_0) + \frac{<v_1>}{\alpha^{\frac{1}{2}}}f_1(\zeta,\zeta_0) \tag{3.16}$$

In equation (3.16), the function f_1 is the similarity velocity profile defined in equation (3.7), and g_1 is a vertical structure function describing the well-known helical part of the cross-stream velocity, as given by the first term on the right-hand side of equation (2.37). The integral of g_1 from z_0 to the water surface is zero; by definition, there is no net cross-stream discharge associated with the helical circulation. Note that the second term on the right hand side of equation (3.16) is simply the similarity part of the cross-stream velocity field, as defined in equation (3.6).

There are two interesting asymptotes to equation (3.16). If no streamwise variations occur in the topography or curvature, then from equation (3.13) it is clear that $<v_1> = 0$, which results in a cross-stream velocity field which is entirely helical (i.e., there is no net cross-stream discharge). This solution corresponds to the classical case of well-developed

bend flow, wherein streamwise variations in topography and curvature are considered negligible (cf., Rozovskii, (1957); Engelund, (1974)). The orientation of the velocity vector is inward (i.e., toward the center of curvature) near the bed, and is directed outward near the free surface. The production of inward velocity and, therefore, inward boundary shear stress, is intimately connected to the production of point bars on the inner banks of curved bends, as discussed in detail below.

The second case of interest is that of a straight channel ($R \rightarrow \infty$). In this case, the vertical structure of both the downstream and cross-stream velocities are given by the similarity profile f_1. For a typical choice of the eddy viscosity, $f_1 = 2.5 \ln \left[\zeta / \zeta_0 \right]$, so the direction of the velocity vector is constant in the vertical, and its magnitude is distributed in a logarithmic manner. This solution corresponds to the case of "pure" topographic steering, wherein the flow is steered by downstream variations in the topography, but, in contrast to the case of well-developed bend flow, the orientation of the velocity vector does not vary in the vertical.

The mathematical model which led to equation (3.15) is specifically designed for application to meander bends, and the argument which leads to this formulation is inappropriate for the case of straight or weakly sinuous channels with streamwise topographic nonuniformities. In this situation ("pure" topographic steering), the inclusion of the effects of streamline curvature solely through the specification of the channel radius of curvature omits the production of helical flow and the associated perturbation boundary shear stress. This is a consequence of assuming that the curvature of the channel centerline is a good approximation to the curvature of the streamlines, a hypothesis that is relatively accurate in the case of fully-developed meander bends, but which is a poor approximation in straight channels with irregular bathymetry. As the flow is steered around the bars or other topographic obstructions in a straight channel, the induced streamline curvature will produce

convective accelerations in the cross-stream equations that are not included in equation (3.15). These convective accelerations produce cross-stream surface slope and a helical component of cross-stream velocity, just as the centrifugal force term in equation (3.15) produces cross-stream superelevation and helical circulation in a meander bend.

In order to develop a more general model, which includes the salient physical effects in both curved and straight channels with irregular bathymetry, it is useful to examine the ordered equations which result from the perturbation expansion employed in Chapter 2 for the situation where the radius of curvature is infinite (a straight channel). For this case, the three lowest-order cross-stream momentum equations in the perturbation expansion are given by

$$O(1): \qquad 0 = \frac{\partial E_0}{\partial n} \qquad\qquad (3.17)$$

$$O(\varepsilon): \qquad 0 = -g\frac{\partial E_1}{\partial n} + \frac{\partial}{\partial z}K_0\frac{\partial v_1}{\partial z} \qquad\qquad (3.18)$$

$$O(\varepsilon^2): \quad \frac{u_0}{1-N}\frac{\partial v_1}{\partial s} + v_1\frac{\partial v_1}{\partial n} + w_2\frac{\partial v_1}{\partial z} = -g\frac{\partial E_2}{\partial n} + \frac{\partial}{\partial z}K_0\frac{\partial v_2}{\partial z} + \frac{\partial}{\partial z}K_1\frac{\partial v_1}{\partial z} \qquad (3.19)$$

When $R \to \infty$, the O(1) solution tells us nothing about the flow field, it only provides the lowest-order value of the cross-stream surface slope, which is zero. The O(ε) equation may be solved immediately using the boundary conditions described above; the result is simply the similarity part of the cross-stream velocity.

This solution is identical to the non-helical component of the cross-stream velocity

field given by equation (3.16). However, in the case of a straight channel, the production of a helical component of the cross-stream velocity occurs at one order higher in the perturbation expansion, in equation (3.19). The first two terms in equation (3.19) make up the lowest-order convective accelerations associated with the curvature of the streamlines in the horizontal plane. As such, they are directly analogous to the centrifugal force term in equation (3.15), as can be verified using either a coordinate transformation or simple formulae for the geometry of curves in space. The third term on the left-hand side of equation (3.19) is associated with streamline curvature in the vertical, while the right-hand side of the equation encompasses the momentum fluxes associated with the higher-order pressure gradient and stress divergence.

To include the effects of helical flow in the case of a straight channel, the first two terms on the left hand side of equation (3.19) are moved down one order. By doing so, the effect of streamline curvature in a straight channel is brought into the model in the same manner that it is included in the case of the meander bend calculations. Note that, in doing this, the perturbation expansion is not violated; if the meander scaling presented in Chapter 2 had been carried out in a cartesian coordinate system, these terms would have appeared in both the vertically-averaged equations and equation (3.15), essentially replacing the centrifugal acceleration terms. Employing equations (3.5) and (3.6), it is easy to show that moving these cross-stream spatial accelerations to $O(\varepsilon)$ yields the following replacement for equation (3.15):

$$\frac{u_0}{1-N}\frac{\partial v_s}{\partial s} + v_s\frac{\partial v_s}{\partial n} + \frac{u_0^2}{(1-N)R} = -g\frac{\partial E}{\partial n} + \frac{\partial}{\partial z}K_0\frac{\partial v_1}{\partial z} \qquad (3.20)$$

In practice, equations (3.11), (3.12), and (3.13) are solved for the values of $<u_0>$ and $<v_1>$,

and then these values are employed to find u_0 and v_s using equations (3.5) and (3.6). Inserting these expressions in equation (3.20) and integrating employing the boundary conditions described above yields analytical expressions for the cross-stream velocity and stress. The equations for the velocity and stress are given by

$$v_1 = v_* f_1(\zeta, \zeta_0) + \left[\frac{h}{1-N} \frac{\partial v_*}{\partial s} + h \frac{v_*}{u_*} \frac{\partial v_*}{\partial n} + \frac{h u_*}{(1-N)R} \right] g_1(\zeta, \zeta_0) \quad (3.21)$$

and

$$\left[\tau_{zn} \right]_1 = \rho u_* v_* (1 - \zeta) + \left[\frac{h u_*}{(1-N)} \frac{\partial v_*}{\partial s} + h v_* \frac{\partial v_*}{\partial n} + \frac{h u_*^2}{(1-N)R} \right] g_2(\zeta, \zeta_0) \quad (3.22)$$

where $v_* = <v_1>/\alpha^{1/2}$ and g_2 is given by analogy with equation (2.38).

In typical meander bends, the first two terms in the bracketed expression in equation (3.21) above are much smaller than the last term. Thus, equation (3.21) is essentially equivalent to equation (3.16) for meander bends with typical sinuousity. However, in the case of very low sinuousity or straight channels, the first two terms in the bracketed expression will be larger than the last term. In this case, the dominant part of the cross-stream velocity will be the component associated with topographic steering, but the effect of streamline curvature in producing helical flow is not neglected, as it would be if the meander model described in Chapter 2 was applied without modification. As will be made clear below, the helical circulation generated by the curvature of the primary flow streamlines plays a significant role in determining the morphology of alternate bars in straight channels. Thus, by including the convective accelerations in the cross-stream equation in the manner described above, a model is formulated which includes the salient physical

processes active in both low and high sinuosity channels.

The above solution for the cross-stream velocity may be used along with the similarity streamwise velocity to calculate the forcing terms originally set to zero in the vertically-averaged equations. If these terms are calculated and inserted in equations (3.2) and (3.3), the resulting solutions for the boundary shear stress and vertically-averaged velocity will include the effects of helical redistribution of streamwise momentum. Although this effect may only be important in few, if any, natural streams, it has been shown to be operative in certain specialized laboratory experiments. For example, in extremely long bends with constant curvature and no streamwise bathymetric variations, this effect is responsible for the tendency of the high velocity core to move toward the outer bank as the bend is traversed. In general, however, this weak effect is totally overwhelmed by convective accelerations stemming from the streamwise nonuniformity present in most natural streams.

There is also a vertical structure equation describing the deviations of the streamwise velocity and stress from the similarity profiles. This equation predicts changes in the streamwise vertical structure associated with accelerations and decelerations, as well as with the redistribution of downstream momentum by the helical component of cross-stream velocity. Although this equation may be solved via simple vertical integrations, as in the case of equation (3.20), there are important physical implications which must be considered. By bringing in this equation, a perturbation streamwise stress is produced. Unlike the bottom stress that is predicted by the vertically-averaged solution, this perturbation stress is not phase locked to the vertically-averaged velocity field. This allows the prediction of bedform instabilities, as explained by Smith (1970). Since the primary aim of this chapter is to investigate the formation and evolution of bars, there is some disadvantage in adding this complicating effect. Furthermore, it is not at all clear that the assumption of local

equilibrium used in the turbulence closure is accurate enough to be employed in predicting the streamwise perturbation velocity and stress. Wake effects must be present in flow over bars, and the spatial adjustments in the turbulence field may be as important as accelerations and decelerations in setting the deviation vertical structure for the streamwise flow. One possible rectification of this last problem is to formulate a higher order closure wherein the similarity flow structure is used to advect the turbulence field and thereby calculate the errors associated with the simple eddy viscosity formulation. Thus, the simple eddy viscosity is used at lowest order, but a $k-\varepsilon$ type formulation is used to correct this assumption at next order. This would allow the decoupling of the momentum equations from the equations describing the advection of the length and velocity scales of the turbulence, an enormous numerical advantage. However, before applying this technique, physical insight into the interaction of wake turbulence and the vertical flow structure is highly desirable, which succinctly describes the original motivation for the work presented in Chapter 4 of this dissertation. At any rate, the equation for the perturbation velocity and stress in the streamwise direction is not solved here for two reasons. First, it is advantageous to consider the bar problem completely separate from the bedform problem and second, the accurate treatment of some of the effects appearing in this equation may require a more sophisticated turbulence closure than that employed herein.

In summary, all flow calculations presented in this chapter are based on the numerical solution of equations (3.11), (3.12), and (3.13). These solutions, which are obtained using a prescribed channel geometry, discharge, and roughness distribution, yield the lowest-order values for the streamwise surface slope, velocity, and boundary shear stress, as well as the value of the vertically-averaged cross-stream velocity. These values are inserted in equations (3.21) and (3.22) in order to calculate the cross-stream velocity and stress. Convective accelerations associated with streamwise nonuniformities are included in the lowest-

order downstream momentum equations, as required by a consistent scaling of the full momentum equations (as discussed in Chapters 1 and 2). The flow solutions obtained from the algorithm described may be expected to be good approximations of the flow fields present in natural channels.

3.3. The Sediment Transport Algorithm

The results of the flow model described above may be used to calculate sediment fluxes associated with bedload transport and suspended load transport. In the case of bedload transport, in which case the particles making up the bed travel by rolling or saltation, the sediment fluxes are calculated using an bedload equation. This empirical equation predicts the flux given the particle size, the critical shear stress τ_c, and the skin friction boundary shear stress acting on the bed. For the case of transport by in suspension, the sediment fluxes must be found by the numerical solution of an advective-diffusion equation employing the diffusivities and velocities from the flow model. This requires knowledge of the settling velocities of the particles in suspension, which may be found using the results of Dietrich (1982). Specification of a reference flux lower boundary condition, wherein the upward flux of particles off the bed into suspension is calculated as a function of the boundary shear stress, is also a requisite part of this technique. The solution of the advection-diffusion equation will yield both the horizontal and vertical distribution of suspended sediment, as well as the exchange of sediment with the bed (i.e., the erosion and deposition). In cases where the vertical stratification of the water column by sediment is large enough to damp the turbulence in the flow, a stratification correction such as that presented by Smith and McLean (1977) and subsequently tested by Gelfenbaum and Smith (1987) must be employed and the flow and suspended sediment models must be coupled iteratively. In the

present work, the evolution of bed morphology in the case where sediment transport occurs exclusively as bedload is examined; however, it is important to note that the approach described is of general validity, and may be extended to the case of mixed or suspended load transport.

The results presented in this paper are based on the use of the bedload equation presented by Yalin (1963) in conjunction with a simple algorithm for including the effect of bed slope on the sediment fluxes. If τ_{SF} is the magnitude of the vector skin friction boundary shear stress on the bed, then the sediment flux in the vector direction of the stress is given by the Yalin equation as

$$Q_{tot} = 0.635 \left[\frac{\tau_{SF}}{\rho}\right]^{\frac{1}{2}} DS \left[1 - \frac{1}{\gamma S}\ln(1 + \gamma S)\right] \qquad (3.23)$$

where D is the particle diameter, S is the local excess shear stress defined by $(\tau_{SF} - \tau_c)/\tau_c$, and $\gamma = 2.45 \ (\rho_s/\rho)^{-0.4} \ (\tau_c/(\rho_s - \rho)gD)^{0.5}$. The variables ρ and ρ_s are the density of the fluid and the sediment, respectively, and are taken to be 1.0 gm/cm^3 and 2.65 gm/cm^3 .

For the case in which the downstream bottom stress is much greater than the cross-stream value, as is consistent with the model scaling presented above and with measurements made in natural rivers and streams, the components of the vector sediment flux in the cross- and streamwise directions are given by

$$Q_s = 0.635 \left[\frac{(\tau_s)_{SF}}{\rho}\right]^{\frac{1}{2}} DS \left[1 - \frac{1}{\gamma S}\ln(1 + \gamma S)\right] \qquad (3.24)$$

and

$$Q_n = 0.635 \left[\frac{(\tau_n)_{SF}}{\rho} \right]^{\frac{1}{2}} \left[\frac{(\tau_n)_{SF}}{(\tau_s)_{SF}} \right]^{\frac{1}{2}} DS \left[1 - \frac{1}{\gamma S} \ln(1 + \gamma S) \right] \tag{3.25}$$

where the subscripts n and s refer to the streamwise and cross-stream direction, respectively, and $(\tau_s)_{SF}$ and $(\tau_n)_{SF}$ are the downstream and cross-stream skin friction boundary shear stresses. In the sense used here, "skin friction" denotes the value of the boundary shear stress after the form drag associated with various types of channel irregularities has been removed (see Chapter 2).

If the actual bottom stress values predicted by the flow model are inserted in equations (3.24) and (3.25), the calculated sediment fluxes will not include the modification of those fluxes by gravitational forces, since the bedload equation does not take the effect of bed slope into account. The slope effect is expected to be relatively large in cases where the boundary shear stress is only slightly larger than the critical shear stress for the initiation of particle motion (i.e., low transport stages). This is due to the fact that, at these low transport stages, sediment particles tend to roll, rather than saltate, and therefore remain in contact with the bed most of the time (Wiberg and Smith, 1985). Conversely, we expect the gravitational correction to be relatively small in the case of saltation (higher transport stages), wherein the direction of travel of the moving particle is almost entirely determined by the direction of flow. While the actual numerical error incurred by neglecting the effect of bed slope may be negligible compared to the total sediment flux, the small variation in the direction of the sediment flux vector on the bed can be important in the calculation of stable channel morphologies, especially in the case of low transport stages.

The effect of gravitational effects on bedload sediment fluxes is often invoked in the case of well-developed bend flow. In this situation, which has been studied in detail both experimentally and theoretically (Rozovskii, 1957; Engelund, 1974; Odgaard, 1981),

channels bends are approximated as circular arcs and bathymetry is assumed to vary only in the cross-stream direction. The constraints that streamwise changes in the radius of curvature and topography are negligible are typically satisfied only near the apices of very long meander bends, and are inappropriate in many reaches of natural channels. However, this relatively simple case does demonstrate the importance of gravitational effects. In the meander coordinate system described above, the equation relating bedload sediment fluxes on the bed to the rate of erosion and deposition is given by

$$\frac{\partial B}{\partial t} = -\frac{1}{c_B}\left[\nabla \cdot \vec{Q}\right] = -\frac{1}{c_B}\left[\frac{1}{1-N}\frac{\partial Q_s}{\partial s} + \frac{\partial Q_n}{\partial n} - \frac{Q_n}{(1-N)R}\right] \tag{3.26}$$

where B denotes the elevation of the bed with respect to an arbitrary datum and where c_B is the concentration of sediment in the bed ($c_b \approx .65$). If the bed is in equilibrium, the left-hand side of equation (3.26) will be zero. Furthermore, for the case of well-developed bend flow, all derivatives with respect to s will be zero, since there is no streamwise variation in the flow. For this case, equation (3.26) reduces to a simple first-order ordinary differential equation for Q_n. Applying the boundary condition that there be no sediment flux at the stream bank yields the result that, if the bed of a well-developed bend is stable, Q_n must everywhere be equal to zero. However, noting that v_* is zero for the case of well-developed bend flow, it is easy to see from equation (3.22) that the cross-stream bottom stress will always be non-zero and directed toward the inner bank.

This result appears paradoxical. The boundary shear stress and the resulting sediment flux clearly have an cross-stream component directed toward the inner bank; however, the stability criterion requires that the cross-stream sediment flux be zero. This calculation indicates that there will continuously be a flux of sediment away from the pool side bank and

toward the inner or point bar side bank, resulting in an ever-deepening pool and a point bar which grows until the critical shear stress is not exceeded at its top. In reality, the pool will deepen and the point bar grow only until the gravitational effect associated with the sloping face of the point bar is great enough to make $Q_n = 0$. This line of reasoning leads to the conclusion that the bar is stable when the fluid drag force up the face of the bar (toward the inner bank) is precisely balanced by the gravitational force down the face of the point bar, a balance that has been used extensively in simple models of point bar stability in the case of well-developed bend flow (cf. Engelund, 1974; Zimmerman and Kennedy, 1978). It is crucial to note that this balance is obtained only in the very special and restricted case of well-developed bend flow; in most natural channels, the presence of streamwise nonuniformity, troughwise flow in the lee of bedforms, and multiple grain sizes may invalidate this result, as discussed by Dietrich (1982). Nevertheless, the gravitational modification of the sediment flux on the bed can be of considerable importance in the determination of the stable channel morphology. Simply inserting the boundary shear stresses obtained from the flow model into the bedload equation neglects this effect and is undesirable for the work presented here.

To include the effects of bar and bank slopes in the calculations of channel evolution, the gravitational forces acting on sediment particles are parameterized in terms of an equivalent gravitational shear stress vector, $\vec{\tau}_g$. This psuedo-stress is defined as a vector in the local plane of the bed directed along the line of steepest descent. On a slope equal to the bulk angle of repose of the sediment ($\phi_0 \approx 30^\circ$), the gravitational psuedo-stress is required to be equal to the critical shear stress. Thus, even if there is no fluid mechanical shear stress acting on the sediment particles, motion will occur if the slope of the bed is greater than the bulk angle of repose. Using the fact that $\vec{\tau}_g = 0$ on a flat bed and postulating that $\vec{\tau}_g$, like the gravitational force, depends linearly upon the sine of the angle of bed

slope, one obtains

$$\vec{\tau}_g = \tau_c \frac{\sin\alpha_0}{\sin\phi_0} \frac{\nabla B}{|\nabla B|}$$

(3.27)

where

$$\alpha_0 = Arctan\Big[|\nabla B|\Big]$$

(3.28)

If water surface slopes are much less than the local slopes of the bottom topography, as is often the case in natural alluvial streams and rivers, then B, the bed elevation, may be replaced by h, the local flow depth, in equations (3.27) and (3.28).

To include the gravitational psuedo-stress vector in calculations of bedload sediment fluxes, this quantity is added in a vector sense to the fluid dynamical boundary shear stress predicted by the flow model. This is shown in schematic form in Figure 3.1. The resulting bottom stress vector is used to calculate sediment fluxes on the bed from equations (3.24) and (3.25). By using the generalized vector form for $\vec{\tau}_g$, this model explicitly treats the effect of bed slopes in both the streamwise and cross-stream directions. For example, if the fluid dynamical boundary shear stress is oriented in the direction of steepest descent on a sloped bed, the addition of $\vec{\tau}_g$ produces an enhanced sediment flux in that direction, as is physically appropriate. This effect is not included in models for making gravitational corrections to sediment fluxes which consider only the slope of the bed perpendicular to the flow direction (e.g., Odgaard, 1981; Kikkawa et al., 1976; Parker, 1978). In addition, this simple approach only requires the specification of two relatively well-known empirical constants, the bulk angle of repose and the critical shear stress. This model has also been
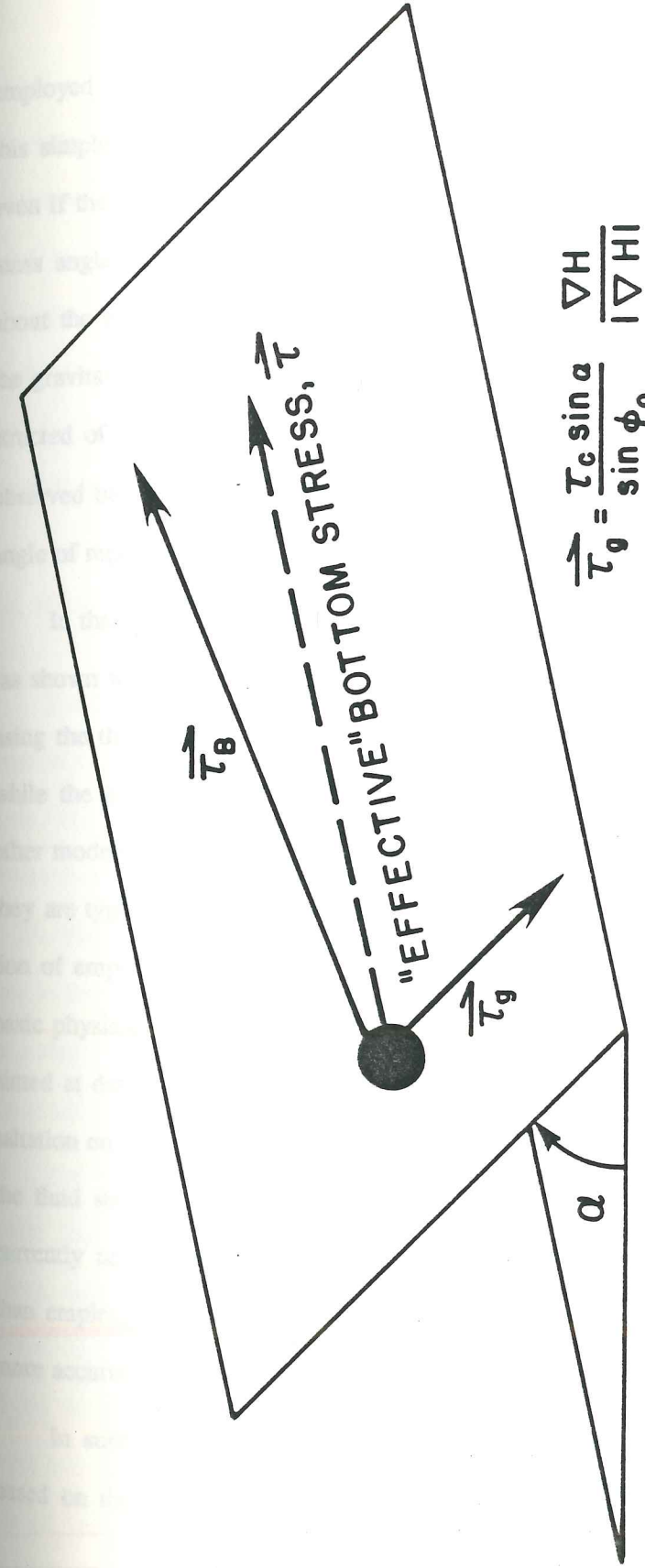
Figure 3.1. Schematic diagram of the gravitational pseudo-stress vector used in the gravitational correction.

employed for investigating the migration of channel banks. If the bank slope exceeds 30°, this simple gravitational correction will predict some small sediment flux down the bank, even if the fluid stress is zero. This flux continues until the bank slope is decreased to the mass angle of repose. Thus, this model has the effect of maintaining the bank slopes at about the mass angle of repose. For cases in which stabilized vertical banks are present, the gravitational psuedo-stress is set equal to zero, but in the case where the banks are constructed of cohesive (but not fully stabilized) material, the value of ϕ_0 is set equal to the observed bank angle. Thus, the cohesivity of the banks is characterized entirely by the bulk angle of repose.

In the results presented here, the critical shear stress is set using the results of Shields [as shown in Wiberg and Smith, 1985] for the case of a single grain size, and is specified using the theoretical model of Wiberg and Smith [1987] for the case of mixed grain sizes, while the bulk angle of repose is taken to be 30° for noncohesive sediment. Although other models for making slope corrections to sediment fluxes are available in the literature, they are typically more complicated than the one offered here, often rely on the determination of empirical constants which are specific to each application, and do not address the basic physical problem in a mechanistic manner. Clearly, future work in this area must be aimed at developing a theoretical model for calculating sediment fluxes due to rolling and saltation on an arbitrarily-sloping (i.e., sloping both in the direction of and perpendicular to the fluid stress vector) bed made up of natural grains. Because results of this nature are currently unavailable, the simple, well-defined technique discussed above is used, rather than employing techniques with more degrees of freedom which, although they may yield more accurate results in specific cases, parameterize the physical processes incorrectly.

In summary, the sediment transport algorithm employed in the evolution model is based on the calculation of streamwise and cross-stream sediment fluxes using equations

(3.24) and (3.25). The components of the stress used in these equations are calculated from the vector sum of the fluid dynamical boundary shear stress predicted by the numerical model and a gravitational psuedo-stress, given by equations (3.27) and (3.28). The calculated sediment fluxes are inserted in equation (3.26) in order to determine the rate of change of bed elevation. These erosion and deposition rates predict the temporal evolution of the bed topography. By using suitably small time increments, this calculation can be used to predict the adjustment of the channel to an equilibrium condition, as described in the introduction to this chapter.

3.4. Evolution and Stability of Point Bars

The salient features of point bar development on a flat bed are related to the fact that channel curvature forces both streamwise and cross-stream convergences of sediment transport. The cross-stream sediment convergences and divergences are initially forced by the production of helical circulation, as has been well-described by others (e.g., Rozovskii, 1957). The streamwise effects are produced as a result of variations of the radius of curvature in the downstream direction. This variation produces a change in the cross-stream surface slope which, due to coupling through the elevation field, inevitably forces a change in the streamwise surface slope (and boundary shear stress).

The relative importance of cross-stream divergences to streamwise divergences of sediment flux determines the position of the point bar in a curved reach. As the point bar grows, large spatial accelerations are produced as a result of the topographic nonuniformity. These play a crucial role in the finite amplitude stability. Essentially, the Bernoulli response of the flow to the point bar produces a surface elevation rise over the upper end of the point bar. This elevation change weakens the helical circulation, as well as the associated inward boundary shear stress. Thus, the point bar grows until topographic steering effects

become large enough that the flow (and sediment) is steered around the upstream end of the point bar. This idea was discussed in detail by Dietrich and Smith [1983].

In Figures 3.2 and 3.3, bottom topography and shear stress fields are shown for a typical evolution run using the finite amplitude model described above. For the case shown, the planform geometry of the channel is given by a sine-generated curve, which was identified by Langbein and Leopold [1966] as a simple shape which adequately characterizes many natural channel bends. The radius of curvature for a sine-generated curve is given by

$$R = \left[\frac{\pi \Omega}{M_0} \sin\frac{\pi s}{M_0} \right]^{-1} \tag{3.29}$$

where M_0 is the meander length along the channel centerline, s is the streamwise distance, and Ω is the angle in radians between the downvalley direction and the channel centerline at the crossings (where R is infinite). For the evolution case shown in these figures, M_0 was chosen to be twelve widths and Ω was taken as 45°. This yields a downvalley wavelength of about ten for these meander bends. The width-to-depth ratio for this test case is 12.5, the Froude number is 0.6, and the transport stage (ratio of reach-averaged skin friction shear stress to critical shear stress) is about three.

The evolution of the point bar and pool bathymetry shown in Figure 3.2 is typical of point bar formation in general. The growth of the bar on the initially flat bed is primarily produced by the convergence of sediment toward the inner bank. This convergence of sediment flux arises as a result of the production of helical circulation, as described above. The pattern of deposition is only weakly modified by the occurrence of streamwise convergences and divergences of sediment, which result from modification of the streamwise
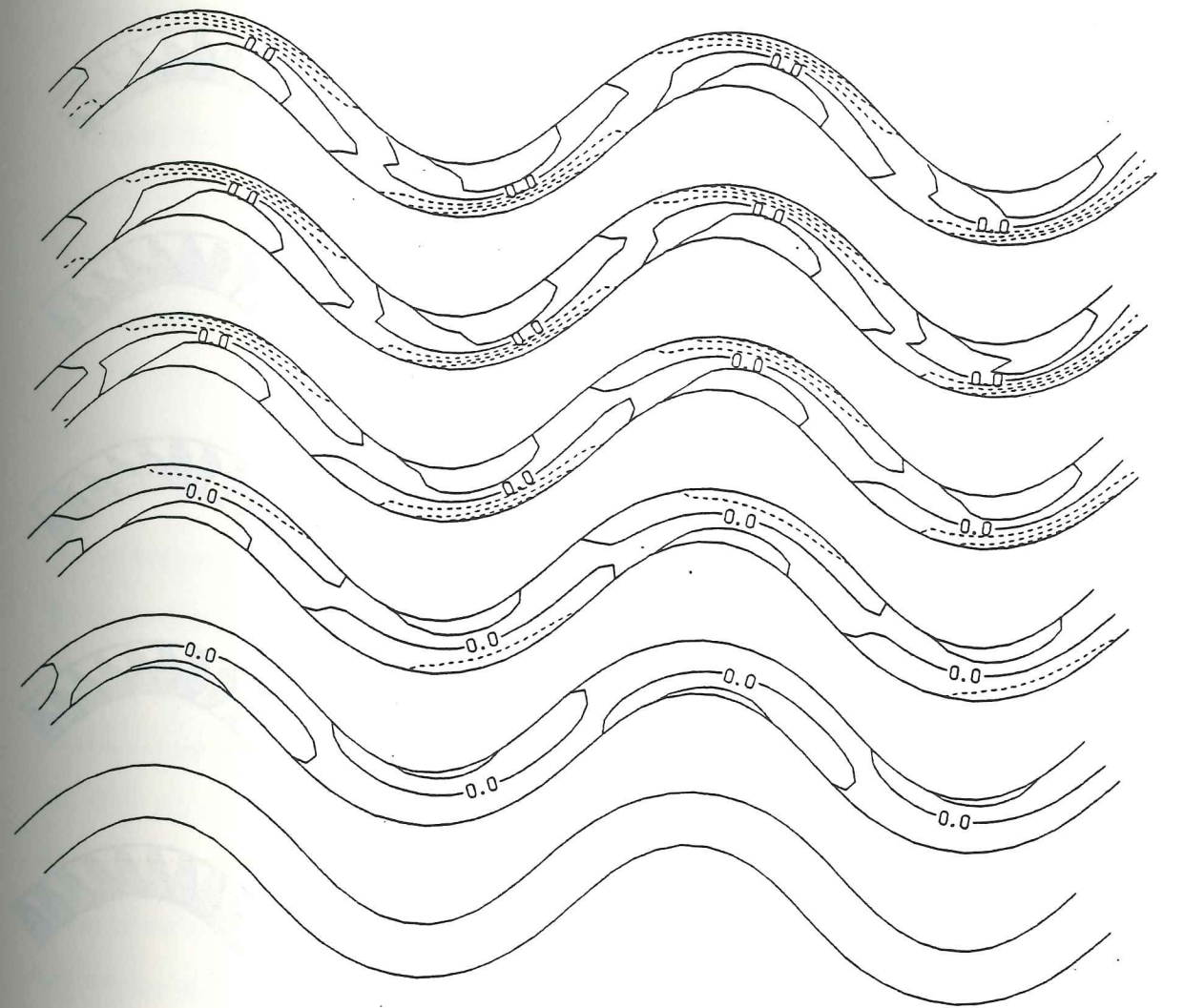
Figure 3.2. Evolution of bottom topography for a typical point bar case. The channel planform is given by a sine-generated curve with $\Omega = 45^o$, the width-to-depth ratio is 12.5, and the down-valley meander wavelength is about 10 widths. The Froude number is 0.6 and the transport stage is about 3. The contour interval is one fourth of the mean depth.
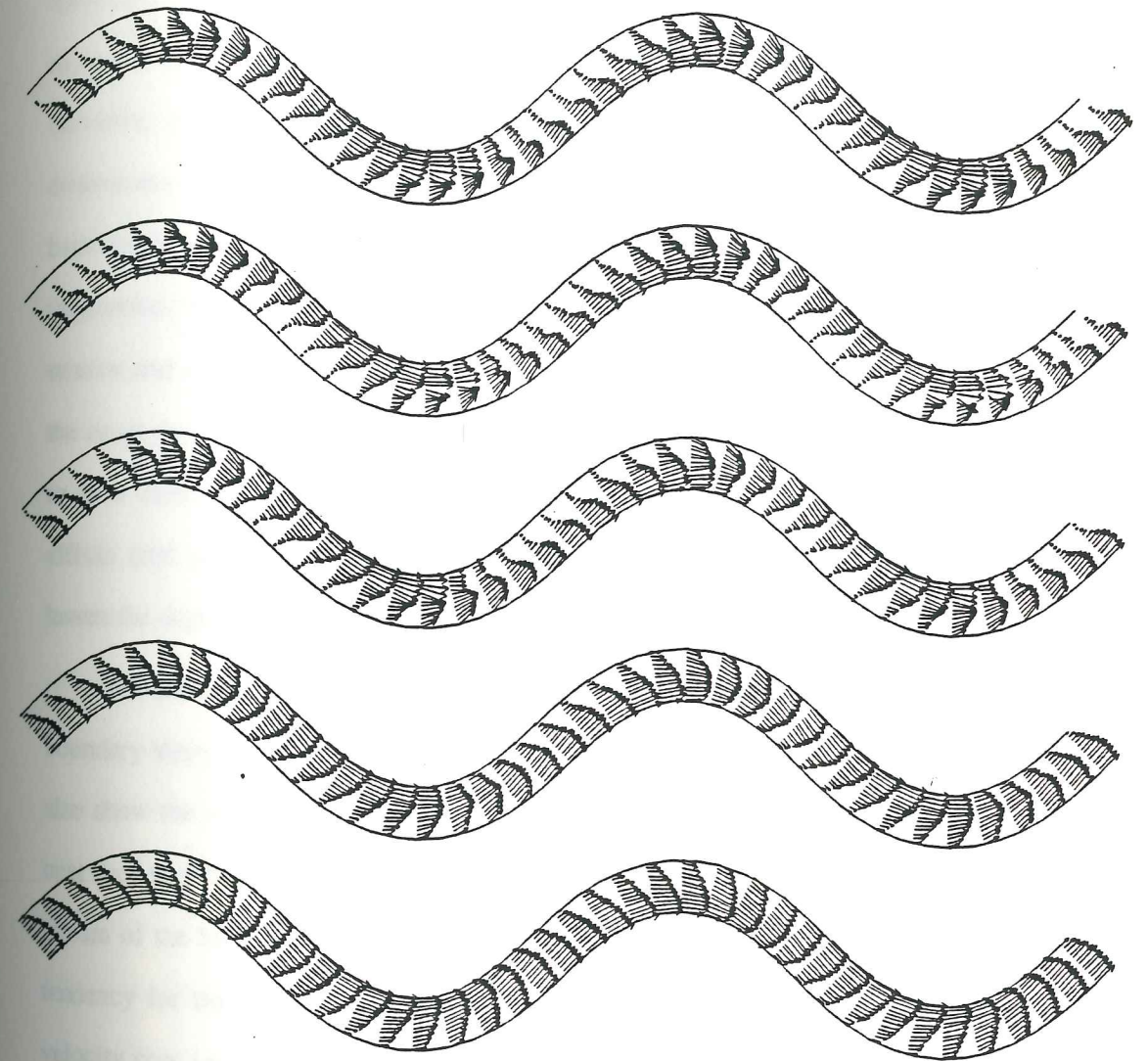
Figure 3.3. Evolution of the vector boundary shear stress field for the conditions given in Figure 3.2.

pressure field by the varying radius of curvature. If the depositional features were produced only as a result of the helical circulation (or more correctly, the cross-stream stress associated with the helical flow), the point bar would grow most rapidly at the minimum radius of curvature, which is located at the bend apex. However, the fact that the radius of curvature decreases as the apex of the bend is approached from upstream and decreases downstream of the apex results in increasing streamwise stress (erosion) near the inner bank in the upstream half of the bend, and decreasing streamwise boundary shear stress (deposition) near the inner bank in the downstream half of the bend. When this pattern of erosion and deposition is superimposed on the much larger depositional pattern induced by the cross-stream stresses all along the inner bank, the final result is that the point bar tends to grow most rapidly slightly downstream of the bend apex. In other words, the streamwise effects tend to augment point bar deposition downstream of the bend apex, and tend to lessen the deposition along the inner bank upstream of the bend apex.

The skewing of the bottom stress vectors toward the inner bank is clear in the lowest boundary shear stress map in Figure 3.3, which is for the initial flat bed. These predictions also show the streamwise variations in bottom stress discussed above, with increasing stress near the inner bank upstream of the apex, and decreasing stress along the inner bank downstream of the bend apex. The shear stress distribution on the flat bed also shows the weak tendency for the high velocity core to cross the channel. In this train of bends, the high velocity core enters each bend near the inner (point bar side) bank and slowly crosses the stream as the bend is traversed. The high velocity core does not actually cross the channel centerline until the downstream crossing is reached. This is in marked contrast to the situation found in the case of equilibrium topography.

As the point bar grows (both upward and outward), convective accelerations and modification of the surface elevation field are inevitably produced in reponse to the

topographic nonuniformity this feature presents to the flow. As described above, and in more detail by Dietrich and Smith [1983], the result of this modification is, in simplest terms, the "steering" of the flow around the point bar. This steering causes the high velocity core to cross the channel centerline further upstream and more abruptly than in the flat-bedded case, as is clear from Figure 3.3. In fact, for the equilibrium case, the high velocity core crosses the stream just downstream of the bend apex, rather than at the downstream crossing.

In Figure 3.4, expanded plots of the equilibrium bathymetry and boundary shear stress are given along with the equilibrium sediment flux field. The steering effect has important implications for the production of equilibrium morphology in channel bends. In the past, models of point bar stability have been almost exclusively based on balancing the the component of inward boundary shear stress associated with the helical circulation against a gravitational force that is directed down the face of the point bar (e.g., Allen, 1970; Engelund, 1974; Kikkawa, et al, 1976). These models are predicated on the existence of "well-developed" bend flow, wherein all streamwise variations in topography and curvature are neglected. Unfortunately, both simple scalings and measurements taken in natural streams indicate that this is commonly a very poor approximation (see Chapter 2), except perhaps in very limited segments of meander bends. The steering effect produces outward flow over the upstream end of the point bar; thus, both gravitational and fluid drag forces act to move sediment outward in this locale. Clearly, the balance producing stability in this area is one between the streamwise convergence of sediment flux and the cross-stream divergence of sediment flux, rather than a purely cross-stream balance. In other words, the steering of the high velocity core forces steering of the path of high sediment flux, as one would expect. Balancing circulation-induced inward boundary shear stress against a downslope gravitational force for a single sediment size results in particle trajectories with
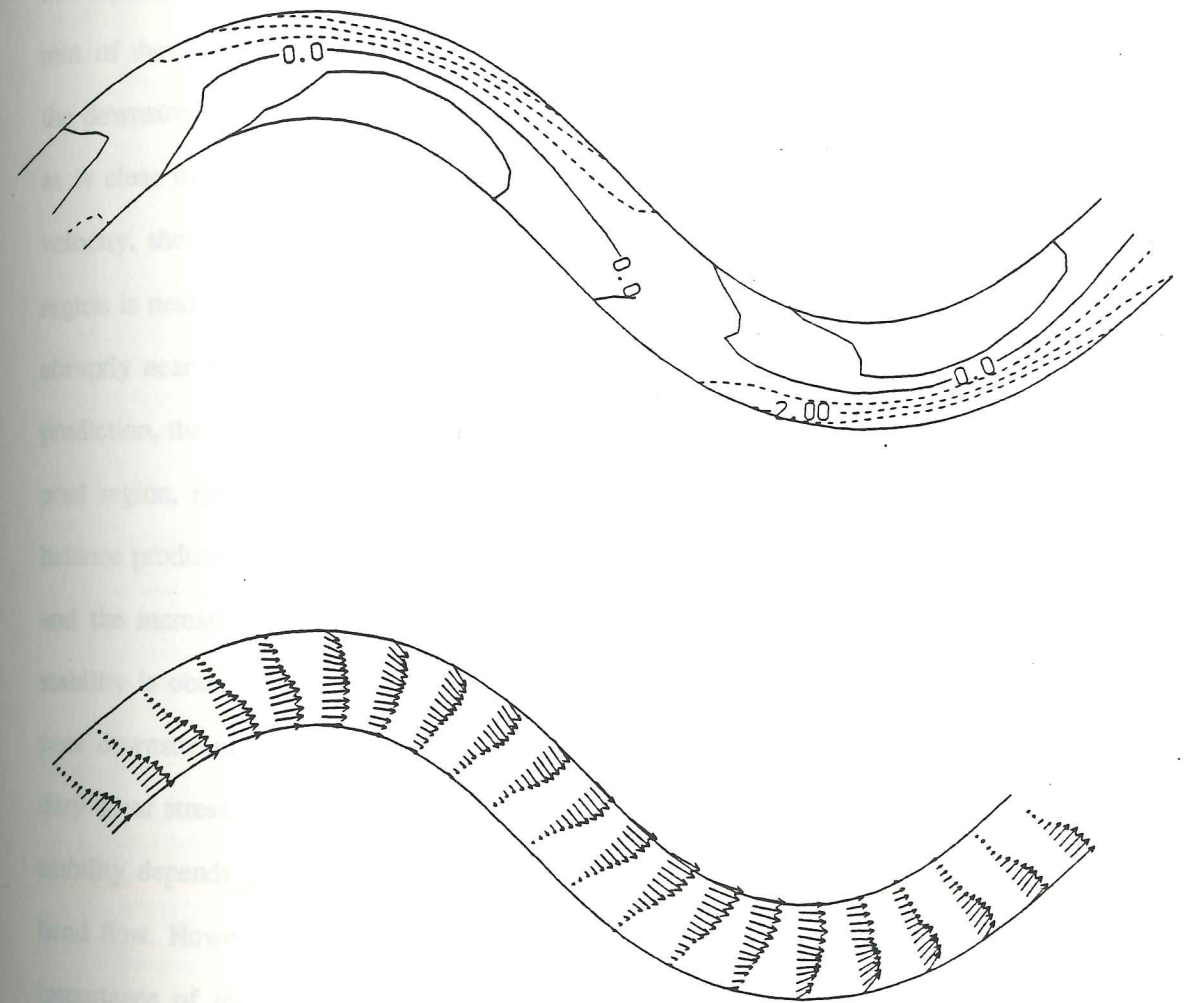
Figure 3.4. Equilibrium bathymetry and boundary shear stress calculated from the model for the conditions given in the caption of Figure 3.2.

no cross-stream component, which is inappropriate.

In Figures 3.5 and 3.6, contours of streamwise and cross-stream velocity are shown at five equally spaced sections through the predicted equilibrium bend. The section at the bottom of these plots corresponds to the upstream crossing, while the top section represents the downstream crossing. The inner bank is located on the right-hand side of these sections, as is clear from the topographic profiles. In the contours of the streamwise component of velocity, the steering of the high velocity core is readily apparent. The highest velocity region is near the inner bank at the upstream end of the bend, crosses the channel relatively abruptly near the bend apex, and exits the bend near the outer bank. In accord with this prediction, the cross-stream flow contours exhibit helical flow only in the deeper part of the pool region, rather than uniformly throughout the bend. Since the principle sediment flux balance producing equilibrium over the point bar is between the decreasing streamwise flux and the increasing cross-stream flux, gravitational effects are essentially negligible. Thus, stability is obtained with a relatively flat point bar top, as is commonly observed. In the pool downstream of the bend apex, helical circulation and an inward component of boundary shear stress is present, as is a relatively steep transverse slope. In this region, the bed stability depends primarily on the gravitational effects, as is the case in well-developed bend flow. However, this balance is restricted to a very small region of the bend, and the importance of including streamwise nonuniformity should be clear. The balance in this region is also strongly controlled by physical effects which have been included only parametrically through the gravitational correction. For example, the complex near-bed flow field induced by bedforms exerts a significant influence on the channel-scale bed morphology, as described by Dietrich [1982]. More precise predictions of channel morphology depend crucially upon the development of physical models which specifically treat the effects of bed slopes on sediment transport, both for the case when the bed is locally

107

DOWNSTREAM VELOCITY
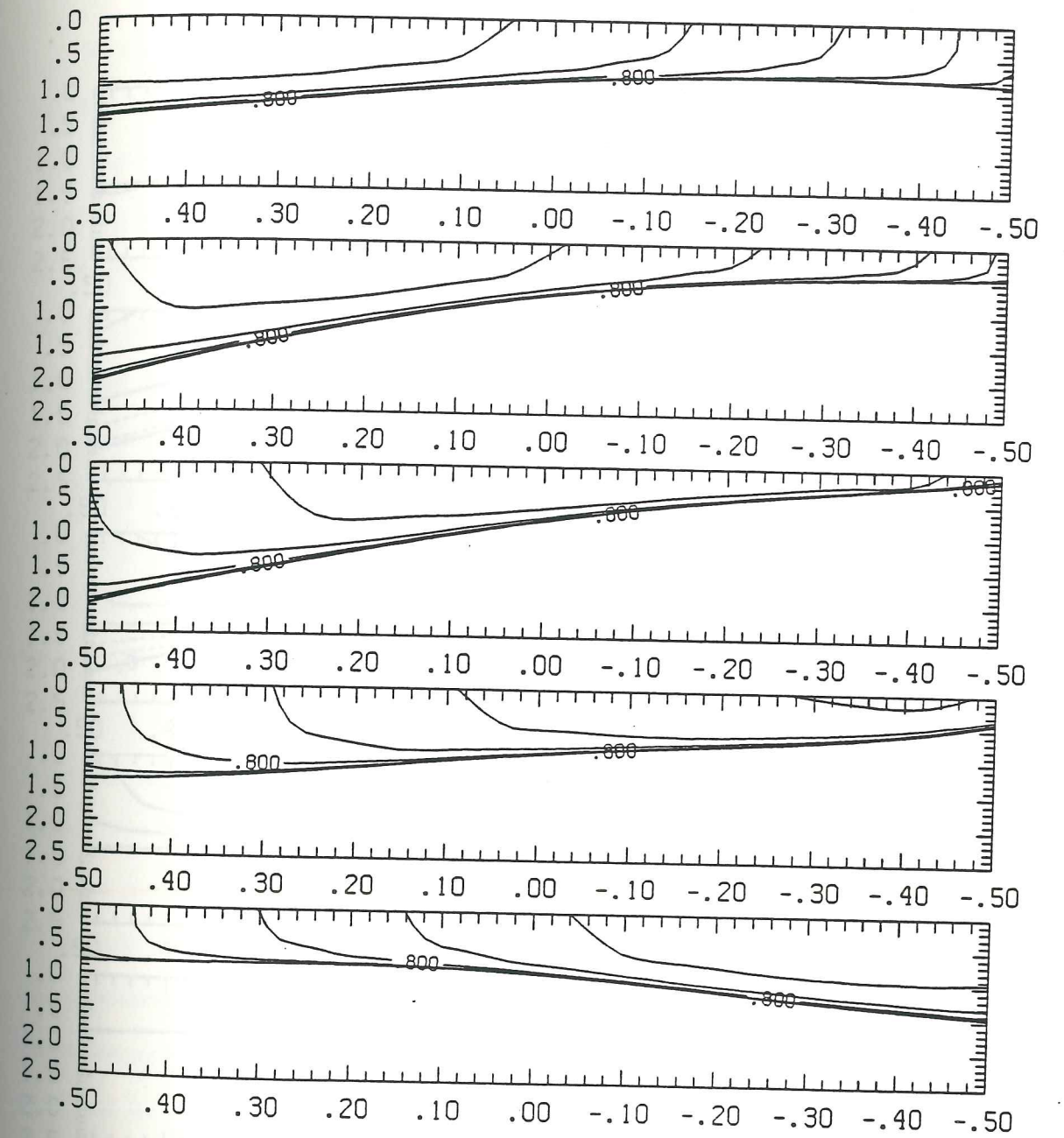
Figure 3.5. Contours of streamwise velocity at five sections in the test bend described in the text. The sections are equally spaced in the bend, with the lowest plot representing the upstream section. Velocity values are normalized by the mean velocity, and contours are drawn at intervals of 0.2. The vertical coordinate is nondimensionalized with the reach-averaged depth, and the cross-stream coordinate is normalized with the width of the channel.

CRØSS-STREAM VELØCITY
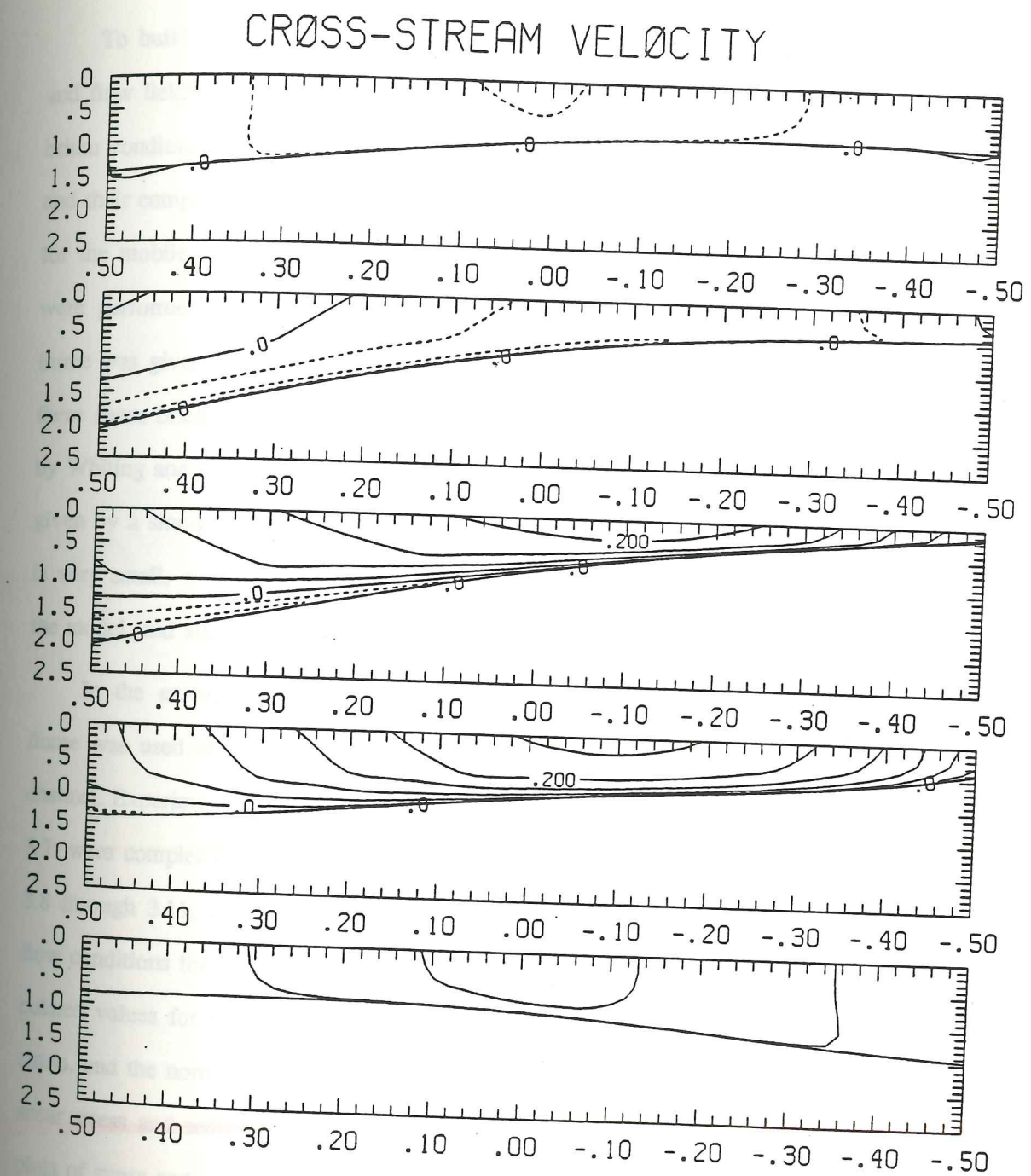

Figure 3.6. Contours of cross-stream velocity at five sections in the test bend. Velocities are normalized by the mean streamwise velocity, and contours are drawn at intervals of 0.05.

uniform and in the case when bedforms are present.

To build confidence in the evolution model, it is necessary to reproduce bathymetry and flow fields measured either in laboratory flumes or natural channels for which equilibrium conditions have been obtained. The next few paragraphs describe model predictions and their comparison to measured data for several cases. First, model predictions are made for the mobile bed experiments performed by Hooke [1974, 1975]. Hooke's experiments were performed at four different discharges in a laboratory bend. The planform of the flume was given by a sine-generated curve with $\Omega = 55^o$. After presenting and discussing these cases briefly, model predictions are shown along with experimental results obtained by Whiting and Dietrich [pers. comm.]. Like Hooke's flume, the planform of their flume is given by a sine-generated curve. However, in this latter case, the amplitude of meandering is very small, with $\Omega = 10^o$. These five different situations offer a comprehensive test of the model, and allow both its strengths and weaknesses to be examined.

In the experiments performed by Hooke [1974,1975], a mobile-bedded laboratory flume was used to investigate the adjustment to equilibrium topography in a meandering channel. Experimental runs in this laboratory bend, which is shown schematically in Figure 3.7, were completed at four different discharges: 10, 20, 35, and 50 liters/sec. In Figures 3.8 through 3.11, results of the evolution model are shown for each of these runs. The flow conditions for each run are given in the captions of these figures. The plots show calculated values for the bed topography, the helix strength, the normalized boundary shear stress, and the normalized sediment fluxes. Also included are vector plots of the boundary shear stress and sediment flux fields. The normalization factors employed in the contour plots of stress and sediment flux are the average values measured by Hooke, rather than the average of the values calculated here. Thus, these plots indicate both the spatial structure of these fields and the overall comparison with the magnitude of the measured values. To
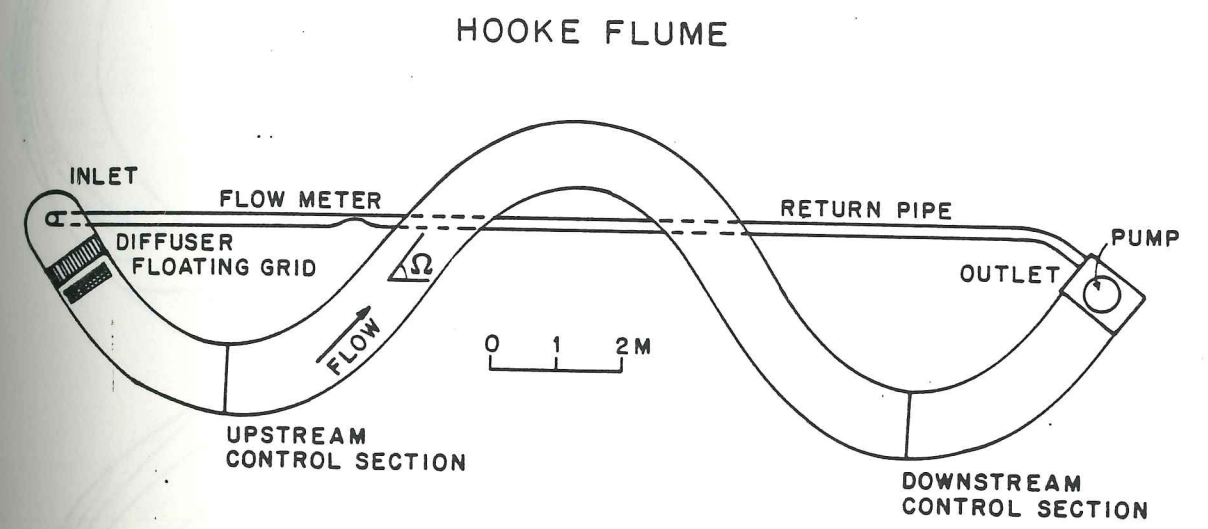
Figure 3.7. Schematic diagram of the flume used in the Hooke [1974, 1975] experiments. Note the presence of the upstream control section, which may have precluded the establishment of a "natural" upstream boundary condition.
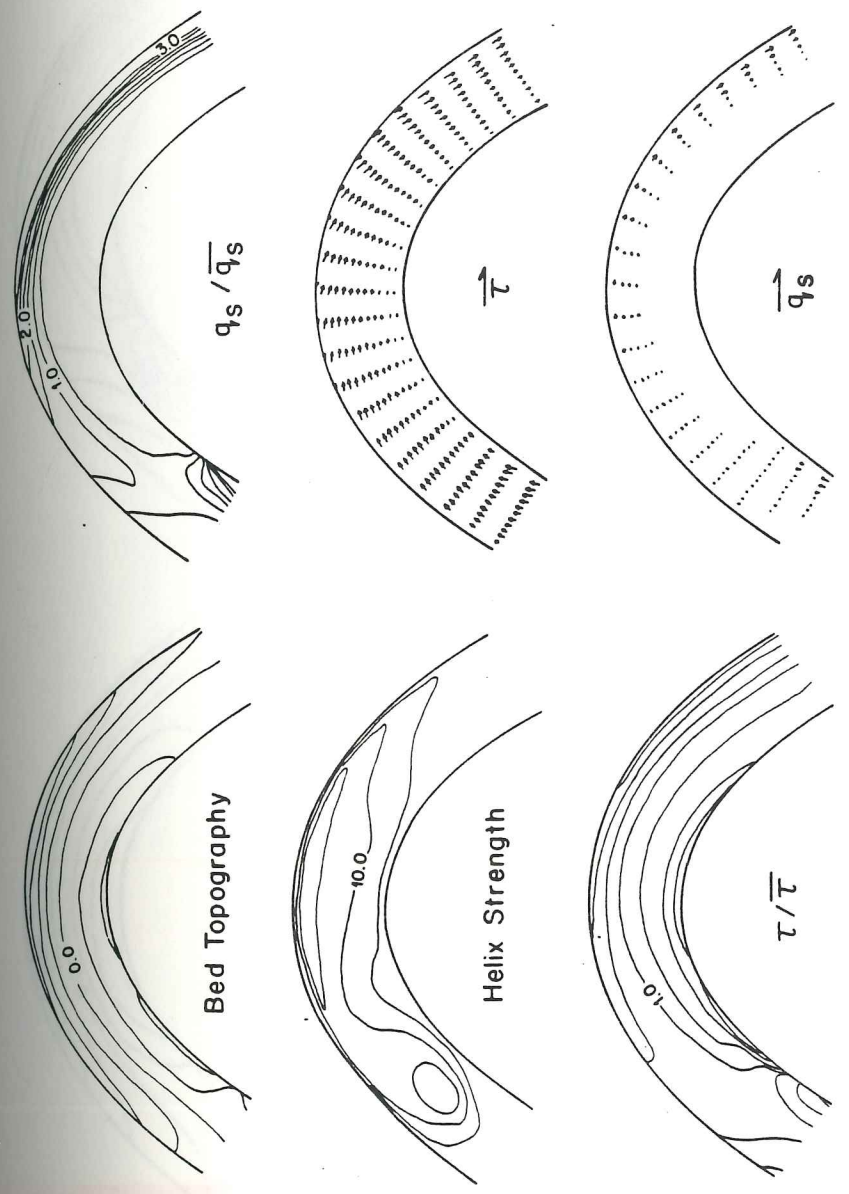
Figure 3.8. Predicted equilibrium conditions for the Hooke 10 liter/sec run. In this and the following figures, contours of topography, helix strength, normalized bottom stress, and normalized sediment flux are at intervals of 2 cm, 5°, as follows: discharge, 10 liters/sec; mean depth, 5.2 cm; mean velocity, 19.2 cm/sec; slope, .0021. Topographic contours are relative to the mean depth. Flume width and sediment size are given in all cases as 100 cm and .03 cm, respectively. Calculated values of bottom stress and sediment flux are normalized using the values measured by Hooke.
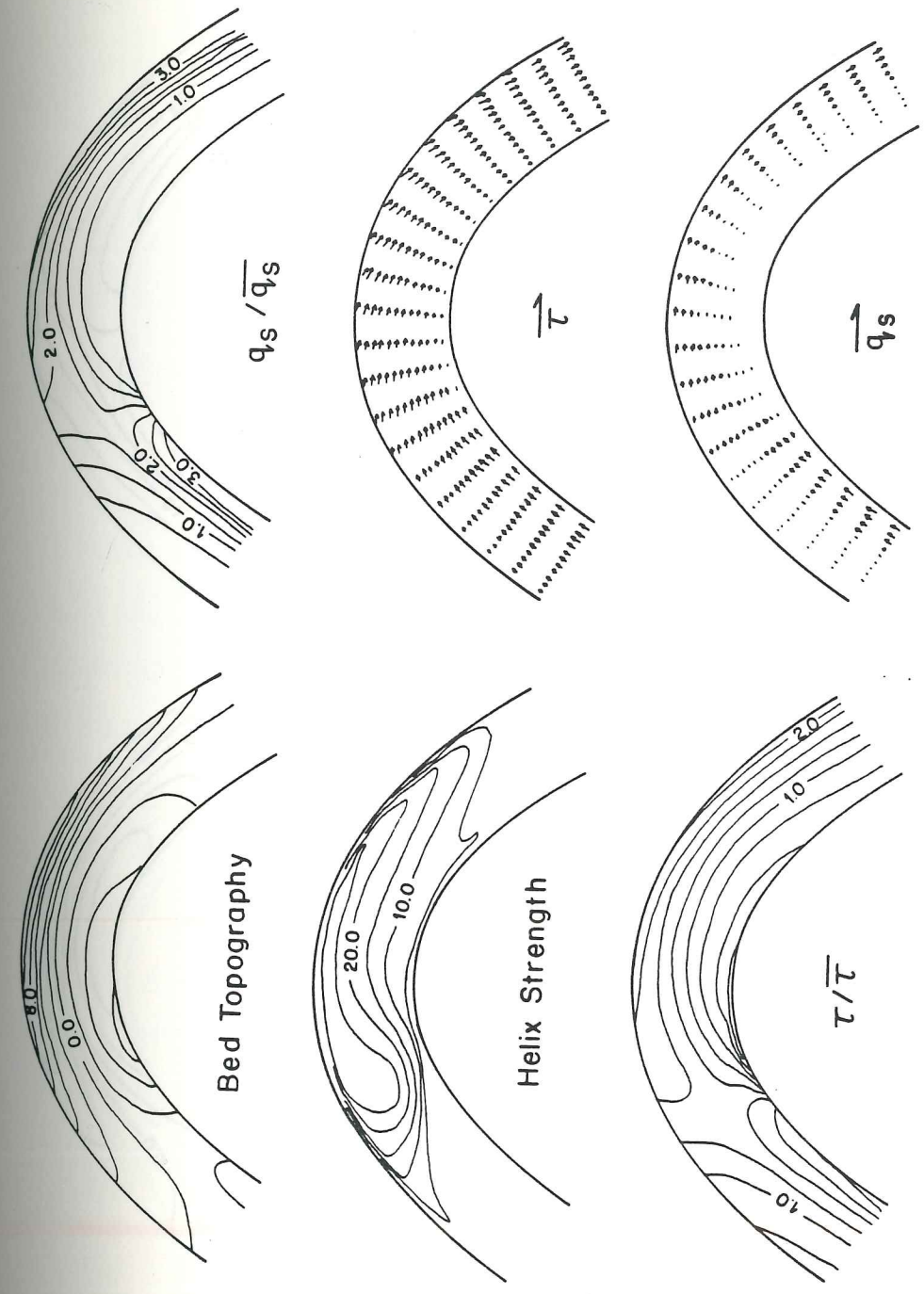
Figure 3.9. Predicted equilibrium conditions for the Hooke 20 liter/sec run. See Figure 3.8 for contour intervals. The conditions for this run were as follows: discharge, 20 liters/sec; mean depth, 7.3 cm; mean velocity, 27.5 cm/sec; slope, .0021.
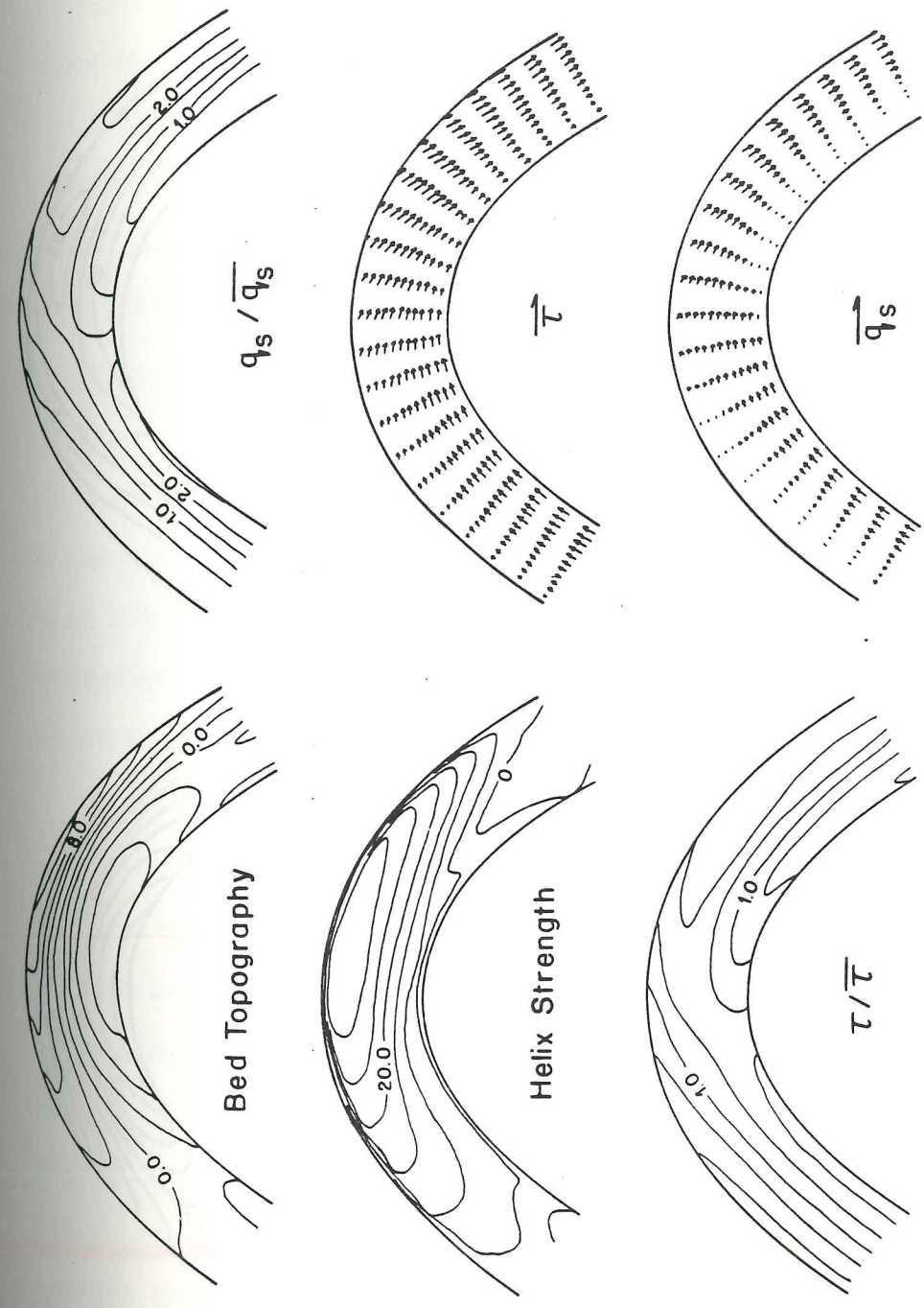
Figure 3.10. Predicted equilibrium conditions for the Hooke 35 liter/sec run. See Figure 3.8 for contour intervals. The conditions of this run were as follows: discharge, 35 liters/sec; mean depth, 9.5 cm; mean velocity, 36.8 cm/sec; slope, .0022.

Figure 3.11. Predicted equilibrium conditions for the Hooke 50 liter/sec run. See Figure 3.8 for contour intervals. The conditions for this run were as follows: discharge, 50 liters/sec; mean depth, 12.8 cm; mean velocity, 39.4 cm/sec; slope, .0022.

facilitate the comparison with Hooke's measurements, his graphs are shown in Figures 3.12 through 3.15. In these model runs, the overall roughness was constrained such that the experimental water surface slope was reproduced in the numerical solution, thus ensuring that all of the form drag effects were taken into account. This roughness was distributed spatially according to the approximation $\zeta_0 =$ constant, which is generally a good approximation (see Chapter 2). The form drag was removed from the predicted total boundary shear stress using the form drag model described in Chapter 2.

In general, the comparisons between the measured and predicted topography is reasonable. Although there are clearly some local discrepancies in each of the four cases, the only consistent difference between the predicted and measured topography is in the location of deepest scour. All of the Hooke results indicate that this point occurs slightly upstream of the apex of the bend, while the model results place this point somewhat downstream of the bend apex. This is true even when the agreement for the shape and location of the point bar is quite good, as in the 35 l/s case.

There are two potential reasons for this discrepancy, although neither of them is entirely conclusive. First, the results of the model were found assuming periodic boundary conditions and an initially flat bed in all four cases. However, as is clear from the schematic of Hooke's flume, the upstream condition in these bends probably were not representative of the situation obtained if a train of bends were located upstream of the test bend. The flow passes over a control section halfway through the bend immediately upstream, and cannot be expected to adjust to the appropriate upstream condition in only half of a meander bend. However, a computational run performed for the 35 l/s case using a uniform upstream condition half a bend upstream of the study bend still did not produce a pool as far upstream as that found in the experimental case. Further investigation was not possible without a more detailed description of the upstream conditions present in the

Figure 3.12. Experimental measurements taken by Hooke for the 10 liter/sec case. See Figure 3.8 for run conditions. Boundary shear stress and sediment fluxes were not given for this discharge. Reproduced from Hooke [1975].

$q_s / \overline{q_s}$

$\tau / \overline{\tau}$

Helix Strength

Bed Topography

Figure 3.13. Experimental measurements taken by Hooke for the 20 liter/sec case. See Figure 3.9 for run conditions. Reproduced from Hooke [1975].

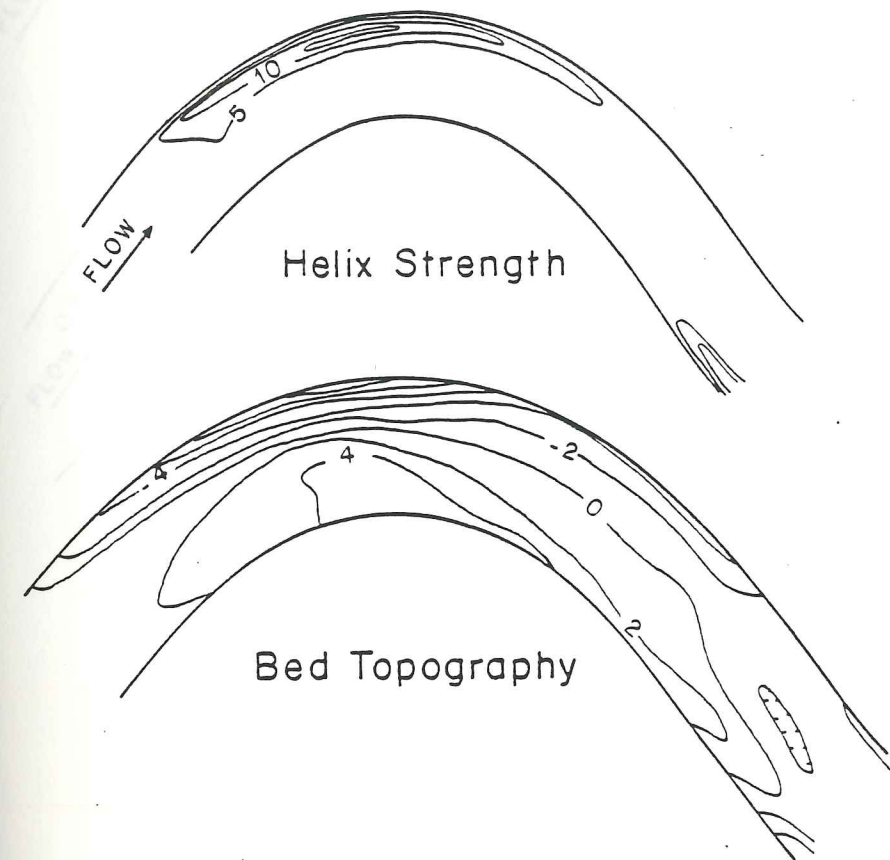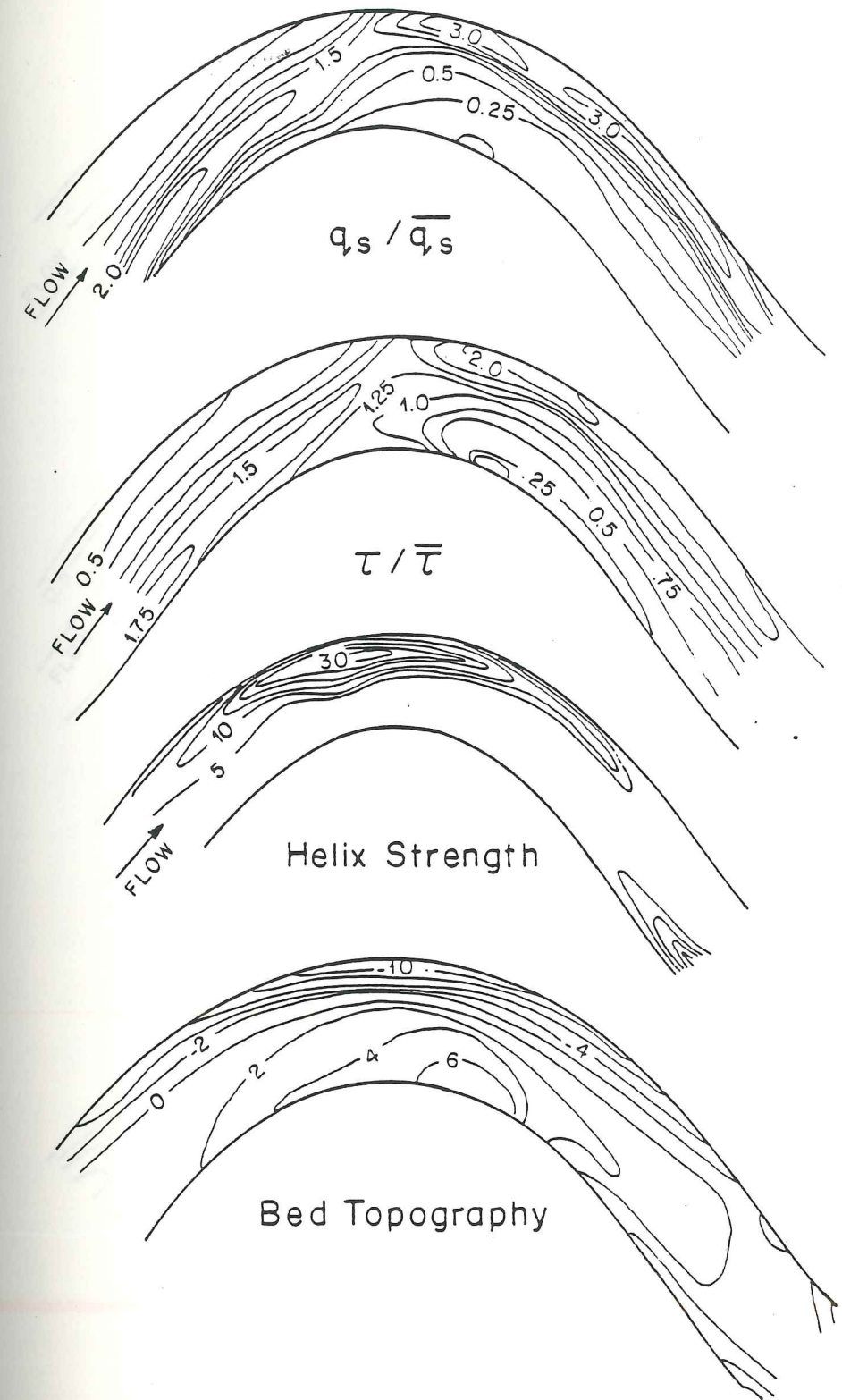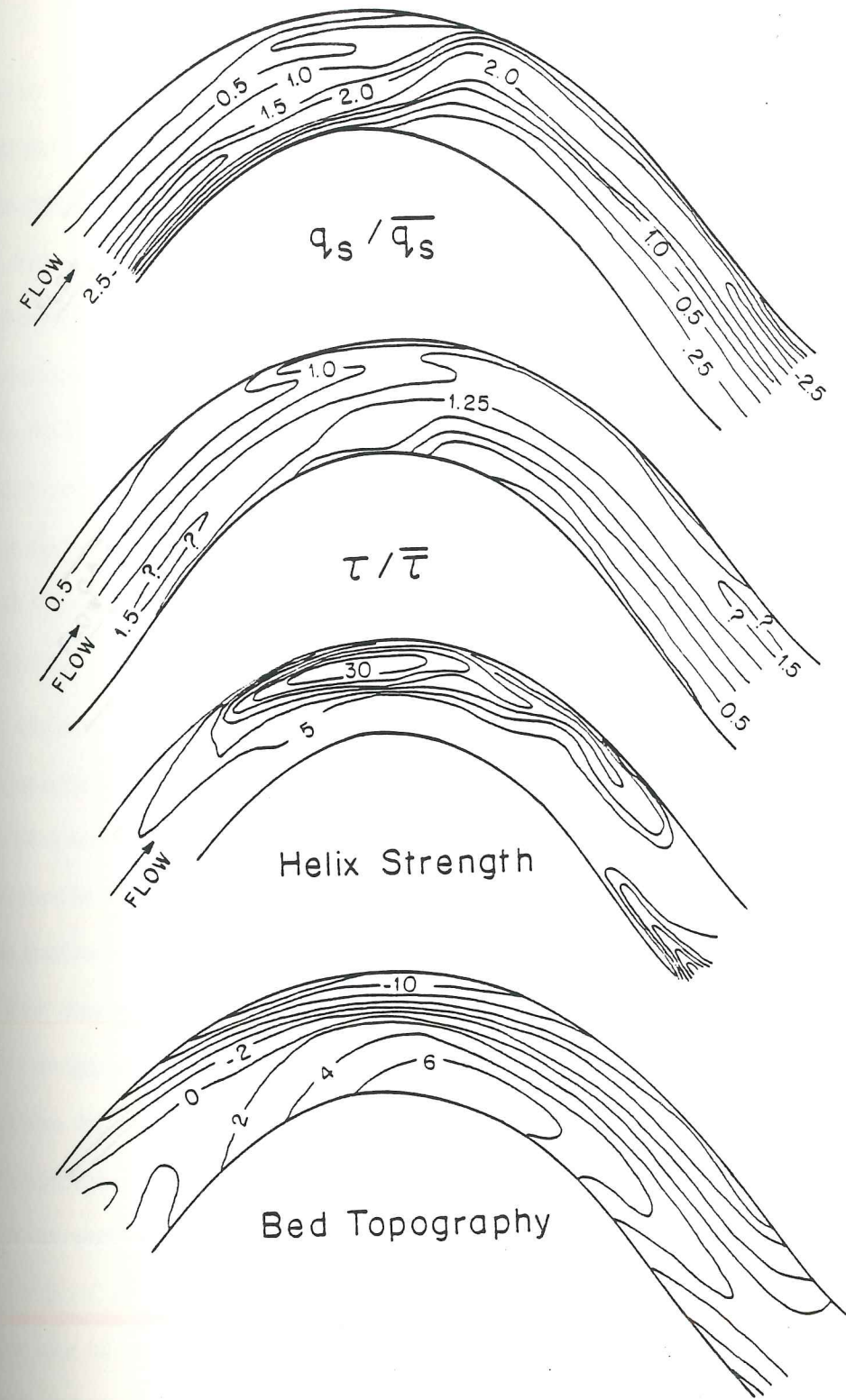Figure 3.14. Experimental measurements taken by Hooke for the 35 liter/sec case. See Figure 3.10 for run conditions. Reproduced from Hooke [1975].
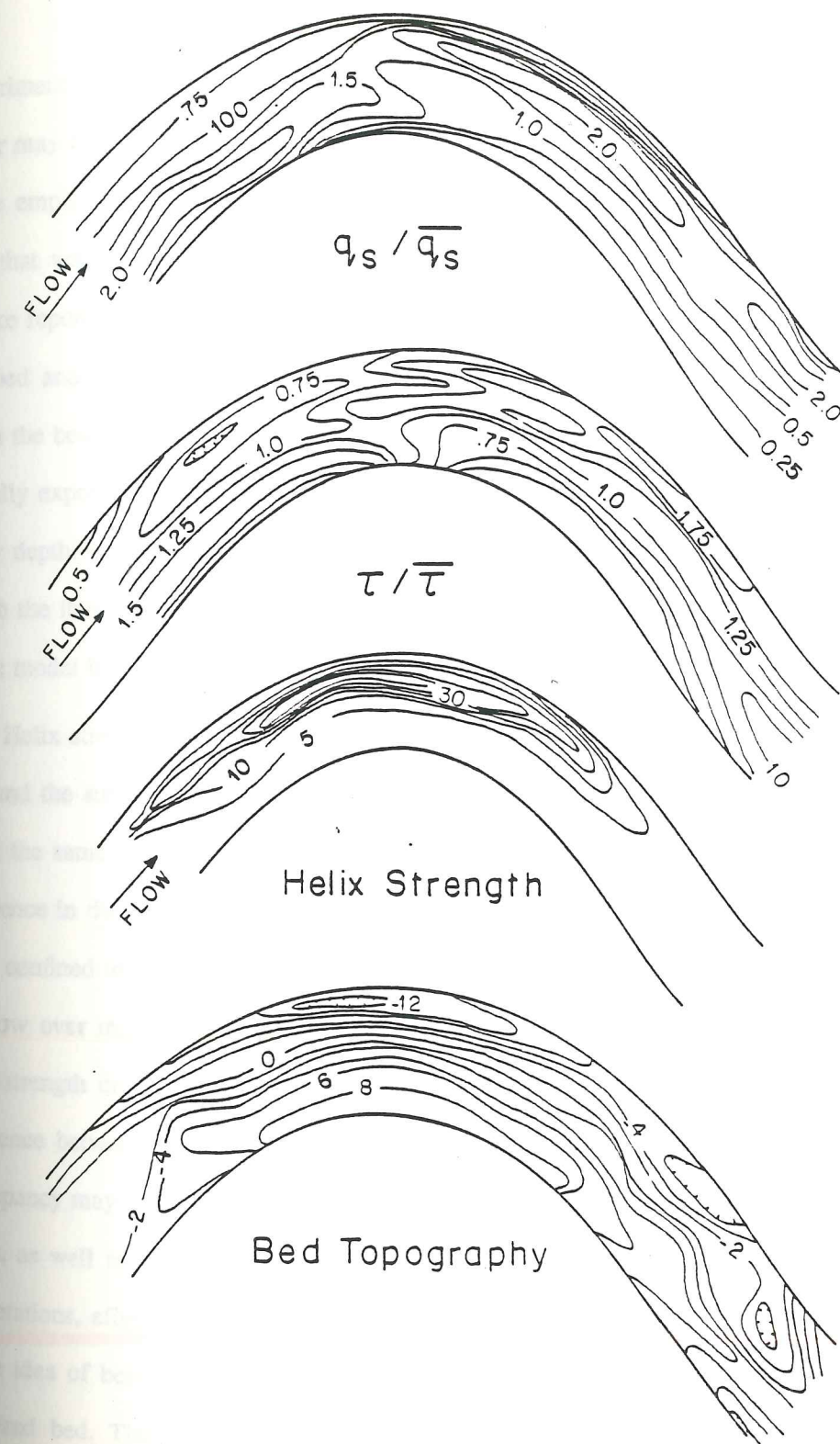
Figure 3.15. Experimental measurements taken by Hooke for the 50 liter/sec case. See Figure 3.11 for run conditions. Reproduced from Hooke [1975].

experimental runs. Another possible reason for the difference in the position of maximum scour may be that the initial bed conditions for the experimental runs were not the same as those employed in the calculations. Computed evolution sequences began with an initial bed that was completely flat. This was probably not the case in the experiments, since Hooke reports that a rounded radius was constructed of cement at the intersection between the bed and the outer bank. Furthermore, he reports that this region was often exposed when the bed reached equilibrium and, in fact, that the cement floor of the flume was occasionally exposed in dune troughs. Thus, there may have been some external control on the scour depth. In the computations, the scour depth was not allowed to exceed the depth at which the flume bottom would be exposed, but this end result may not have been achieved in the model in the same manner as in the flume.

Helix strength is defined as the angular difference between the near-bed velocity vectors and the surface velocity vectors. In general, the predicted values of helix strength are about the same in maximum amplitude as those measured. However, there is a consistent difference in the spatial distribution of helicity. In the measurements, the helical flow tends to be confined to the region near the outer bank, while the calculations tend to predict helical flow over most of the point bar. It is important to point out that a positive value of helix strength does not imply inward flow near the bottom, since this represents only the difference between the angular orientations of near-bed and surface velocities. The noted discrepancy may be at least partially associated with the near-bed flow modification by bedforms, as well as changes in streamwise vertical structure due to spatial accelerations and decelerations, effects that were not included in the fluid dynamical model. Credence is led to the idea of bedforms effecting the flow by measurements Hooke made of flow over a stabilized bed. The bedforms were removed from the bed before stabilization, so their effect on the helical flow was removed. Measurements over the smoothed, immobile bed

showed higher helix strength present over a larger portion of the bend than found in an identical case where bedforms were present. However, some of these differences may also be associated with the difficulty in measuring small angular deviations in the flow over the water depth. Hooke estimated that the error in these measurements varied from $\pm 1^o$ to $\pm 5^o$, depending on the turbulence level. The face of the point bar was covered with bedforms, so it may have been quite difficult to make accurate measurements in this region due to the boils. If the measurements were only accurate to $\pm 5^o$, the lower values of helix strength may have been essentially unobservable. However, this helicity may explain the location of the scour pool in the measurements relative to the predictions, and certainly should not be discounted. At present, this issue can probably be resolved only experimentally, or perhaps by inclusion of the streamwise vertical structure changes in the model.

Overall, the agreement between the predicted bottom stress and sediment fluxes and those measured is quite good. The most notable differences are associated with lateral boundary layer effects. Typically, the numerical results predict high stresses (and sediment fluxes) right up to the bank whereas the measurements show the maxima to be slightly away from the bank. This is not surprising, since the development presented herein neglects the momentum exchanges associated with lateral friction. A careful treatment of the lateral boundary layers requires both consideration of the lateral diffusion of momentum by turbulence and the characterization of bank roughness. This task is not part of this dissertation, although it is clear that these effects must be considered in the future if this model is to be extended to investigate planform evolution of channels.

Although there are clearly some discrepancies which point out important areas of research in the future, the comparison to Hooke's measurements indicates the power of the evolution technique. In order to explore the predictions of the model in a somewhat different case, model runs were also done for the low amplitude meander bends studied by

Whiting and Dietrich [pers. comm.]. As shown in Figure 3.16, the flume planform for this experiment was given by a sine-generated curve with $\Omega = 10^\circ$. Various other geometric and dynamic parameters pertinent to Whiting and Dietrich's run S-25 are also given in Figure 3.16. In contrast to Hooke's flume, which had a bend wavelength of about 10.5 widths, this experiment was performed with a bend wavelength of only 8 widths. Furthermore, while the ratio of minimum radius of curvature to width in the Hooke flume was 2.2, this parameter was 7.3 in the Whiting and Dietrich experiment. Thus, one expects streamwise variations in boundary shear stress and sediment flux to be larger relative to cross-stream effects in the Whiting and Dietrich case than in the Hooke case.

In Figure 3.17, the predicted topographic evolution of run S-25 is presented. The initial bed was taken to be flat and, since significant bedforms were absent, form drag effects were neglected. Equilibrium topography was predicted to occur after roughly one hour in this small scale experiment. As expected from the simple scalings in the previous paragraph, the point bars tend to form well downstream of the bend apices. In the discussion of point bar stability above, it was noted that on a flat bed the initial effect of cross-stream sediment convergences due to helical flow was to produce deposition near the inner bank around the apex of the bend. In contrast, the streamwise convergences and divergences of sediment flux associated with the streamwise variations in the radius of curvature tended to produce erosion near the inner bank upstream of the bend apex, and deposition downstream. The short, low-amplitude bend used in run S-25 is a case where the streamwise effects dominate the cross-stream convergences. This produces a point bar downstream of the bend apex, forced primarily by the streamwise convergences of sediment transport, rather than by inward boundary shear stress associated with helical flow.

In Figure 3.18, the predicted equilibrium topography is shown along with the bathymetric contours measured by Whiting and Dietrich. As in the Hooke cases, the agreement

RUN S-25
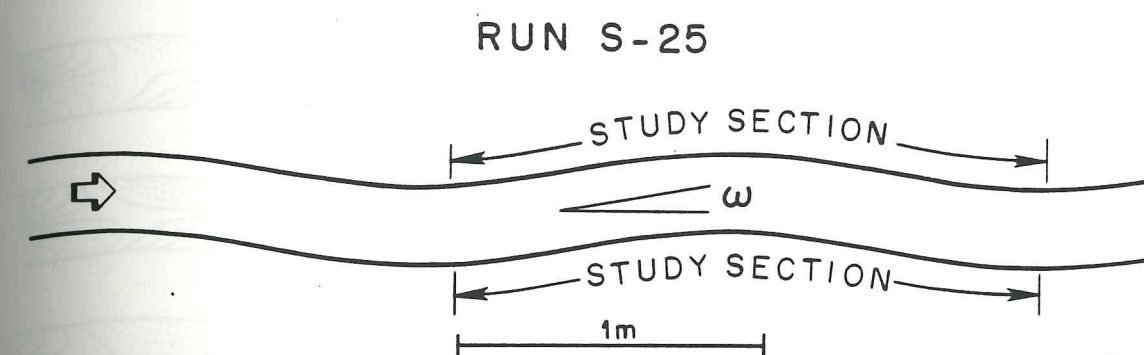
$\omega = 10°$ $Q = 1670\ cm^3/sec$

$W = 25\ cm$ $U = 33\ cm/sec$

$H_{init} = 2.0\ cm$ $Fr = 0.74$

$\lambda = 8W$ $D = 0.06\ cm$

Figure 3.16. Schematic view of the flume employed by Whiting and Dietrich [pers. comm.].
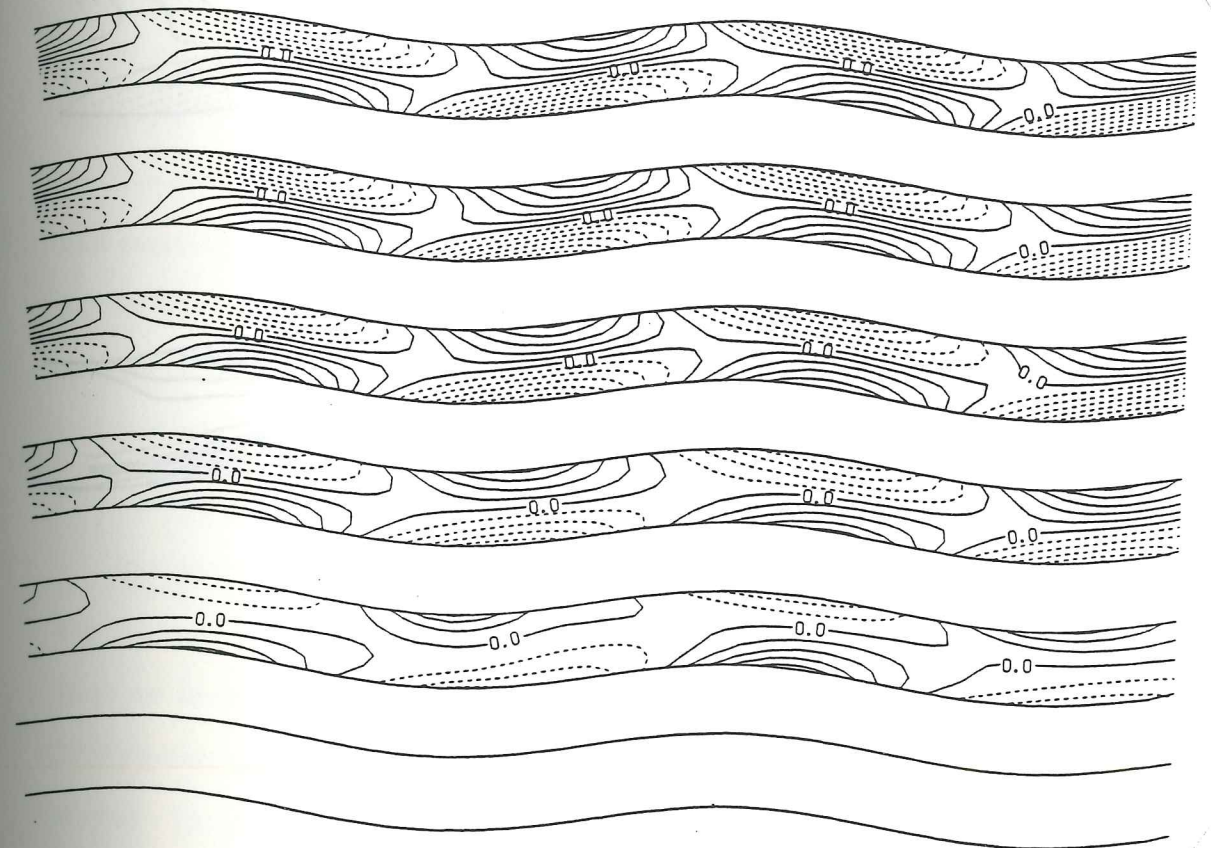
Figure 3.17. Topographic evolution predicted theoretically for the Whiting and Dietrich case S-25. Run conditions are given in Figure 3.16. Contours are drawn at intervals of 0.2 cm. Time increases upwards in this plot, and the time increment between plots is about 8 minutes.

RUN S-25
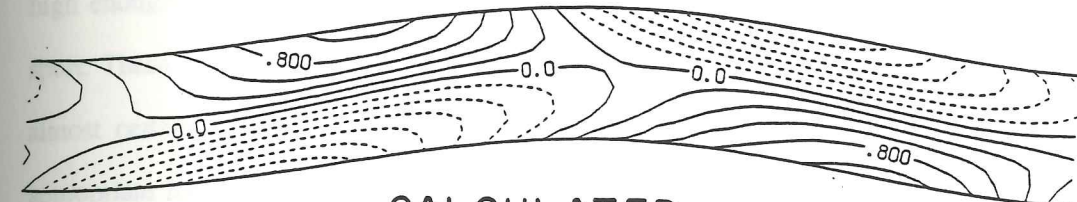
CALCULATED

OBSERVED

$Q = 1670 \text{ cm}^3/\text{s}$ $S = .005$

$\omega = 10°$ $\overline{\tau}_b = 10$

$\overline{h} = 2 \text{ cm}$ $d_{50} = .06 \text{ cm}$

$W = 25 \text{ cm}$

Figure 3.18. Comparison between measured and predicted equilibrium topography for run S-25. Contours are drawn at 0.2 cm intervals in both cases.

between the predicted and measured topography is reasonable, but there are some noteworthy discrepancies. First, the numerical model underpredicts the steep slopes of the bars at the upstream end of the pool regions. The measured slopes approach 20°, which is high enough to expect that grain flow mechanisms may play a part in the sediment transport. These slopes also are high enough that changes in vertical structure of the flow are almost certainly important. Neither the flow or sediment transport models employed are appropriate for these steep slopes. The model also fails to predict some of the small scale structure observed near the upstream end of the pool region. This is probably a result of the grid scales employed, rather than a failing in the model formulation. The computational grid for this case consisted of thirteen points in the cross-stream direction and eleven sections per bend in the streamwise direction. Thus, while the cross-stream structure should be well-resolved, some detail in the streamwise variations may have been neglected. Despite these problems, the general shape and location of the bars are predicted fairly well.

In Figure 3.19, various flow variables are plotted for the equilibrium case. The boundary shear stress is normalized by the reach-averaged value of 10 $dynes/cm^2$. Sediment fluxes are normalized by the value of 0.04 cm^2/sec measured by Whiting and Dietrich. Local measurements of flow variables are not presently available, so a comparison was not possible. The helix strength results for this case are of particular interest. The largest values for the angular deviation between the bed and the surface are found somewhat downstream of the bend apex. This demonstrates the importance of treating streamline curvature in low amplitude bends, rather than just channel curvature. As is clear from the vector bottom stress plot, the flow curvature is actually greatest downstream of the bend apex. Topographic steering near the bend apex essentially compensates for the channel curvature, resulting in relatively weak curvature of the flow. As will become clearer in a subsequent discussion, the stability in this low amplitude case is actually somewhat similar to that

RUN S-25 25 cm

BED TOPOGRAPHY

$\vec{\tau}$

$\tau_b / \bar{\tau}_b$

$\vec{q}_s$

$q_s / \bar{q}_s$
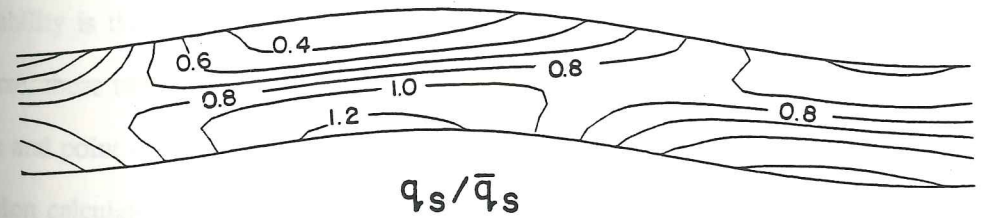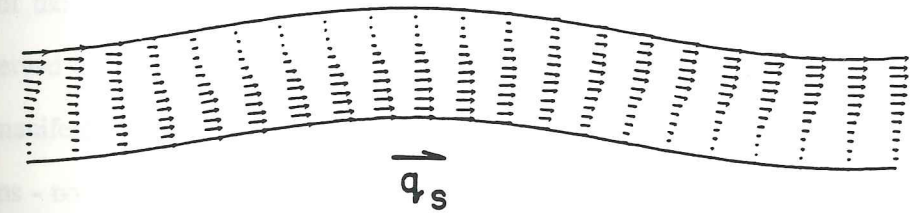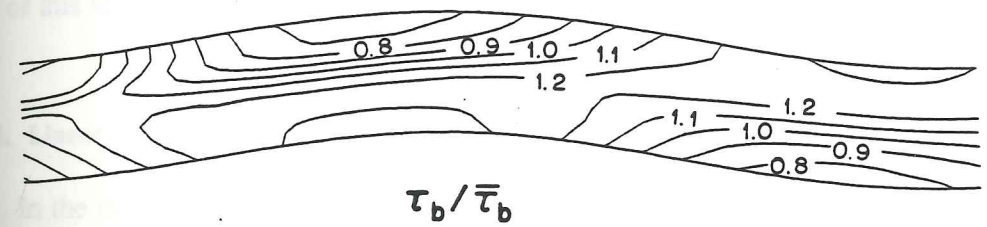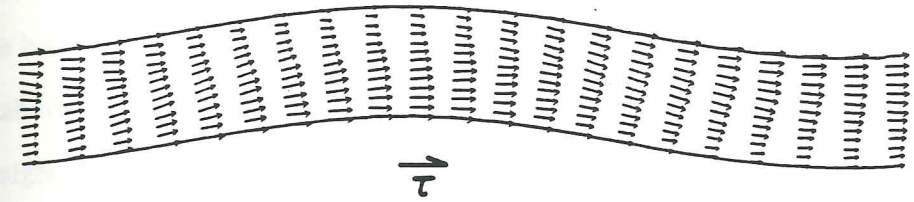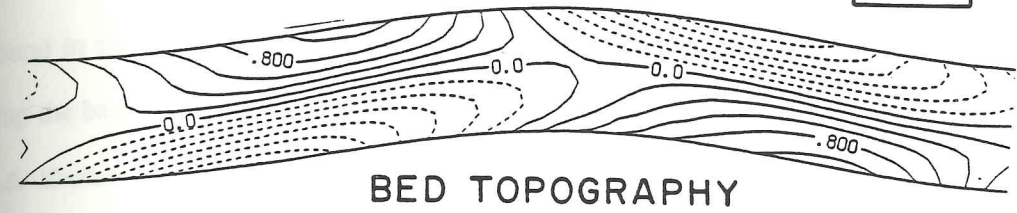
HELIX STRENGTH

Figure 3.19. Predicted flow variables for run S-25 at equilibrium conditions. Contours intervals for topography, normalized bottom stress, normalized sediment flux, and helix strength are 0.2 cm, 0.1, 0.2, and 5°, respectively.

found in the case of alternate bars, with the exception that the channel curvature tends to trap the bars and prevent migration.

3.5. Evolution and Stability of Alternate Bars

In this section, the initial development and the finite amplitude growth and stability of alternate bars are treated. In some sense, these features are the fundamental ones related to bar instability in river channels, since they arise spontaneously from any small perturbation to a straight, uniform channel. In order to investigate the genesis of these forms, the first part of this section contains a linear stability analysis of the governing equations.

3.5.1. Linear Stability Analysis

In the case of point bars, the initial instability of the flat bed is produced by the curvature of the channel planform. Thus, for that case, curvature essentially acts as to force the observed instability. In the case of alternate bars, this is no longer true. Alternate bars are a manifestation of a fundamental instability in the coupled flow-sediment transport equations - no forcing is required. By analogy with harmonic oscillations, the alternate bar instability is the "free" response of the system, while point bars are a forced response. Of course, these two problems are not decoupled - there is a genetic link between the alternate bars and point bars. Examination of that link, however, requires the incorporation of a bank erosion calculation into the bar evolution model, which is beyond the scope of this dissertation.

To investigate the physical effects responsible for the initiation of the alternate bar instability, and to determine the initial wavelength of these features, it is useful to employ the techniques of linear stability analysis. This analysis is performed using the vertically-averaged equations expressing mass and momentum conservation for the fluid in conjunction with the equation expressing conservation of sediment mass and a bedload equation.

The analysis presented here uses equations (3.1), (3.11), (3.12), and (3.26) in conjunction with the modified Meyer-Peter-Mueller bedload equation, which is given by

$$Q = \gamma(\tau_b - \tau_c)^{3/2} \qquad (3.29)$$

where

$$\gamma = \frac{8}{\rho^{\frac{1}{2}}(\rho_s - \rho)g}$$

In this equation, Q is the volume flux of sediment per unit width along the direction of the vector boundary shear stress, the magnitude of which is τ_b. The choice of this bedload equation rather than the Yalin equation, which is used in the evolution calculations, is due to the mathematical simplicity of the modified Meyer-Peter-Mueller equation. This choice simplifies the formulation of the linear stability analysis without removing any salient physical effects. The five equations listed above are linearized about a steady uniform flow in a straight channel using

$$<u> = U_0 + \varepsilon u_1(s,n) + \ldots$$

$$<v> = \varepsilon v_1(s,n) + \varepsilon^2 v_2(s,n) + \ldots$$

$$E = E_0 + \varepsilon E_1(s,n) + \ldots \qquad (3.30)$$

$$h = H_0 + \varepsilon h_1(s,n) + \ldots$$

This leads to the following set of coupled linear equations :

$$h_0\frac{\partial u_1}{\partial s} + u_0\frac{\partial h_1}{\partial s} + h_0\frac{\partial v_1}{\partial n} = 0 \tag{3.31}$$

$$u_0\frac{\partial u_1}{\partial s} = -g\frac{\partial E_1}{\partial s} - C_d\left[2\frac{u_0}{h_0}u_1 - \frac{u_0^2}{h_0^2}h_1\right] \tag{3.32}$$

$$u_0\frac{\partial v_1}{\partial s} = -g\frac{\partial E_1}{\partial n} - C_d\frac{u_0}{h_0}v_1 \tag{3.33}$$

$$-c_b\frac{\partial}{\partial t}\left[E_1 - h_1\right] = \left[3\gamma C_d(\tau_0 - \tau_c)^{\frac{1}{2}}u_0\right]\frac{\partial u_1}{\partial s} + \left[\frac{\gamma(\tau_0 - \tau_c)^{3/2}}{u_0}\right]\frac{\partial v_1}{\partial n} \tag{3.34}$$

where $\tau_0 = C_d u_0^2$, and the fact that $B = E - h$ has been used to eliminate B from the analysis. Note that either h or E could have been eliminated instead, but the choice of B results in slightly simpler algebra, and the final result is clearly unaffected by the choice made here.

To examine the growth and migration characteristics of alternate bar perturbations of various wavelengths, the perturbation quantities are expressed in terms of complex exponential functions, as shown in equation (3.35). This is equivalent to perturbing a flat bed with a small amplitude doubly harmonic wave, as shown in the three-dimensional plot in Figure 3.20.
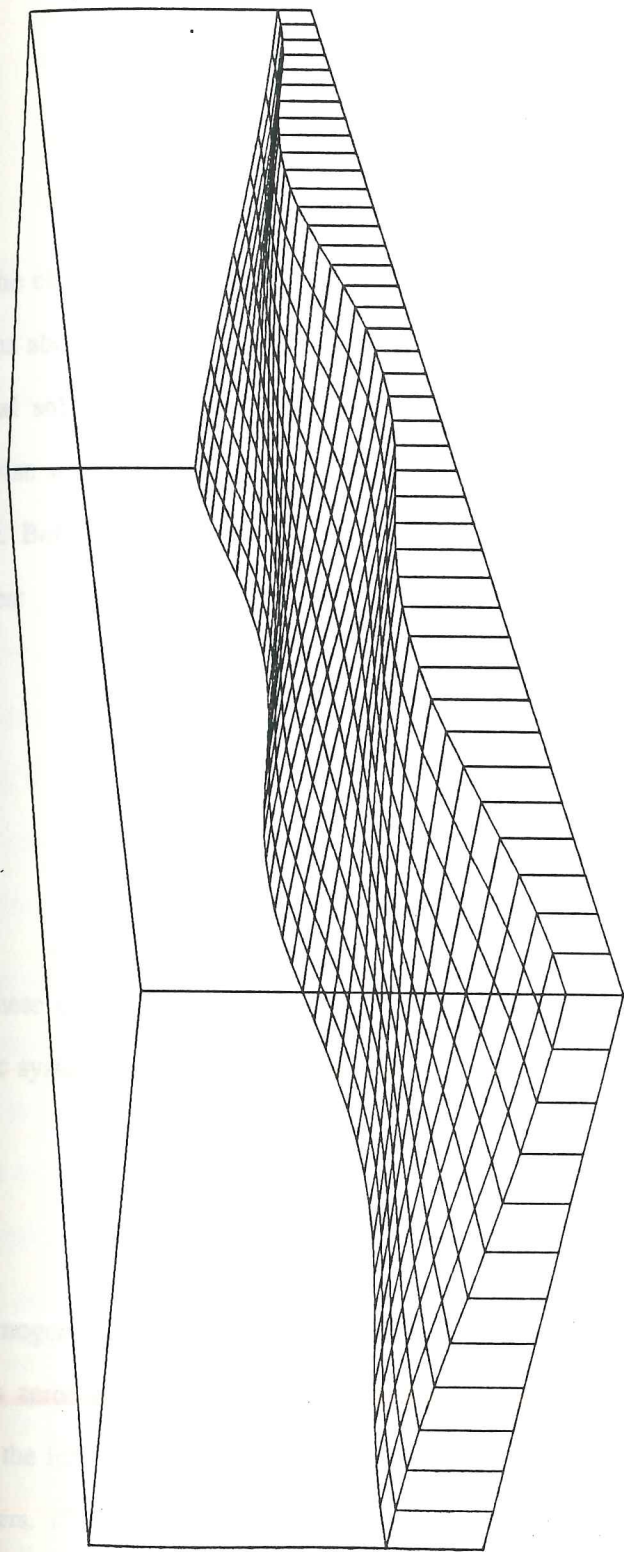
Figure 3.20. Three-dimensional plot of the doubly harmonic bed perturbation employed in the linear stability analysis.

$$
\begin{bmatrix} u_1 \\ v_1 \\ h_1 \\ E_1 \end{bmatrix} = \begin{bmatrix} \hat{u} \\ \hat{v} \\ \hat{h} \\ \hat{E} \end{bmatrix} e^{i(\frac{2\pi s}{\lambda} + \frac{\pi n}{b} - \sigma t)} \tag{3.35}
$$

where the circumflex designates a complex amplitude. Inserting these in the system of four equations above yields an algebraic system of four equations in four unknowns. To obtain a nontrivial solution to these equations, a condition relating σ to the drag coefficient, the streamwise wavelength of the bars, the transport stage, and the width-to-depth ratio must be satisfied. Before finding this relation, it is useful to define the following nondimensional quantities:

$$
\overline{u} = \frac{\hat{u}}{U_0} \quad \overline{v} = \frac{\hat{v}}{U_0} \quad \overline{h} = \frac{\hat{h}}{H_0} \quad \overline{E} = \frac{\hat{E}}{H_0} \quad Fr = \frac{U_0}{(gH_0)^{\frac{1}{2}}} \tag{3.36}
$$

$$
\alpha = \frac{2\pi H_0}{\lambda} \quad \beta = \frac{\pi H_0}{b} \quad \omega = \frac{c_b \sigma H_0^2}{\gamma \tau_0^3 T^{\frac{1}{2}}} \quad T = 1 - \frac{\tau_c}{\tau_0} \tag{3.36}
$$

Using these definitions and equation (3.35) in the system (3.31) through (3.34) gives the algebraic system below.

$$
\begin{bmatrix} 1 & \beta/\alpha & 1 & 0 \\ i\alpha + 2C_d & 0 & -C_d & i\alpha/Fr^2 \\ 0 & i\alpha + C_d & 0 & i\beta/Fr^2 \\ 3\alpha & \beta T & \omega & -\omega \end{bmatrix} \begin{bmatrix} \overline{u} \\ \overline{v} \\ \overline{h} \\ \overline{E} \end{bmatrix} = 0 \tag{3.37}
$$

This homogeneous system only yields nontrivial solutions if the determinant of the matrix above is zero. This condition yields the desired expression for the growth and migration rates of the infinitesimal alternate bar perturbations as a function of dynamic and geometric parameters. The equation for the nondimensional frequency is given by

$$\omega = \frac{(3\alpha^3 + \alpha\beta^2 T) + i(3(\beta^2 - \alpha^2)C_d - 3\beta^2 C_d T)}{\alpha^2 + \beta^2 + Fr^2(3C_d^2 - \alpha^2) - i(\alpha C_d + 2\frac{\beta^2}{\alpha}C_d - 4\alpha C_d Fr^2)} \qquad (3.38)$$

The growth rate and migration velocity of the alternate bar perturbation are given by σ_i and $\lambda\sigma_r/2\pi$, respectively, where the subscripts r and i refer to the real and imaginary parts of σ. Equivalent nondimensional growth and migration rates are given by ω_i and ω_r/α, respectively. Since α is positive definite, the sign of the migration rate is always determined by ω_r and the wavelength for which no migration occurs corresponds to $\omega_r = 0$. Thus, it is possible to ascertain the fastest-growing wavelength and the migration characteristics of alternate bar perturbations simply by examining ω_i and ω_r. The values of these nondimensional parameters are plotted versus λ/b for a typical case in Figure 3.21. As expected, a fastest-growing wavelength is found for the alternate bar perturbations, corresponding to the peak in ω_i. Since ω_r is positive at the selected wavelength, the fastest-growing features will travel downstream.

The primary purpose in presenting the linear stability analysis is to ascertain the physical processes responsible for the initial instability of alternate bars. To pursue this goal, it is useful to introduce "switches", denoted s_1 and s_2, in the equation for ω. The switch s_1 is set equal to zero when results are desired for the case in which the streamwise convection of streamwise momentum (the first term in equation (3.32)) is neglected in the analysis, and set equal to one otherwise. Similarly, s_2 is set equal to zero when results of the stability analysis are desired that do not include the streamwise convection of cross-stream momentum (the first term in equation (3.33)), and is set equal to unity otherwise. Using this technique, it is possible to precisely identify the roles of the various terms in creating the observed instability. Using the definitions for s_1 and s_2, the equation for ω becomes
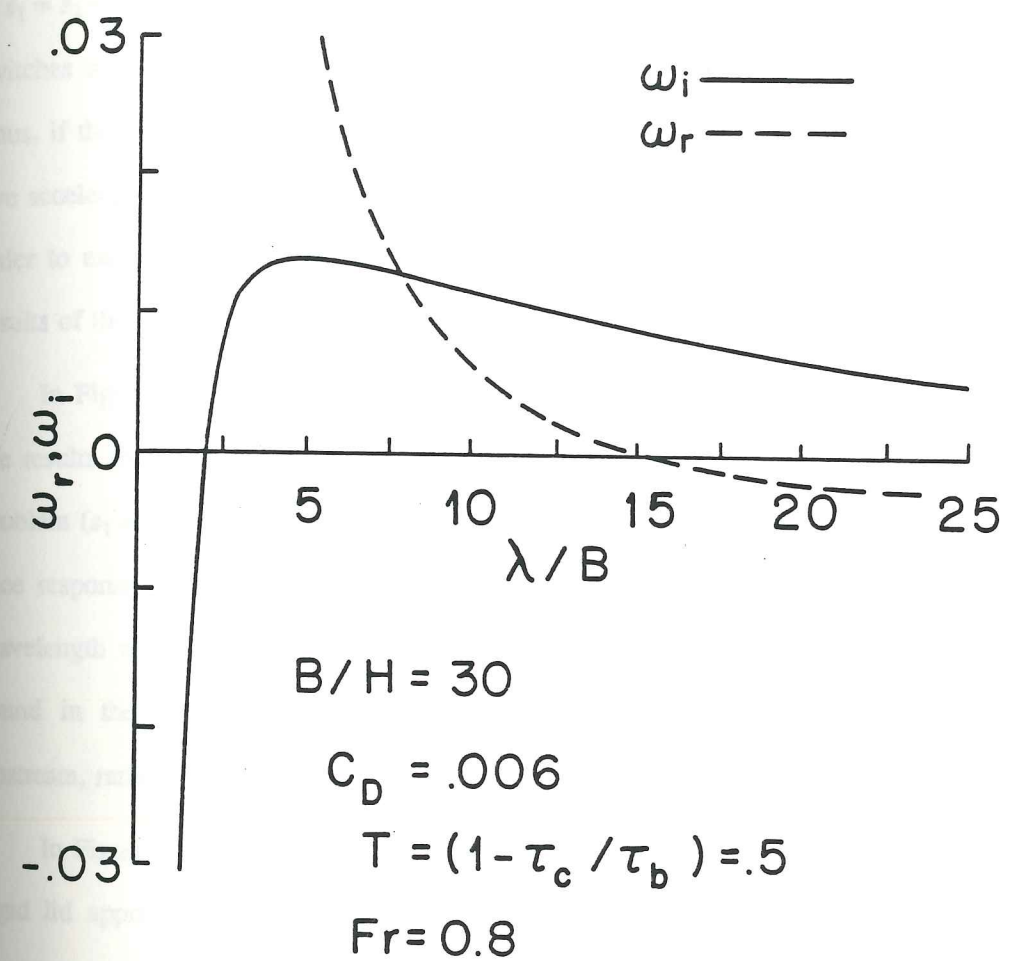
Figure 3.21. Real and imaginary parts of ω plotted versus the ratio of bar wavelength to width for typical values of the width-to-depth ratio, drag coefficient, transport stage, and Froude number. These results are predicted by the full linear analysis, including the pertinent convective accelerations and the free surface effects.

$$\omega = \frac{(3\alpha^3 s_1 + \alpha\beta^2 T s_2) + i(3(\beta^2 - \alpha^2)C_d - 3\beta^2 C_d T)}{\alpha^2 s_2 + \beta^2 s_1 + Fr^2(3C_d^2 - \alpha^2 s_1 s_2) - i(\alpha C_d + 2\frac{\beta^2}{\alpha}C_d - \alpha C_d Fr^2(3s_2 + s_1))} \quad (3.39)$$

If $s_1 = s_2 = 1$, equation (3.39) reduces to equation (3.38), as expected. If both of these two switches and the Froude number are set equal to zero, the expression for ω is pure real. Thus, if the rigid lid approximation is made and both streamwise and cross-stream convective accelerations are neglected, the alternate bar instability is removed from the analysis. In order to explore the roles of these three effects in producing the alternate bar instability, results of the stability analysis are presented which include each of these effects separately.

In Figure 3.22, results of the stability analysis are shown for the same conditions as the results shown in Figure 3.21, but with the convective accelerations removed from the problem ($s_1 = s_2 = 0$). Thus, this case includes only the destabilizing effect of the free surface response to the bed perturbation. An instability is found, with the fastest-growing wavelength at about four channel widths. The instability is quite weak compared to that found in the full analysis and, because $\omega_r < 0$, the fastest-growing features propagate upstream, rather than downstream.

In Figure 3.23, the real and imaginary parts of ω are shown for the case in which the rigid lid approximation is employed and the convective acceleration in the cross-stream equation is neglected ($s_1 = 1$, $s_2 = Fr = 0$). Again, an instability is found, the fastest-growing wavelength of which occurs at about six or seven widths. Although this is slightly longer than the wavelength defined from the full analysis (Figure 3.21), the growth and migration curves for this case are very similar to the full analysis and are, in fact, asymptotic to the curves in Figure 3.21 as the ratio of wavelength to width becomes large. If the linear analysis is applied neglecting the free surface deformation, eliminating the streamwise convective acceleration term, and including the cross-stream term ($s_1 = Fr = 0$,
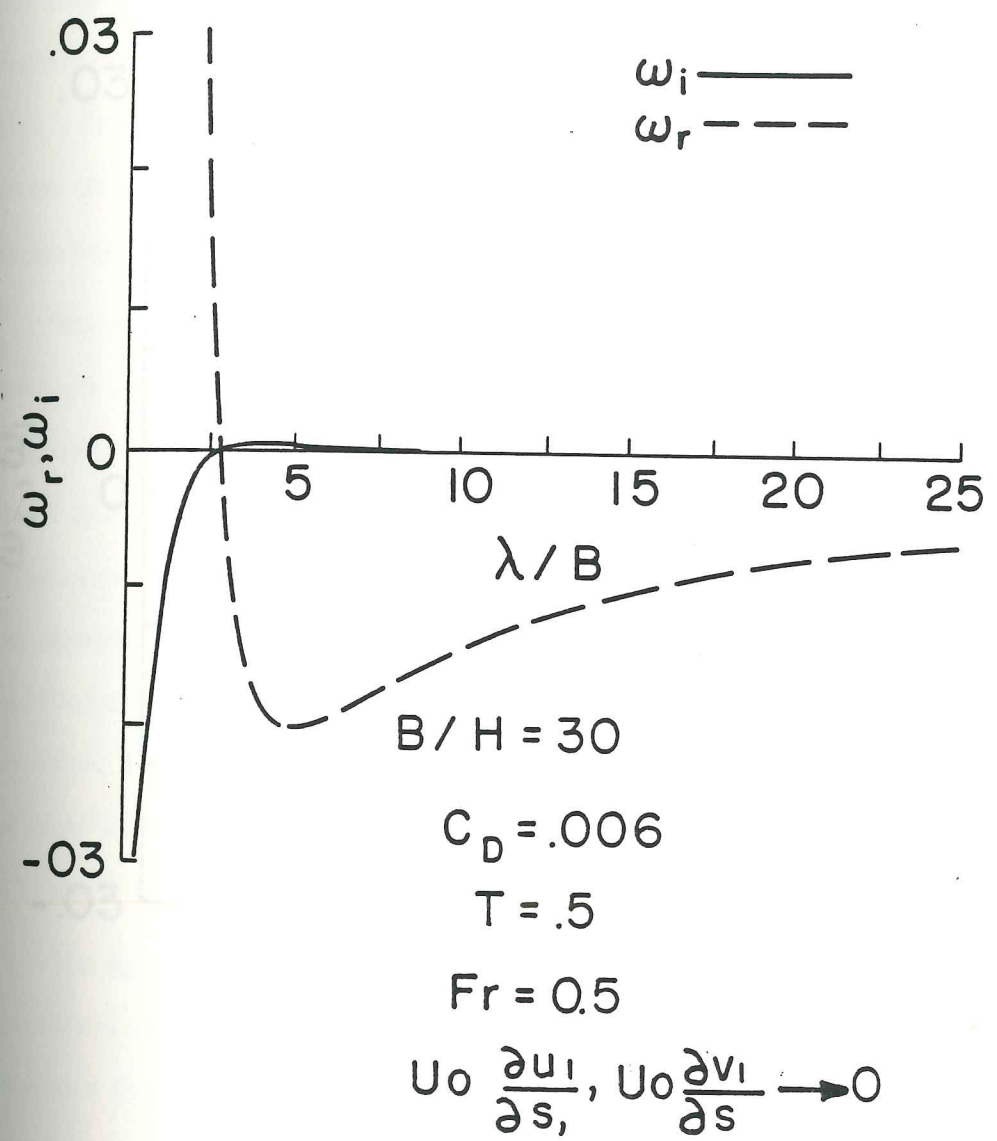
Figure 3.22. Results of the stability analysis for the case in which the linearized convective accelerations in the cross and downstream momentum equations are neglected.

Figure 3.23. Results of the stability analysis for the case in which free surface effects are neglected (Fr=0) and the streamwise convection of cross-stream momentum is neglected.

$s_2 = 1$), the results shown in Figure 3.24 are obtained. As in the other two cases an instability is found with a fastest-growing wavelength near the one selected in the full analysis. The magnitude of the growth rate in this case is much larger than that found in the full analysis (note the change in scale on the vertical axis), indicating that the neglected terms have a damping effect on the instability produced by the streamwise convection of cross-stream momentum. As in the case of the full analysis, the fastest-growing features propagate downstream.

The important conclusion from these three cases is that any of the three effects described above is sufficient to produce an alternate bar instability, and each selects a fastest-growing wavelength near that found in the full analysis. These features are not particular to the values of the parameters chosen for these runs, rather, they are typical of the entire range of conditions found in natural streams. The analysis performed including only the streamwise convection of streamwise momentum yields results most similar to the full analysis, and clearly dominates the large response found including only the cross-stream advection. However, the selected wavelength in the full analysis is dependent on all three of these effects, and all must be retained in order to make correct predictions of the wavelength of infinitesimal alternate bars.

The figures presented and discussed above provide some insight into the fluid dynamical effects that play a role in the alternate bar instability, and this insight can be used to provide a simple, physical understanding of the instability. This may be obtained by considering the response of the flow to a single perturbation located on one side of a straight channel. In other words, one considers the flow around a symmetric bump with some specified streamwise length and a cross-stream width of half the channel. As the flow approaches the bump, the convective accelerations induced by the spatial nonuniformity will produce an alteration in the pressure gradient (surface elevation) field. This is precisely
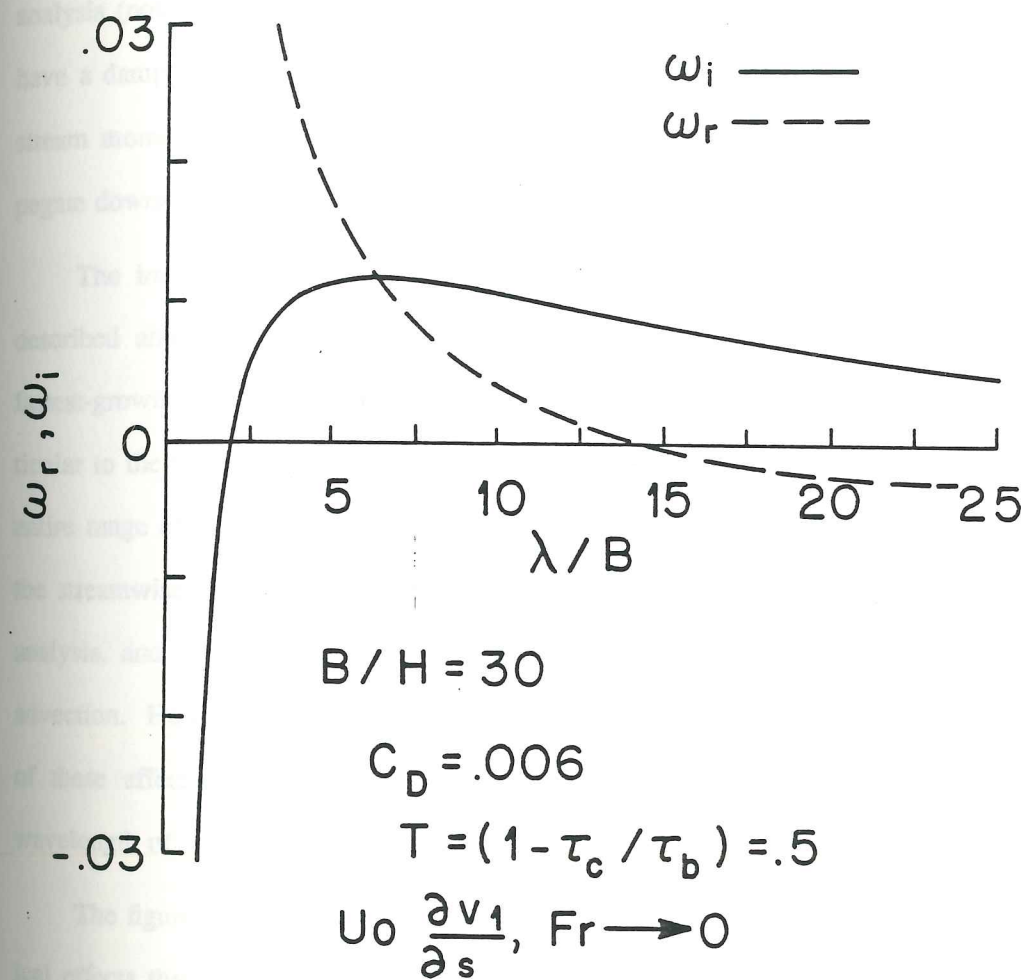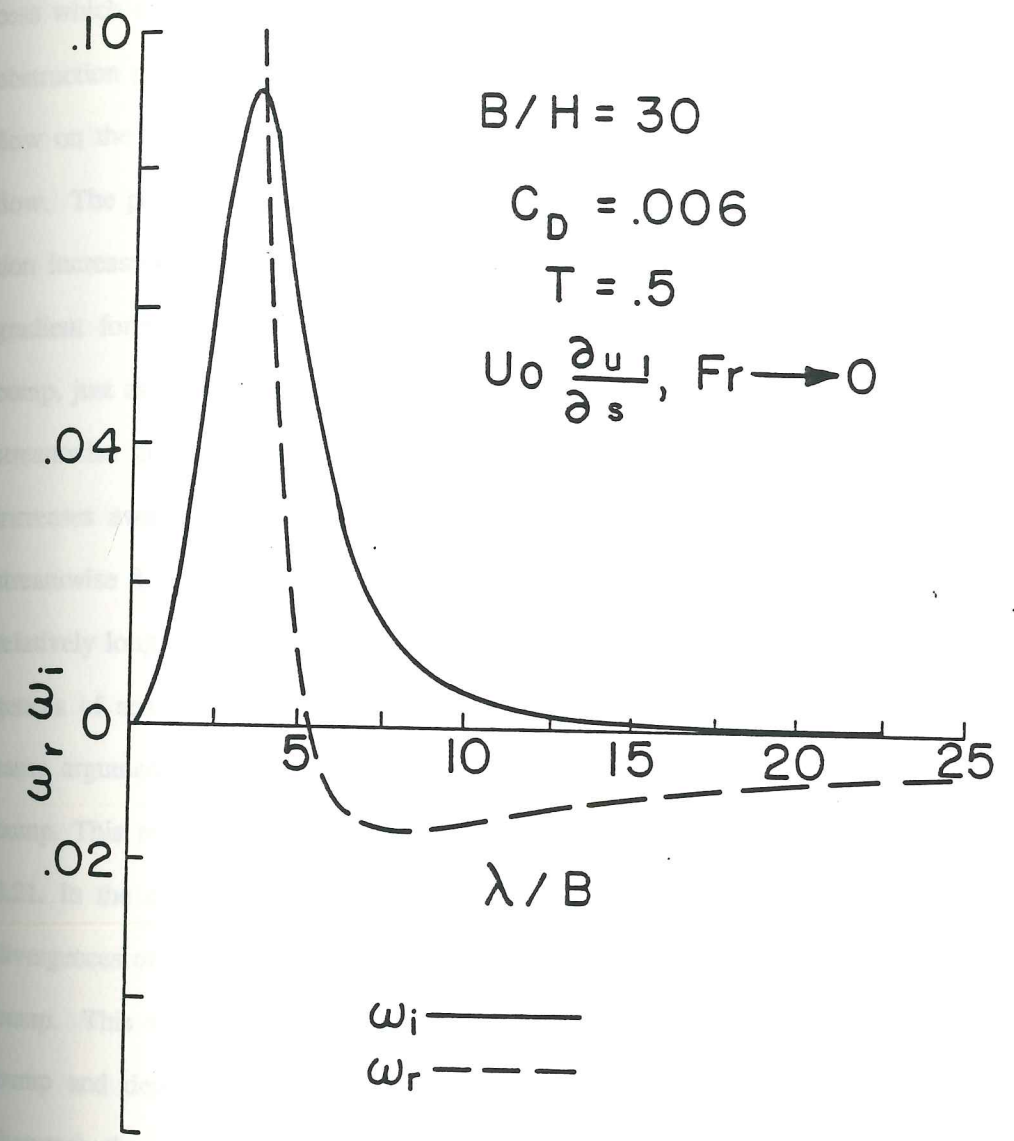
Figure 3.24. Results of the stability analysis for the case in which free surface effects are neglected (Fr=0) and the streamwise convection of downstream momentum is neglected.

the same effect one observes upstream of any obstacle, and is analogous to a stagnation pressure. Thus, the surface elevation increases on the upstream side of the bump in a process which is intuitively understood in terms of the Bernoulli response of the flow to the obstruction presented by the bump. This effect produces a streamwise deceleration of the flow on the upstream side of the bump, and an accompanying production of cross-stream flow. The production of the cross-stream flow is an inevitable result of the surface elevation increase on the upstream side of the bump, which produces a cross-stream pressure gradient force. This reasoning reduces to the fact that the flow is "steered" around the bump, just as flow is steered around a stick inserted vertically into flowing water. Since the streamwise flow decelerates on the upstream side of the bump and the cross-stream flow increases away from the bank, one expects a convergence of sediment flux due to the streamwise flow field, and a divergence of sediment flux due to the cross-stream flow. For relatively long bumps, the streamwise convergences are greater than the cross-stream divergences of sediment, and one expects deposition on the upstream side of the bump. The same argument leads to the fact that erosion will occur on the downstream side of the bump. This means that the longer features will migrate upstream, in accord with Figure 3.21. In the case of shorter features, the cross-stream steering is such that cross-stream divergences of sediment outweigh the streamwise convergences on the upstream side of the bump. This results in downstream migration, with erosion on the upstream part of the bump and deposition on the downstream side. In either case (relatively long or short features), the pattern of sediment fluxes is such that one expects a transition from erosion to deposition (or vice versa) near the apex of the bump. The location of this point relative to the top of the bump determines whether the bump will grow or not. For very short features, the streamwise advection of cross-stream momentum will be such that there is still significant cross-stream velocity and sediment flux at the apex of the bump. Thus, in this case, erosion will occur at the crest, and the bump will not grow. As the wavelength is

increased, the point of transition from erosion to deposition shifts upstream. This is essentially due to the lessening of the inertial lag between the topography and the flow. For sufficiently long wavelengths, the results is deposition on the crest of the bump and, therefore, growth of the bump. However, as the feature becomes even longer, the rate of growth will begin to decrease asymptotically to zero, since the topographic steering effect becomes weaker and weaker. Thus, one expects a maximum rate of growth at some intermediate wavelength. This wavelength is short enough that the topographic steering produces significant adjustments in the pressure and velocity fields, but long enough that the inertial effects do not act to shift the locus defining the transition from erosion to deposition beyond the obstacle crest. These simple arguments are in agreement with the results of the linear stability analysis and are obtained primarily through insight gained from this analysis. The linear theory also provides a method whereby the dependence of the alternate bar growth and migration on flow and sediment transport parameters may be investigated. In Figure 3.25, the real and imaginary parts of ω are plotted versus the ratio of wavelength to width for several values of the drag coefficient, C_d. These values for the drag coefficient are chosen to cover the range of values typically found in natural streams and rivers. In all cases, a fastest-growing wavelength is identified, but this wavelength tends to increase as the stream roughness decreases. Thus, for $C_d = .01$ the wavelength of fastest growth is about four widths, and in the case of $C_d = .002$, this wavelength is about seven widths. Furthermore, the wavelength of fastest growth is more poorly selected as the bed becomes smoother, as evidenced by the flattening of the curve of ω_i as C_d decreases. This analysis suggests that, in streams that are relatively smooth, the wavelength of alternate bars may be more susceptible to alteration as a result of finite amplitude effects or some external forcing. This point can be further developed by examining the dependence of the fastest-growing wavelength on the ratio of width to depth.
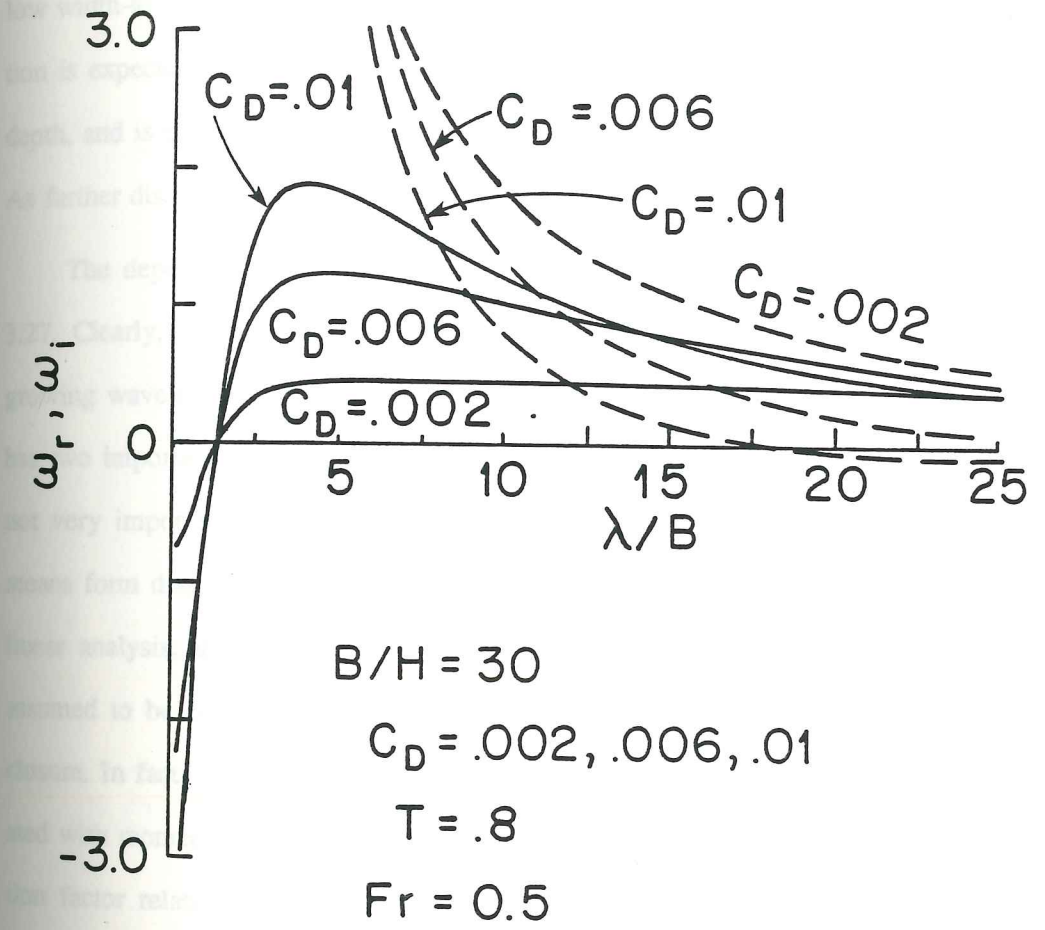
Figure 3.25. Results of the full stability analysis for three values of the drag coefficient, holding other variables constant.

In Figure 3.26, the results of the linear analysis are shown for several values of the width-to-depth ratio. The value of the fastest-growing wavelength is only weakly dependent on the ratio of width to depth, with the longer features being associated with the relatively narrow, deep streams. This wavelength tends to be more poorly selected in streams with low width-to-depth ratios. In conjunction with the result described above, wavelength selection is expected to be quite weak in relatively smooth streams with low ratios of width to depth, and is expected to be much more robust in rough streams that are wide and shallow. As further discussed below, this has important implications for meander development.

The dependence of the linear results on the transport stage, T, is shown in Figure 3.27. Clearly, the value of T has only a weak effect on the specification of the fastest-growing wavelength, although it does have a substantial effect on the migration rate. This has two important implications. First, this means that the transport stage of the sediment is not very important in calculating the infinitesimal alternate bar wavelength. Second, this means form drag is not an important factor in the determination of the wavelength. In the linear analysis, the boundary shear stress available for sediment transport was explicitly assumed to be equivalent to the total boundary shear stress given by the drag coefficient closure. In fact, if ripples or dunes are present on the bed, some of this friction is associated with momentum extraction by pressure forces on the bedforms. If a form drag correction factor relating the overall boundary shear stress to the skin friction shear stress is included in this analysis, it appears only in the expression for T. Because T has only a weak effect in determining the wavelength of instability, this complication is unnecessary. For the cases shown on Figure 3.27, the transport stage (defined as the ratio of boundary to critical shear stress) varies from 1.25 to ∞, with only a very small variation in the fastest-growing wavelength. For typical streams, the variation in T with and without the form drag correction is quite small (about 10% for the Muddy Creek site described in Chapter 2), so
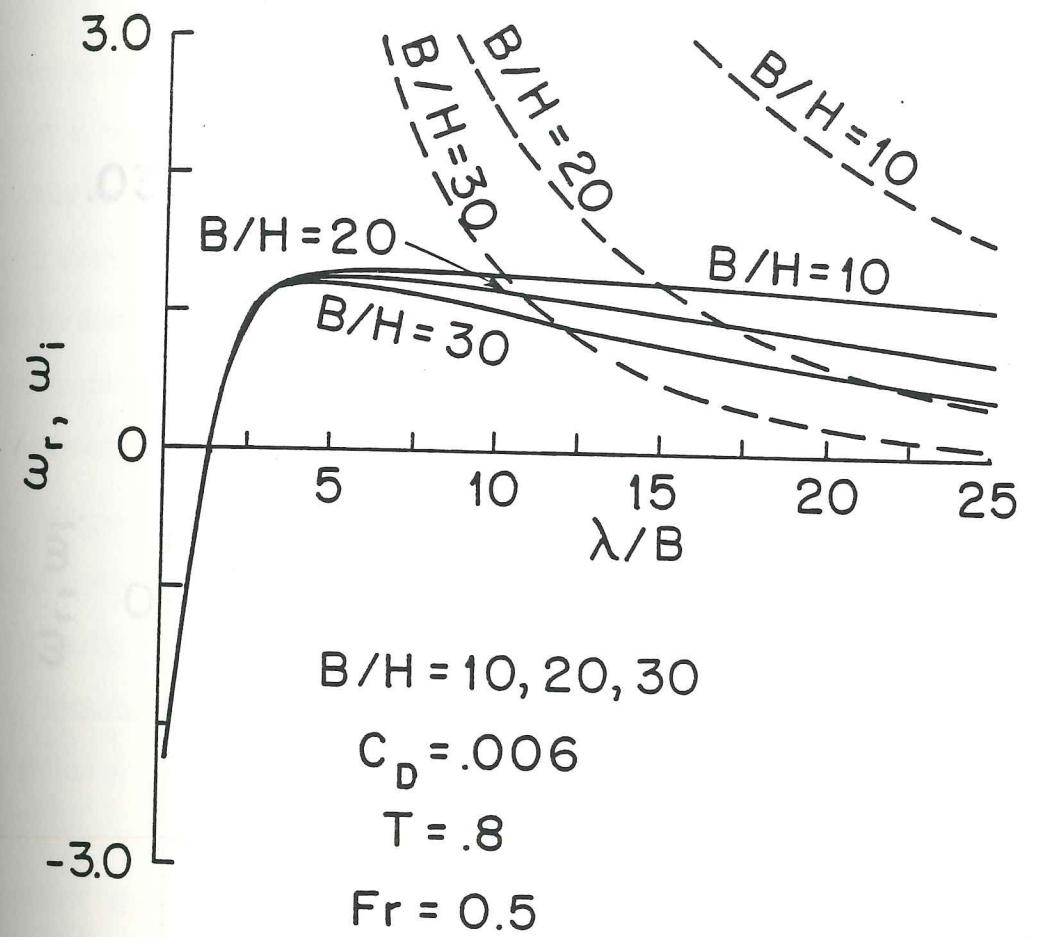
Figure 3.26. Results of the full stability analysis for various values of the width-to-depth ratio, holding other parameters constant.
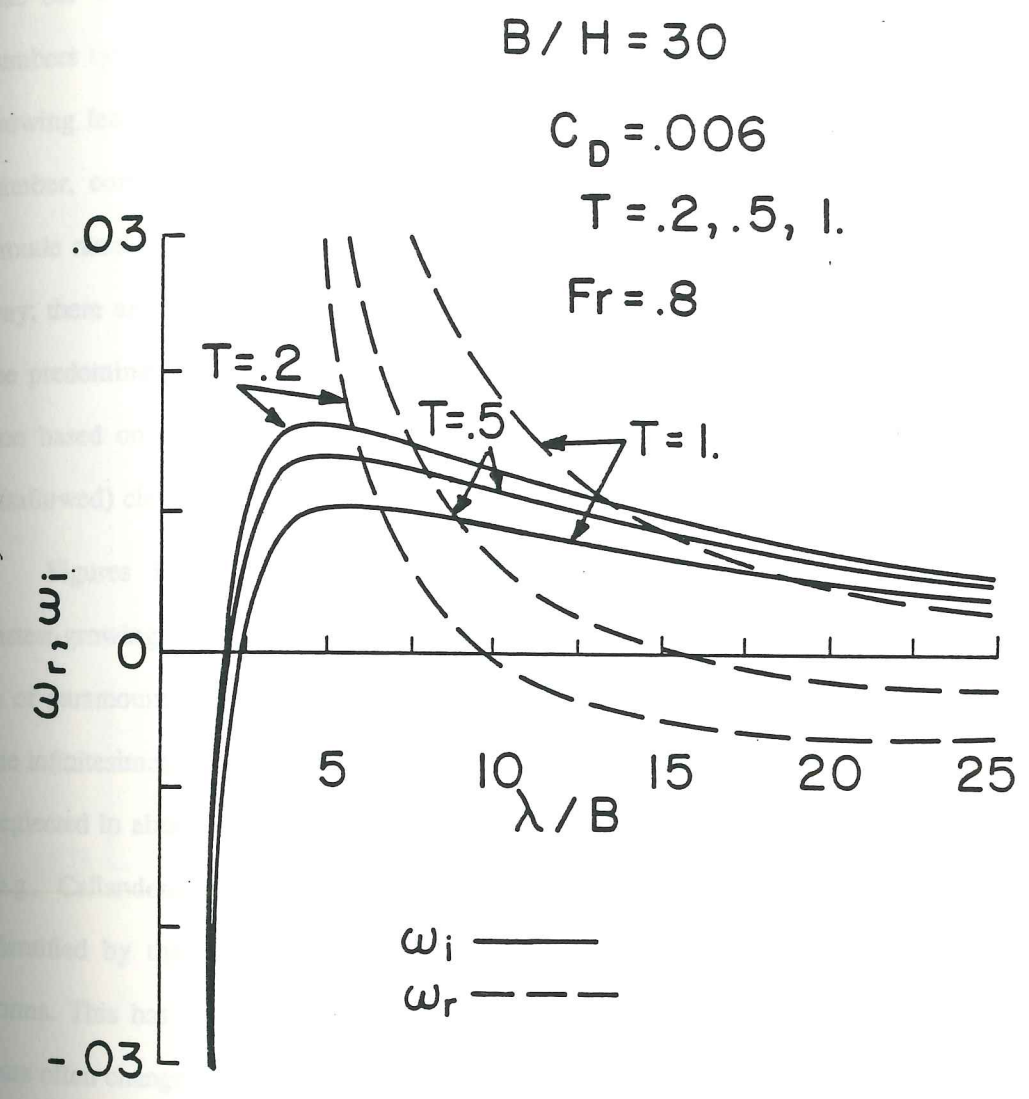
Figure 3.27. Results of the stability analysis for various values of T, where T is defined as unity minus the inverse of the transport stage.

the effect on varying the selected wavelength is negligible.

In Figure 3.28, the effect of Froude number variations on the determination of alternate bar wavelengths is depicted. For all three cases, which span the range of Froude numbers typically found in natural flows wherein bars occur, the migration of the fastest-growing features is downstream. The selected wavelength increases with increasing Froude number, corresponding to the increasing dominance of inertial effects. Interestingly, the Froude number only effects the flow and pressure gradient patterns in a smoothly varying way; there are no sudden transitions or critical values of the Froude number. This is due to the predominance of the three-dimensional nature of the flow around alternate bars. Intuition based on the extension of two-dimensional theories (wherein steering of the flow is disallowed) clearly would lead to erroneous results.

Figures 3.25 through 3.28 yield information that can be used to approximate the fastest-growing alternate bar wavelength in most, if not all, natural situations. However, it is of paramount importance to note that the selected wavelength is the one associated with the infinitesimal perturbations, and may be altered by finite amplitude effects. This has been neglected in almost all previous treatments used to identify the wavelength of alternate bars (e.g., Callander, 1968; Parker, 1976). Previous analyses assume that the wavelength identified by the infinitesimal amplitude theory is the length of the well-developed bar forms. This has been shown, however, to be incorrect experimentally; observed alternate bars often change in wavelength as they evolve.

In Figure 3.29, predicted bar wavelengths from the linear theory are shown along with values measured in flume experiments by Whiting (pers. comm.), Fujita and Muramoto (1985), and Fukuoka (1983). This same relationship is shown in nondimensional form in Figure 3.30. As is clear from these figures, the linear theory systematically under-predicts the finite amplitude wavelength for these cases, typically by 30-40%. The linear
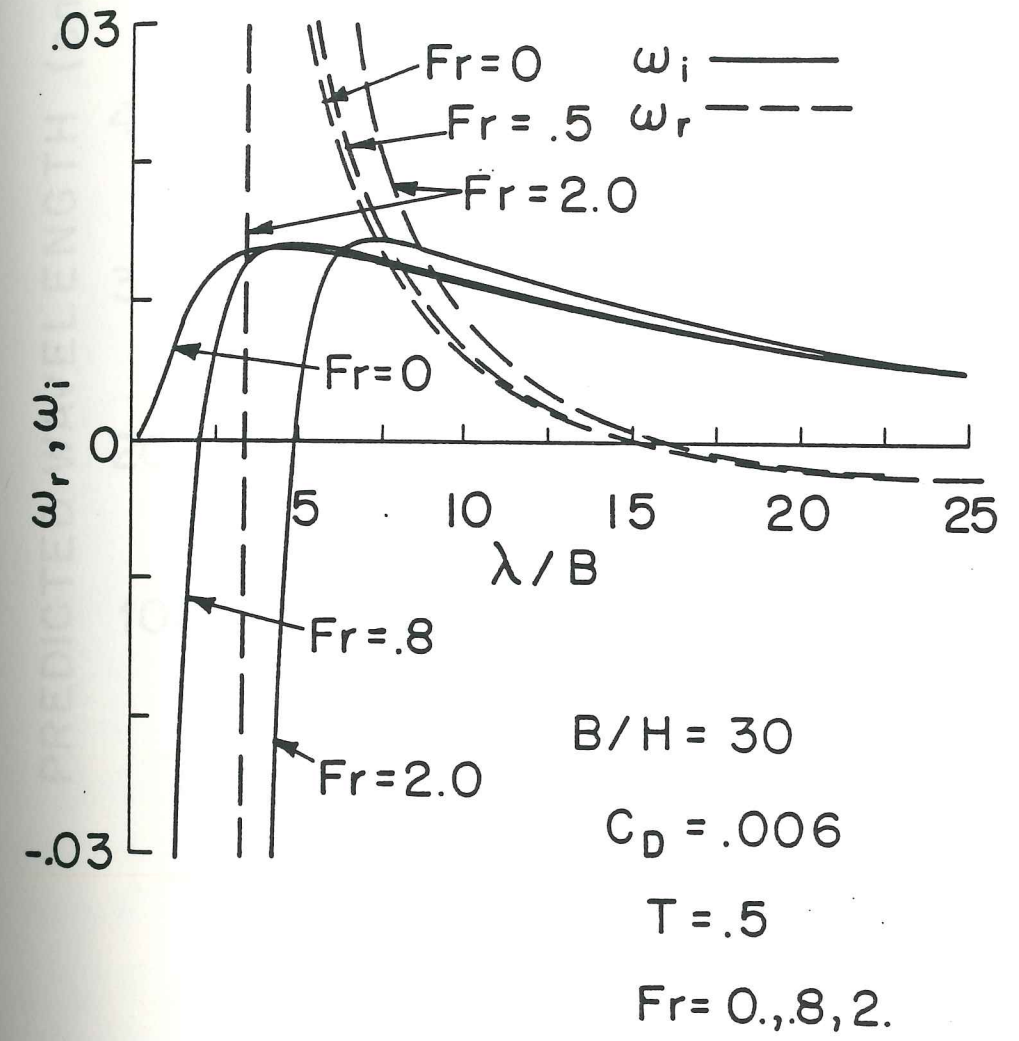
Figure 3.28. Results of the linear stability analysis for various values of the Froude number.
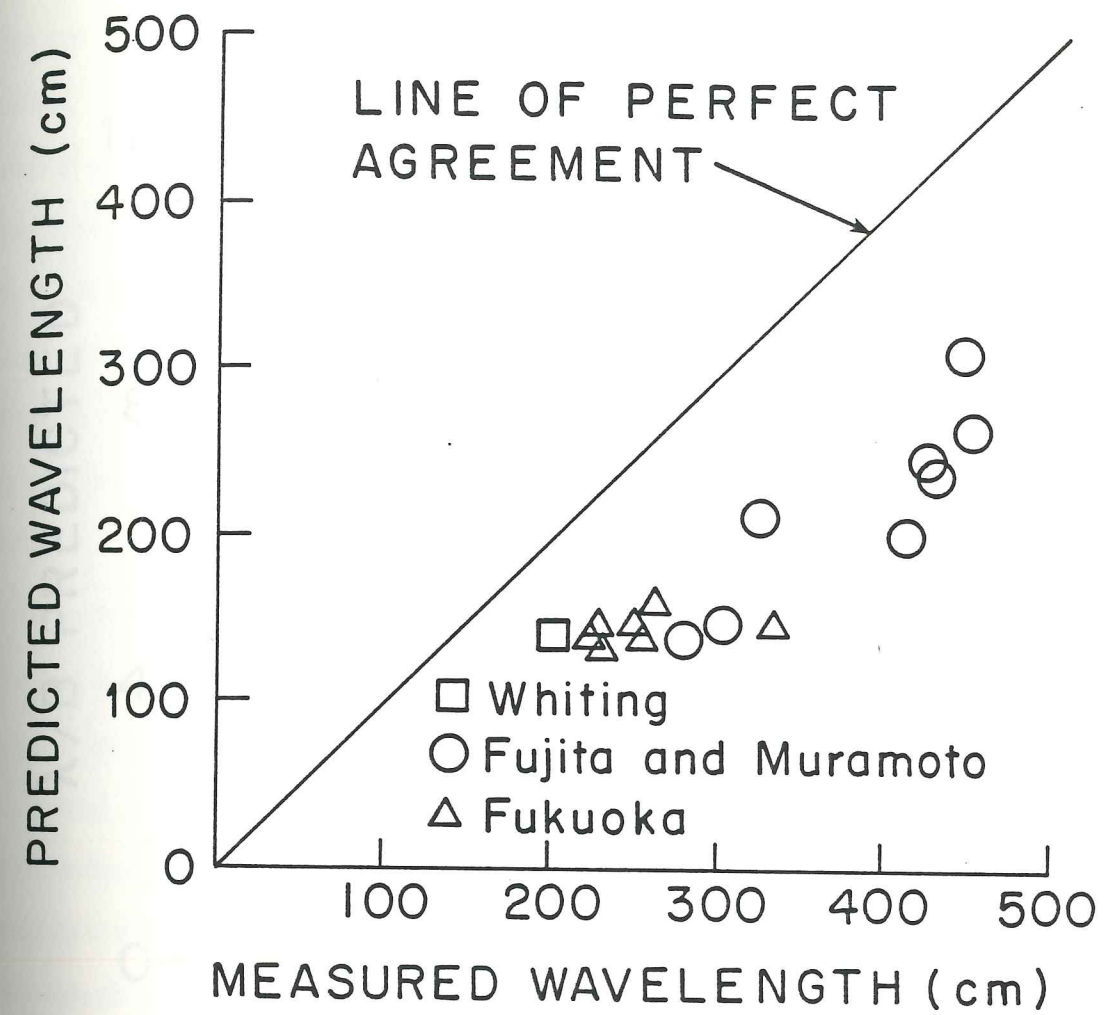
Figure 3.29. Predicted versus measured values of alternate bars for the experimental results of Fujita and Muramoto [1985], Fukuoka et al. [1983], and Whiting and Dietrich [pers. comm.]. Predicted values are found from the linear stability analysis.
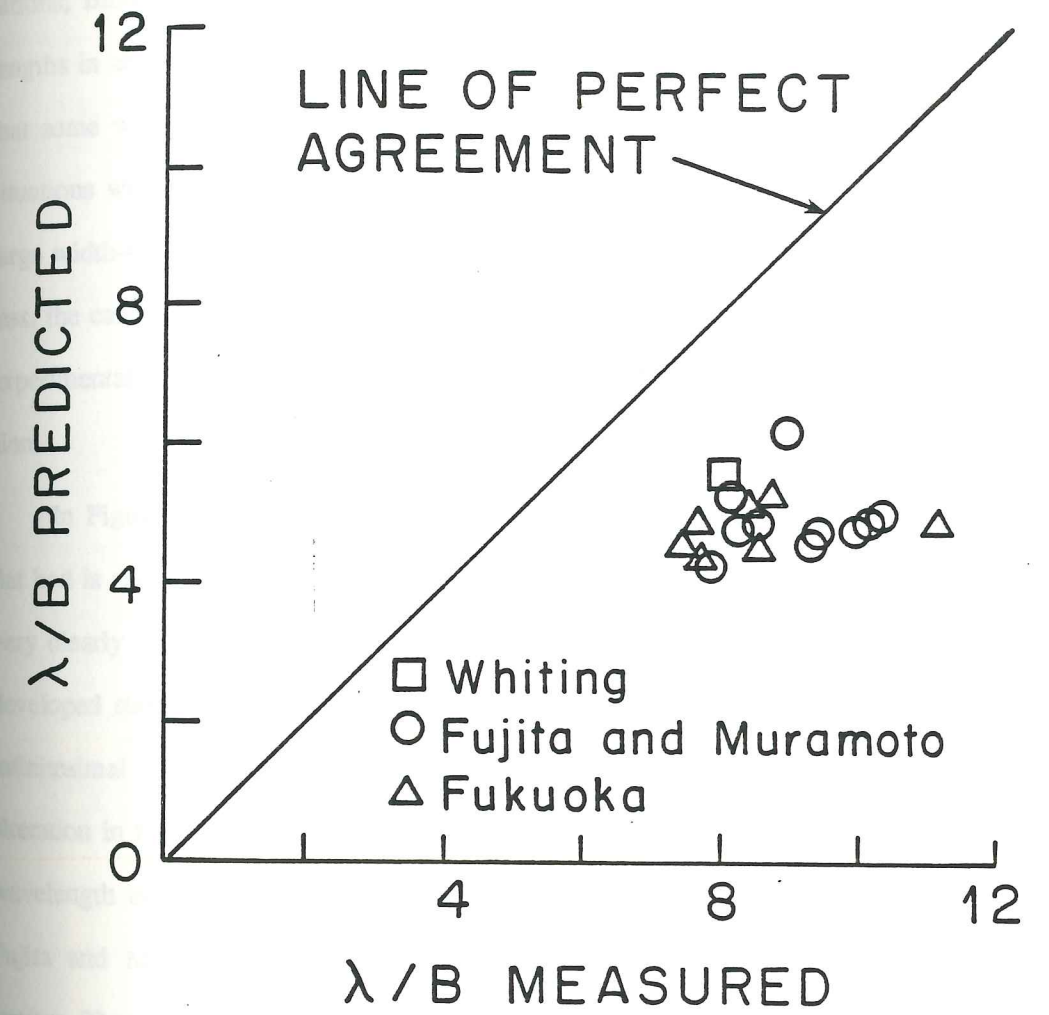
Figure 3.30. Predicted versus measured values of wavelength over width for various flume experiments.

theory presented by Blondeaux and Seminara (1984) also underpredicts the observed wavelengths for these cases, although their analysis used a different sediment transport relation and included a gravitational correction. In fact, using data from a wide variety of conditions, Blondeaux and Seminara found that the linear theory underpredicted observed bar lengths in about 75% of the experimental cases. Nevertheless, their computations did show that some wavelengths are slightly overpredicted by their theory. These cases may be for situations where the infinitesimal wavelength is strongly selected (i.e., rough streams with large width-to-depth ratios), so that the infinitesimal theory performs adequately. Nevertheless, the cases shown in Figures 3.29 are clearly poorly treated by the linear theory, and the experimental observations described by Fujita and Muramoto (1985) support this conclusion.

In Figure 3.31, the temporal evolution of a series of alternate bars from an initially flat bed is shown for one of the cases studied by Fujita and Muramoto (1985). This sketch very clearly shows the alteration of the wavelength of the bars as they grow to their well-developed state. The initial wavelength of the evolving bars is predicted very well by the infinitesimal theory, as one would expect. However, finite amplitude effects produce an alteration in this wavelength. This effect is not an isolated observation. In Figure 3.32, the wavelength evolution of alternate bars is shown for all the flume studies performed by Fujita and Muramoto. In all cases, the wavelength increases substantially as the bars evolve. Thus, it is not at all surprising that the linear theory predicts poorly the well-developed wavelengths of the bars. This observation also has important implications for the formation of meander bends.

In their excellent treatment of the bar-bend instability problem, Blondeaux and Seminara (1984) demonstrate that the alternate bar linear analysis substantially underpredicts the wavelengths of meanders. If true as stated, this would be surprising, since meander bends

Run H-2-1

t = 17'45"

0.35

45'53"   0.45   0.15   wave height of bar (cm)

0.70   0.35   0.50 0.40

76'56"   1.05   0.70   0.35 0.50

1.65   0.80   0.85   0.30 0.75

120'   2.80   2.35   0.80

0.95   3.15   1.80   0.80

200'   1.70   1.40   2.80   3.20

1.00   3.05   2.90

300'   1.75   3.20   3.35

2.60   2.30   0.85

0   5   10   15

X (m)
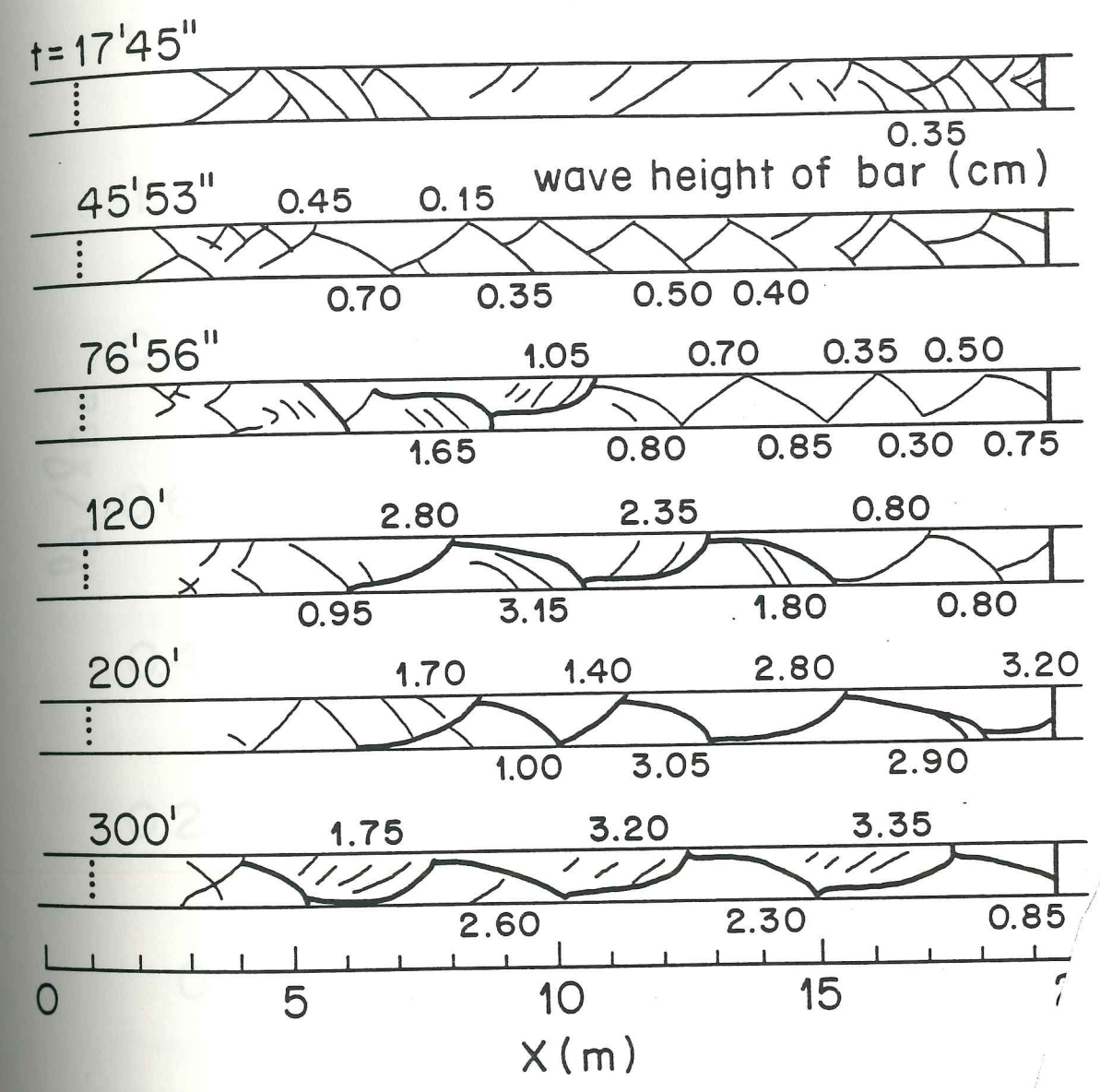
Figure 3.31. Sketch of alternate bar evolution in an initially flat-bedded channel. Reproduced from the work of Fujita and Muramoto [1985]. See Figure 3.37 for the experimental run conditions for run H-2. Numbers next to the banks represent bar heights in cm.
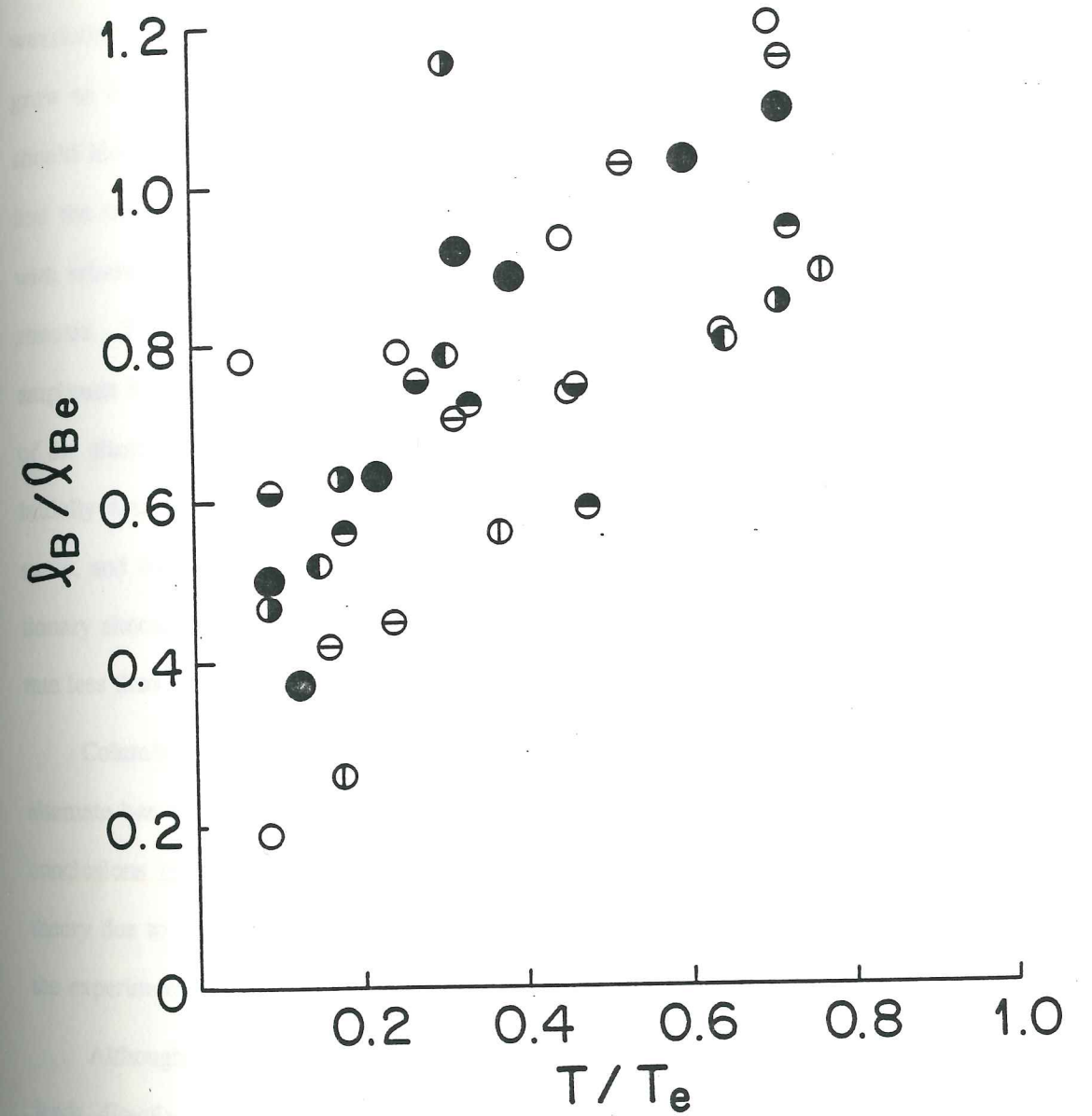
Figure 3.32. Bar wavelength evolution measured by Fujita and Muramoto [1985] in their experimental investigation. Each symbol corresponds to a different experimental run. T and l_b denote elapsed time and bar wavelength, respectively, while the subscript E refers to these variables in the equilibrium case.

are typically associated genetically with the formation of alternate bars. However, in light of the ideas discussed above, this is easily explained. Meanders are expected to form at the wavelength of well-developed alternate bars. If the wavelength of the bars increases as they grow to their equilibrium morphology, there is no reason to expect that the linear theory should identify the meander wavelength. Furthermore, the results of the linear theory show that the small amplitude wavelength is very poorly selected in smooth streams (low C_d) with relatively small width-to-depth ratios. These characteristics are typical of meandering streams. Thus, the linear theory is expected only to identify the wavelength for small amplitude features, while the meander wavelength is set by the finite amplitude wavelength of the alternate bars. One possible exception to this case in in a situation where the bed is initially flat, but there is some bank irregularity. The bank irregularity is fixed in a spatial sense, and therefore must force stationary bars. As is clear from the stability analysis, stationary alternate bars are still growing features (see Figure 3.21), although they amplify at a rate less than that of the fastest-growing features.

Columbini, Seminara, and Tubino (1986) constructed a weakly nonlinear theory of alternate bar development. While this theory seems to predict bar heights well, one of the conclusions of their analysis is that the adjustment to the wavelength found in the linear theory due to the weakly nonlinear effects is negligible. However, this is not in accord with the experimental evidence, and indicates the need for a fully nonlinear model.

Although the presentation of the linear theory here has been a lengthy digression, it leads directly back to the central subject of this chapter: the finite amplitude model. Clearly, the infinitesimal amplitude treatment yields important insight into the development of alternate bars. However, this theory yields only uncertain values of the bar wavelength, and little or no information about the finite amplitude shapes, migration rates, and heights of the bars. Since these quantities are precisely what one typically wants to know for

natural channels, the need for a finite amplitude bar evolution theory is clear.

3.5.2. Finite Amplitude Evolution

In this section, results of the finite amplitude evolution model are presented for the case of alternate bars for two cases studied by Fujita and Muramoto [1985]. In the first case, denoted by Fujita and Muramota as run C-2, the calculations concentrate on examining the evolution of the wavelength of the bar forms. The second calculation, which is for Fujita and Muramoto's run H-2, examines the full evolution problem, concentrating on the processes producing the stable morphology of the migrating features.

In Figure 3.33, the predicted evolution of run C-2 is shown. For this case, the initial bed of the straight channel was taken to be flat, with the exception of a small perturbation introduced at the cross-section furthest upstream. Subsequently, the computational grid was moved such that the initial point of perturbation remained at the upstream end of the computational grid. This effectively removes the migration of the bars from the problem, thereby allowing more precise observation of the alteration of bar wavelength as time passes. The experimental conditions for run C-2 are given in the caption of Figure 3.33.

For these conditions, the linear analysis predicts a fastest-growing wavelength of about five widths. Fujita and Muramoto [1985] report values of bar wavelength averaged over the entire inspection reach, as well as the value of wavelength found over what they call the "averaged" reach. The value found in the averaged reach apparently is the mean wavelength of a smaller number of bars well downstream of the flume entrance. Even in the case of the mean wavelength averaged in the inspection reach, the region near the upstream end of the flume was not considered. For run C-2, the initial half-wavelengths reported in the evolution process were 107 and 126 cm in the inspection reach and the averaged reach, respectively. The flume was 40 cm wide, so these measurements yield

RUN C-2
BED TOPOGRAPHY

40cm

T = 0

T = 23 min.

T = 39 min.

T = 1 hr. 18 min.

T = 2 hrs. 36 min.

T = 5 hrs. 51 min.
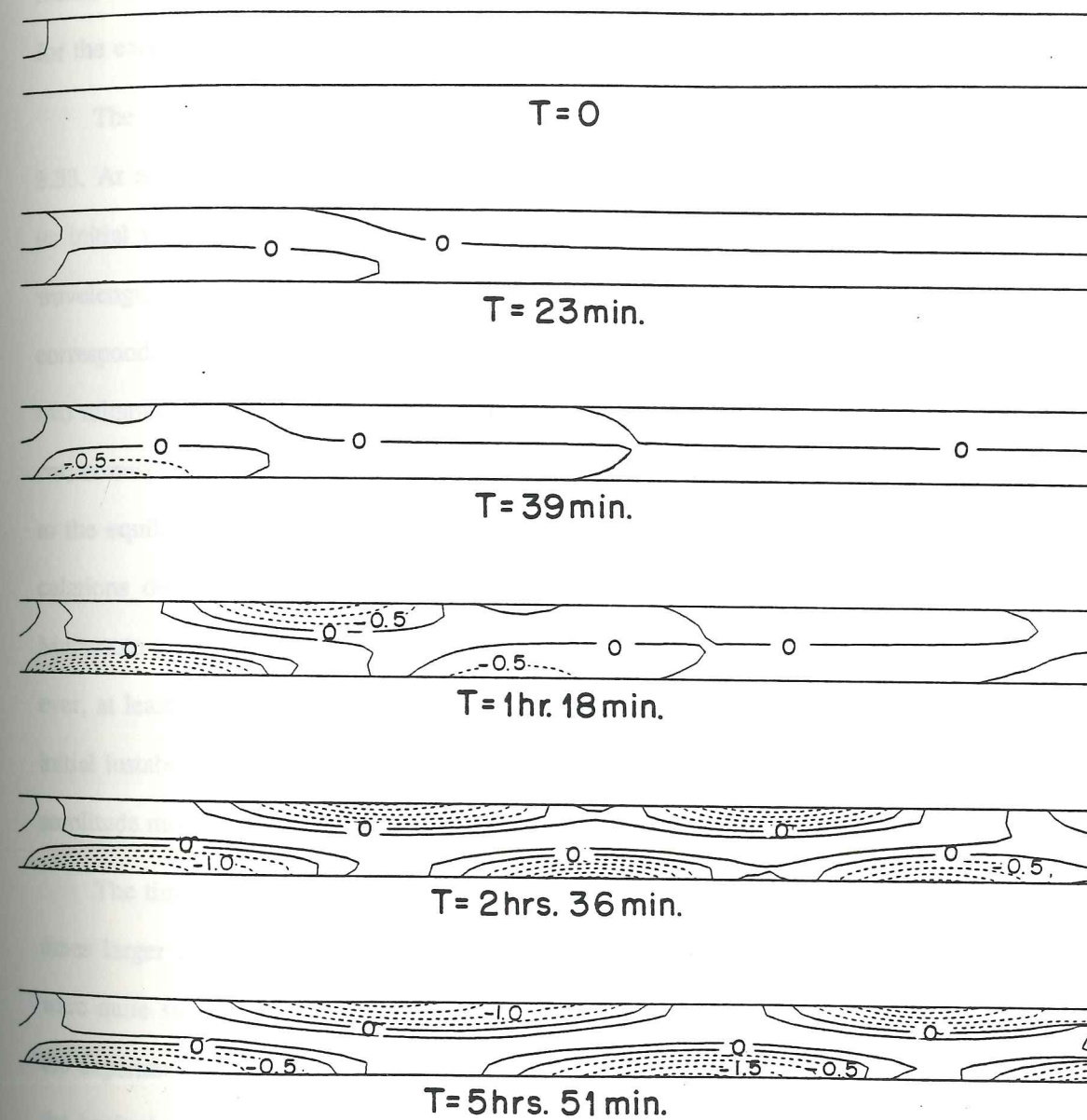
Figure 3.33. Evolution sequence for flume experiment C-2, performed by Fujita and Muramoto [1985]. The conditions for this run were as follows: channel width, 40 cm; mean depth, 1.26 cm; discharge, 1.95 liters/sec; slope, 0.0093; sediment size, 0.1 cm.

initial wavelength-to-width ratios of 5.3 and 6.3, which are in reasonable agreement with the results of the infinitesimal analysis. These values also are in good agreement with the results of the model displayed in Figure 3.33, from which a value of 5.5 widths is found for the earliest case in which a wavelength can be defined.

The tendency for the bar wavelength to increase with time is clearly shown in Figure 3.33. At equilibrium, the wavelength is about 7.5 widths, an increase of almost 40% over its initial value. After one hour and six minutes elapsed, Fujita and Muramoto report half-wavelengths in the inspection and averaged reaches of 177 and 206 cm, respectively, corresponding to wavelength-to-width ratios of 8.8 and 10.3. After two hours and forty two minutes, they report half-wavelengths in both the inspection and averaged reach of 145 cm, corresponding to a wavelength over width ratio of 7.25. This latter value is very close to the equilibrium wavelength observed in the calculations shown in Figure 3.33. The calculations do not reproduce the overshooting of the wavelength observed by Fujita and Muramoto [1985], and the physical reason for this behavior is not known at present. However, at least in this case, it is clear that there is a marked increase in wavelength from the initial instability to the well-developed bar form, and this increase is predicted by the finite amplitude model presented herein.

The time required to reach equilibrium in the numerical computations was about three times larger than that required in the experiments, although the predicted sediment fluxes were quite similar. The primary difference seems to lie in the initiation of bar growth. In the experiments, bar trains were distinguishable on the flume bed only a few minutes after the beginning of the run. In the numerical experiments, it took well over an hour before a train of bars was observed. This difference is probably due to the nature of the initial perturbation to the system. In the numerical model, a very small depth perturbation is introduced in order to start the evolution process. Typically, a bump with a height equal to

about 10% of the mean depth is introduced at one cross-stream section over approximately 20% of the width. This is a very small perturbation on the uniform flow situation, so the induced erosion and deposition rates are extremely small. In the experimental case, there are many sources of initial perturbation: small-scale bedforms, "patchiness" in the sediment transport field, and even waves on the free surface. The lack of all these random perturbations in the numerical calculations results in a much longer "spin-up" time for the system.

Some of the overprediction of time to reach equilibrium may also be due to the fact that vertical structure changes are neglected in the streamwise velocity field. The omission of these vertical structure changes results in an overprediction of the throughput of sediment at each bar front compared to sediment fluxes going into bar front migration. This occurs because the model underpredicts the rate of decrease of the boundary shear stress on a downstream-sloping face. This means that the rate of deposition on these faces will be underpredicted, and that, as a result, the rates of migration and growth of the bars will be underpredicted.

In Figure 3.34, predicted bed evolution is shown for run H-2 from Fujita and Muramoto [1985]. In this case, the computational grid is held fixed relative to the bed, so migration of the bars can be observed. As discussed briefly above, the calculation is started with a very small perturbation. If this is not done, the numerical solution will consist simply of the maintenance of the uniform flow and bed topography. The perturbation in the case shown was located in the center of the streamwise reach near the lower bank. The depth change was about 10% of the mean flow depth, and the cross-stream and streamwise scale of the perturbation were 0.2 widths and 1.0 widths, respectively. Other weak departures from uniform flow were also tested as initial conditions, including small perturbations to the surface elevation field and the upstream stress boundary condition, and the equilibrium topography was found to be independent of the form of the initial perturbation,
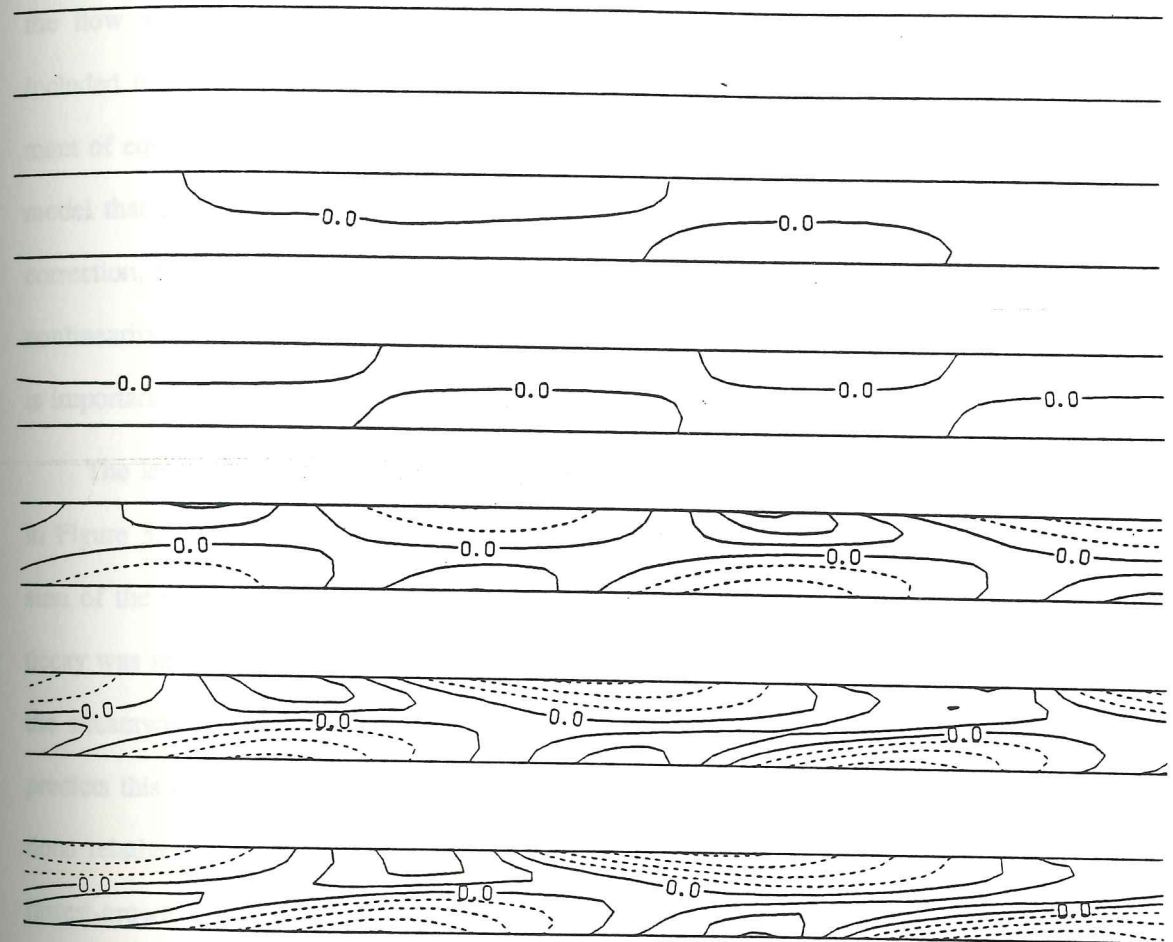
Figure 3.34. Model predictions of the evolution of bed topography for flume experiment H-2 of Fujita and Muramoto [1985]. The conditions for this run were as follows: channel width, 50 cm; mean depth, 2.11 cm; discharge, 4.02 liters/sec; slope, .0056; sediment size, 0.1 cm. The time interval between each plot is about one hour.

provided that the introduced departure from uniformity was very small.

The instability that leads to the formation of alternate bars has been discussed in depth in the section on the linear theory, and is related primarily to topographic steering of the flow around a bump. As the bars grow in amplitude, finite amplitude effects not included in the linear analysis become important and are, in fact, crucial to the establishment of equilibrium bar morphology. The features present in the finite amplitude evolution model that distinguish it from the linear analysis presented above are (1) the gravitational correction, (2) the production of helical flow due to streamline curvature, and (3) the full nonlinearity of the equations governing the flow and sediment transport. Each of these three is important in calculating equilibrium bar shapes.

The lengthening of the bar wavelength discussed above, which is also easily observed in Figure 3.34, is related to the nonlinearity of the convective accelerations. In the discussion of the infinitesimal analysis, the tendency for relatively short bars to grow slower or decay was related to the development of an inertial lag between the bar and the flow due to the streamwise advection of momentum. For finite amplitude bars, the linear theory underpredicts this inertial lag, because it underpredicts the magnitude of the convective accelerations relative to the zero-order pressure gradient and stress. Thus, the wavelength of the fastest-growing wave must increase as the degree of nonlinearity of the momentum flux terms increases.

In Figure 3.34, the tendency for the bars to form diagonal fronts across the channel is clear. This behavior is also shown in Figure 3.35. In this three-dimensional depiction of the equilibrium topography, both the tendency for diagonal front formation and a steepening of the bar fronts is clear. Initially, the scour pools tend to be roughly symmetrical, in reasonable agreement with the topographic form assumed in the linear theory. However, as the bars grow, the downstream faces of the diagonal fronts become much steeper than their
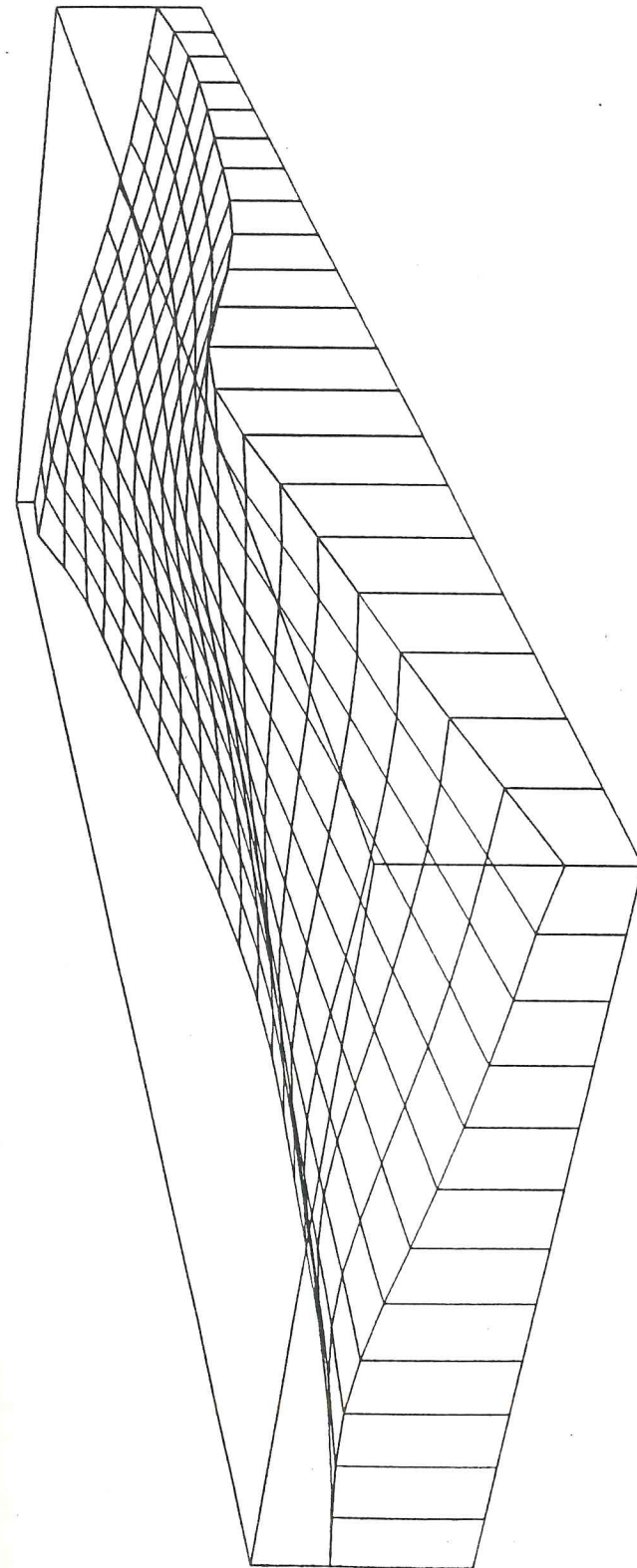
Figure 3.35. Three-dimensional plot of the equilibrium topography for run H-2. Note that the width has been exaggerated relative to the wavelength in order to make the three-dimensional structure of the bar easier to discern.

upstream surfaces. The steepening of the lee sides of the alternate bars is brought about in precisely the same manner as steepening of bedform lee faces. The nonlinearity in the stress and sediment transport relationships produce more rapid migration of the bar tops as they grow to finite amplitude. This produces deformation of the originally symmetrical shape, as found by Exner [reported by Leliavsky, 1955, p. 24]. In the case of two-dimensional bedforms, this process continues until flow separation and grain flow mechanisms become important. However, in the case of alternate bars, the flow is not directed perpendicularly to the diagonal bar front, and other mechanism are brought into play, like the production of helical flow.

The pattern of flow through a train of alternate bars is fairly well described by the meandering of the high velocity core from scour pool to scour pool. As the bars grow and the pools deepen, this meandering becomes more pronounced. This produces secondary circulation, as discussed in the development of the flow model. Streamline curvature in the horizontal plane produces a helical component of velocity perpendicular to that streamline, as well as an associated perturbation bottom stress. In Figure 3.36, an expanded view of the equilibrium bed contours are shown along with equilibrium bottom stress and helix strength results. In the bottom stress vector plot, the tendency of the flow to meander through the bars is evident. The production of secondary flow due to this meandering is demonstrated in the contours of helix strength. The secondary flow tends to produce a cross-stream stress component directed up the face of the bars. This opposes the tendency of both the gravitational and topographic steering effects to force sediment fluxes into the pool region. If the secondary circulation terms are suppressed in the model, much greater flow curvatures occur in conjunction with much more concentrated jets of high velocity and sediment flux. In other words, the secondary circulation acts to counteract the tendency for the flow to meander more and more strongly as the bars grow larger.

BED TOPOGRAPHY
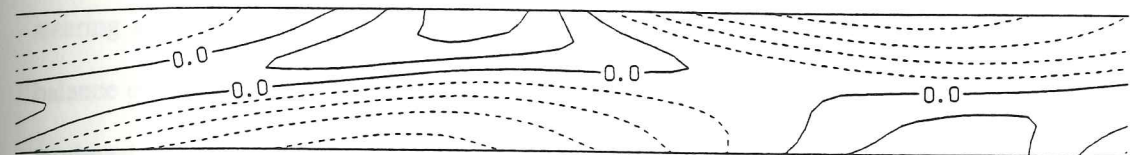
BOTTOM STRESS
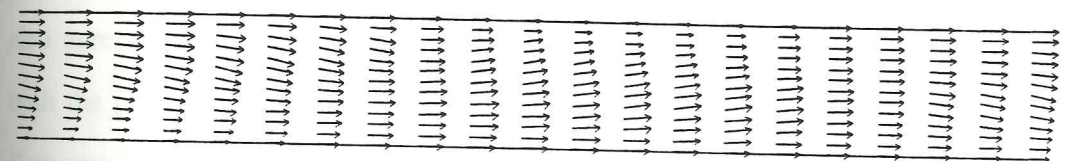
HELIX STRENGTH
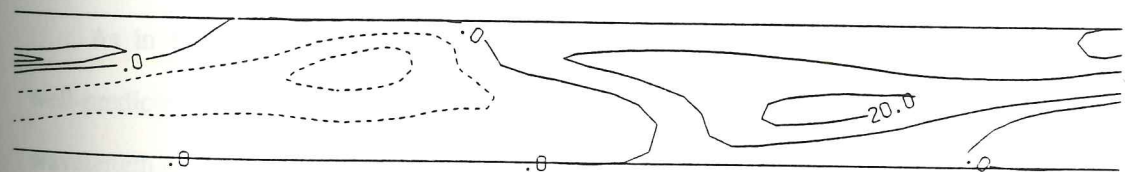
Figure 3.36. Equilibrium values of bathymetry, bottom stress, and helix strength predicted by the evolution model for run H-2. Contours for bottom topography are at intervals of 0.5 cm, while helix strength contours are shown at 10° intervals. The mean value of the boundary shear stress is about 11 *dynes/cm*².

This point can be made clearer by analogy with the point bar evolution and stability. In the point bar case, helical flow due to the curvature forced by the channel geometry causes the initial instability. As the bar grows, topographic steering effects act to oppose the tendency of the helical flow to cause erosion near the outer bank and deposition near the inner one. The final stability requires the inclusion of gravitational effects, topographic steering effects, and the secondary flow. In the case of alternate bars, the same sensitive balance eventually is obtained, but in a slightly different sequence. The initial instability is produced primarily by topographic steering but, as the bars grow, secondary circulation effects become important in determining the sediment transport fluxes on the bed. In this case, curvature of the streamlines due to the topographic steering produces the helical flow, rather than the channel curvature. The prediction of helical flow adjacent to alternate bars also agrees with the experimental measurements made by Leopold [1982], who observed both the presence of helical circulation and the occurrence of regions wherein the helical flow was in the opposite direction on either side of the channel centerline. This behavior is predicted to occur just downstream of the bar top, as shown in the central portion of the helix strength plot in Figure 3.36.

As in the case of run C-2, the fully developed wavelength of the alternate bars is well-predicted by the model. Fujita and Muramoto report an equilibrium bar half-wavelength of 213 cm. Since the flume width for run H-2 was 50 cm, this yields a ratio of wavelength to width of about 8.5. The value predicted by the evolution model is 8.2. The linear theory predicts that the fastest-growing wave has a ratio of wavelength to width of five, demonstrating the importance of the nonlinear effects.

The sketch of run H-2 presented by Fujita and Muramoto [1985] and reproduced here as Figure 3.34 indicates that the maximum amplitude of the observed bars (defined as the difference between the topographic minimum and maximum on any single bar) was about

three cm, in good agreement with the heights predicted by the model. Their sketch also indicates that the rate of bar migration was about 0.1 cm/sec. In contrast, the numerical calculation predicts a migration rate of about .03 cm/sec. This discrepancy is almost certainly due to the inability of the sediment transport and flow models to deal with the processes important on the steep downstream faces of the bedforms. As already discussed above, better treatment of this region requires both the inclusion of streamwise vertical structure changes in the model, and a more rigorous treatment of the effects of streamwise bed slopes in the sediment transport model.

3.6. Summary of the Bar Evolution Model

In this chapter, coupling of a fully nonlinear flow model with sediment transport calculations has been described. The resulting evolution model clearly reproduces the growth and stability of point bars in curved bends, as well as the growth of alternate bars in straight channels. The insight gained from examining results for these two fundamental bar types is easily generalized to more complex bar forms. In fact, although the results presented herein have concentrated on these two simple cases, the mathematical formulation is quite general. Thus, this model can be employed to investigate bar behavior in channels with complicated planform geometries. Importantly, the method presented allows calculation of both equilibrium topography and the temporal changes that occur in cases where the flow and the bed are not in equilibrium. Thus, this technique can also be used to investigate the behavior of complex bars for which discharge variations play a role.

Discrepancies between the model and empirical data appear results seem to be linked to the fact that the streamwise vertical structure is held constant in the fluid mechanical model. However, as argued earlier, modification of the similarity structure may be related to changes in the spatial structure of the turbulence field, as well as to spatial accelerations

and decelerations. To explore the interplay of these effects, and to gain physical insight into how changes in vertical structure are produced by topographic variations, the focus of this investigation now shifts to the case of two-dimensional bedforms. As discussed in the following chapter, the production and stability of these features is intimately linked to the vertical flow structure.

4.1. Overview

A striking feature of many natural beds on which sediment transport occurs is the deformation of those beds into trains of waves. For flows with low Froude numbers, these bedforms are typically classified as ripples or dunes, depending on the bed morphology. Their equilibrium (fully-developed) shapes are determined by complex interactions between the flow, the bed geometry, and the sediment transport field; the bedform is created by the flow and, conversely, the flow is acted on by the bedform. The result of this coupling is that neither the local nor the spatially averaged velocity field can be accurately predicted without knowledge of the bed geometry. Furthermore, a detailed physical understanding of these flow-sediment-bed interactions comprises the basis for developing better methods for computing effective roughnesses of channels in which ripples or dunes are present, thereby permitting formulation of more accurate stage-discharge relationships. This makes an understanding of the interaction between the flow and the bed morphology of considerable importance to hydrologists interested in rivers and streams with erodible beds. Similarly, sedimentologists attempting to interpret paleoenvironmental conditions using segments of bedforms preserved in the stratigraphic record must have the ability to relate the observed geometric features of those bedforms to the flows that created them. An understanding of the flow-bedform interaction is also part of making accurate predictions of sediment transport over rippled or duned beds, since the form drag on the bedforms must be calculated and extracted from the total boundary stress to obtain the component of the boundary shear stress related to sediment movement. Thus, the problem of characterizing the interaction of the flow, sediment transport, and bed geometry to make precise predictions of each is of

fundamental importance in several diverse areas of environmental science and engineering.

Previously, this problem has been investigated theoretically in several ways. Most investigators have used classical linear stability analyses as a starting point [e.g., Kennedy, 1963; Engelund, 1970; Smith, 1970; Fredsoe, 1974; Richards, 1980; Kobayashi and Madsen, 1985]. While these analyses yield insight into the mechanisms causing the initiation of ripples and dunes, it is important to realize that the extension of these results to the finite amplitude situation is predicated on an assumption that the least-stable wavelength identified in the small amplitude theory is not altered by the introduction of finite amplitude phenomena. Unfortunately, observations indicate that this is not the case for ripple and dune fields; bedform sets tend to change in wavelength structure while growing to their fully developed form from a small initial perturbation [Yalin, 1977, p. 212; Raudkivi, 1966]. In addition, it is finite amplitude phenomena, such as wake formation, that ultimately set the height, steepness, and shape of bedforms. While a few of these stability analyses contain parts of the finite amplitude problem, none provides a complete treatment of the flow separation problem and, as a result, none can be expected to make accurate predictions of the velocity and boundary shear stress fields over typical well-developed bedforms. A classical stability analysis primarily indicates whether or not a ripple or dune will form; such an analysis yields very little information about the geometric characteristics of stable bed features and the effects that these features have on the flow, a point clearly made by Fredsoe [1982], and Sumer and Bakioglu [1984].

The principle finite amplitude effects governing the geometry of well-developed bedforms in low Froude number flows are: (1) the deformation of a sinusoidal disturbance into an asymmetric feature, as explained by Exner [in Leliavsky, 1955, p. 24], (2) flow separation and wake production resulting from that deformation, and (3) the modification of this wake by nonhydrostatic effects as the bedform grows in height. The wake region has a

substantial effect on both the flow velocity over the bedform and on the spatial pattern of boundary shear stress. Owing to the sensitivity of bedform geometry to the fluid mechanical character of the near-bed region, wake effects must be included in considerations of finite amplitude stability [Smith, 1970; Fredsoe, 1982; McLean and Smith, 1986].

In recognition of this situation, Fredsoe [1982] developed a finite amplitude model using the wake data presented by Smith [1970] and Bradshaw and Wong [1972]. This semi-empirical model predicted the geometry of bedforms using boundary shear stress fields measured downstream of an abrupt decrease in bed elevation (usually referred to as a backward or negative step) and was one of the first efforts made toward developing a model for bedform geometry that includes the mechanical processes of flow separation and wake formation. To remove the dependence of predicted flow fields on empirical analyses of wake data that inevitably oversimplify salient components of the fluid dynamical situation, McLean and Smith [1986] developed a simple model for low Froude number flow over finite amplitude two-dimensional bedforms of typical shape. This model, which includes the dominant effects of the wake, was shown to reproduce flow and boundary shear stress fields that had been measured over large amplitude dunes in the Columbia River with reasonable accuracy.

In the present study, three improvements have been made in the model presented by McLean and Smith. First, short wavelength effects are incorporated in a more accurate manner in the wake region, thereby improving the predictive capability of the model for features with wavelengths that are short compared to the flow depth. Second, a method is employed whereby the vertical structure of the flow well above the bedform is determined from the coalescing of wakes of upstream bedforms. This permits detailed examination of the effects that bedforms have on the interior flow structure, as is required for calculations of form drag and effective roughness, as well as for accurate suspended sediment

computations in situations where some fraction of the bed material is fine enough to travel as suspended load. Third, the technique described by McLean and Smith, which is valid only from the reattachment point of the wake to the crest of the downstream bedform, is extended to the region downstream of the crest but upstream of the reattachment point, thereby providing a spatially complete set of velocities and shear stresses.

To test the accuracy of the model in general and the validity of these improvements in particular, model predictions are compared to a set of high-resolution velocity measurements taken over a field of immobile bedforms in a recirculating laboratory flume. The measurements were made using a three-beam laser-Doppler velocimeter, with which it is possible to obtain both horizontal and vertical velocities very near the bed without disrupting the flow. The comparison demonstrates both the necessity of including separation effects and the validity of the improved finite amplitude model.

In a brief discussion near the end of this chapter, the flow model is shown to accurately reproduce the subtle interactions between the velocity field and the bed topography that ultimately are responsible for the growth and finite amplitude geometry of natural bedforms.

4.2. Formulation of the Model

The dynamics of turbulent flows over well-developed bedforms is complicated by the fact that different regions of these nonuniform flows are characterized by different turbulence structures and length scales. In particular, these flows typically contain regions in which the mean and fluctuating velocity fields are primarily wake-like, other regions which have the scaling and structure of a boundary layer, and still others in which the principal response to the boundary nonuniformity is wave-like. While the dominant processes in

each of these regions may be treated separately using turbulence closures based on similarity arguments or available computational algorithms, it is much more difficult to treat the complete multiply-scaled problem without resorting to ad hoc assumptions or to a model for the turbulence that is not physically based. An alternative approach is to treat the flow in a piecewise fashion, using suitable formulations for each region and then matching the flow fields for each of these regions in an appropriate manner. Using this technique, a solution for the entire flow field is found by satisfying matching conditions between the various regions in the flow, rather than by performing a full numerical integration of the primitive equations. This alternative approach is taken in the chapter at hand. In the model presented herein, regional flow solutions are combined with matching constraints on the velocity and shear to calculate a complete flow field. This method is predicated on the observation that the flow is governed by relatively simple, low-order momentum balances in both the wake and the boundary layer regions. The disadvantages of neglecting higher order terms are far outweighed by the gain in physical insight into the governing processes and the enormous decrease in computational complexity afforded by such a model.

The method used in this investigation is an extension of the approach presented by McLean and Smith [1986]. Their model divides the flow into three distinct regions, as shown in Figure 4.1. Near the boundary, the growing boundary layer downstream of the reattachment point is treated using a regular perturbation expansion about a zero-order logarithmic profile. Above the internal boundary layer, the flow is modeled using the far-field wake theory presented by Schlicting [1979, p. 739]. The matching conditions enforced between the wake and internal boundary layer require that both the velocity and shear be continuous, and that the pressure gradient driving the internal boundary layer be set by the Bernoulli pressure at the bottom of the wake. Above the wake, the height of which is set by the far field solution, the flow is assumed to be quasi-inviscid, and the flow field is

QUASI-INVISCID INTERIOR REGION

$z = \eta(x)$

REATTACHMENT
POINT (X = 0)
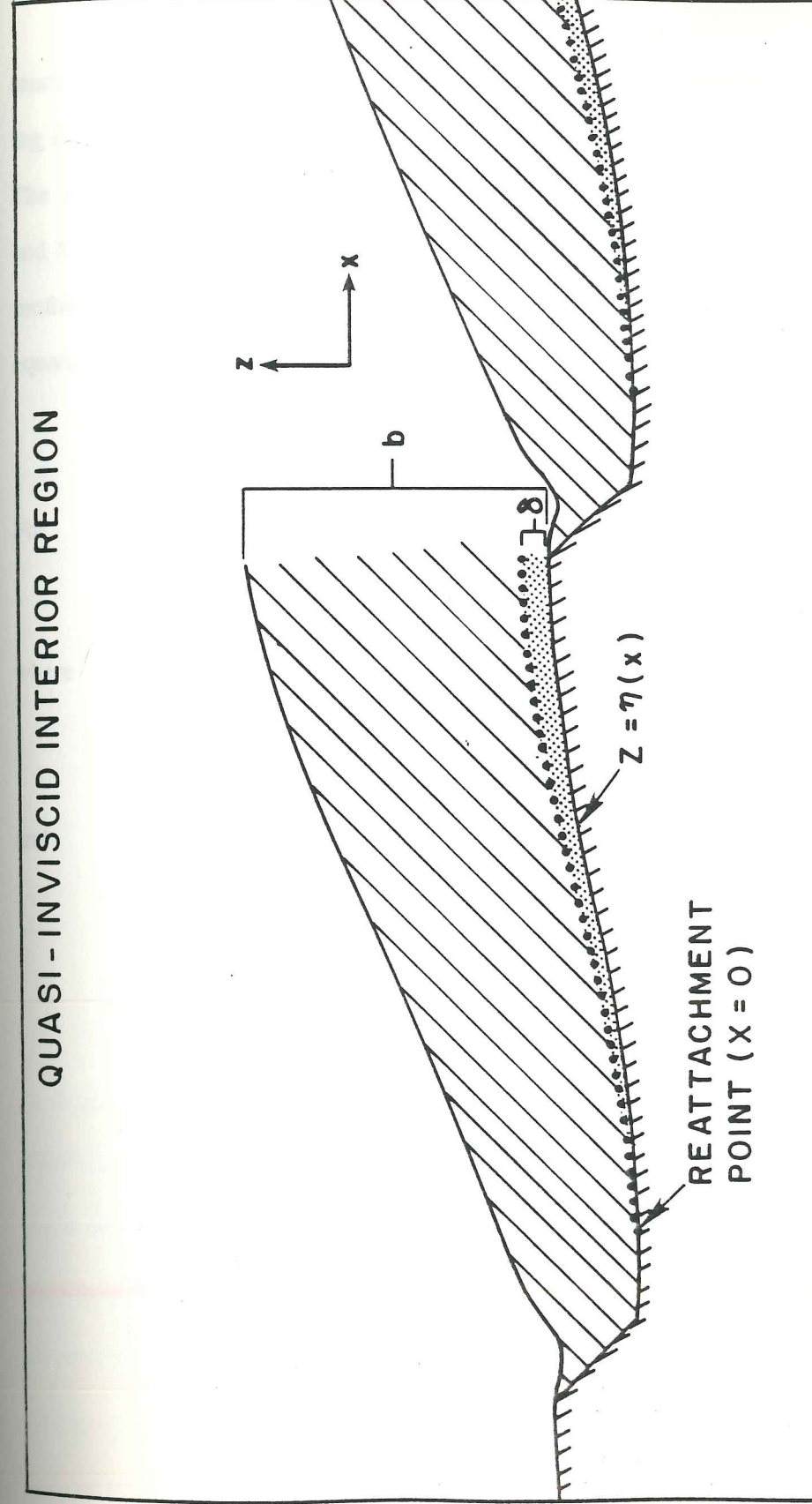
Figure 4.1. Schematic diagram depicting typical bedform geometry along with the boundary layer, wake, and interior regions of the flow. The height of the internal boundary layer developing downstream of the point of reattachment is denoted by δ, while b denotes the height of the wake associated with flow separation at the bedform crest immediately upstream. In the coordinate system used here, z is the vertical distance from an arbitrary datum, and x is the horizontal coordinate, the origin of which is chosen at the point of reattachment.

171

treated by combining a potential flow solution with a spatially-averaged logarithmic weighting function, and requiring that the velocity be continuous with that at the top of the wake. The ramifications of this approach are discussed in detail by Smith and McLean [1977], and McLean and Smith [1986]. Combining the solutions for the three regions, the velocity profiles at any location downstream of the reattachment point are given by the following equations:

For $\quad z_0 < z - \eta \leq \delta$

$$u = u_0 + u_1 \tag{4.1}$$

where

$$u_0 = \alpha U_\delta \ln \frac{z - \eta}{z_0}$$

and

$$u_1 = \frac{\alpha \delta}{2k^2} \left\{ \left[\frac{dU_\delta}{dx} - \frac{\alpha U_\delta}{\Delta} \frac{d\Delta}{dx} \right] \left[\zeta \left(\ln \frac{\zeta}{\zeta_0} \right)^2 - 5\zeta \ln \frac{\zeta}{\zeta_0} \right. \right.$$

$$+ 9(\zeta - \zeta_0) - \frac{\zeta_0}{2} \left(\ln \frac{\zeta}{\zeta_0} \right)^2 - \left[\frac{1}{\alpha} - 5 + 9\alpha \right] \ln \frac{\zeta}{\zeta_0} \right]$$

$$- \frac{U_\delta}{z_0} \frac{dz_0}{dx} \left[\zeta \ln \frac{\zeta}{\zeta_0} - 3(\zeta - \zeta_0) + \frac{\zeta_0}{2} \left(\ln \frac{\zeta}{\zeta_0} \right)^2 - (1 - 3\alpha) \ln \frac{\zeta}{\zeta_0} \right]$$

$$\left. + \frac{1}{\rho \alpha^2 U_\delta} \frac{\partial \rho_1}{\partial x} \left[(\zeta - \zeta_0) - \alpha \ln \frac{\zeta}{\zeta_0} \right] \right\}$$

For $\quad \delta \le z - \eta \le b$

$$u = \beta U_\delta \left[1 - g(x) f\left[\frac{z-\eta}{b} \right] \right] \qquad (4.2)$$

where

$$g(x) = A_2 \left[\frac{x + x_{0g}}{C_D H} \right]^{-\frac{1}{2}} \qquad f\left[\frac{z-\eta}{b} \right] = \left[1 - \left[\frac{z-\eta}{b} \right]^{\frac{3}{2}} \right]^2$$

and

$$b = 2 A_1 C_D H \left[\frac{x + x_{0b}}{C_D H} \right]^{\frac{1}{2}} \qquad \beta = \left[1 - g(x) f\left[\frac{\delta}{b} \right] \right]^{-1}$$

For $\quad b \le z - \eta \le h$

$$u = \beta U_\delta \left[\frac{B u_{*t}}{k} \ln\left[\frac{z-\eta}{z_{0t}} \right] \right] \left[1 + \frac{2\pi}{\lambda} \eta \frac{\cosh\left[\frac{2\pi(z-h_0)}{\lambda} \right]}{\sinh\left[\frac{2\pi h_0}{\lambda} \right]} \right] \qquad (4.3)$$

In these equations, z is defined to be height above an arbitrary datum, z_0 is the roughness length, $z = \eta$ is the elevation of the bed, δ is the height of the internal boundary layer, U_δ is the velocity at the top of the boundary layer, and $\alpha = (\ln \frac{\delta}{z_0})^{-1}$. Furthermore, k is von Karman's coefficient (= 0.40), ζ and ζ_0 are $(z - \eta)/\delta$ and z_0/δ, respectively, and the quantity Δ is the nondimensional boundary layer height, defined as δ/z_0. The horizontal structure function g(x), the wake height b(x), and the similarity function $f(\frac{z-\eta}{b})$ are set from the

Schlicting wake solution, as are the constants A_1 and A_2, which are equal to 0.40 and 1.38, respectively. The two-dimensional wake solution presented by Reichardt [see Schlicting, p. 742] could be used just as well, but here the Schlicting solution is chosen, following the work of McLean and Smith [1986]. In fact, the differences in the two solutions are very small. In the expressions for the wake height and the horizontal structure function, x_{0b} and x_{0g} are the virtual origins of the wake and the momentum deficit, respectively. C_D is the obstacle drag coefficient, which is set empirically. In the expression for the flow in the interior region, h is the local flow depth, h_0 is the mean flow depth, H and λ are the height and wavelength of the bed form, and B is defined using the spatially averaged flow model of Smith and McLean [1977] such that the spatially averaged flow over the bedform is approximately given by a logarithmic profile characterized by u_{*_t} and z_{0t}.

Using these equations along with the matching conditions described above and a constraint that the streamwise discharge remains constant, McLean and Smith [1986] obtained two strongly coupled ordinary differential equations for the nondimensional height of the internal boundary layer, Δ, and the velocity at the top of the boundary layer, U_δ. They are:

$$\frac{dU_\delta}{dx} = R_1(x)U_\delta + R_2(x) \tag{4.4a}$$

$$\frac{d\Delta}{dx} = R_3(x)\Delta + R_4(x) \tag{4.4b}$$

where R_1 and R_2 are strong functions of Δ and R_3 and R_4 are strong functions of U_δ. The derivation of these equations is presented in detail in Appendix 1 of McLean and Smith's paper, and will not be repeated here. The numerical solution of these equations along with the piecewise flow model yields the horizontal and vertical velocity field over the bedform,

as well as the boundary shear stress necessary for carrying out sediment transport calculations.

When averaged over a wavelength, the expression presented above for the interior flow (4.3) gives an outer log profile characterized by u_{*t} and z_{0t}, which are the shear velocity and roughness length including the effects of form drag on the bedform. To use equation (4.3) in a particular problem, a method must be developed for relating the skin friction and roughness length to the total boundary shear stress and roughness length u_{*t} and z_{0t}. McLean and Smith used a semi-empirical method that they had developed earlier [Smith and McLean, 1977] to accomplish this task, and one of the goals of the research described herein is to develop an appropriate theoretical approach to this part of the nonuniform flow problem.

4.2.1. The Stacked Wake Model

The basic physical process responsible for producing an outer spatially-averaged log profile is precisely the same as the one responsible for the logarithmic profile in hydraulically rough, turbulent boundary layer flow. In both cases, the logarithmic or quasi-logarithmic velocity profile is caused by the outward diffusion and interaction of wakes associated with locally nonuniform flow over roughness elements on the boundary. Thus, an alternative to the application of McLean and Smith's semi-empirical techniques for closing the interior flow problem is to develop a model for the interaction of wakes as the momentum defects diffuse outward from the boundary, and to employ that model to predict the flow structure in the interior. For the case of hydraulically rough flow, this is relatively difficult, since the obstacles are typically steep, three-dimensional, irregularly spaced, and of varying sizes. However, in the bedform problem examined here, these difficulties are minimized.

In keeping with this idea, the flow outside the internal boundary layer in the model is

treated by stacking up the wakes of upstream bedforms. This method, which is shown schematically in Figure 4.2, both removes the need for the Smith and McLean [1977] form drag closure and makes possible the prediction of the development of outer flow structure in a streamwise transition from a flat to a duned bed, as discussed below. Following McLean and Smith [1986], it is assumed that, outside the internal boundary layer, the wake of each bedform can be approximated by the Schlicting far-field wake theory with the wake centerline conformed to the boundary. However, if this technique is employed for approximating the vertical structure of the streamwise velocity throughout the flow depth, the model is explicitly limited to the long wave bed topography. In other words, if acceleration of the flow over the bedform is assumed to have no effect on the vertical structure, intermediate and short wave responses are precluded. Since typical bedforms cannot be treated as long-wave features, this is undesirable. This problem is rectified by including the lowest order potential flow vertical structure as a weighting function on the wake solution. Thus, the wake solution is modified by the nonuniform vertical acceleration associated with intermediate and short wave responses, as required by the ratio of the wavelength of the bed feature to the flow depth. This approximation is justified by noting that, outside the internal boundary layer, the mean momentum and the turbulence are being advected together and, therefore, are affected by an inviscid, wave-like distortion in a similar manner. The potential flow shear does not produce a lowest order change in the turbulence field. This reasoning indicates that the potential flow response may be included as a multiplicative weighting function on the wake solution for the mean flow, which leads to the following expression for the vertical structure in each of the wake regions shown in Figure 4.2:

For $\quad (z_m)_i \leq z - \eta \leq (z_m)_{i+1}$
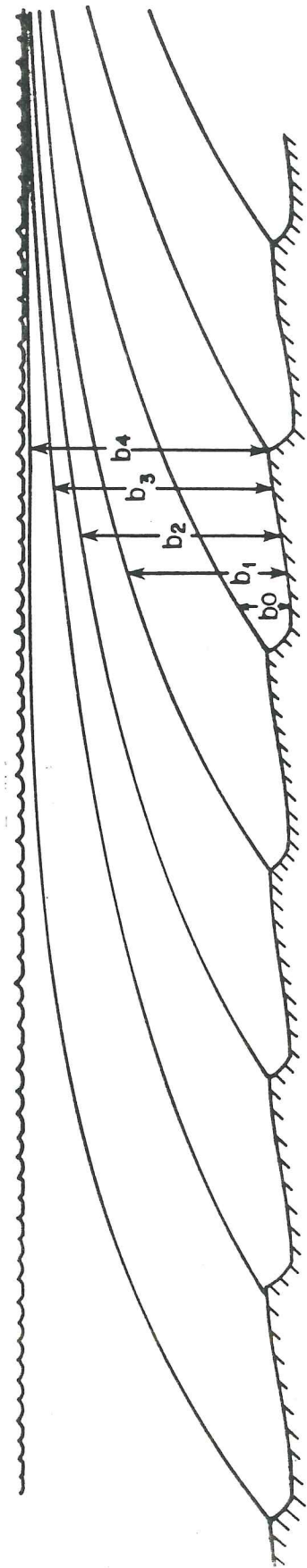
Figure 4.2. Diagram of the wake heights over a train of bedforms, where b_i denotes the heights of wakes emanating from upstream dune crests. The vertical structure of the flow above the internal boundary layer is set by "stacking" wake solutions, as described in the text.

$$u = B_i \beta U_\delta \left[1 + \frac{2\pi}{\lambda} \eta \frac{\cosh\left[\frac{2\pi\left[z - h_0\right]}{\lambda}\right]}{\sinh\left[\frac{2\pi h_0}{\lambda}\right]} \right] \left[1 - g_i\left[x\right] f\left[\frac{z - \eta}{b_i}\right] \right] \qquad (4.5)$$

where

$$b_i(x) = 2A_1 C_D H \left[\frac{x + x_{0b} + i\lambda\lambda}{C_D H}\right]^{\frac{1}{2}} \qquad g_i(x) = A_2 \left[\frac{x + x_{0g} + i\lambda\lambda}{C_D H}\right]^{-\frac{1}{2}}$$

and

$$\beta = \left\{ \left[1 + \frac{2\pi}{\lambda} \eta \frac{\cosh\left[\frac{2\pi\left[\delta - h_0\right]}{\lambda}\right]}{\sinh\left[\frac{2\pi h_0}{\lambda}\right]} \right] \left[1 - g_0\left[x\right] f_0\left[\frac{\delta}{b_1}\right] \right] \right\}^{-1}$$

and where

$$i = 0, 1 \ldots N \quad .$$

In these equations, $(z_m)_i$ are the matching heights between the stacked wakes, and N is set such that the wakes stack up to the free surface. In accordance with the matching between the internal boundary layer and the lowest wake proposed by Smith and McLean,

$$(z_m)_0 = \delta \qquad \text{and} \qquad B_0 = 1.$$

This approach neglects nonlinear interactions between the wake structure and the nonhydrostatic part of the pressure field; however, these terms can be shown to be of higher order in a perturbation expansion about the wake solution, provided the obstacle

height is small compared to its wavelength. This condition, which is well satisfied by natural bedforms, ensures that the response of the interior flow to the bed topography can be separated into two parts, one of which is primarily inviscid or wave-like, and the other of which is primarily wake-like. It is worth noting that this method allows nonhydrostatic effects to be retained even in the wake region nearest the bed, in contrast to the original McLean-Smith model. This substantially improves the predictions of the model in the case of bedforms with wavelengths comparable to, or smaller than, the flow depth (ie., intermediate and short wavelength features).

In order to apply (4.5), which replaces equations (4.2) and (4.3) in the original Smith-McLean formulation, matching conditions must be specified between the various wakes. The matching used here requires that both the velocity and the shear be continuous across the interfaces between wakes, in keeping with the matching conditions used at the top of the internal boundary layer. When applied to (4.5), these matching conditions can be cast as simple algebraic expressions for B_i and the matching heights, $(z_m)_i$. Enforcing the condition that the velocity be continuous at the matching height leads to the following relation for the values of B_i:

$$B_i = B_{i-1} \left[\frac{1 - g_{i-1} f\left[\dfrac{z_{mi} - \eta}{b_{i-1}} \right]}{1 - g_i f\left[\dfrac{z_{mi} - \eta}{b_i} \right]} \right] \qquad i = 1, \ \cdots N \qquad (4.6)$$

The condition that the shear be continuous at the matching heights leads to a polynomial expression for $q = (z_m)_i^{1/2}$ as follows:

$$a_1 + a_2 q^2 + a_3 q^5 + a_4 q^6 + a_5 q^8 = 0 \qquad (4.7)$$

where

$$a_1 = \left[\frac{g_i - g_i g_{i-1}}{b_i^{3/2}} - \frac{g_{i-1} - g_i g_{i-1}}{b_{i-1}^{3/2}} \right] \qquad a_2 = \left[\frac{g_i g_{i-1} - g_i}{b_i^{5/2}} - \frac{g_i g_{i-1} - g_{i-1}}{b_{i-1}^{5/2}} \right]$$

$$a_3 = \left[\frac{2 g_i g_{i-1}}{b_{i-1}^{3/2} b_i^{3/2}} (b_{i-1}^{-1} - b_i^{-1}) \right] \qquad a_4 = \left[\frac{g_i g_{i-1}}{b_{i-1}^{3/2} b_i^{3/2}} \left[b_i^{3/2} - b_{i-1}^{3/2} \right] \right]$$

$$a_5 = \left[\frac{g_i g_{i-1}}{b_i^{5/2} b_{i-1}^{5/2}} \left[b_{i-1}^{1/2} - b_i^{1/2} \right] \right]$$

Solution of these polynomials yields the matching heights between the wake layers, $(z_{m)_i}$. In all cases, there is only one physically meaningful root to these eighth order polynomials, so no ambiguity is involved. Equations (4.1), (4.4), and (4.5) along with solutions of (4.6) and (4.7) yield a complete specification of the horizontal velocity field and the boundary shear stress. Vertical velocities are calculated using the continuity equation. Both velocities and shears are continuous throughout the flow.

4.2.2. Flow in the Separation Eddy

The solution obtained from the model discussed up to this point is based on a streamwise integration of (4.4a) and (4.4b), beginning at the reattachment point and progressing up the stoss side of the dune to the crest. As noted above, that solution along with the boundary layer and stacked wake formulations yields the entire flow field. However, this does not include the region upstream of the reattachment point and downstream of the dune crest. The ultimate goal of this research is to combine results of the flow field calculations with sediment transport models to make quantitative predictions of bedform characteristics, so it is clear that the flow model must be extended to include the separation zone over the lee face of the dune. This is especially important for predicting suspended sediment transport and depositional patterns.

To treat the lee eddy region, essentially the same model is employed, but instead of integrating equations (4.4a) and (4.4b) from the reattachment point downstream, the equations are integrated from the point of reattachment upstream to the dune crest. Thus, there is a growing boundary layer with upstream directed velocity matched to the wake solution. This is shown schematically in Figure 4.3. From (4.5), it is clear that specification of the reattachment point determines the position of the virtual origin of the momentum deficit, x_{0g}. Since the velocity must be zero at the bottom of the wake by definition, $x_{0g} = C_D H A_2^2$. If this definition is employed in the near-field region, however, the wake height approaches zero well downstream of the obstacle crest and, at the same point, the upstream directed near-bed velocity approaches an infinite value. To avoid this clearly nonphysical behavior, we introduce an effective origin for the wake height that is physically reasonable, and we use a simple symmetry argument to develop an appropriate x-dependence for the horizontal structure function, $g_0(x)$, in the eddy region.

To prescribe a virtual origin for the wake which is realistic, x_{0b} is given a different value than x_{0g}. In the far field, both x_{0b} and x_{0g} are much less than x, so the momentum integral is still satisfied to lowest order, as in the Schlicting solution. An obvious choice for x_{0b} is the value which forces the wake height to go to zero at the crest. In practice, better results are obtained by setting x_{0b} such that the wake height goes to zero slightly upstream of the crest. This accounts for the finite thickness of the boundary layer at the point of separation, and thereby allows parameterization of the effect of the transformation of the boundary layer into a free shear layer at this point. The virtual origin in our calculations is set by requiring the wake height at the crest to be equal to the thickness of the separating internal boundary layer.

The x-dependence of the velocity in the lee eddy is approximated using the simple argument that the near bed velocity in the eddy is roughly symmetrical about a point
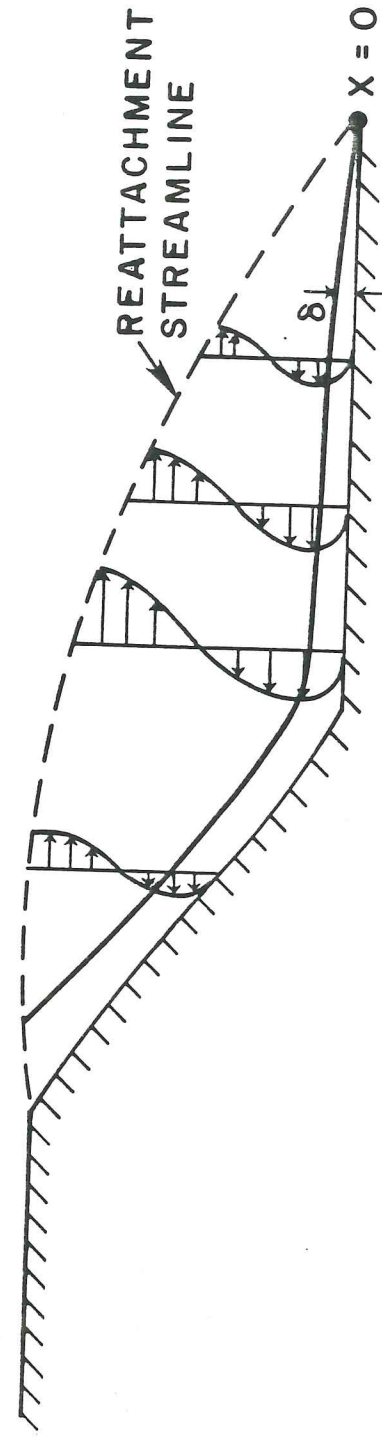
REATTACHMENT
STREAMLINE

δ

$X = 0$

Figure 4.3. Schematic diagram of velocity profiles in the lee eddy region. The maximum upstream-directed velocity is found near the eddy midpoint, and the velocity profiles can be roughly approximated as similar above δ, where δ is the height of the internal boundary layer.

midway between the bedform crest and the reattachment point. From (4.5), it is easy to see that at the reattachment point and at the separation point at the crest, the function $g_0(x)$ must have a value of unity. In the case of the reattachment point, $g_0(x)$ is unity by definition, whereas near the crest $g_0(x)$ must approach one because we require that the upstream directed velocity in the wake to go to zero, in keeping with the definition of the point of separation. Applying the symmetry argument described above, it is clear that $g_0(x)$ must be symmetrically distributed between the bedform crest and the point of reattachment. Since the velocity near the bed is directed upstream in the lee eddy (u is negative), $g_0(x)$ must also be greater than unity in this region. The maximum value of $g_0(x)$, which is required to occur at the eddy midpoint, yields the maximum upstream velocity as a percentage of the velocity above the lowest wake region. This number has been measured experimentally for flows over backward steps and is typically between 18% and 22%. Eaton and Johnson [1980] measured a value of 21%, while Etheridge and Kemp [1978] found this ratio to be about 18% in their experiments. These numbers agree well with the measurements made over the cement dunes used in the experiments described herein. Thus, the maximum of the function g(x) must be around +1.20.

The model presented here uses a semi-empirical function for $g_0(x)$ based on the above constraints. Although this approach clearly strains the similarity assumption, the constraints on the x-dependence of the velocity are quite strong. The function $g_0(x)$ is required to be unity at the crest and reattachment point and to have a value of about +1.20 at the point midway between them. The simplest smooth function that achieves these values and satisfies the symmetry argument is as follows:

$$g_0(x) = 1 - 4\Omega \frac{x}{x_r} \left[1 + \frac{x}{x_r} \right] \qquad x < 0 \qquad (4.8)$$

where x_r is the reattachment distance and Ω is the ratio of maximum upstream-directed velocity to the velocity above the lowest wake, as described above. This near-field expression for $g_0(x)$ is used in integrating equations (4.4a) and (4.4b) from the reattachment point backwards to the crest of the bed feature, thus providing a spatially complete solution. Although the x-dependence of the velocity field is semi-empirical in this region, the rough symmetry of the lee eddy and the well-constrained value of the maximum upstream-directed flow allow very little room for error in the predicted velocity field. As mentioned above, one of the goals of this research is to be able to employ this fluid dynamical model along with sediment transport algorithms to predict bedform geometry under a wide range of conditions. The geometry of the lee side of bedforms over which flow separates is primarily determined from gravitational effects and, as a result, the geometry is insensitive to minor errors in the velocity and stress fields in this region, so there is no advantage to be gained from formulating a more complicated model for the lee eddy.

In synopsis, the model presented here is based on the combination of equations (4.1) and (4.5) with the constraints that both the velocity and the shear be continuous in the vertical. These conditions result in a pair of tightly coupled differential equations for the velocity at the top of the boundary layer and the height of the boundary layer, (4.4a) and (4.4b), along with a set of algebraic expressions, (4.6) and (4.7), that are solved for the matching heights between the wake regions from upstream bedforms. Equations (4.1) through (4.7) are solved numerically, and the solutions are employed along with the assumed vertical structure functions (4.1) and (4.5) to calculate horizontal and vertical velocity fields, as well as boundary shear stresses. This approach removes the need for a semi-empirical form drag closure, and permits detailed examination of the coupling between the bedforms and the flow field, both through the inclusion of the appropriate potential flow (inviscid) response, and by retaining the effects of coalescing of upstream

wakes.

4.3. Experimental Procedure

The primary goal in developing the fluid dynamical model described in the previous section is to provide a tool whereby reasonably accurate predictions of flows over two-dimensional finite amplitude bedforms may be made. Before applying the model to natural bedforms it is desirable to compare predictions from the model with carefully made measurements of flow over a typical dune field. If this is to be a comprehensive test, the measurements must include velocities determined in the nonuniform internal boundary layer, as well as measurements in the wake and interior regions of the flow. To resolve the structure of the internal boundary layer, which is intimately related to the skin friction (the actual shear stress on the bedform surface), it is imperative that a high density of measurements be taken very near the bed. Unfortunately, this region is also the one in which it is most difficult to procure accurate data, and most, if not all, velocity measurements made previously are inadequate in this regard.

Owing to the lack of a comprehensive data set, a simple flume experiment was designed to obtain the information necessary to test the model. The flume employed is a recirculating, "racetrack" style system (see Figure 4.4) consisting of two straight sections, each about eight meters in length, connected by two 180° circular annuli. One of the two straight sections is used as the test section, while the other contains a paddlewheel drive system. The channel is approximately 70 centimeters wide and flow depth can range up to about 30 centimeters. Typical mean velocities of 50 cm/sec result in Reynolds numbers around 10^5. The development of secondary currents in the upstream bend was avoided by the emplacement of several curved baffles within the annulus. Velocity profiles taken on a

PADDLEWHEEL DRIVE SECTION
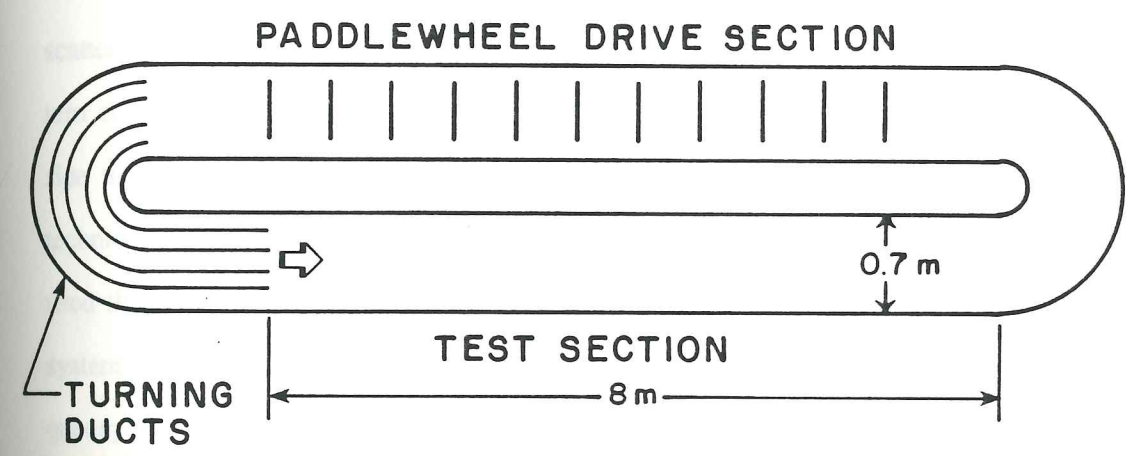
0.7 m

TURNING DUCTS

TEST SECTION

8 m

Figure 4.4. Plan view of the recirculating flume employed in the flow experiments.

flat bed at various cross-stream and downstream locations in the test section indicated that the unperturbed flow was uniform, as desired. Sidewall corrections were calculated using the method of Williams [1970], and were found to be negligible; there was a maximum 3% error in the boundary shear stress due to wall effects. A more complete description of the flume and driving mechanism has been given elsewhere [Nowell et al., 1986].

Velocity measurements in the flume were made with a TSI laser-Doppler velocimeter. Using this technique, it is possible to make high-accuracy measurements very near the bed without disrupting the flow. Velocities are obtained by measuring the frequency of light scattered by a particle following the flow when it crosses the fringes of an interference pattern created by crossing two beams of coherent light. Since the laser beams originate outside the flow and the scattered light is received by photomultipliers outside the flow, this technique allows velocities to be measured noninvasively. The actual system employed used three beams crossed at a point, so two velocity components could be measured. The system also used frequency shifting on the beams to provide greater accuracy. The frequency shift is set such that the fringes in the interference pattern are moving at a velocity near that of the mean flow, thereby improving the capability of the velocimeter to resolve small deviations about that mean velocity.

The output of the photomultipliers is filtered and then the Doppler frequencies are found from the raw data by a TSI signal processor. These data are then reduced to velocities and various statistics are calculated using an Apple microcomputer. Probability distribution functions, mean velocities, turbulent intensities, and Reynolds' stresses (if desired) are plotted on the computer screen only a few moments after each measurement is made. All velocity measurements presented in this paper are calculated from an average over at least 256 particles passing through the sampling volume. The velocimeter averages over particles, not time, so the actual number of particle measurements procured in each case

should be set by requiring that the time needed to take an entire sample be much longer than the time scale associated with the turbulent fluctuations. This depends on the number of scatterers in the flow, the sensitivity of the photomultipliers, and the confidence levels set in extracting Doppler frequencies from the raw data. A complete description of the theory and technical details involved in laser velocimetry can be found in Durst et al. [1974].

Typically, there are enough small particles even in tap water to provide an adequate reflected signal. To ensure that the particles scattering light from the measurement volume formed by the intersection of the beams were actually following the flow, however, the water used was pumped through a 5 micron filter, thereby retaining only particles that follow the flow very closely, even on very small scales.

Despite the ever-improving ability to make accurate velocity measurements at a point in laboratory flumes, there are still some inherent problems in trying to measure velocity profiles at carefully specified positions over natural bedforms. These problems are related to the lack of flow stationarity and the difficulty in determining local bedform geometry, both of which are associated with the migration of the bedforms. In light of these problems and the need for high accuracy to test the essential features of the theory described above, synthetic bedforms of typical natural shape were constructed for the experiments. Because these features were immobile, the flow was stationary, and because the geometry could be set very accurately in the construction process, any ambiguity about the shape of the obstacles was avoided.

The bedforms used in the experiment were constructed of concrete. This material has the advantage that it is inexpensive, simple to cast into exact geometries, and is much denser than water, thus removing the need to fasten the bedforms in the flume bottom. The mold was constructed of very fine sand using a simple wooden template. Using this

method, the mold can be easily reconstructed with high accuracy after each use, so we were able to make several bedforms of identical shape. The shape selected was a half-cosine for the stoss and a simple 30° slip face for the lee side, as shown in Figure 4.5 along with the actual dimensions of the features. The surfaces of the concrete bedforms were painted with polyurethane paint and then covered with natural fine sand grains while the paint was still wet. This procedure yields values of z_0 that agree very well with the empirical relations of Nikuradse [in Schlicting, 1979, p. 620].

The measurements were made with five bedforms in the flume, as shown in Figure 4.6. This allowed examination of the development of the interior flow structure due to coalescing of the upstream wakes, and also ensured that the flow structure over the last two dunes was typical of what one would measure over natural trains of bed waves. This is discussed in more detail below.

4.4. Results of the Calculations

4.4.1. Evaluation of the Similarity Assumption

The most crucial assumption in the model is that the far-field similarity profile for the wake velocity and the wake height expression are valid relatively near the obstacle. In the classical wake formulation, the domain of validity of the far field solution is defined as the region where the momentum integral (J) may be linearized [see, for example, Schlicting, 1979, p. 733]. The two-dimensional version of J is given by

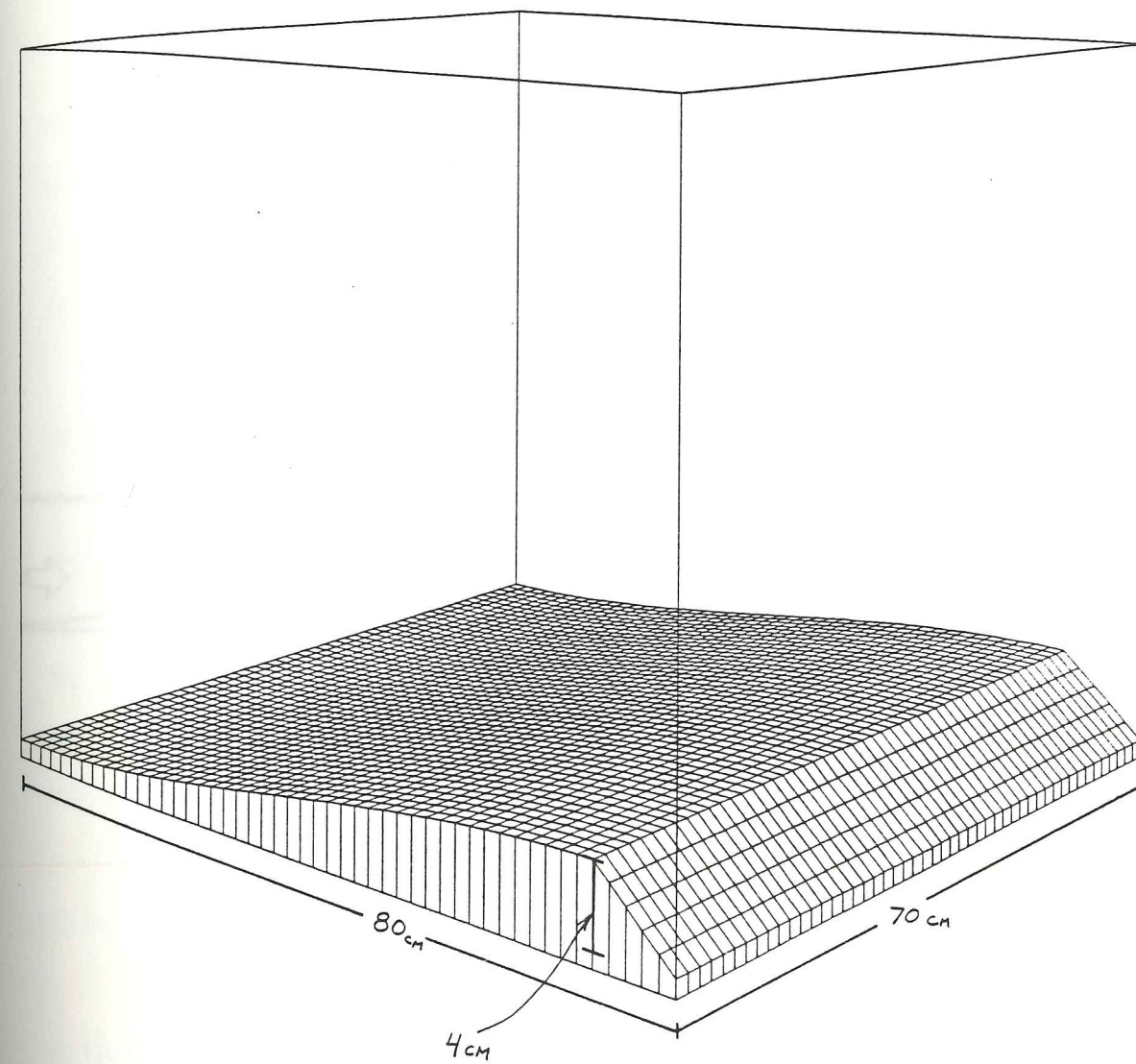$$J = \rho \int_0^b (U_b - u)u\,dz = \tfrac{1}{2}\rho C_D H U_b^2 \qquad (4.9)$$

Figure 4.5. Shape and dimensions of the cement bedforms used in the flume experiment. The stoss side shape is given by a sine wave between $-\pi/2$ and $\pi/2$. The models, which are 70 cm wide, fit tightly against the flume walls.
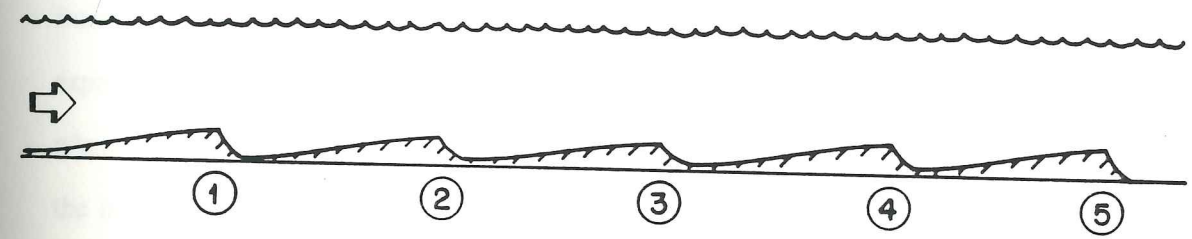
Figure 4.6. Cross-sectional view of the dune models in the flume, along with the numbering system employed.

where U_b is the velocity at the top of the wake.

Thus, the far-field solution is only considered to be valid if the deficit velocity $U_b - u$ is small compared to U_b. Typically, this condition is met only well downstream of the obstacle ($x > 40H$), and certainly is not valid in the region where the model employs the similarity solution. However, the lack of validity of the linearized momentum integral does not necessarily indicate that the vertical and horizontal similarity structure functions are incorrect and, in fact, the experimental observations indicate that departures from the similarity structure are small, even in the near field.

The drag coefficient for the cement sand waves was calculated from a direct evaluation of the momentum integral using measured velocity profiles and wake heights digitized from measured velocity profiles. Results of these integrations are shown in Figure 4.7. As expected, the value of the momentum integral increases rapidly in the near field region, where pressure forces are large compared to the downstream momentum flux. However, the momentum deficit approaches a constant value about 10 dune heights downstream of the crest, as shown in Figure 4.7. The drag coefficient is found to have a value between 0.5 and 0.6. Comparing this information with the wake height calculations suggested the use of an overall best value of about 0.6 for the synthetic dunes, and this value was used in all calculations presented below.

In Figure 4.8, the height of the wake over one of the dunes in the flume experiment is shown. These data were obtained by digitizing the wake height from velocity profiles. To avoid subjectivity in the measurements, three investigators independently digitized the wake heights from 14 vertical profiles of downstream velocity taken at various streamwise locations over a single dune. These three values were averaged and a simple linear regression was performed on the logarithms of the data points taken beyond the reattachment point. As shown in Figure 4.8, the best power law fit to the data downstream of the reattachment
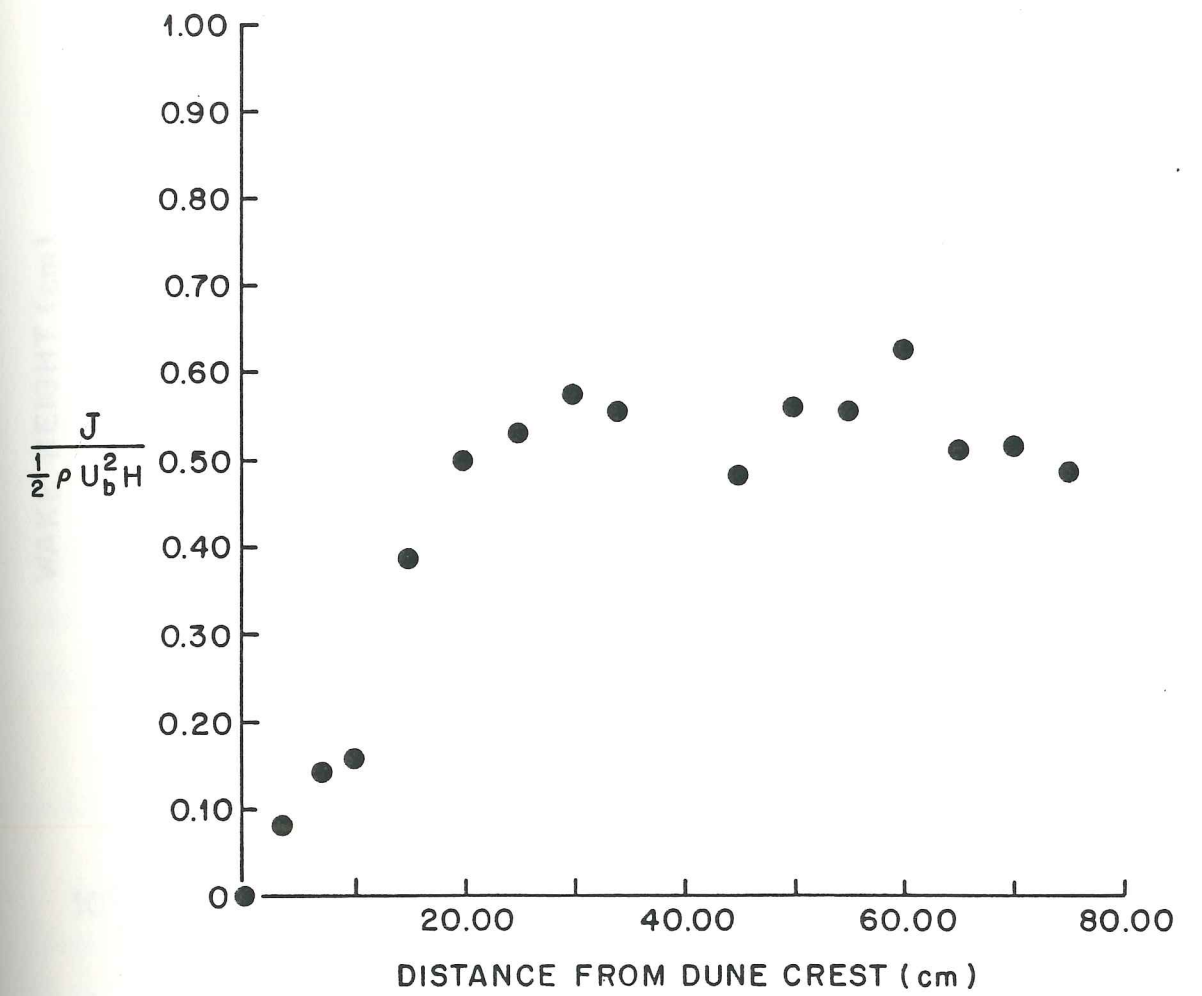
Figure 4.7. Effective drag coefficient versus distance downstream from a dune crest, as calculated from numerical evaluations of the momentum integral using velocity profiles measured over dune 4 (see Fig. 4.6).
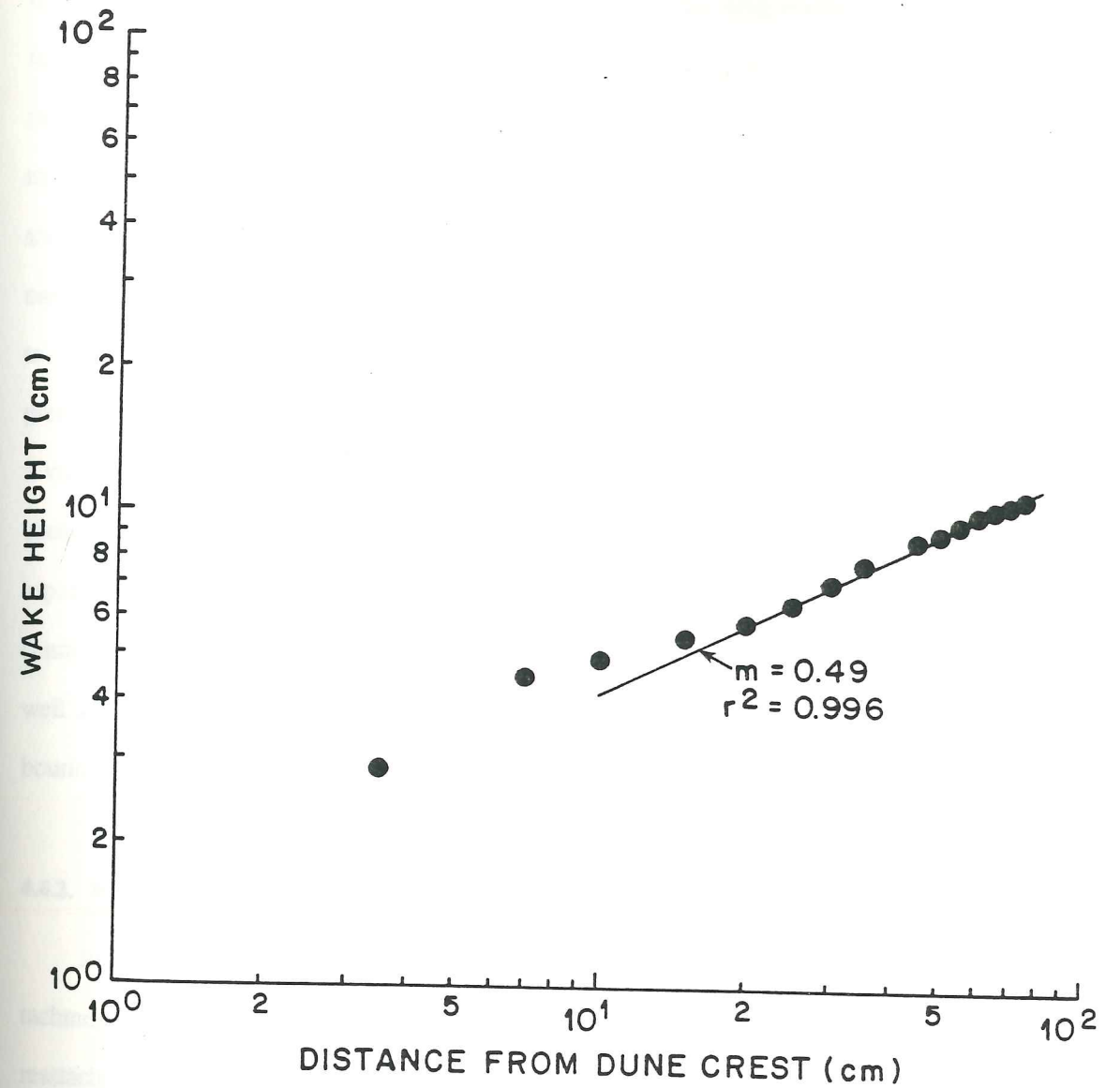
Figure 4.8. Logarithmic plot of the measured wake height versus distance downstream from the crest of dune 3. The regression shown was performed only on the points downstream of the reattachment point (11 measurements). The best power law fit using a least squares criterion was found to have an exponent of 0.49, in excellent agreement with the value of 0.50 found by Schlicting using similarity theory.

point gives a wake height dependent on downstream location to the 0.49 power, very close to the 0.5 power predicated by the similarity solution. The drag coefficient for this fit was found to be about 0.7. As mentioned above, the similarity solution is quite accurate in predicting the near field x-dependence of the wake height, even though the linearized momentum integral is a poor approximation. In Figure 4.9, the digitized wake heights are shown along with the far field wake heights calculated from the Schlicting solution for the case where the virtual origin is set at the crest and the case where the virtual origin is set to yield a wake height at the obstacle crest equal to the boundary layer thickness. The fit presented in Figure 4.8 is also shown. As discussed above, good results are obtained using a virtual origin at the dune crest, but even better results are obtained if the virtual origin is chosen upstream of the dune crest, in order to account for the finite thickness of the separating shear zone. The calculations presented below employ a virtual wake origin three centimeters upstream of the dune crest. This value both predicts the observed wake heights well and yields a wake height at the obstacle crest equal to the thickness of the internal boundary layer, as discussed above.

4.4.2. Reattachment Lengths

In addition to the drag coefficient, the model described above requires that the reattachment point be specified. For each discharge at which measurements were made, the reattachment point was found accurately by making streamwise profiles of downstream velocity at a distance of about 0.2 cm from the bed using the laser-Doppler velocimeter. To ensure that these crucial measurements were accurate, velocities measured consisted of an average over 2048 samples, rather than the 256 used in most other measurements. Results for a typical case are shown in Figure 4.10, indicating that reattachment of the shear layer occurs at about 3.75 heights downstream from the obstacle. This value is lower than that
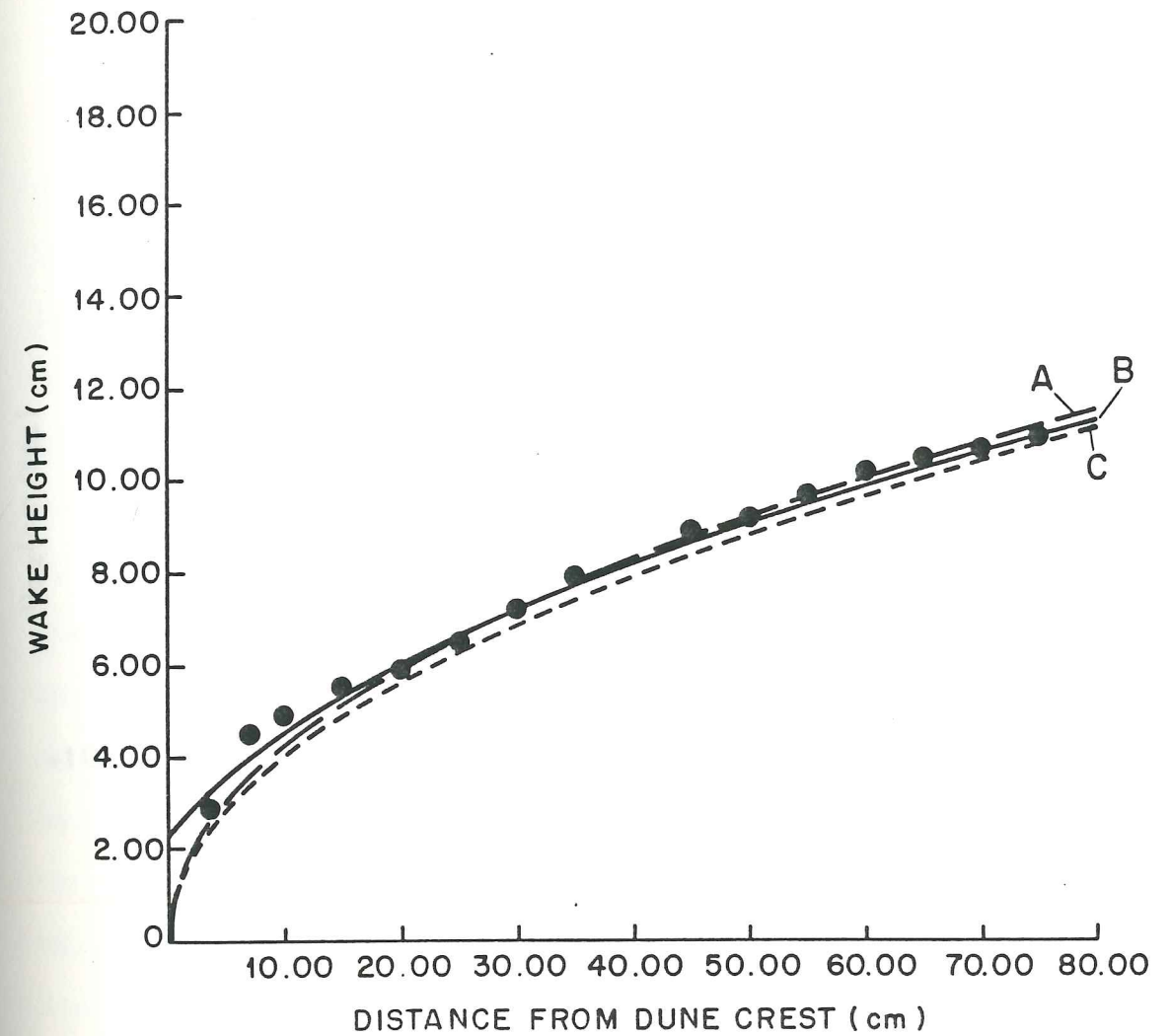
Figure 4.9. Linear plot of the digitized wake heights shown with heights calculated from the Schlicting far-field expression using a drag coefficient of 0.60 and the best far-field fit to the measured heights (see Fig. 4.8). Curves (C) and (B) are the far-field results for the case in which the wake origin is chosen at the dune crest, and for the case in which the virtual origin is chosen such that the wake height at the crest is equal to the boundary layer thickness at the crest, respectively. Curve (A) is the best power law fit to the points downstream of the reattachment point, as shown in Fig. 4.8.
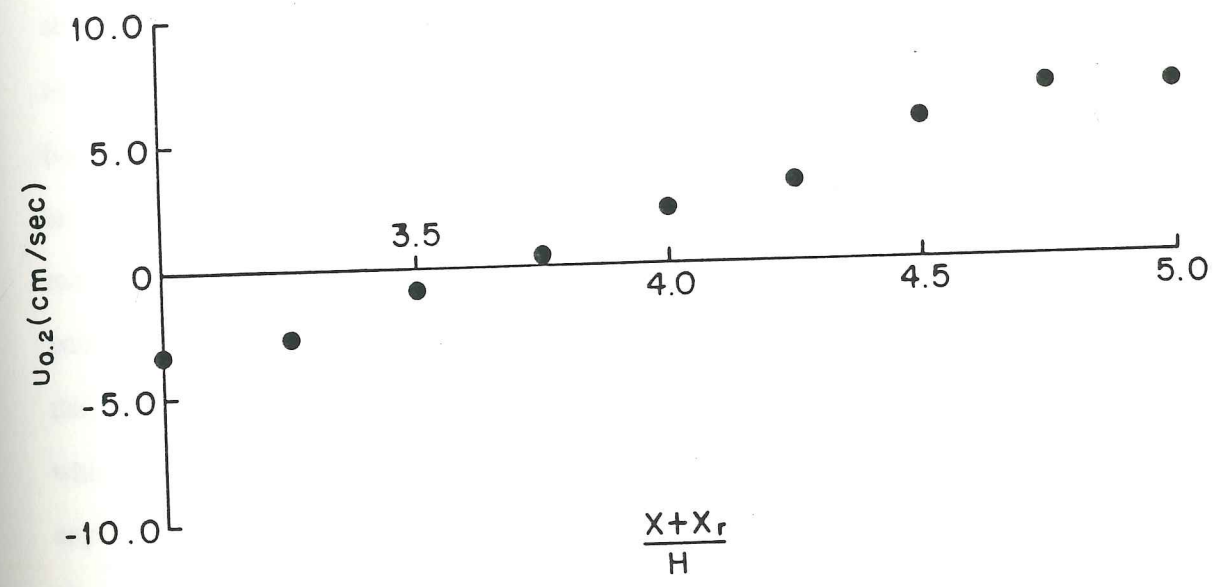
Figure 4.10. Velocity measurements taken 2 mm above the bed versus nondimensional distance from the obstacle crest. The distance from the crest is denoted $x + x_r$ and H is the bedform height. For this case, $Re \doteq 10^5$.

typically found in flows over negative steps, for which reattachment lengths are usually observed to be between 5 and 8 step heights, depending on (1) the flow Reynolds number, (2) the thickness of the boundary layer on the obstacle, and (3) the pressure gradient forcing over the obstacle caused by the expansion of the flow.

The reattachment distance is essentially independent of Reynolds number as long as the flow is fully turbulent. For the experiments presented herein, the Reynolds number was about 10^5, so this condition was certainly met and the dependence of the reattachment length on Reynolds number can be assumed to be negligible. The effect of the initial boundary layer height is weak unless the boundary layer is thicker than the obstacle height, as shown in Eaton and Johnston [1980]. This was clearly not the case in the dune experiment, so this effect was also unimportant. Because the thickness of a developing turbulent boundary layer scales with the roughness length z_0, the effect of the initial boundary layer thickness is often parameterized in terms of the surface roughness of the obstacle over which flow separates [e.g., Engel, 1981]. Observations made downstream of synthetic triangular dunes by Engel [1981] demonstrated that reattachment lengths decrease as roughness increases (i.e., the initial boundary layer gets thicker), as expected. However, in accordance with the conclusion of Eaton and Johnson, Engel's data clearly show that this effect becomes negligible if the obstacle height is large compared to the thickness of the internal boundary layer. Engel parameterized this effect in terms of the steepness of his plywood bedforms and concluded that the roughness effect on reattachment was only important for bedforms with small stoss-side slopes (ripple indices greater than 20). However, the steepness of the models used in his experiment was set by holding their height constant and varying the length of the stoss side. Thus, the steeper dunes have shorter stoss sides and offer less distance over which the internal boundary layer can develop before separation occurs. This effect, in conjunction with the fact that the acceleration produced by the bed

the step. For the case of bedforms, the acceleration is greatest near the bottom, because it is topographically forced and the response is not entirely hydrostatic, so this effect may be expected to be even stronger than predicted by Keuhn's measurements. Engel [1981] measured the reattachment distance downstream of synthetic triangular bedforms of varying steepness and showed that the downstream acceleration had a substantial effect on this length. His measurements indicated that the reattachment distance is significantly reduced compared to that found for a flat bed if the slope of the bedform downstream is greater than 0.02, corresponding to a ripple index of 50. For ripple indices of 14 and 20, which are typical of natural bedforms, Engel found reattachment lengths of between 4.2 and 4.4 dune heights. Thus, one expects the reattachment distance downstream of well-developed two-dimensional dunes to be 3.5 to 4.5 dune heights, in accord with the measurements over the cement bedforms, and that this length would be the same or even shorter for ripples, since they are steeper than dunes and, therefore, produce greater near bed accelerations. This reasoning is supported by the observation that ripple indices (defined as the ratio of obstacle wavelength to height) may be as low as seven or eight for two-dimensional current ripples, while sediment transport considerations demand that the sediment flux and shear stress be directed downstream at all points on the stoss side. This constraint must be met for the ripple to migrate downstream without a change in shape in a bedload-transporting flow, provided that the sediment flux is determined entirely by the time-averaged boundary shear stress. If the sediment flux is zero at the reattachment point (where the boundary shear stress is zero), reattachment must occur at the topographic minimum between adjacent crests for ripples produced by bedload transport. In reality, turbulence near the point of reattachment alters the position of this point relative to the topographic minimum somewhat, but this relatively small shift does not change the essential geometrical constraints on the ripple problem. If the reattachment point/topographic minimum is located more than four heights downstream from the bedform crest, which corresponds to half the wavelength

of the shortest ripples, the stoss side of these ripples must be quite steep. Thus, the topographically-induced acceleration will be large and we expect that the reattachment point will be forced back toward the obstacle crest. Although further experimental investigation of the link between topographically-induced acceleration and reattachment length certainly is in order, this mechanism seems to provide a powerful feedback between the morphology of the bedform (i.e., steepness of the stoss side) and the spatial extent and structure of the wake region nearest the bed. The coupling between the reattachment distance and the downstream acceleration can also be extended to explain why scour pits in the lee of three-dimensional dunes tend to occur farther downstream than the topographic minimum in the lee of two-dimensional ripples or dunes. In the three-dimensional case, the flow is partially steered around the obstacle, so the streamwise acceleration is reduced compared to the two-dimensional case. This allows longer reattachment lengths, in agreement with observations. This feedback between topographically-induced acceleration and reattachment length has been neglected in discussions of the development of bedforms, and appears to play an important role in determining height to wavelength ratios.

4.4.3. Streamwise Flow Development

In Figure 4.11, the streamwise development of dune crest velocity profiles is shown from both measurements and model results. The calculated results were obtained by running the model with one wake, then two stacked wakes, then three and finally four. Above the top of the highest wake, the velocity profile is set by the interaction of the potential flow solution with the turbulence structure advected from the region upstream of the first dune. Because the flume bed was smooth plexiglass upstream of the test area, the weak quasi-logarithmic shear in this region is completely overwhelmed by the potential flow response, and the upstream structure can be neglected. Over the second dune crest, where
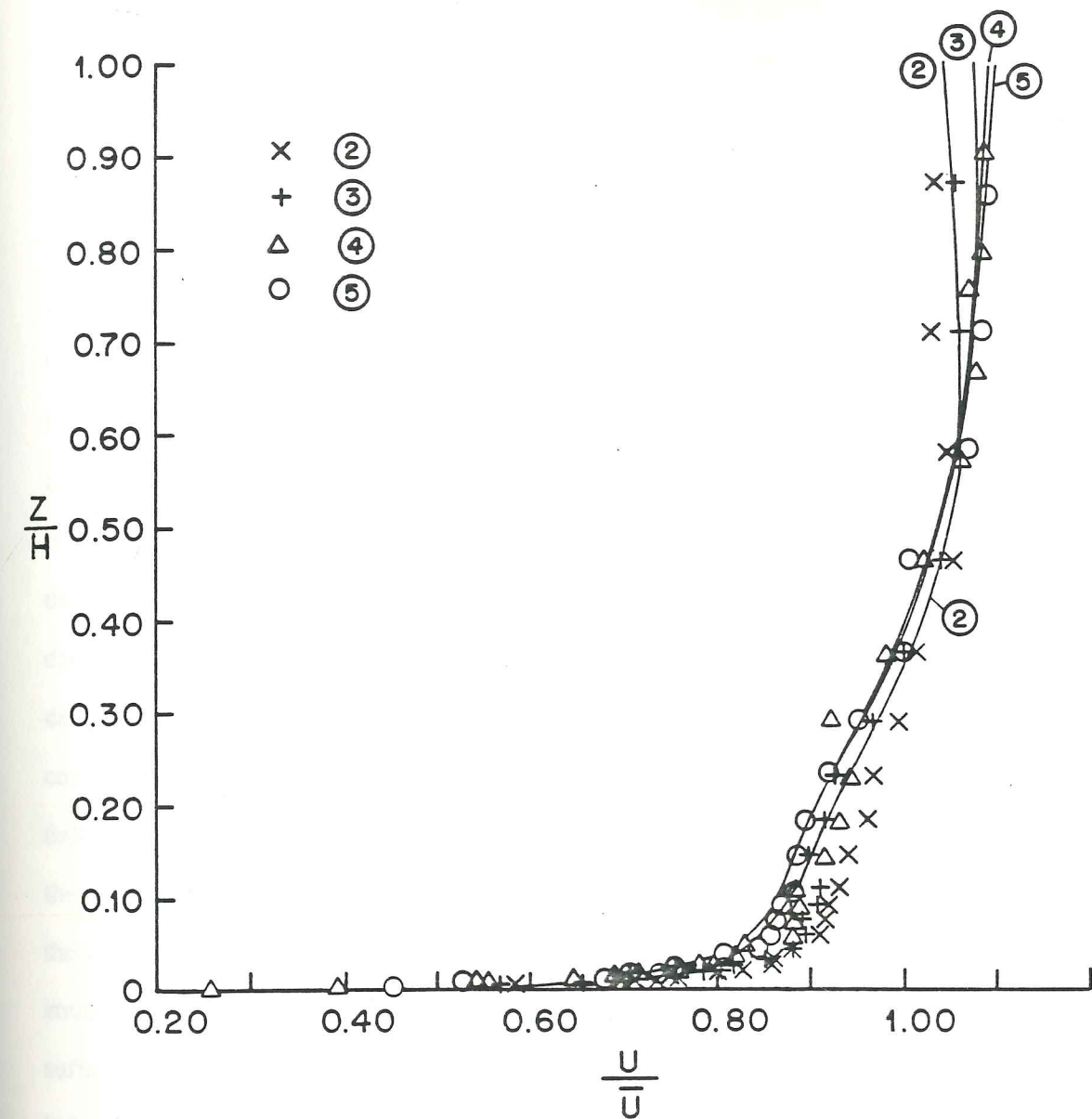
Figure 4.11. Velocity profiles measured at the crests of dunes 2, 3, 4, and 5 along with the profiles predicted by the model. The velocities are normalized by $\overline{U}$, the vertically averaged velocity, which was about 50 cm/sec.

only one upstream wake is present, both the measurements and the model predict a velocity maximum beneath the free surface. This is due to the shear induced by the potential flow response to the feature, and indicates the importance of including short wave effects through the potential flow weighting function, as described above.

Both the measurements and the model results indicate that the flow is essentially well-developed after the crest of the fourth dune, indicating that the experimental setup used the minimum number of dunes necessary for examining flows over natural trains of bedforms. While the downstream evolution is predicted at least qualitatively quite well by the simple model presented here, there are some notable discrepancies. First of all, the comparison indicates that, although the stacked wake model quantitatively predicts the flow over the last two dunes quite well, it overpredicts the momentum deficit of the flow above the second dune. This indicates that the interaction of the wakes produces an enhanced drag on the obstacle. If this is correct then the drag coefficient of 0.6, which was set using data taken over the downstream dunes, is valid only for the case of bedform trains. A drag coefficient of about 0.45 produced much better results for the upstream dune. This is partially a result of the choice of reference velocity in calculating the drag coefficient, since the velocity at the top of the wake of the first dune is not precisely equal to the velocity at the top of the wake of the dune located furthest downstream due to changes in the vertical structure of the flow. The difference in the reference velocities alone, however, is not sufficient to explain the discrepancy, and it is concluded here that the interaction of the turbulent length scales in the stacked wakes is sufficient to produce a greater drag than found in the case of a single wake. This is accounted for in the model by setting the drag coefficient for the stacked wake case.

The second notable discrepancy between the model results and the measured velocity profiles is the difference in the vertical structure at the matching point between the wake

and the internal boundary layer. The measured profiles in this region typically have less shear than predicted by the model. This is almost certainly a result of the interaction between the turbulent length scales in the wake with those in the boundary layer. In other words, the turbulent diffusivity near the top of the boundary layer may be characterized sporadically by length scales larger than the distance to the boundary in some sort of wake-boundary layer buffer zone. Nevertheless, the predicted velocities are typically only a few percent different than the measured ones and the boundary layer height at the dune crests is clearly accurately presented by the fluid dynamical model. Considering the complexity of the flow and the simplicity of the theoretical approach, the results are reasonable, and suitably accurate to be used in making predictions of sediment transport over natural bedforms.

4.4.4. Results for Well-developed Flow

Measured vertical profiles of downstream velocity along with the results of the calculations are shown in both linear and logarithmic form in Figure 4.12. These profiles are for a mean velocity of about 50 cm/sec and were measured over the fourth dune. The depth for this run was 20 centimeters, yielding a flow Reynolds number of about 10^5. The calculated profiles are in good agreement with the measurements. The only inputs to the flow model are the position of the reattachment point, the topography, the discharge, and the drag coefficient. The similarity vertical profile is only marginally correct in the near field, especially on the slip face, where vertical accelerations may become large. In general, however, the calculations reproduce the flow accurately in both a qualitative and quantitative sense, indicating that the lowest-order physics are contained in the model equations. In addition to downstream velocities, the theory and calculations produce shear stresses, vertical velocities, and diffusivities, thus providing the fluid dynamical component of a
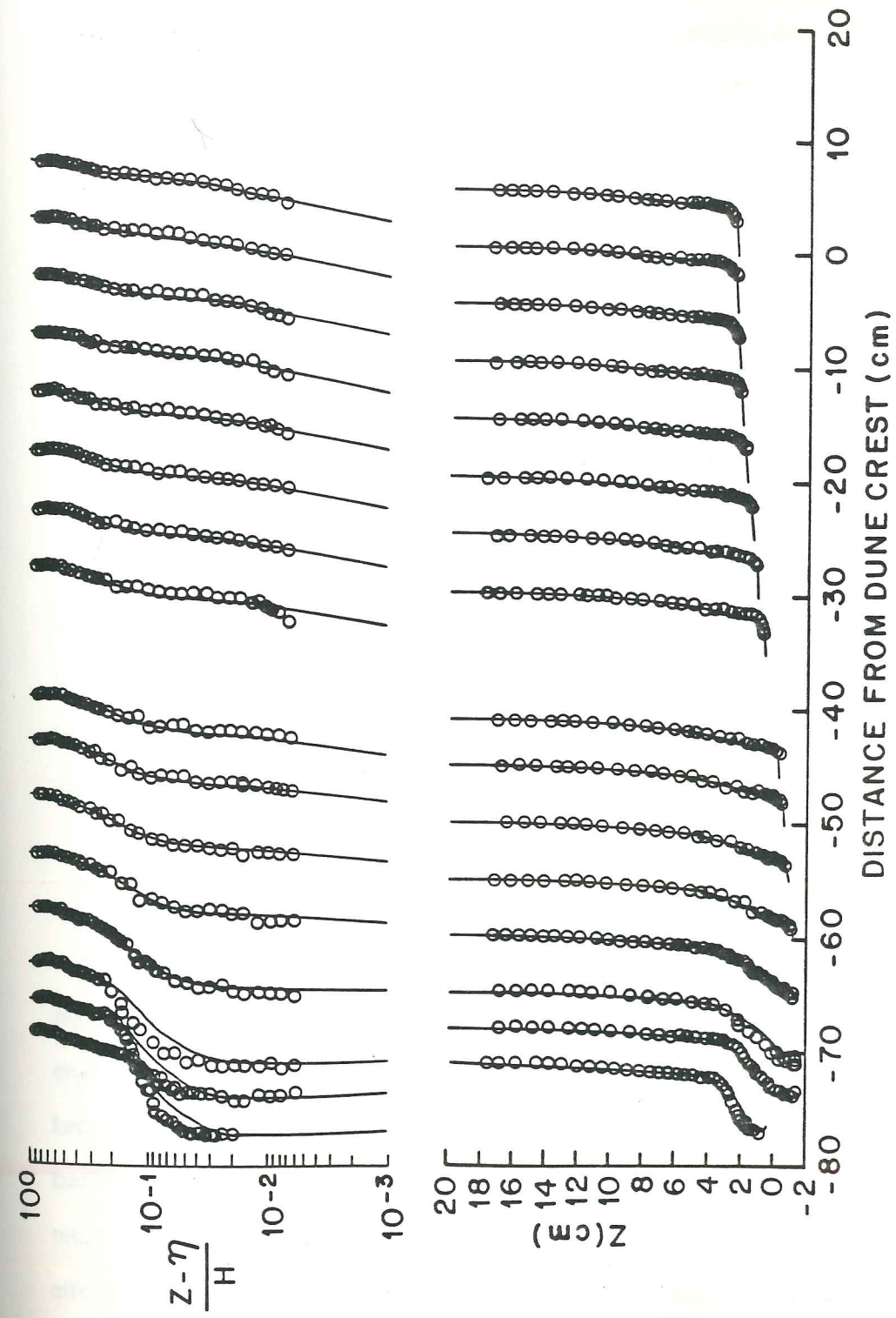
Figure 4.12. Linear and logarithmic velocity profiles over dune 4. The open symbols are the measured values and the solid lines are the velocity profiles predicted by the model. Flow depth was 20 cm and the mean velocity was 50 cm/sec for these measurements.

comprehensive theory of bedform sediment transport. For general application of the model to normal two-dimensional ripple and dune fields, the reattachment length can be set at 4.0H and the drag coefficient can be estimated as 0.60. The half-cosine geometry is a suitable first estimate, but should be modified iteratively using a specific sediment transport model if high accuracy is desired.

4.5. The Flow-Bed Coupling

One of the goals of the theoretical and experimental investigation described herein was to employ the model to investigate the stability and morphology of bedforms. To make specific quantitative predictions in this area, the fluid dynamical calculations must be linked to a comprehensive model of bedload and suspended load transport on a sloping bed. However, the results of the flow model can be used to generate physical insight into the interactions between the flow and the bed topography without resorting to a specific sediment transport model.

In the past, inquiries into bedform stability have been based primarily on the use of stability analysis, a technique by which the stability of bedforms is characterized by examining the behavior of sinusoidal disturbances on the bed. The pioneering study employing this approach was by Kennedy [1963], who applied a two-dimensional potential flow model in conjunction with an assumed phase lag, ϕ , between the flow velocity near the bed and the flux of sediment. This approach allowed Kennedy to identify various types of bedforms and the flow regimes in which they may be expected to occur based on the magnitude of ϕ. Although Kennedy's approach specifically neglected the complex real fluid effects ultimately responsible for the instability of the fluid-bed interface, he correctly showed that the production of bedforms was tied to a spatial shift between the sediment

flux and the fluid velocity. More recent work on bedforms fields in low Froude number flows has indicated that ϕ, the phase difference between the velocity and the sediment flux, can be separated into an upstream shift of the boundary shear stress relative to the flow velocity, which is entirely due to the mechanical response of the flow to the bedform, and a downstream shift of the sediment flux relative to the boundary shear stress, which is produced by sediment inertia effects [Smith, 1970], gravitational effects [Fredsoe, 1974], and suspended load transport [Engelund, 1970]. In this discussion, only the fluid mechanical effects responsible for the spatial lag between the boundary shear stress and the velocity are addressed; the coupling of this flow calculation to precise sediment transport algorithms is discussed elsewhere [Nelson and Smith, 1986a,b; Nelson, Wiberg, and Smith, in preparation].

Concentrating on the fluid dynamical aspects of the problem, Smith [1970] showed that, in the absence of a spatial lag between the boundary shear stress and the sediment transport, infinitesimal sinusoidal bed perturbations of all wavelengths are unstable in low Froude number shear flows and that no fastest growing wavelength is selected. His analysis showed that the interaction of topographically-induced acceleration with near-bed shear in the flow produces a maximum boundary shear stress slightly upstream of the crest of a bed feature. Thus, the bottom stress decreases near the obstacle crest and, because sediment flux is a monotonically increasing function of the shear stress, sediment is deposited near the crest of the feature, resulting in growth of the perturbation. The instability is a result of shifting the maximum boundary shear stress, and hence the maximum sediment flux, slightly upstream of the bedform crest. This is in agreement with the result obtained by Kennedy [1963]. For the case of lower regime bed features, Kennedy's analysis predicted that instability would occur only if the sediment flux was shifted downstream relative to the velocity by more than 3/4 of a wavelength but less than a full wavelength.

Since velocity is in phase with the topography for flows with low Froude numbers, this corresponds to shifting the sediment flux upstream up to 1/4 of a wavelength relative to the topography, in accord with the predictions from the fluid mechanical analysis.

In Figure 4.13, stoss side patterns of boundary shear stress are shown from model calculations for several dunes with the same heights but different wavelengths. The shape of the bedform used in the calculations was the same as shown in Figure 4.6 and the dune height was chosen relative to the water depth such that the features were growing. The spatial patterns of boundary shear stress that are displayed in this figure can be used along with calculations of bedload and suspended load transport to determine stable bed shapes. This is done iteratively, using the method described by Fredsoe [1982]. As shown in Figure 4.13, the upstream shift in the boundary shear stress in typically $O(\lambda/10)$. This is forced primarily by the topographically-induced acceleration and modified only weakly by the wake structure. The model reproduces the primary mechanism that causes boundary instability in flow over an erodible bed [Engelund, 1970; Smith, 1970], thereby permitting examination of the evolution of perturbed beds from an initial irregular state to an equilibrium set of bedforms.

In addition to the acceleration associated with the bed topography, there is a spatial acceleration associated with the diffusion of high momentum fluid into the wake region. In the absence of topographic nonuniformity, this acceleration interacts with the growing boundary layer downstream of the reattachment point in a manner that produces a boundary shear stress maximum downstream of the obstacle as discussed by McLean and Smith [1986], and measured by Jones [1978] and Bradshaw and Wong [1972]. This effect is important in the determination of bedform wavelengths, and in the development of bedforms downstream of an initial disturbance [Raudkivi, 1966; Smith 1970]. To predict velocities and bottom stresses in this situation without including the effects of topographically-

209
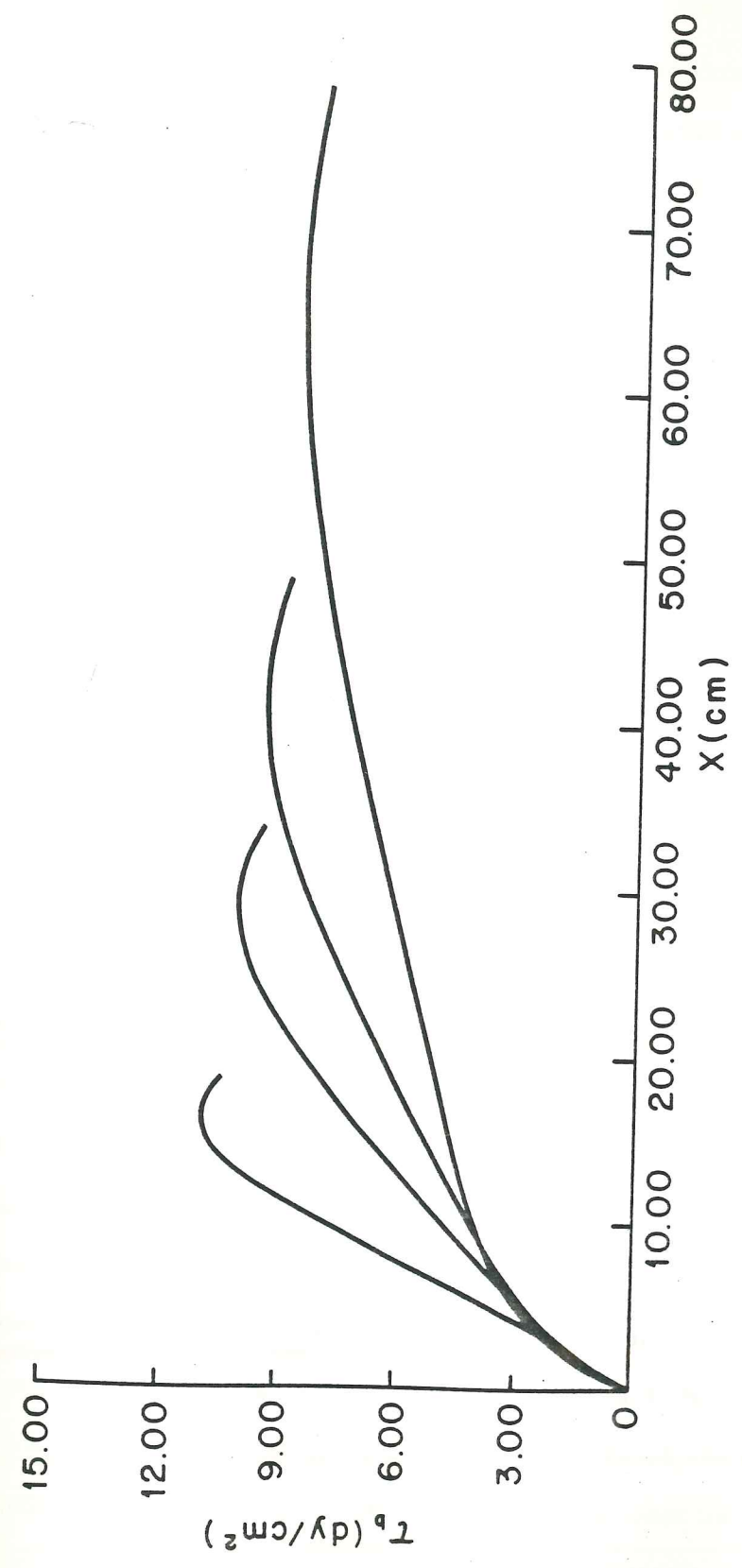
Figure 4.13. Calculated boundary shear stress profiles between the reattachment point and the downstream crest for several values of the wavelength. The reattachment point is located at x=0. For these runs, the flow depth was chosen to be 20 cm, the mean velocity was about 50 cm/sec, and the dune height was 3 cm. The wavelengths in these four cases were chosen to be 30, 45, 60, and 90 cm, corresponding to ripple indices of 10, 15, 20, and 30.

induced accelerations, the calculations described above are done assuming a flat bed downstream of a single backward step. In Figure 4.14, the model results are shown along with the values measured in the experiments of Jones [1968]. Physically, the maximum in the boundary shear stress is related to the competing processes of boundary layer growth and decreasing momentum deficit in the wake. Near the obstacle, the acceleration in the velocity at the top of the boundary layer associated with the diffusion of momentum into the wake region overwhelms the growth of the boundary layer, resulting in increasing bottom stress. Far downstream, the acceleration in the wake is relatively weak and the growth of the boundary layer acts to decrease the shear across the layer, resulting in decreasing bottom stress, as explained by McLean and Smith [1986]. The agreement found between the measured and predicted location of the boundary shear stress maximum provides further confidence in the techniques employed herein.

One of the defining features of dunes is that they have heights that are set by the depth of the flow in which they are formed. The ratio of flow depth to height for typical dunes in low Froude number flows was reported to be about 5.2 by Jones [1978], based on flume experiments. Yalin empirically found this ratio to be about five, but calculated a theoretical value of 2π [Yalin, 1977, p. 226]. Clearly, the cessation of growth of dunes at some fraction of the flow depth must be produced by an interaction between the flow and the topography. In Figure 4.15, boundary shear stress plots are shown for dunes with the same wavelength, but with various ratios of height to flow depth. The boundary shear stress maximum upstream of the crest producing the growth of the feature is weakened and finally destroyed as the obstacle grows to about one-fifth of the flow depth. This same result is found if the ratio of the height to wavelength of the bedform is held constant while the ratio of the flow depth to the dune height is decreased. As the dune grows, the Bernoulli pressure gradient at the crest becomes greater, since the velocity increases. This
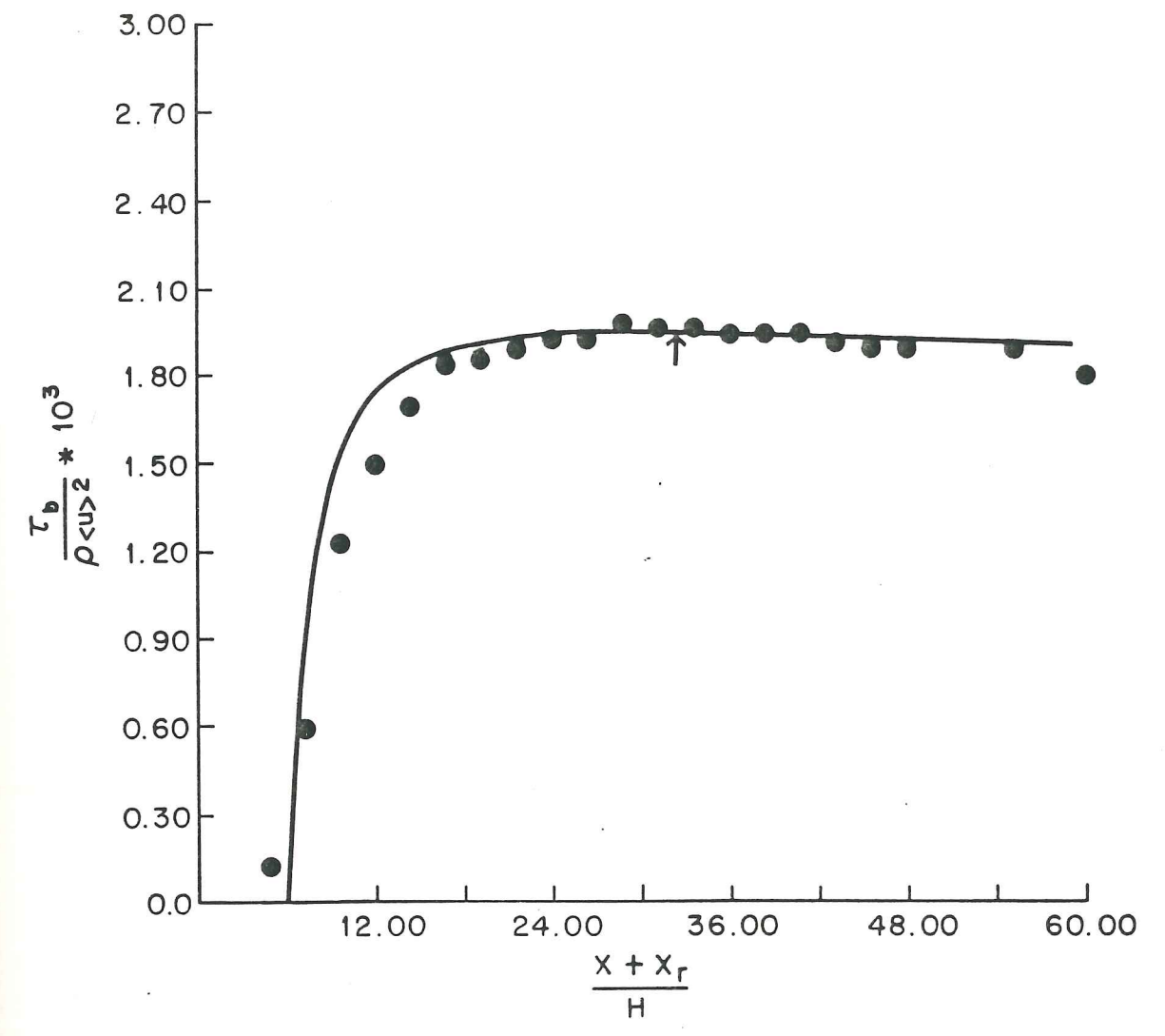
Figure 4.14. Nondimensional bottom stress versus distance from the obstacle crest. Data points are taken from Jones (1978), and the solid line is the prediction of the model described herein. The position of the maximum calculated stress is marked with an arrow.
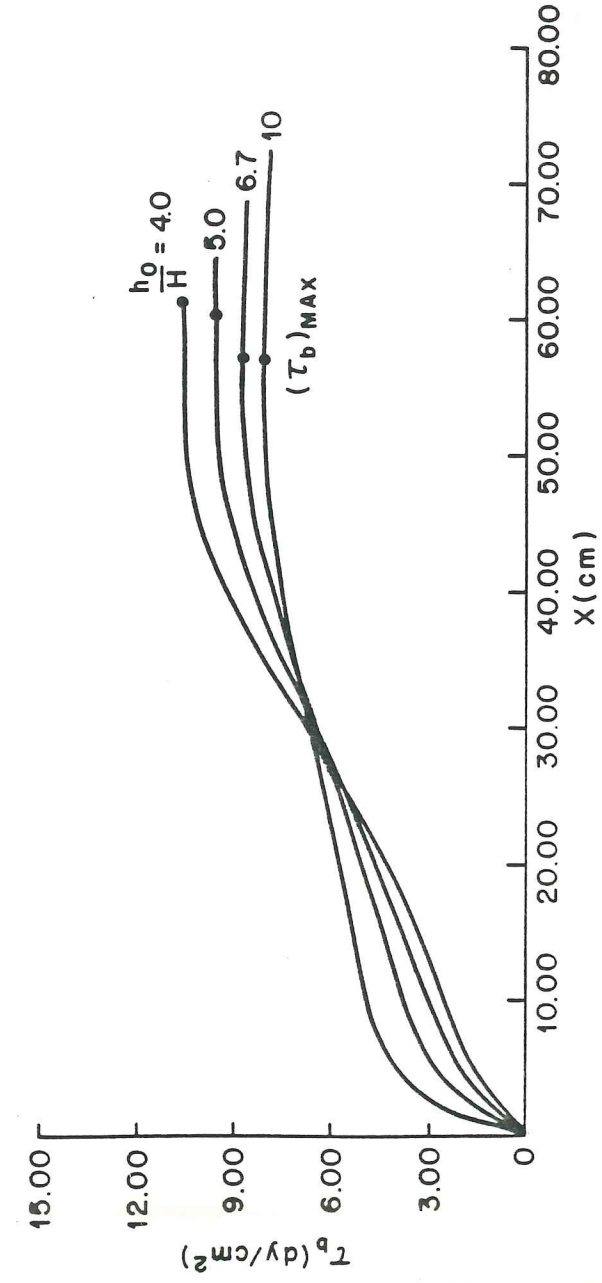
Figure 4.15. Streamwise profiles of bottom stress calculated for several values of flow depth to dune height. For these cases, the wavelength was held constant at 80 cm and the bedform height was varied (2, 3, 4, and 5 cm). The flow depth was 20 cm. The position of the maximum stress for each case is shown by a solid circle.

tends to compress the internal boundary layer near the crest, resulting in larger shears across the boundary layer and, therefore, larger boundary shear stresses. Accurate prediction of this effect requires both the interaction of the wake and boundary layer and the inclusion of the correct inviscid response of the flow to the obstacle such as the model described herein provides.

4.6. Summation of the Bedform Model Results

The morphology of natural bedforms is determined by complicated interactions between the flow, bed topography, and sediment transport. The first component in the development of a precise understanding of the processes active in this problem is a fluid dynamical model that can predict velocities and bottom stresses over realistic bed features accurately enough for sediment transport calculations to be made reliably. The comparison between calculated and experimental results displayed in this paper indicates that the theoretical approach taken herein provides that degree of accuracy. The success of the approach is a result of the preservation of appropriate turbulent length scales in the wake and boundary layer regions, as well as the inclusion of a nonhydrostatic wave response of the flow to the bedform.

By using the stacked wake theory to calculate the vertical structure well above the bedform, our formulation allows a coherent link to be made between the bed geometry and the interior flow structure. As discussed above, this link is important for understanding form drag and overall roughness in rivers and streams with duned or rippled beds. Furthermore, this approach permits accurate computations of local flow structure by retaining the effects of the diffusion and advection of momentum deficits in the interior region. In contrast, employing a spatially averaged logarithmic profile with a potential flow weighting

function assigns all of the horizontal structure to the wave-like part of the flow response, thereby ignoring additional structure associated with the wakes emanating from bedforms upstream.

In the last part of this chapter, it has been shown that the flow model reproduces the subtle interactions between the velocity field and the bed topography that are ultimately responsible for the growth and finite amplitude geometry of natural bedforms. First, it was demonstrated that the model correctly predicts an upstream shift in the position of the maximum boundary shear stress relative to the bedform crest for a feature of typical shape. This shift, which is associated with the interaction of near-bed shear in the flow with topographically-induced acceleration [Benjamin, 1959], has been identified as the boundary instability mechanism in low-Froude number flow over wavy surfaces [Smith, 1970]. Furthermore, the model is shown to predict a boundary shear stress maximum on a flat bed downstream of backward step. This fluid dynamical effect, which was also predicted by calculations presented by Smith [1970] and McLean and Smith [1986], is well-documented experimentally in the engineering literature [e.g., Bradshaw and Wong, 1972], and is related to the process by which bedforms evolve downstream from an initial disturbance [Raudkivi, 1966], as well as one of the factors exerting an influence on the wavelength of fully-developed bedforms [Smith, 1970; Fredsoe, 1982]. Finally, these calculations predict the cessation of bedform growth when the bedform height exceeds some fraction of the flow depth, as is commonly observed [e.g., Yalin, 1977, p. 226]. These features in conjunction with the comparison between the measured and calculated velocity fields demonstrate the validity of the model but, more importantly, they indicate the potential of using this approach to investigate the morphology of natural bedforms, which is the ultimate goal of this research.

The next step in this investigation is the combination of the flow model with sediment

transport algorithms. Some preliminary calculations coupling the flow model with a bedload equation and an advection-diffusion equation for suspended sediment have produced good predictions of the so-called 'dune to upper plane bed transition' [Nelson and Smith, 1986b], as well as the dependence of dune geometry and sedimentology on suspended load transport [Nelson and Smith, 1986a]. Present efforts are being directed toward integration of the flow model with a sediment transport model that better includes the effects of bed slope and sediment inertia. The coupling of this sediment transport theory with the fluid dynamical model presented here will lead to an understanding of natural bedforms in terms of the basic mechanics of the flow and sediment transport.

Chapter 5: Summary and Future Research Directions

Development of a fundamental understanding of the fascinating spectrum of erodible bed phenomena must be firmly grounded in the basic principles of physics. Following this philosophy, the work presented in this dissertation addresses two distinct types of flow-bed interactions: those primarily associated with changes in the horizontal structure of the flow, and those associated with changes in the vertical structure of the flow. Employing this bipartite approach yields two classes of problems, each of which is tractable at a level that does not preclude physical understanding of the dominant processes.

In formulating the bar and bedform problems, emphasis has been placed on creating the simplest model possible while still retaining the complexity necessary to treat natural flows. Bars and bedforms observed in riverine and estuarine flows are almost always fully-developed features. Thus, in both cases, salient nonlinearities associated with finite amplitude responses have been included. The techniques presented herein concentrate on treating the highly nonuniform flow and sediment transport fields typically observed, rather than examining weak perturbations about some simple zero-order flow.

The bar evolution model presented in Chapter 3 is constructed by coupling sediment transport calculations with an expanded version of the meander flow model developed and tested in Chapter 2. Using the evolution algorithm, the principle dynamic effects responsible for both the growth and finite amplitude stability of point and alternate bars have been identified. Assuming an initially flat bed and a sinuous planform, it has been demonstrated that the growth of the point bar is produced by an inward component of bottom stress induced by helical circulation. This is modified somewhat by variations in the streamwise bottom stress, which arise due to changes in the channel curvature. As the bar grows, convective accelerations associated with the streamwise variations in the topography become

increasingly important. As discussed in both Chapters 2 and 3, this flow response results in the steering of the fluid around the point bar. The equilibrium morphology of the channel bed is dependent on a balance of these two effects. Essentially, the bed deforms until the path of the highest sediment flux is forced to follow the high stress (velocity) core of the fluid flow field. Thus, outward sediment fluxes are found over much of the point bar, in sharp contrast to many earlier theories, but in good agreement with experimental observations.

For the case of alternate bars growing in an initially straight, flat-bedded channel, the evolution model has been used in conjunction with a linear stability analysis of the governing equations to examine the bar dynamics. The initial growth of alternate bars depends primarily on the topographic steering instability. As a bar grows in height, finite amplitude effects produce an increase in the wavelength and a steepening of the downstream face. At this point, both gravitational effects on the bedload fluxes and curvature of the flow streamlines begin to play a role in determining the bar morphology. Although the initial instability is easily found without these two effects, they are of crucial importance in predicting the equilibrium shape and migration rates of the bars.

Although the work described herein has concentrated on two well-defined bar types, the formulation is a general one, and is capable of predicting bed deformation and stability in a wide variety of situations. Thus, this work not only provides some very specific insights with respect to the mechanics of point and alternate bars, it also yields a tool with which even very complex bar morphologies may be investigated. In a sense, this work consists of the development and testing of a technique, the potential applications of which are vast. For instance, since the point bar evolution calculation predicts depositional patterns as the bar evolves, this technique can be used to investigate the development of point bar stratigraphy. Some simple evolution calculations for mixed grain sizes have reproduced

both upward and streamwise fining patterns in point bar deposits. Thus, with development, the theory presented herein may be employed to provide some very precise information about paleoflows based on observed stratigraphy. Similarly, the technique clearly has important applications in hydrology and river engineering.

The model for flow over bedforms developed and tested as part of this dissertation yields an understanding of the interactions between the flow structure and the bed nonuniformity. One of the most important aspects of this model is the use of the stacked wake idea, which is a powerful technique for examining changes in the vertical flow structure in the interior associated with the form drag of the bedforms. In conjunction with a simple potential flow solution and a nonuniform boundary layer theory, the wake stacking provides a technique whereby the flow field over bedform trains may be calculated without an empirical form drag closure. As discussed in Chapter 5, this model yields good predictions of measured velocity fields, and also reproduces the physical effects associated with bedform formation and finite amplitude morphology.

The next step in this work is the coupling of the flow model to sediment transport calculations in order to compute equilibrium bedform shapes. Some preliminary calculations of this nature have been performed [Nelson and Smith, 1986a] including both bedload and suspended load. While these calculations yield good predictions of the washout of bedforms due to suspended load [Nelson and Smith, 1986b], specific computations of stoss-side bedform profiles are critically dependent on the effects of gravitational forces on the sediment flux. Currently, this problem can only be treated using empirical gravitational corrections, similar to that employed in the bar evolution modelling.

The weakest link in the finite amplitude evolution modelling for either bars or bedforms is clearly the gravitational corrections to local sediment fluxes on the bed. Future work will concentrate on developing an appropriate treatment of this problem using the

theoretical saltation model presented by Wiberg and Smith [1985]. The application of their approach to beds that slope either along or transverse to the direction of the fluid boundary shear stress vector will provide a mechanistic treatment of the gravitational effects. Combination of this approach with the nonuniform flow theories described herein will eliminate the necessity for an empirical slope correction, and will permit the calculation of bedform shapes independent of empirical input. At present, shapes can easily be calculated using results presented in Chapter 4 along with any of the empirical bed slope corrections currently available. Calculations of this nature have been done previously using flow models which rely on empirical data [see, for example, Fredsoe, 1982].

It is appropriate to conclude this dissertation with a brief discussion of how the two different types of flow responses treated separately herein may be brought together in a single unified model. In Chapter 3, brief mention of this topic was made in the discussion of the perturbation equation for the streamwise velocity and stress field. It was argued that this equation, although easily soluble, may contain corrections to the streamwise similarity structure that are of the same order as corrections associated with errors in the simple turbulence closure model employed. In other words, local disequilibrium in the turbulence field may be as important in determining the variations in vertical structure as the spatial accelerations and decelerations. This leads to the necessity for a turbulence closure which accounts for the advection of turbulence. In the future, these effects will be explored using the turbulence closure described briefly in Chapter 3, wherein an eddy viscosity based on the local boundary shear stress and distance from the boundary is used at lowest order, and deviations about that simple structure are calculated subsequently using the lowest-order similarity solutions to advect the turbulent kinetic energy field. This allows the inclusion of wake-like effects in the flow structure over and around riverine bars, albeit only weakly (i.e., no flow separation). This improvement will allow the vertical structure changes

discussed in the bedform model to be brought into the bar model.

To investigate the mechanics of three-dimensional dunes and ripples, it is necessary to introduce cross-stream structure into the bedform model. This can be accomplished by first examining the case of two-dimensional bedforms with weakly sinuous crests. For this case, the two-dimensional similarity wake structure is still approximately correct, and one needs only to develop a three-dimensional potential flow model and account for the cross-stream fluxes of near-bed momentum in the boundary layer perturbation equations. This is relatively straightforward, and should yield insights into the mechanism by which two-dimensional features evolve into three-dimensional ones. However, this approach probably does not yield good flow and bottom stress predictions for fully-developed three-dimensional bedforms, because the wake structure must eventually become completely three-dimensional. The case of full three-dimensionality including separation effects is complicated, and is essentially the end member of both the bar problem and the bedform problem. The initial work to be done on this problem involves the development of a theory for lateral flow separation. Hopefully, the insight gained thereby will lead to a general theory of separation in three-dimensional flows accurate enough to employ in sediment transport problems.

In conclusion, the analysis and results presented herein lay the groundwork on which an understanding of a wide variety of erodible bed phenomena can be founded. The key to the future development and application of these techniques is strict adherence to fundamental principles of physics. This philosophy, in conjunction with careful experimental verification and an unswerving desire to exchange empiricisms for physical understanding, will lead to interpretations of channel morphology in terms of basic physical processes.

REFERENCES

Ascanio, M.F., and J.F. Kennedy, Flow in alluvial river curves, J. Fluid Mech., 133(1), 1-16, 1983.

Benjamin, T.B., Shearing flow over a wavy boundary, J. Fluid Mech., 6, 161-205, 1959.

Blondeaux, P. and G. Seminara, A unified bar-bend theory of river meanders, J. Fluid Mech., 157, 449-470, 1985.

Bradshaw, P. and F.V.F. Wong, The reattachment and relaxation of a turbulent shear layer, J. Fluid Mech., 52, 113-135, 1972.

Callander, R. A., Instability and river channels, J. Fluid Mech., 36, 465-480, 1969.

Columbini, M., G. Seminara and M. Tubino, Finite-amplitude alternate bars, J. Fluid Mech., 181, 213-232, 1987.

De Vriend, H.J., A mathematical model of steady flow in curved shallow channels, J. Hydraul. Res., 15(1), 37-54, 1977.

Dietrich, W.E., Flow, boundary shear stress, and sediment transport in a river meander, Ph.D. dissertation, 261 pp., Univ. of Wash., Seattle, 1982.

Dietrich, W.E. and J.D. Smith, Influence of the point bar on flow through curved channels, Water Resour. Res., 19(5), 1173-1192, 1983.

Dietrich, W.E., and J.D. Smith, Bedload transport in a river meander, Water Resour. Res., 20(10), 1355-1380, 1984.

Durst, F., A. Mellin, and J.H. Whitelaw, *Principles and Practices of Laser-Doppler Anemometry,* A.C. Press, 1974.

Eaton, J.K., and J.P. Johnston, *Turbulent Flow Reattachment: An Experimental Study of the Flow and Structure Behind a Backward-Facing Step,* Dept. of Mech. Eng. Report MD-39, Stanford University, 1980.

Engel, P., Length of flow separation over dunes, J. Hydraul. Div. ASCE, 107, 1133-1143, 1981.

Engelund, F., Instability of erodible beds, J. Fluid Mech., 42, 225-244, 1970.

Engelund, F., Flow and bed topography in channel bends, J. Hydraul. Div. ASCE, 100(HY11), 1631-1648, 1974.

Etheridge, D.W., and P.H. Kemp, Measurements of turbulent flow downstream of a rearward-facing step, J. Fluid Mech., 86, 545-566, 1978.

Fredsoe, J., On the development of dunes in erodible channels, J. Fluid Mech., 64, 1-16, 1974.

Fredsoe, J., Shape and dimensions of ripples and dunes, J. Hydraul. Div. ASCE, 108, 932-947, 1982.

Fujita, Y., and Y. Muramoto, Studies on the process of development of alternate bars, Bull. Disast. Prev. Res. Inst., Kyoto Univ., 35(3), 55-86, 1985.

Fukuoka, S., K. Uchijima, M. Yamasaka, and H. Hayakawa, Distribution of sediment transport rate over alternate bars, Proc. of the 30th Japanese Conference on Hydraulics, 1983.

Hooke, R. L., Shear-stress and sediment distribution in a meander bend, Uppsala Univ. Naturgeografiska Inst. Rapport 30, 1974.

Hooke, R. L., Distribution of sediment transport and shear stresses in a meander bend, J.Geol., 83, 543-565, 1975.

Ikeda, S., Prediction of alternate bar wavelength and height, J. Hyd. Eng., 110(4), 371-386, 1984.

Jones, D.F., An experimental study of the distribution of boundary shear stress and its influence on dune formation and growth, M.S. thesis, Univ. of Washington, Seattle, WA, 1978.

Kennedy, J.F., The mechanics of dunes and antidunes in erodible-bed channels, J. Fluid Mech., 16, 521-544, 1963.

Keuhn, D.M., Some effects of adverse pressure gradient on the incompressible reattaching flow over a rearward-facing step, AIAA Journal, 18, 343-344, 1980.

Kikkawa, H., S. Ikeda, and A. Kitagawa, Flow and bed topography in curved open channels, J. Hyd. Div. ASCE, 102(HY9), 1327-1342, 1976.

Kobayashi, N., and O.S. Madsen, Formation of ripples in erodible channels, J. Geophysical Res., 90, 7332-7340, 1985.

Langbein, W.B., and L.B. Leopold, River meanders - Theory of minimum variance, U.S. Geol. Surv. Prof. Pap., 422-H, H1-H15, 1966.

Leliavsky, S., *An Introduction to Fluvial Hydraulics*, Constable, London, 1955.

Leopold, L. B., Water surface topography in river channels and implications for meander development, in *Gravel-bed Rivers*, ed. R. D. Hey, J. C. Bathurst, and C. R. Thorne, John Wiley, London, 1982.

McLean, S.R., and J.D. Smith, A model for flow over two-dimensional bed forms, J. Hyd. Eng. ASCE, 112, 300-317, 1986.

Narayanan, M.A.B., V.N. Khadgi, and P.R. Viswanath, Similarities in pressure distribution in separated flow behind backward-facing steps, Aero Quarterly, 25(4), 305-312, 1974.

Nelson, J.M., and J.D. Smith, The role of suspended sediment in the dune to upper plane bed transition, abstract published in EOS Transactions, 67 (44), 959, 1986.

Nelson, J.M., and J.D. Smith, Formation of tangential foresets on the lee side of two-

dimensional dunes, abstract published in SEPM Mid-year Meeting Abstracts, vol. 3, 82, 1986.

Nowell, A.R.M., P.A. Jumars, and R.F.L. Self, The effects of sediment transport and deposition in deposit feeders: Results obtained in a specially designed flume, in *Deposit Feeding,* ed. G.R. Lopez and G.L. Taghon, Springer Verlag, in press.

Odgaard, A. J., Transverse bed slope in alluvial channel bends, J. Hyd. Div. ASCE, 107(HY12), 1677-1694, 1981.

Onishi, Y., Effects of meandering on sediment discharges and friction factors of alluvial streams, Ph.D. dissertation, 158 pp., Univ. of Iowa, Iowa City, 1972.

Parker, G., On the cause and characteristic scales of meandering and braiding in rivers, J. Fluid Mech., 76, 457-480, 1976.

Raudkivi, A.J., Bed forms in alluvial channels, J. Fluid Mech., 2, 507-514, 1965.

Richards, K.J., The formation of ripples and dunes on erodible bed, J. Fluid Mech., 99(3), 597-618, 1980.

Rozovskii, I.L., *Flow of Water in Bends of Open Channels,* Israel Program for Scientific Translation, originally published by Academy of Sciences of the Ukranian SSR, 233 pp., 1957.

Schlicting, H., *Boundary Layer Theory,* McGraw-Hill, New York, 1979.

Shimizu, Y., and T. Itakura, Practical computation of two dimensional flow and bed deformation in alluvial streams, Civil Engineering Research Institute Report, Hokkaido Development Bureau, Sapporo, 1985.

Smith, J.D., Stability of a sand bed subjected to a shear flow of low Froude number, J. Geophysical Res., 75, 5928-5940, 1970.

Smith, J.D., Modeling of sediment transport on continental shelves, in Goldberg, E.D., ed., *The Sea: Ideas and Observations on Progress in the Study of the Sea,* Wiley and Sons, New York, 1977.

Smith, J.D., and S.R. McLean, Spatially averaged flow over a wavy surface, J. Geophysical Res., 82, 1735-1746, 1977.

Smith, J.D., and S.R. McLean, A model for flow in meandering streams, Water Resour. Res., 20(9), 1301-1315, 1984.

Struiksma, N., K. W. Olesen, C. Flokstra, and H. J. de Vriend, Bed deformation in curved alluvial channels, Jour. Hyd. Res., 23(1), 57-77, 1985.

Sumer, B.M. and M. Bakioglu, On the formation of ripples on an erodible bed, J. Fluid Mech., 144, 177-190, 1984.

Wiberg, P.L., and J.D. Smith, A theoretical model for saltating grains in water, J. Geophysical Res., 90(4), 7341-7354, 1985.

Williams, G.P., Flume width and water depth effects in sediment transport experiments, U.S. Geol. Survey Prof. Paper 562-H, 1970.

Yalin, M.S., An expression for bedload transportation, J. Hydraul. Div. ASCE, 89(HY3), 221-250, 1963.

Yalin, M.S., *Mechanics of Sediment Transport,* Pergamon, 1977.

Yen, C., Bed configuration and characteristics of subcritical flow in a meandering channel, Ph.D. dissertation, 123 pp., Univ. of Iowa, Iowa City, 1967.

Yen, C., and B.C. Yen, Water surface configuration in channel bends, J. Hydraul. Div. ASCE, 97(HY2), 303-321, 1971.

Zimmerman, C., and J. F. Kennedy, Transverse bed slopes in curved alluvial streams, J. Hydraul. Div. ASCE, 104(HY1), 33-48, 1978.

JONATHAN MARK NELSON

Born:

June 19, 1959
Seattle, Washington

Education:

Kent-Meridian High School, 1977
Kent, Washington

B.S., Physics (M.C.L.), 1981
University of Puget Sound
Tacoma, Washington

M.S., Geophysics, 1986
Ph.D., Geophysics, 1988
University of Washington
Seattle, Washington